

# **Use of Geoelectrical Techniques with Numerical Modelling for Surveying and Monitoring of Engineered Water Retaining Structures**



**John Ball**

**This thesis is submitted for the degree of Doctor of Philosophy on  
March 2023**

**Lancaster Environment Centre**



## Declaration

This thesis has not been submitted in support of an application for another degree at this or any other educational institution. The work entailed has been undertaken by myself, except for collaboration with individuals who have been specifically credited. Much of the ideas presented are the product of discussion with my supervisors, Prof. Andrew Binley, Prof. Jonathan Chambers and Dr. Paul Wilkinson, as well as Prof. Karl Butler for work concerning Mactaquac Dam in Canada. The information gathered from the literature has been duly acknowledged in the text and given in a reference list provided.

John Ball

## Abstract

Water retaining structures are societally and economically important barriers which degrade through various erosional processes over time. Walkover surveys and geotechnical investigations are traditionally used to examine such structures but are limited by a lack of knowledge of internal structure. Near-surface geophysics can provide comprehensive information about the internal structure of embankments, and several techniques exist which can survey and monitor water retaining structures. One such technique is electrical resistivity tomography (ERT), where the resistivity profile of the ground can be linked to moisture content, porosity, and composition, making it a useful tool for use in detecting defects and changes in ground conditions within water retaining structures. However, several uncertainties exist with ERT for use on embankments. A key problem is whether results will be impacted by a 3D effect, where off-line features influence resistivities in the inversion. Such features may be the water body itself, or complex engineering structures within the barrier.

This thesis explores the impact of a 3D effect arising from the water body and structural geometry. The work was undertaken using synthetic numerical modelling of an embankment in a tidal setting and a fluctuating water level and resistivity, which was then compared to real ERT data. Further synthetic numerical modelling of the Mactaquac dam, Canada, was used as a case study assessing the influence of a large concrete structure within the dam on ERT data. The study also examined the effect of resistivity variation in the headpond of the dam through time.

Comparisons between 2D and 3D inversions were also assessed to determine the possibility of 3D inversions mitigating any 3D effects. This was undertaken for sites at Bartley Dam, Birmingham, UK and Paull Holme Strays, Yorkshire, UK. The Bartley Dam case study utilised time-lapse ERT to determine the value of 3D inversions over 2D inversions in a monitoring scheme and to identify whether 3D or 2D inversions could adequately identify water seepage present with changes in ground conditions. The Paull Holme Strays case study focussed on use of crosslines in a 3D inversion for a tidal embankment and compared outcomes to a 2D inversion without use of crosslines.

The results of the research shows that 3D effects are likely to be significant when undertaking ERT surveys of a water retaining structure, e.g. artefacts induced by a river with changing water level and resistivity, in addition to the impact of engineering structures that may be present in the embankment. Analysis of time-lapse ERT data at the at Mactaquac Dam site has revealed that changing headpond resistivity can create compensatory effects in an ERT data inversion. No seepage pathways could be reliably identified in time-lapse analysis of Bartley Dam with 2D inversions, likely because of 3D effects and sensitivity issues, whereas 3D inversions had more reliable evidence of seepage pathways. However, analysis of Paull Holme Strays showed that when a large proportion of the measurements have been filtered, there might be artefacts induced by another electrode array along the crest. However, use of crosslines enhanced the ability for a 3D inversion to reduce 3D effects at Paull Holme Strays.

This research has shown that 3D effects can be detrimental to ERT surveys, particularly in 2D inversions. However, 3D inversions can mitigate the effect where differences in data filtering between lines are minimal. For further reduction in the impact of the 3D effect it is recommended that smaller crosslines are used between the major electrode lines. Also, results should be compared with geological, geotechnical and hydrological information for understanding the reliability of the inversion.

There is a need for further exploration of the impacts of 3D effects on ERT in other water retaining structures and environments, as well as undertaking more comprehensive studies into dynamic changes within embankments and how they impact the 3D effect. By incorporating dynamic change into a synthetic model, a greater understanding of how 3D effects can impact ERT surveys of water retaining structures can be made, especially for time-lapse ERT.

## Acknowledgements

Firstly, I am thankful for the Engineering and Physical Sciences Research Council (EPSRC) for providing the financial support and research costs which made my PhD possible (grant reference: SEF6818). Alongside this I would like to thank the British Geological Survey (BGS) for providing further research funding for my PhD, as part of the BGS University Funding Scheme (BUFI) (grant reference: GA/205/001/A1).

I would like to express my thanks and gratitude to my supervisor, Prof. Andrew Binley for providing excellent guidance throughout my PhD, and devoting so much time and effort to ensure my work is the best it can be. I would also like to thank him for providing me with support and opportunities which have enabled me to complete this PhD and progress my skills and expertise within science. I would also like to thank him for developing collaborative opportunities throughout my PhD, primarily with the BGS, which have enabled me to develop as a student and scientist.

I would like to thank my supervisors at the BGS Tomography team, Prof. Jonathan Chambers and Dr. Paul Wilkinson, for their discussions, support and guidance throughout my PhD during the monthly meetings between Lancaster University and the BGS. The forum of ideas shared from all supervisors helped me to understand the subject from different angles and allowed my work to develop greatly. I would also like to thank them for their provision of excellent resources which have helped me complete this PhD, including data for the Hadleigh Marsh and Bartley Dam field sites which have formed key components of my thesis. In relation to this, I would also like to thank Nick Slater and Socotec for providing details regarding piezometric and other groundwater related data for Bartley Dam. Alongside these I would like to thank Dan Normandale and the Environment Agency for reaching out and collaborating with fieldwork along embankments across the Humber region, including Paull Holme Strays which formed the basis of a chapter in my thesis.

Further gratitude is owed to Prof. Karl Butler of the University of New Brunswick, who gave excellent advice and mentorship, as well as being a very welcoming and accommodating host, as a host supervisor for a Globallink placement scheme between the UK and Canada. This provided an exciting opportunity to study abroad, where I undertook research into the Mactaquac Dam field study, which formed the focus of one chapter for my thesis. I would also

like to thank the UKRI and Mitacs for their financial support which made this placement possible (grant reference: NE/V010123/1).

I would like to thank my colleagues from Lancaster University and the BGS who have provided me with endless support with my PhD, including in providing me with help in using software I was unfamiliar with, to being fieldwork support and moral support. This includes Guillaume Blanchy, Jimmy Boyd, Adrian White, Michael Tso, Paul McLachlan, Tuvia Turkeltaub, Arnaud Watlet, Vassil Karluokovski, Line Madsen, Madhuri Sugand and Martina Tabaro. I would like to thank Lee Slater and the team at Rutgers University for being accommodating hosts when I visited Rutgers University and attended American Geophysical Union (AGU) Fall Meetings in 2021 and 2022. I would also like to give further thanks to Adrian White for his collaboration on Paull Holme Strays, providing me with the 3D models needed for analysis.

Finally, I would like to thank my parents, family and friends for their invaluable moral support and patience during my PhD, as well as for being there when I needed them. Without them it would have been much harder to sustain my self-belief during the good times and the bad.

## Contents

<b>1.0 THESIS INTRODUCTION AND AIMS</b> .....	<b>1</b>
1.1 Introduction .....	1
1.2 Thesis Aims .....	1
1.3 Thesis Structure .....	4
<b>2.0 LITERATURE REVIEW</b> .....	<b>6</b>
2.1 Introduction .....	6
2.2 Degradation of Water Retaining Structures.....	8
2.2.1 Overtopping.....	10
2.2.2 Internal Erosion .....	10
2.2.3 Surface and Biological Erosion .....	13
2.2.4 Slope Instability .....	15
2.2.5 Other Defects .....	16
2.3 Geophysical Approaches .....	16
2.3.1 Electrical Resistivity Tomography (ERT) .....	17
2.3.1.1 Time-lapse ERT .....	21
2.3.1.2 Recent Developments .....	21
2.3.2 Induced Polarisation (IP) .....	22
2.3.2.1 Recent Developments .....	24
2.3.3 Self Potential (SP) .....	24
2.3.4 Seismic Surveying .....	26
2.3.4.1 Active and Passive Seismic Surveying .....	27
2.3.4.2 Recent Developments .....	27
2.3.5 Electromagnetic Induction (EMI).....	28
2.3.5.1 Recent developments .....	30
2.3.6 Electrical Current Imaging.....	30
2.3.7 Magnetometric Resistivity (MMR) .....	31
2.3.8 Ground Penetrating Radar (GPR) .....	32
2.3.9 Distributed Temperature Sensing (DTS) .....	33
2.3.9.1 Recent developments for distributed optical fibre sensors (DOFS) .....	35



2.3.10 Numerical Modelling .....	36
2.3.11 Physical Modelling and Geophysical-Geotechnical Relationships .....	39
2.4 Discussion .....	42
2.4.1 Characterisation of Degradation within Water Retaining Structures .....	42
2.4.2 Applicability of Geophysics .....	47
2.4.3 Differences in Application of Geophysics between Different Water Retaining Structures .....	49
2.4.3.1 Geophysical Monitoring of Tailings and Reservoir Dams.....	49
2.4.3.2 Geophysical monitoring of Levees, Dykes and Flood Embankments .....	52
2.4.4 Uncertainties and Limitations in Geophysics.....	52
2.4.4.1 Modelling.....	52
2.4.4.2 Site Specific Considerations .....	54
2.4.5 Routes for Future Development of Geophysical Applications for Water Retaining Structures.....	55
2.5 Summary.....	56
<b>3.0 RESISTIVITY IMAGING OF RIVER EMBANKMENTS: 3D EFFECTS DUE TO VARYING WATER LEVELS IN TIDAL RIVERS.....</b>	<b>57</b>
<b>3.1 Introduction .....</b>	<b>57</b>
<b>3.2 Synthetic Numerical Modelling.....</b>	<b>58</b>
3.2.1 Methodology .....	58
3.2.2 Synthetic Modelling Results.....	62
3.2.2.1 Array Configurations .....	62
3.2.2.2 Distance of River from Electrode Array.....	64
3.2.2.3 River Salinity .....	66
3.2.2.4 Electrode Spacing .....	67
3.2.2.5 Embankment Heterogeneity.....	68
3.2.2.6 Sensitivity Distribution .....	69
3.3 Hadleigh Marsh, Essex, United Kingdom.....	70
3.3.1 Hadleigh Marsh Results.....	72
3.4 Discussion .....	79
3.4.1 Synthetic Numerical Modelling .....	79
3.4.2 Hadleigh Marsh, Essex, United Kingdom.....	81

3.4.3 Recommendations.....	83
3.5 Summary.....	84
<b>4.0 ACCOUNTING FOR RESERVOIR AND INFRASTRUCTURAL EFFECTS AT THE MACTAQUAC DAM, NEW BRUNSWICK, CANADA: A CASE STUDY MODELLING IMPACTS OF CONCRETE STRUCTURES AND RESERVOIR ON ERT DATA.....</b>	<b>87</b>
4.1 Introduction .....	87
4.2 Mactaquac Dam .....	88
4.3 Synthetic Modelling.....	92
4.3.1 Methodology.....	92
4.3.2 Results.....	106
4.3.2.1 Effect of the concrete wingwall on resistivity imaging .....	106
4.3.2.2 Effect of headpond resistivity changes on resistivity imaging .....	110
4.3.2.3 Incorporation of a seepage zone into the core .....	115
4.3.2.4 2D Modelling of L1 .....	119
4.4 Inversion of Mactaquac field data .....	120
4.5 Discussion .....	122
4.5.1 The Effect of the Concrete Abutment.....	122
4.5.2 The Effect of Headpond Resistivity.....	124
4.5.3 Incorporation of a Seepage Zone .....	125
4.5.4 Comparison of the Synthetic Numerical Models to Inversions at Mactaquac Dam.....	126
4.5.5 Recommendations.....	127
4.6 Summary.....	128
<b>5.0 COMPARISON AND ASSESSMENT OF 2D AND 3D INVERSIONS FOR DETERMINING THE MOST APPROPRIATE INVERSION, FROM BARTLEY DAM, BIRMINGHAM, UK.....</b>	<b>130</b>
5.1 Introduction .....	130
5.2 Bartley Dam, Birmingham, United Kingdom.....	131
5.3 Methodology.....	136
5.3.1 Data Quality Control.....	138

5.4 Results .....	140
5.4.1 Geological and Hydrological Data .....	140
5.4.2 2D Inversions .....	143
5.4.3 3D Inversions .....	150
5.4.4 Electromagnetic Induction Survey .....	155
5.5 Discussion .....	156
5.5.1 Differences Between 2D and 3D Inversions for a Singular Inversion .....	156
5.5.2 Differences Between 2D and 3D Inversions for Time-Lapse Modelling .....	157
5.5.3 Accounting for the Presence and Cause of Seepage .....	157
5.5.4 Recommendations .....	159
5.6 Summary .....	160
<b>6.0 A COMPARISON OF 2D AND 3D INVERSIONS, USING CROSSLINES, AT PAULL HOLME STRAYS, YORKSHIRE, UNITED KINGDOM .....</b>	<b>162</b>
6.1 Introduction .....	162
6.2 Paull Holme Strays, Yorkshire, United Kingdom .....	163
6.3 Methodology .....	168
6.4 Results .....	172
6.4.1 2D Inversions .....	172
6.4.2 3D Inversions .....	174
6.4.3 EMI .....	179
6.5 Discussion .....	181
6.5.1 Use of Crosslines and Comparisons Between 2D and 3D Inversions .....	182
6.5.2 Recommendations .....	184
6.6 Summary .....	185
<b>7.0 DISCUSSION .....</b>	<b>186</b>
7.1 Introduction .....	186
7.2 Thesis Outcomes .....	187
7.2.1 The Impact of 3D Effects on Water Retaining Structures .....	187
7.2.2 The Applicability of Using 3D Inversions over 2D Inversions to Account for 3D Effects .....	189

7.2.3 <i>Temporal Changes and the 3D Effect, and use of 3D Versus 2D Inversions</i>	190
7.2.4 <i>Mitigation of 3D Effects</i> .....	191
7.3 The Applicability of the Research Outcomes to the Academic Literature .....	194
7.4 Future Developments for Geophysical Monitoring of Water Retaining Structures .....	196
7.4.1 <i>Future Developments for Understanding the Impacts of a 3D Effect on Water Retaining Structures and how 3D Inversions may Improve Results</i> .....	196
7.4.2 <i>Future Developments for the use of Other Geophysical Methods for Monitoring Water Retaining Structures</i> .....	198
<b>8.0 CONCLUSIONS</b> .....	<b>200</b>
8.1 Thesis Summary .....	200
8.2 Limitations .....	201
8.3 Future Research .....	202
<b>References</b> .....	<b>204</b>
<b>Appendix A – Resistivity Imaging of river embankments: 3D effects due to varying water levels in tidal rivers (accepted manuscript)</b>	<b>231</b>
<b>Appendix B – Input File Codes for Modelling</b> .....	<b>247</b>

## List of Figures

<b>Figure 2.1:</b> a) A model of how progression of erosion can lead to a continuous path for water to flow through a dam, and how this can lead to breaching (Foster & Fell 1999). b) A photograph of a slope failing on an embankment. Erosional processes, as shown in Figure 1.0, can form planes of weakness in which slopes may later fail (Polemio & Lollino 2011). .....	9
<b>Figure 2.2:</b> Modes of internal erosion within embankments, where TWL is the water level and a) shows propagation of a crack from concentrated erosion, b) shows the migration of fines, propagating upwards, from backward erosion and c) is migration of fines from suffusion. (Almog et al., 2011). .....	12
<b>Figure 2.3:</b> Modes of surface erosion in an embankment, where a) is a representation of erosion caused by vegetation and b) is a representation of burrowing by different animals (Almog et al., 2011). .....	14
<b>Figure 2.4:</b> Schematic for an ERT survey, showing the electrode setup, potential and current electrodes ( $\Delta V$ and $I$ ), the ERT data collection instrument ( $\Omega$ ) and the electrical current in the ground (Binley & Slater, 2020). .....	18
<b>Figure 2.5:</b> Distortions upon resistivity caused by the dam's topographic structure for a) a pole-dipole array and b) a dipole-dipole array (Cho et al., 2014). .....	20
<b>Figure 2.6:</b> : The principles of IP, showing the injection of current from two current electrode, the two potential electrodes and the charges resulting from a chargeable mass in the ground (Gandhi & Sarkar, 2016). .....	23
<b>Figure 2.7:</b> The different arrays for self-potential surveying, where a) is the leap-frog method and b) is the fixed base method (Wang et al., 2018). .....	25
<b>Figure 2.8:</b> A seismic survey showing the reflection and refraction of waves from a layer boundary. The Geophones can be used to detect the reflected and refracted waves from a source (Hunter et al., 2022). .....	26
<b>Figure 2.9:</b> Principles of an EMI survey, where a transmitter coil generates a primary magnetic field, which induces eddy currents and a secondary magnetic field. This is then detected by the receiver coil (Mester, 2015). .....	28
<b>Figure 2.10:</b> Three methods of utilising electrical current imaging along an electrode array. Where a) is a cross potential array, which measures the differences in potential across singular upstream and downstream poles and b) is its associated plot. c) is a direct potential array, which measures the potential difference between adjacent electrodes in each line and d) is its associated plot. e) is a D-lux array which measures the potential difference between all the upstream and downstream poles and f) is the resultant matrix, which is similar to a tomogram (Lee & Oh, 2018). .....	31
<b>Figure 2.11:</b> Schematic representation of a GPR survey, showing the transmission of the waves and detection by a receiver, as well as a 1D electromagnetic trace, with high amplitude signals at layer boundaries (Lavigne et al., 2013). .....	33
<b>Figure 2.12:</b> The use of DTS for monitoring seepage through an embankment. Th optical fibres used for DTS can be emplaced riverside, landside or underneath the embankment to monitor temperature associated changes which might arise from the water body (Schenato, 2017). .....	35
<b>Figure 2.13:</b> A representation of a helical array of DOFS cables for sensing strain. The horizontal plane, and dots on it show how each cable is placed at an equidistance (Ning & Sava, 2018). .....	36
<b>Figure 2.14:</b> Inversion of a synthetic 2D model, showing the resistivity model, with assigned resistivity values for the forward model, and the output of an inversion for the model (Binley & Slater, 2020). .....	37

**Figure 2.15:** Resistivity variations from increased gravimetric moisture contents from laboratory analysis of samples of the Whitby Mudstone Formation taken from a railway embankment near Nottingham (Chambers et al., 2014). This shows the relationship which can be derived from field samples, which can be later used to validate moisture induced changes on resistivities from ERT surveys. .... 41

**Figure 2.16:** An example of an ERT inversion showing a decrease in resistivity through an embankment, which has been interpreted as seepage (Sentenac et al., 2018). .... 48

**Figure 3.1:** Geometrical representations of the synthetic model problem. a) The layout of the embankment, river, and electrode array orientation for the homogeneous model. The electrode array is located parallel to the river and is situated at the centre of the embankment crest. b) The heterogeneous model, including the clay core. c) A 2D cross sectional image of the synthetic embankment, showing the adjustments to river geometries with each iterant model and modelled river resistivities, representing salinity changes. .... 59

**Figure 3.2:** Geometrical representations of the synthetic model problem. a) The layout of the embankment, river, and electrode array orientation for the homogeneous model. The electrode array is located parallel to the river and is situated at the centre of the embankment crest. b) The heterogeneous model, including the clay core. c) A 2D cross sectional image of the synthetic embankment, showing the adjustments to river geometries with each iterant model and modelled river resistivities, representing salinity changes. .... 63

**Figure 3.3:** Profiles of resistivity variation below the synthetic ERT array for different river levels in different modelled river resistivities a) Where the river is 1  $\Omega\text{m}$  and the model is homogeneous. b) 5  $\Omega\text{m}$  and the model is homogeneous. c) 10  $\Omega\text{m}$  and the model is homogeneous. d) 1  $\Omega\text{m}$  and the model is heterogeneous. e) 10  $\Omega\text{m}$  and the model is heterogeneous. The models associated with a river of 20  $\Omega\text{m}$  are not shown, due to the lack of distorted resistivities underlying the electrode array for all distances of river to electrode. .... 65

**Figure 3.4:** Resistivities directly underneath the modelled ERT array across the embankment crest, showing resistivity across depth below surface, for different electrode spacings. a) When the river is 1.7 m from the electrode array. b) When the river is 3.5 m from the electrode array. .... 68

**Figure 3.5:** Cumulative sensitivity distribution for the synthetic model outputted from R3t, including an outline of the river region and electrode array for where the river is at its furthest. This sensitivity map is cropped half-way across the mesh, in the direction perpendicular to the embankment, to show how sensitivity is distributed. The electrode array is located at 9.5 m in the y orientation. .... 69

**Figure 3.6:** Layout of the PRIME array at Hadleigh Marsh, Essex, where L1-L2 are ERT lines parallel to the river front and P1-P3 are ERT lines perpendicular. .... 71

**Figure 3.7:** 2D inversions of the ERT data taken from L2 at Hadleigh Marsh (see Figure 3.2) where each inversion represents the start of a tidal cycle, where it is at a tidal minimum. a) A reference inversion from 08-Dec-19 (water level 1.08 m). b) 03-Apr-20 (water level: 1.65m). c) 26-Oct-20 (water level: 1.35 m). Water levels were taken from at the nearby Sheerness tidal gauge, so water levels are not directly representative of Hadleigh Marsh, but are analogous. .... 73

**Figure 3.8:** 2D difference inversions for L2 at Hadleigh Marsh. Each difference inversion shown corresponds to the reference inversion of the same letter shown in Figure 7. a) 17-Dec-19 (water level: 5.64 m, reference inversion: 03-Dec-19). b) 12-Apr-20 (water level: 5.75 m, reference inversion: 03-Apr-20). c) 05-Nov-20 (water level: 5.47 m, reference inversion: 26-Oct-20). Water levels were taken from Sheerness tidal gauge, so water levels are an analogous correspondence to Hadleigh Marsh. .... 74

**Figure 3.9:** 2D inversions of lines P1-P3 on 08-Dec-19. a) Line P1. b) Line P2. C) Line P3. The array type used for all measurements was a dipole-dipole array. .... 76

<b>Figure 3.10:</b> 2D difference inversions of lines P1-P3 on 08-Dec-19. a) Line P1. b) Line P2. C) Line P3.....	77
<b>Figure 3.11:</b> 3D reference inversion for Hadleigh Marsh, taken from the beginning of the tidal cycle (08-Dec-19), where the maximum tidal ingress is lowest. L2 is adjacent to the River Thames..	78
<b>Figure 3.12:</b> A 3D time-lapse inversion for Hadleigh Marsh (17-Dec-19), using Figure 11 as a reference, taken from a time period where the maximum tidal height was at its peak. L2 is adjacent to the River Thames.....	79
<b>Figure 4.1:</b> Mactaquac Dam. a) The location of Mactaquac Dam within Canada and its more localised location in New Brunswick, Canada (45.95°N, 66.87°W) (Google Earth, 2023). b) An annotated photograph captured of Mactaquac Dam, showing the features of the dam and the area where the ERT survey is located (modified from Butler & Boulay, 2020).....	89
<b>Figure 4.2:</b> Electrode layout, as of 2022, for Mactaquac ERT monitoring, showing the 5 principal lines (L1-5) and L0. The concrete wingwall is found to the north, while the headpond is westward from the survey (Butler, 2022).....	90
<b>Figure 4.3:</b> A model showing the different resistivity zones incorporated into the synthetic model, as well as the ERT survey area. a) Sub-vertical view of the model. b) Aerial view of the model.....	94
<b>Figure 4.4:</b> Representations of the mesh used for the synthetic modelling at Mactaquac Dam. a) An image of the entirety of the mesh. b) Representation of the mesh extracted from within the ERT survey. c) Representation of the mesh showing the entire survey area and concrete wingwall. d) Representation of the mesh, showing the mesh below each major line used in the ERT survey. e) A 2D slice of the mesh underneath L1..	96
<b>Figure 4.5:</b> Electrode layouts for determining the most appropriate depth for a point source. a) Aerial view of a surface array. b) Cross section of a surface array. c) Cross section of a buried array.99	99
<b>Figure 4.6:</b> Differences between apparent resistivities calculated for point electrodes in a homogeneous half-space and those calculated assuming the electrodes were hyper-conductive cylinders for a) a surface electrode array and b) a buried electrode array at Mactaquac Dam. ....	101
<b>Figure 4.7:</b> Rotation of the optimal electrode point depth from the flat topography of the model to the correct location along the Mactaquac Dam slope, which was approximately 36.2°. ....	102
<b>Figure 4.8:</b> A cross section of the dam core beneath L1, showing a) a homogeneous core as used for most models, b) a shallow seepage zone and c) a deep seepage zone. Note that the crest of the dam lies 1.5 m above the top of the core.....	105
<b>Figure 4.9:</b> 2D slices of the 3D forward model and inversion of Mactaquac Dam with the concrete wingwall at 60 Ωm, where the slice is taken from a) L1 inversion, including zone I and zone II, where zone I is a feature of lower resistivity above the concrete-dry rockfill boundary and zone II is a feature of lower resistivity between core and headpond. b) L3 inversion. Overlays of the true model sections and resistivities are shown in white. ....	108
<b>Figure 4.10:</b> Histograms showing the resistivity frequency across the ERT survey area to a depth of 40 m below the surface for a concrete wingwall modelled at a) 10 Ωm b) 48 Ω c) 60 Ωm d) 75 Ωm and e) 250 Ωm, while the core, rockfill and headpond are the same resistivity for each model.....	109
<b>Figure 4.11:</b> Difference inversions from Mactaquac Dam taken from a reference model where the headpond was 50 Ωm and the wet rockfill was 200 Ωm. a) The reference model used in the difference inversion. The difference inversions used a headpond and wet rockfill resistivity of b) 100 and 500 Ωm and c) 200 and 1000 Ωm. The core was modelled at 50 Ωm, the concrete 60 Ωm and dry rockfill 2000 Ωm for each model. The values assigned to each region in the forward model is shown in brackets. An orange line has been added to a to show the area at which Figure 4.13 represents..	112
<b>Figure 4.12:</b> Histogram showing the resistivity frequency across the core and underlying concrete to a depth of 40 m below the surface for a headpond at 50 Ωm 100 Ωm and 200 Ωm.....	113

<b>Figure 4.13:</b> Variation in the change in resistivity, compared against the 50 $\Omega$ m headpond reference model, for subsequent time-lapse difference inversions at 100, 150 and 200 $\Omega$ m .....	114
<b>Figure 4.14:</b> Inversions from underneath L3 for a) The reference model assuming an intact core, b) an inversion of a seepage zone at shallow depth and c) an inversion of a seepage zone at depth... 116	
<b>Figure 4.15:</b> Histograms showing the resistivity distribution for a seepage zone compared with an intact core for a) a shallow seepage zone and b) a deeper seepage zone.....	118
<b>Figure 4.16:</b> A 2D inversion underneath L1 at Mactaquac Dam, with the concrete wingwall at 60 $\Omega$ m.....	119
<b>Figure 4.17:</b> RES3DINV inversions for Mactaquac Dam showing 2D slices across all the lines. Resistivity images from June 2020, highlighting the decreased resistivities in lines close to the concrete wingwall. These sections extend 19 m below the surface with no vertical exaggeration (Boulay & Butler, 2021).....	121
<b>Figure 5.1:</b> Location of Bartley Dam, circled, within Birmingham and the United Kingdom (52.43°N, 2.00°W). The numbers correspond to the photograph locations for Figure 5.2 (Google Earth, 2023). .....	132
<b>Figure 5.2:</b> Photographs taken from Bartley Dam during site visits and investigations, showing residential areas adjacent to the dam.....	133
<b>Figure 5.3:</b> A cross section of Bartley Dam, taken from underneath the crest, showing the underlying geology, including the sandstone anticline and geology excavated during construction (Birmingham Water Department, 1931). As can be seen the geology is of an interbedded marl and sandstone, where the anticlinal crest has been removed. ....	134
<b>Figure 5.4:</b> Location of the two major electrode lines, Line 1 and Line 2, at Bartley Dam. The map also shows a rubble drain, a piezometer (POR30-A) and two boreholes (SP08SW194 and 214) used for acquiring water flow rates, water levels and geological information. ....	135
<b>Figure 5.5:</b> The uppermost section of the mesh for a) a 2D model and b) a 3D model at Bartley Dam. ....	137
<b>Figure 5.6:</b> Contact resistances for a)Line 1 and b) Line 2 from January 2020 to October 2021. ....	139
<b>Figure 5.7:</b> Median reciprocal errors from Line 1 for the selected datasets for time-lapse analysis. a) June 2020, b) August-September 2020, c) November-December 2020 and d) March-April 2021. Line 2 has not been shown due to similar behaviour for all selected dates. ....	139
<b>Figure 5.8:</b> Groundwater levels compared with effective rainfall for the dates selected for time-lapse analysis. a) June 2020, b) August-September 2020, c) November-December 2020 and d) March-April 2021. ....	141
<b>Figure 5.9:</b> Flow rates compared with effective rainfall for the dates selected for time-lapse analysis. a) June 2020, b) August-September 2020, c) November-December 2020 and d) March-April 2021. ....	141
<b>Figure 5.10:</b> Reference model for the June 2020 dataset, taken from 03-Jun-2020. Nearby geological logs are indicated by I and II, where I is SP08SW214 and II is SP08SW198, as indicated in Figure 5.4. ....	144
<b>Figure 5.11:</b> Difference inversions from the four selected time periods after periods of reservoir level increase and/or rainfall. a) 23-Jun-2020, reservoir level: 184.34 m (reference: 13-Jun-2020, reservoir level: 183.49 m), b) 26-Aug-2020, reservoir level: 184.37 m (reference: 17-Aug-2020, reservoir level: 183.07 m), c) 17-Nov-2020, reservoir level: 184.11 m (reference: 09-Nov-2020, reservoir level: 183.54 m), d) 20-April-2021, reservoir level: 183.69 m, (reference: 25-Mar-2021, reservoir level: 182.98 m). For each model a timestamp is shown along the graph with groundwater level and effective rainfall. A blue circle in a highlights a region of interest (drainage) interpreted from the inversion.....	146



<b>Figure 5.12:</b> Resistivity variation in the area of interest, as indicated on Figure 5.11, through time, showing how resistivity varies with groundwater level. a) June 2020, b) August to September 2020, c) November to December 2020, d) March to April 2021. ....	149
<b>Figure 5.13:</b> A 3D reference model for 03-June-2020. This is the equivalent dataset for the 2D model shown in Figure 5.10, where the same borehole logs are shown. ....	151
<b>Figure 5.14:</b> 3D difference inversion for the 23-Jun-2020 dataset for the corresponding dataset to Figure 5.11a. A timestamp has been shown for the groundwater level and effective rainfall at this time period. ....	152
<b>Figure 5.15:</b> Histograms showing the resistivity distribution across model cells for the 03-Jun-2020 dataset a) from underneath Line 1 and b) from underneath Line 2 for the upper 20 m. ....	154
<b>Figure 5.16:</b> An EMI survey undertaken in February 2022 at Bartley Dam, showing the conductivity map of the subsurface at an estimated 4.2 m depth. ....	155
<b>Figure 6.1:</b> Paull Holme Strays, Yorkshire, United Kingdom (53.71°N, 0.21°W) ( <i>Google Earth, 2023</i> ). a) Paull Holme Strays site location, where the area of the embankment surveyed is circled. b) Photographs from Paull Holme Strays. ....	164
<b>Figure 6.2:</b> Geological boreholes drilled at the Paull Holme Strays embankment (VBA, 2014). a) A map of the boreholes drilled. b) Geological borehole logs and interpolation of geology between boreholes. CP1-3 are located within the ERT survey undertaken. ....	166
<b>Figure 6.3:</b> Electrode lines used for the ERT survey at Paull Holme Strays, where PHSLT lines are those parallel to the crest and PHSX lines are crosslines perpendicular to the embankment. ....	169
<b>Figure 6.4:</b> The mesh for 2D and 3D inversions. a) 2D mesh for PHST2 (10964 elements), b) 2D mesh for PHSC1 (8760 elements), c) 2D mesh for PHSLT1 (6687 elements), d) The 3D mesh through PHSC1 (1362302 elements). ....	170
<b>Figure 6.5:</b> 2D inversions taken from the three longest lines parallel to the embankment, with a) PHST2, b) PHSC1 and c) PHSLT1. The x,y,z coordinates are the same for each line in the survey and the first line has been plotted from a different orientation due to its non-linear nature. ....	173
<b>Figure 6.6:</b> 3D inversions taken from the three longest lines parallel to the embankment, with a) PHST2, b) PHSC1 and c) PHSLT1. The x,y,z coordinates are the same for each line in the survey and the first line has been plotted from a different orientation due to its non-linear nature. ....	175
<b>Figure 6.7:</b> A fence diagram of the 3D inversion, showing PHSLT1 and selected crosslines for visualising the resistivity interaction between the line and that of the core, where intersections of the core resistivity and PHSLT1 are circled. ....	177
<b>Figure 6.8:</b> Histograms showing the resistivity distribution of 2D and 3D inversions underneath each respective electrode line for a) PHST2, b) PHSC1 and c) PHSLT1. ....	178
<b>Figure 6.9:</b> EMI conductivity map for Paull Holme Strays, encompassing the majority of the ERT survey area and salt marsh. The DOI is at 2.1 m with a coil spacing of 2 m. a) The conductivity with extreme values filtered from the salt marsh. I, II and III show the location of three points used for comparison between EMI and ERT data. b) The conductivity without extreme values filtered from the salt marsh. ....	180

## List of Tables

<b>Table 2.1:</b> Selected studies on water retaining structures using various geophysical techniques, including the geological context of the setting in which the investigation was undertaken. ....	43
<b>Table 2.2:</b> Summary of failure mechanisms for dams, their causes and effects .....	51
<b>Table 3.1:</b> Modelling scenarios tested for the synthetic numerical modelling, and associated parameters assigned for each modelling scenario. ....	62
<b>Table 3.2:</b> Summary table for the aims and outcomes of the synthetic numerical modelling and Hadleigh Marsh ERT. ....	83
<b>Table 4.1:</b> Resistivities assigned for each region in the model for each scenario the synthetic models were applied for.....	105
<b>Table 4.2:</b> The (normalised) frequency at which 30 $\Omega\text{m}$ occurs in each synthetic model for a change in headpond resistivity.....	114
<b>Table 4.3:</b> A summary table, outlining the key findings of the modelling aims for Mactaquac Dam... ..	126
<b>Table 5.1:</b> The selected date ranges for the inversion scheme at Bartley Dam, showing the range in reservoir level and maximum in effective rainfall for the given dates selected.....	136
<b>Table 5.2:</b> A summary table detailing key outcomes from the research aims for Bartley Dam.....	159
<b>Table 6.1:</b> The number of data filtered from each electrode line and percentage unfiltered, used for analysis between 2D and 3D inversions. ....	171
<b>Table 6.2:</b> A comparison between the approximate conductivities from the EMI and ERT for both 2D and 3D models, from selected points along PHSLT1, PHSC1 and PHST2.....	181
<b>Table 6.3:</b> Summary of the key outcomes of research at Paull Holme Strays, Yorkshire, United Kingdom.....	183
<b>Table 7.1:</b> A brief overview of steps needed to be undertaken during an ERT survey, with emphasis on ensuring the survey is optimised for a reduction in the 3D effect.....	193

# 1.0 THESIS INTRODUCTION AND AIMS

## 1.1 Introduction

The importance of water for human life as a resource and a potential natural hazard, has led to the development of various water retaining structures for our benefit. These include reservoir dams to ensure the population has a readily available potable water, especially where groundwater supplies are less common, sources of irrigation for agriculture, generation of electric power and storage of contaminants. They can also be used as barriers to prevent flooding of water courses where societally and economically important infrastructure is present (*e.g.* homes, power stations etc). Therefore, maintaining their structural integrity is of utmost importance for human society. Degradation of water retaining structures, by means of erosion, can lead to catastrophic failure, flooding, loss of water resources, contamination, loss of life and damage to infrastructure depending on the purpose of the embankment. Moreover, even minor degradation of an embankment (*e.g.* a seepage pathway) can be detrimental in that it reduces the volume of water as a resource for a dam and can be a sign of deterioration which may worsen. Therefore, it is necessary to assess the ground conditions in water retaining structures to identify issues when deterioration to the ground conditions can be mitigated and before failure. One method of assessing such embankments is near-surface geophysics: this thesis will focus on the use of electrical geophysical data for the characterisation of water retaining structures.

## 1.2 Thesis Aims

The thesis has focussed on four case studies in both dam and flood embankment settings, with use of synthetic modelling in two chapters, for the purpose of generating a better understanding in how electrical resistivity tomography (ERT) can be used for characterising the static and dynamic nature of water retaining structures. Each chapter focuses on producing results and interpretation which can aid a fulfilment of the aims (given below), which can then provide a holistic assessment of how each aim has been met through each case study. The principal aims and research questions examined are as follows:

**1. Do ERT models of water retaining earthworks need to account for 3D effects resulting from their contextual environment?**

ERT inversions are commonly applied in 2D due to familiarity of the user and computational intensity of 3D inversion algorithms. This may provide some insight into the underlying resistivity distribution, but distorted resistivities and artefacts are a possibility due to a simplified 2D geometric assumption for a 3D actual scenario. Features off-line to a 2D ERT survey have the potential to influence results, and this could lead to artefacts, flawed interpretation based off distorted resistivities and obscuration of actual resistivities. In the setting of a dam or river embankment there are several features which have the potential to induce 3D effects, including the water body, topographic variation, heterogeneous composition, different structural components (*e.g.* abutments, core etc) and services (*e.g.* drainage, electrical cables etc).

Synthetic modelling of how off-line features (proximal structures or areas of differing resistivity outside the ERT survey line) were utilised to help address this research question, in chapters three and four. The models could then be compared with case studies to determine whether effects observed in the synthetic modelling were present in real life and whether 3D effects can produce resistivity distributions observed in the field data. If such features are present in the field data, it may be that 3D effects from the sources tested need accounting for when undertaking an ERT survey.

**2. Does a 3D inversion produce a better visualisation of the resistivity distribution than 2D inversions, with fewer 3D effects present?**

The increasing ability of modern computers to use more intensive software has enabled greater use of 3D inversion algorithms for ERT. It has been observed that true 3D surveys have the potential to minimise potential 3D effects and produce more realistic resistivity distributions. However, true 3D surveys often require small distances between lines, so spatial coverage is reduced, and measurements between lines may not be possible for larger ERT surveys. A 3D inversion scheme can be used for a survey comprising of two or more electrode lines and this may have the potential to reduce 3D effects observable in 2D ERT.

Chapters five and six address this question, where chapter five focuses on the use of 3D modelling in a time-lapse system. Chapter six focuses on whether the use of crosslines in a 3D

inversion (secondary electrode lines orthogonal to the primary electrode lines) can generate a 3D model which better visualises the resistivity than a 2D ERT survey for a given line. From comparisons to geological information, this has then been used to discuss whether a 3D model provides a better representation than a 2D model.

### **3. How does temporal variation of resistivity impact upon 3D effects and the results of 2D or 3D resistivity inversions?**

Time-lapse ERT has been increasingly used for several different applications, with the improvement and ease of installation of instrumentation used for such purposes. Time-lapse monitoring can be used for long-term monitoring of resistivity and how it changes with ground conditions. In terms of water retaining structures it is important to identify features indicative of degradation, including seepage and erosion. However, if the change in resistivity is being controlled by a 3D effect it may not be possible to identify whether such changes are related to the ground conditions. Therefore, chapter four and five have included temporal analysis for consideration. Chapter four looks at temporal variation in headpond resistivity and the potential of a seepage pathway developing and how this may impact 3D effects upon data, while chapter five looks at a time-lapse analysis of ERT data and whether a 3D model can better visualise this than a 2D model.

### **4. What measures should be taken in survey design and data processing to reduce the impact of any 3D effects?**

Artefacts resulting from 3D effects can potentially cause misinterpretation of the resistivity image. Therefore, it is imperative for those working with ERT to have knowledge of how to best approach an undertaking of an ERT survey where such effects can be reduced. This includes optimal survey designs for field measurements, i.e. to consider likely 3D effects from the site and during the data processing stages. From assessing every case study from chapters three to six, methods in reducing the impact of 3D effects for future surveys have been considered and resultant recommendations are outlined in the discussion. Every embankment is different and has unique characteristics that may induce 3D effects, so this thesis has considered generalised features across all embankments and how this may cause a 3D effect with varying features at different sites (*e.g.* slope angle, geology etc).

## 1.3 Thesis Structure

The content of the following chapters is as follows:

Chapter 2 outlines the research and literature relevant to the use of near-surface geophysics on water retaining structures. This details the different means by which such structural embankments degrade by erosional processes, as well as the theory behind geophysical techniques which have been and can be used for surveying water retaining structures. Examples of how these methods have been used for dams and river embankments are discussed, as well as the strengths and limitations of geophysical methods for surveying and monitoring water retaining structures, before discussing how this thesis will progress our understanding in the field.

Chapter 3 presents research into exploration of how a 3D effect can impact an ERT survey along a flood embankment in a tidal environment. The water body represents an obvious and key source for a 3D effect, and tidal settings will face different water levels and salinities (and therefore resistivities), which may cause 3D effects of varying magnitudes in the ERT. A synthetic model of an ERT survey, along the crest, was tested for assessing whether 3D effects are likely from differing water levels and resistivities to understand when it is likely to be an issue for ERT surveys. The results of the synthetic modelling were compared with real data from Hadleigh Marsh, a flood embankment in a tidal environment, to understand the validity of features observed in the synthetic model.

Chapter 4 focuses on the use of a complex synthetic model of a dam at Mactaquac, Canada, where a time-lapse ERT system has been installed for monitoring potential seepage through a concrete abutment which had undergone alkali-aggregate degradation. Synthetic modelling of different concrete resistivities and headpond resistivities were run to determine whether 3D effects from these features can impact the ERT data at Mactaquac, with comparisons to the real data.

Chapter 5 comprises an analysis of whether 3D inversions can improve modelling of resistivity, in comparison to 2D modelling. This uses a case study at Bartley Dam, UK, which is an embankment dam which has had a time-lapse ERT system for monitoring seepage.

Chapter 6 looks at a further study at a flood embankment in a tidal setting at Paull Holme Strays, UK. The chapter focuses on a standalone ERT survey consisting of multiple 2D datasets, and compares the interpretation based on 2D and 3D modelling. The results are compared with electromagnetic induction (EMI) data and the geological data on Paull Holme Strays for assessment of the better model and recommendations for how ERT should be modelled in embankment settings.

Chapter 7 discusses how the research has addressed the aims of the thesis, how it progresses our understanding of current literature into the topic and how it can lead to future developments of our understanding into the 3D effect and use of near-surface geophysics for assessment of water retaining structures.

## 2.0 LITERATURE REVIEW

### 2.1 Introduction

Water retaining structures, such as dams, are hydraulic barriers to surface water, which prevent ingress and loss of water that may be utilised for water supply, transport, hydroelectric power, crop irrigation or storage of contaminants (*e.g.* tailings dams). River and canal embankments form important hydraulic barriers to prevent flooding of infrastructure. However, there are associated risks of breaching and failure induced by water (Dunbar et al., 2017). In the United Kingdom alone, there are over 34,000 km of flood embankments (Jones et al., 2014) and at least 1654 embankment dams (Almog et al., 2011). Incidents of failure within British dams have occurred throughout recent history, such as at Sheephouses in 1962, Mill Hill in 1979, Greenbooth in 1983, Yarrow in 2002, Ulley in 2007 (Charles et al., 2011) and Whaley Bridge in 2019 (Pytharouli et al., 2019). Global dam disasters include El Cobre, Chile in 1965 (Vargas, 2019), Machchhu, India in 1979 (Noorani, 1984), Belci, Romania in 1991 (Enea et al., 2023), Shadi Kaur, Pakistan in 2005 (United Nations, 2005) and Brumadinho, Brazil in 2019 (Furlan et al., 2020), thus indicating that such structures are still a global risk of structural compromise, despite improved mitigation to such structures. Deterioration with age, increased extreme weather events with climate change and the poor capability of models to predict long-term behaviour of dams means dam failure is a significant risk to society (Michalis & Sentenac, 2021). Historical dam disasters have impacted human life and have led to catastrophic failure, which have caused death, displacement of people, damage to flora, fauna and economic decline (Segura et al., 2016). It is therefore important to characterise deterioration or changes in condition, which may arise in water retaining structures, and monitor them, to prevent hindrance to economically important industries, natural habitats and human society, through breaching and immediate risk to human life or loss of water for consumption, as well as to improve management and upkeep of such geotechnical assets.

Failure within water retaining structures typically occurs as a result of overtopping, internal or surface erosion and slope failure (Dunbar et al., 2017), where internal erosion represents over 50% of reported failures within embankments (Fell & Fry, 2007; Schenato, 2017). Internal and surface erosion can be influenced by processes like suffusion, piping, seepage,



vegetation, and animal burrowing (Almog et al., 2011). Issues with such can be exacerbated by changes in hydrological conditions and effective stress.

Typically, investigations to assess embankments involve visual and geotechnical surveying. However, visual inspections may not be effective for identification of surface features due to changes in vegetative cover throughout the year and soil swelling during wetter periods (Jones et al., 2014; Sentenac et al., 2018). Geotechnical investigations are often required due to the scarcity of contemporary data and the need to assess the internal condition of water retaining structures (Bièvre et al., 2017), but they are limited by a lack of sampling density (Michalis et al., 2016). Parameters obtained from geotechnical testing relate to the sampling location alone and are unable to account for spatial variability, increasing uncertainty in interpretations across the structure when relying on geotechnical instrumentation only (Cardarelli et al., 2014). Site investigations typically use several testing sites from across the sampling area for a more reliable characterisation, but this is limited by scale, where small scale variation may be missed if it is not within a sampling location.

Internal erosion and other hazards to embankment deterioration processes are heavily influenced by moisture content and flow of water through dams and levees (Moore et al., 2011; Fargier et al., 2014) which can be detected with appropriate geophysical methods that can be used to estimate hydrogeological properties (Martínez-Moreno et al., 2018). Hence, geophysical monitoring has been increasingly utilised to non-destructively (Michalis et al., 2016) identify sub-surface features within water retaining structures, which may be impossible to detect from surface observations. Geophysical investigations have been undertaken on several water retaining structures, such as embankment dams (*e.g.* Rittgers et al., 2015), landslide dams (*e.g.* Wang et al., 2018), moraine dams (*e.g.* Moore et al., 2011), flood embankments (*e.g.* Jones et al., 2014) and canal dykes (*e.g.* Bièvre et al., 2017). Commonly used methods for ground investigation of water retaining structures include electrical resistivity tomography (ERT) (*e.g.* Cardarelli et al., 2014), self-potential surveying (SP) (*e.g.* Panthulu et al., 2001), induced polarisation (IP) (*e.g.* Martínez-Moreno et al., 2018), electromagnetic induction (EMI) (*e.g.* Sungkono et al., 2014), active or passive seismic surveying (*e.g.* Planès et al., 2016), and distributed temperature surveying (DTS) (*e.g.* Chen et al., 2018).

Despite the growing prevalence of the use of geophysics for monitoring water retaining structures there is still weak linkage between geophysical and engineering properties (Lin et al., 2018), as well as spatial constraints on preparing field arrays (Michalis et al., 2016) and resolution constraints (Dunbar et al., 2017); therefore it is paramount that careful interpretation is made. Though geophysical surveying may provide more comprehensive coverage than geotechnical testing from boreholes, relationships with borehole data and geophysical properties may be needed to be associated with static properties if the geophysical investigation was used to infer soil properties (Almog et al., 2011).

This review focusses on the issues associated with earthen water retaining structures, outlining the associated hazards, what geophysical techniques can be used and how these geophysical techniques can be employed for different circumstances to identify potential weakness within the structure. Areas where scientific knowledge is lacking will be identified and research plans will be formulated for the thesis. Research on different earthen water retaining structure have been considered, including embankment dams, levees, canal dykes, landslide dams, moraine dams and mudflow dams. 2.2

## **2.2 Degradation of Water Retaining Structures.**

In the United Kingdom, as a means of reservoir safety management, it is required that reservoir owners undertake maintenance, operations, monitoring, examinations of the reservoir area, and an annual statement is submitted to detail yearly changes (Bowles et al., 2013). To achieve appropriate standards of embankment integrity, an embankment must meet criteria, in accordance with Eurocode 7 (European Union, 2004), to meet serviceability limit state (SLS) and ultimate limit state conditions (ULS) (Bond et al., 2013). Limit state analysis must consider the loss of overall site stability, failure in dam or crest, internal and surface erosion, settlement, deformation in transition zones, climatic influences, creep during freeze-thaw periods, degradation of base coarse material, hydraulic deformation and changes in environmental condition due to pollution, vibrations or noise (BSI, 2013). In embankments, ULS is considered not to have been met if there is a loss of structural equilibrium or ground due to uplift by water pressure or hydraulic heave, internal erosion and piping caused by high hydraulic gradients (Orr, 2008). SLS is considered not to have been met if deformation, settlement or other defects cause the structure to no longer be serviceable (BSI, 2013). This

review includes water retaining structures from small scale levees to larger scale embankment dams, and the required legislated precautions differ in the United Kingdom (BSI, 2013), and elsewhere, based on the severity of associated effects of failure.

Issues which may compromise embankments, such as overtopping, internal erosion, surface erosion and slope failure will lead to breaching if resultant erosion causes pipes to be sufficiently enlarged, the downstream slope loses stability, the downstream face unravels or the crest settles with overtopping (Figure 2.1) (Polemio & Lollino, 2011). This section will detail these methods of failure, their severity and problems faced by the engineer for mitigating the issues at hand.

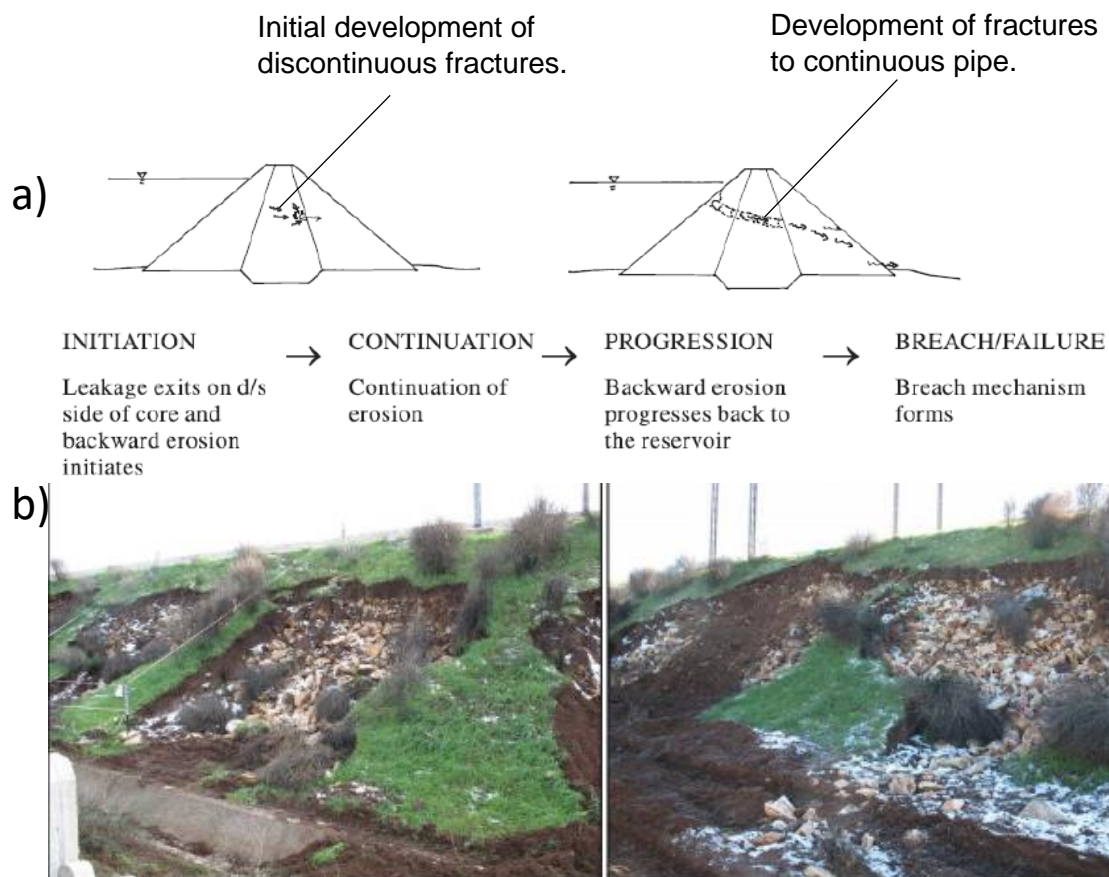


**Figure 2.1:** a) A model of how progression of erosion can lead to a continuous path for water to flow through a dam, and how this can lead to breaching (Foster & Fell 1999). b) A photograph of a slope failing on an embankment. Erosional processes, as shown in Figure 1.0, can form planes of weakness in which slopes may later fail (modified from Polemio & Lollino 2011).

### *2.2.1 Overtopping*

Overtopping occurs when water level exceeds that of the embankment's crown elevation (Dunbar et al., 2017), and occurs by planar or spatial means (Tabrizi et al., 2017). Overtopping can lead to erosion of the underlying embankment, where planar overtopping involves vertical erosion only and spatial overtopping has erosion in vertical and horizontal orientations (Tabrizi et al., 2017). Overtopping typically occurs in lower permeability dams with high shear strength and high volumes of upstream discharge. These factors cause wetting of the dam front, water level increase and rising of water above dam limits, which can cause progressive erosion inside the dam (Chen et al., 2018), as well as flooding (Dunbar et al., 2017). In dams of higher permeability and lower shear strength, more water is likely to flow through the embankment and erode internally (Tabrizi et al., 2017). Erosional processes caused by overtopping may subsequently lead to breaching by water, which would cause violation of ULS conditions, and changes to embankment morphology and roughness of the downstream channel (Xiangang et al., 2018).

Overtopping is prevalent in the failure of moraine dams, where water courses are impeded by glacial sediment due to the melting of interstitial ice increasing reservoir volumes (Moore et al., 2011). Other natural dams prone to overtopping include landslide dams (Schuster, 1998) which are poorly consolidated, at risk of movement and heterogeneous (Wang et al., 2018).

### *2.2.2 Internal Erosion*

Internal erosion is a four stage mechanism, involving the initiation of erosion, continuation of erosion, progression to form a pipe and breaching (Foster & Fell, 1999). In terms of dams, fine grained material is washed out from the core (Sjödahl et al., 2008), and erosion by seepage often occurs as piping, heave, contact erosion, concentrated erosion, suffusion and other methods (Figure 2.2) (Bersan et al., 2018; Cho et al., 2022). In levees, internal erosion involves the flow of seepage water under high hydraulic gradients between the landside and riverside of the embankment, where internal erosion is a common occurrence due to the permeable nature typically encountered in levees (Dunbar et al., 2017). High hydraulic conductivities are

often associated with internal erosion, as evident in areas with high levels of hydraulic fracturing (Flores-Berrones et al., 2011).

Piping is the formation of pore channels in permeable strata, in which particles can be mobilised after continuous internal erosion has propagated to form a continuous channel (Yang & Wang, 2018). It occurs through the embankment body or the foundation (base seepage), especially in dams (Chen et al., 2018) and is controlled by geotechnical properties within the embankment (Rahimi et al., 2018). It can also form through existing, natural conduits in the embankment (Richards & Reddy, 2007). Piping can rapidly induce failure, with the majority of failures occurring between six and twelve hours after initial observations of erosion (Sherard et al., 1972; Charles et al., 2011). Backward erosion from the toe of the embankment to the crest is a particular concern (Planès et al., 2016): particles are expelled upwards, from water pressure, in a cohesionless matrix and the process propagates until a pipe reaches the upstream river or reservoir (van Beek et al., 2010). This is prevalent in permeable foundations, where effective stress is reduced to zero and sand boils form (Yang & Wang, 2018). Piping through conduits (*e.g.* fractures) form 49.8% of all piping phenomenon, globally, followed by piping by backwards erosion at 31.1%, piping along foundations or at abutments at 15% and piping due to biological activity at 4.1% (Richards & Reddy, 2007). Backward propagation is of particular concern in embankment dams with permeable foundations, where underseepage may occur (Planès et al., 2016), and in point (Dunbar et al., 2017). Whereas piping through conduits is only likely to affect dams with a high percentage of fracturing (Richards & Reddy, 2007), which could indicate an already failing structure. Piping can also form in landslide dams, where such internal erosion could trigger catastrophic collapse (Wang et al., 2018).

Other forms of internal erosion, such as heave, occur with zero effective stress and they often occur below impermeable layers that confine seepage flow (Wang et al., 2016). Concentrated leak erosion encompasses seepage flow in the opening of a crack, detaching grains from the opening (Horikoshi & Takahashi, 2015), while suffusion is the erosion of finer grains through voids between coarser particles, induced by seepage flow (Richards & Reddy, 2014). Suffusion is of importance during the first two stages of internal erosion, where particle size distributions, particle shape, confining pressure, hydraulic gradient and flow velocity

controlled suffusion initiation and a lack of an adequate filter or transition zone will help progress the continuation phase (Foster & Fell, 1999).

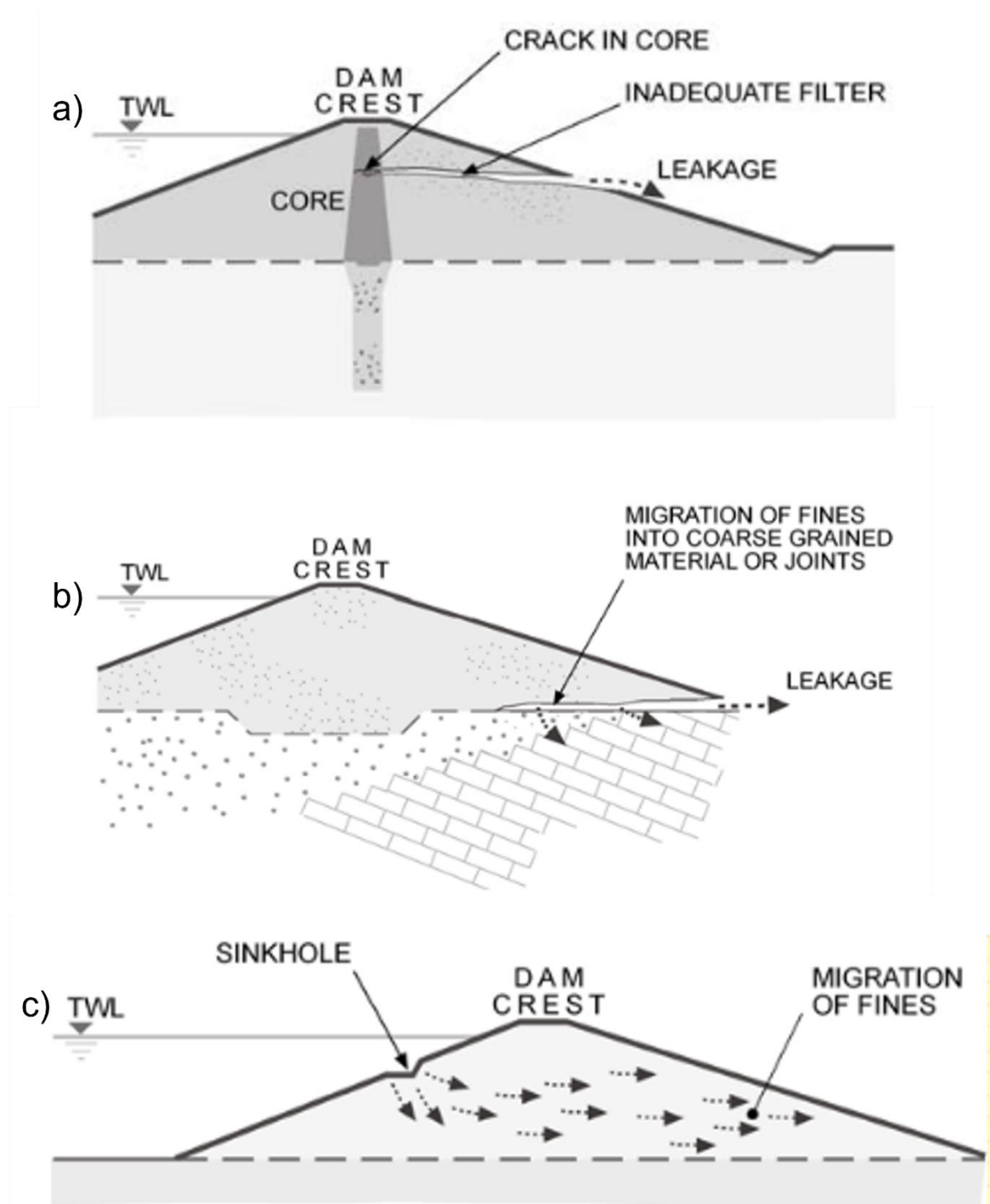


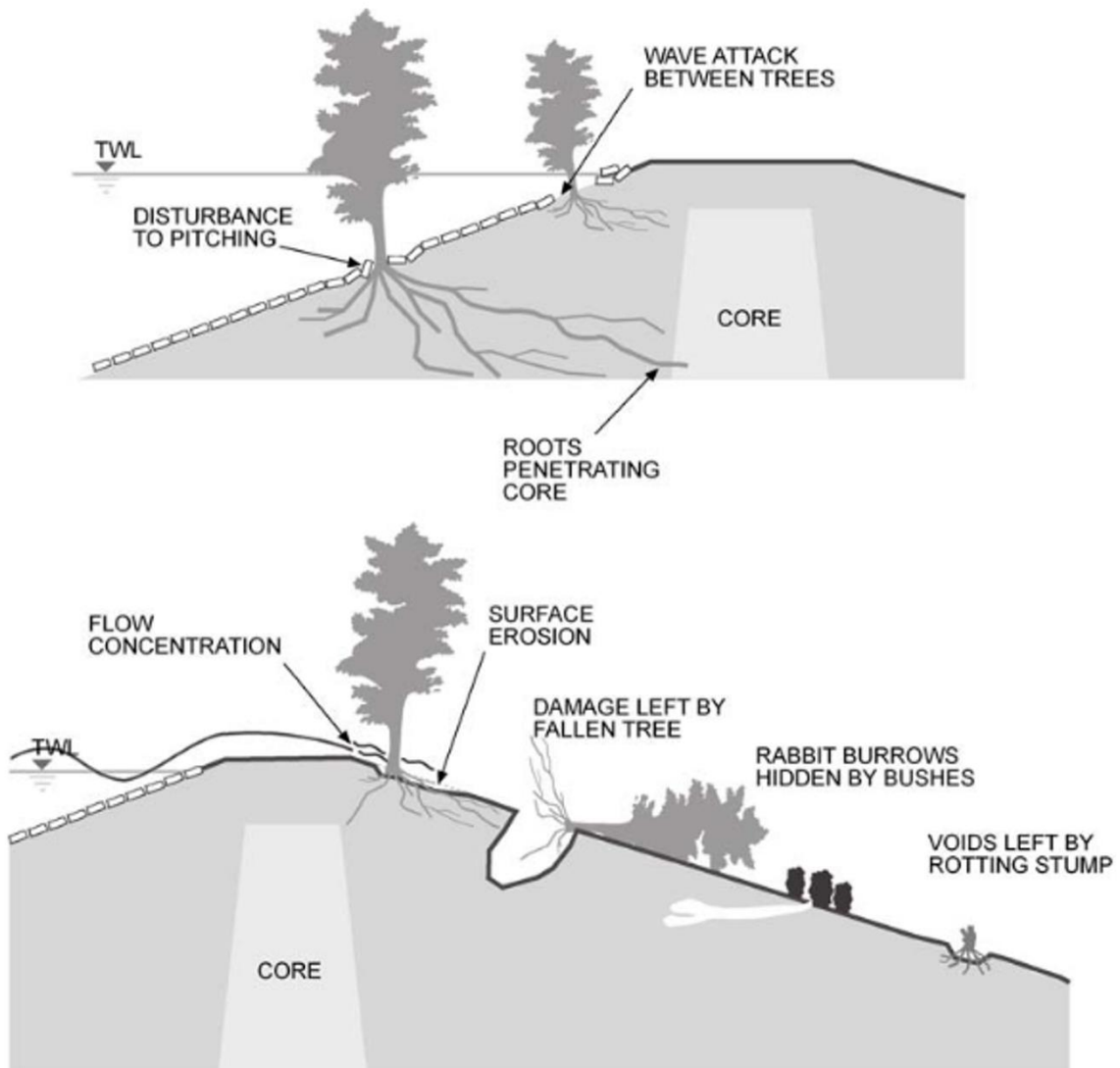
**Figure 2.2:** Modes of internal erosion within embankments, where TWL is the water level and a) shows propagation of a crack from concentrated erosion, b) shows the migration of fines,

*propagating upwards, from backward erosion and c) is migration of fines from suffusion (Almog et al., 2011).*

### ***2.2.3 Surface and Biological Erosion***

Surface erosion and biological activity (Figure 2.3) are problems primarily associated with low cohesion strata, where material is moved from the embankment toe, slope or crest as a result of fluvial scouring caused by a high concentration of local currents oriented against the embankment surface (Dunbar et al., 2017), desiccation cracking (G. Jones et al., 2014) and biotic activity (Borgatti et al., 2017). Water retaining structures are regularly exposed to hydraulic activity and are therefore at high risk of surface erosion (Cantré et al., 2017). Surface erosion is of particular concern during overtopping, when extreme events can amplify damage to shallow layers of the embankment (Pan et al., 2015). However, gradual surface erosion is still of concern, and has led to failure (Zhu et al., 2011), where excessive degradation through time causes scour and reduces the embankment's ability to withstand high water pressures (Dunbar et al., 2017).

a)



b)

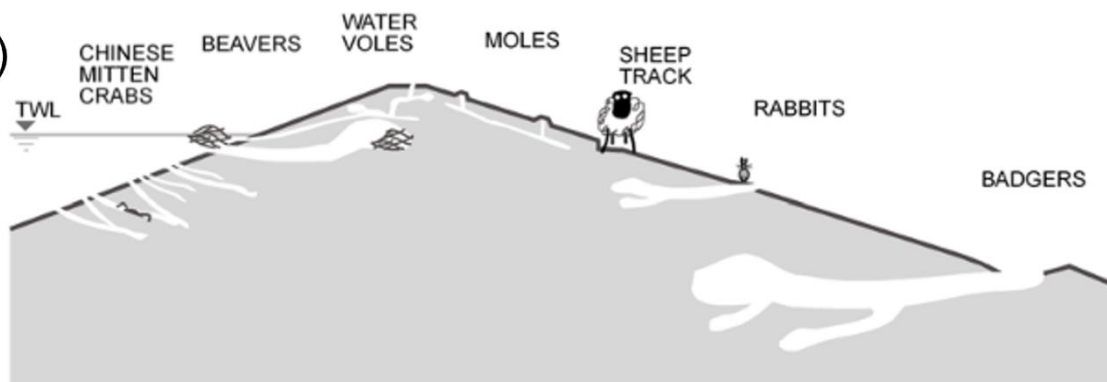


**Figure 2.3:** Modes of surface erosion in an embankment, where a) is a representation of erosion caused by vegetation and b) is a representation of burrowing by different animals (Almog et al., 2011).



Animal activity can disturb the surface of the embankment through burrowing, which can lead to failure by piping (Borgatti et al., 2017; Sentenac et al., 2018). Other topographic irregularities, such as vegetation and man-made obstructions can also negatively impact the integrity of the embankment surface (Dunbar et al., 2017).

#### *2.2.4 Slope Instability*

In slopes, landslides can occur with increased water ingress, and decreased effective stresses, temperature fluctuation, earthquake activity and human alteration (Gariano & Guzzetti, 2016). Engineered slopes in the United Kingdom typically comprise expansive clays (Driscoll, 1983) which may cause damage by shrink and swell, forming eventual propagation of a failure plane due to strain softening from repeated wetting and drying cycles, as well as high seasonal water extraction from localised vegetation (Clarke & Smethurst, 2010). With increased extreme rainfall events likely due to climate change, which may overwhelm drainage (Loveridge et al., 2010), it is likely that increased rates of slope failure will be observed along embankments.

Slope instability within dams and levees occurs in either the body or the foundation (Dunbar et al., 2017), and it is common in high permeability, low shear strength material (Chen et al., 2018). Embankments are vulnerable to slope failure if the watercourse has eroded the toe, oversteepening the side and inducing shear failure in the upper bank, especially where rivers naturally migrate laterally (Dunbar et al., 2017). Rising water levels in embankments reduces effective stress and increases shear strain, leading to progressive slope instability (Lobbestael et al., 2013). Expansive clay rich soils, in areas subjected to seasonal fluctuations in water content may cause shallow landslides in embankments. Surface cracking due to rapid changes in soil suction has been observed to be a primary cause of slope failure (Chen et al., 2004), showing how surface erosion can lead to more significant failure if left untreated.

Seepages have been identified as precursors to subsequent slope failure, as continuous leakage paths can form paths of slope failure (Polemio & Lollino, 2011). Limit equilibrium (*e.g.* Bishop, 1955) and finite element method analyses (*e.g.* Hammouri et al., 2008) have been used to assess slope stability on natural and engineered slopes. More recently, geophysical techniques have been employed to assess slope stability due to improved technological

abilities and ability to monitor the spatial distribution of the subsurface (Perrone et al., 2014; Whiteley et al., 2019).

### **2.2.5 Other Defects**

Other issues arising with potential loss of integrity within a water retaining structure include settlement induced by the fluctuation of water levels within the embankment body or oil or gas extraction creating seepage paths (Almog et al., 2011). Failing to account for higher than expected hydraulic pressure, problematic fill material (*e.g.* peat), congested drainage, overfilled spillways and deterioration of the embankment are other less common problems (Almog et al., 2011).

## **2.3 Geophysical Approaches**

Water retaining structures, especially dams, are heavily monitored to assess for degradation by several means. Often geotechnical and walkover surveying are used, which can give empirical evidence of deterioration. However, walkover surveys cannot visualise internal conditions if there is no surface expression or if its expression is obscured by vegetation. Geotechnical evidence is limited to the locality it was sourced from and cannot give comprehensive coverage of the embankment. Geophysical techniques can provide a comprehensive method able to visualise internal conditions which can help with surveying and monitoring of embankments.

With increased computing power and sophistication of measurement instrumentation, the development of geophysical techniques to image the shallow subsurface increased substantially during the latter half of the 20<sup>th</sup> century and beyond (Telford et al., 1990). As such, there is a wealth of techniques available to image the subsurface, based on the detection of various physical phenomena, where geological, geotechnical or hydrological information can be inferred from the acquired data (Binley et al., 2015). Through petrophysical relationships it is possible to relate geophysical data to hydrogeological and geotechnical information. Changes in pore water concentration or composition (*e.g.* salinity) and changes in flow and material composition are able to be sensed using geophysical methods (Sharma, 1997), enabling such techniques to detect anomalies and variations in these parameters through time. Comprehensive detailing of geophysical theory (*e.g.* Sharma,

1997; Telford et al., 1990) is beyond the scope of this review, but a brief outline of relevant techniques are given, alongside an explanation of forward and inverse modelling techniques. Techniques considered relevant for this review include electrical resistivity tomography, induced polarisation, self-potential, seismic surveying, electromagnetism, ground penetrating radar (GPR) and distributed temperature sensing.

Correlation of geophysical data with secondary evidence, such as rainfall that was contemporaneous to the survey, can give weight to identified seepage zones in geophysical models, and precipitation data can give estimations for lag time between rainfall and infiltration of water into the embankment from the reservoir (Lin et al., 2018).

### ***2.3.1 Electrical Resistivity Tomography (ERT)***

ERT is an imaging technique which is used to determine the distribution of electrical resistivity in the subsurface (Sharma, 1997). ERT utilises a basic four-point measurement of transfer resistance (the ratio of the observed potential difference to injected current), where imaging surveys comprise many such measurements made across the ground surface or within a borehole. From measurements, via an inverse modelling process, the resistivity distribution of the subsurface in the vicinity of the electrode arrays can be estimated (Figure 2.4) (Loke et al., 2013). ERT can be used for 2D or 3D applications (Jones *et al.*, 2014) and for timelapse monitoring (Michalis et al., 2016). ERT can also be undertaken in boreholes for enhanced characterisation at depth (*e.g.* Loke et al., 2014).

ERT can use several different array types, with varying separations between potential and current electrodes. The three most common arrays include Wenner, Schlumberger and dipole-dipole (Figure 2.4), with others including pole-dipole and gradient (Rinaldi et al., 2006; Binley & Slater, 2020). A Wenner array consist of two potential electrodes on the first and fourth electrode in the quadrupole, with two current electrodes in between, where all electrodes are of equal separation. A Schumberger array has the same electrode layout as Wenner, but a different electrode length between potential and current electrodes than between the two inner current electrodes. While a dipole-dipole array has potential and current electrodes adjacent to each other, and equal spacing between current and potential electrodes, but different spacings between the inner potential and current electrode. These arrays have different characteristics which make them more suitable for different

applications; for example, dipole-dipole has greater vertical resolution, while Wenner has greater horizontal resolution.

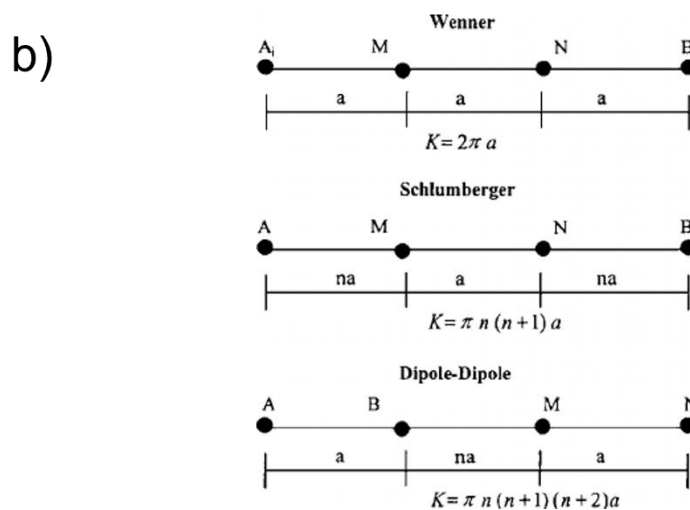
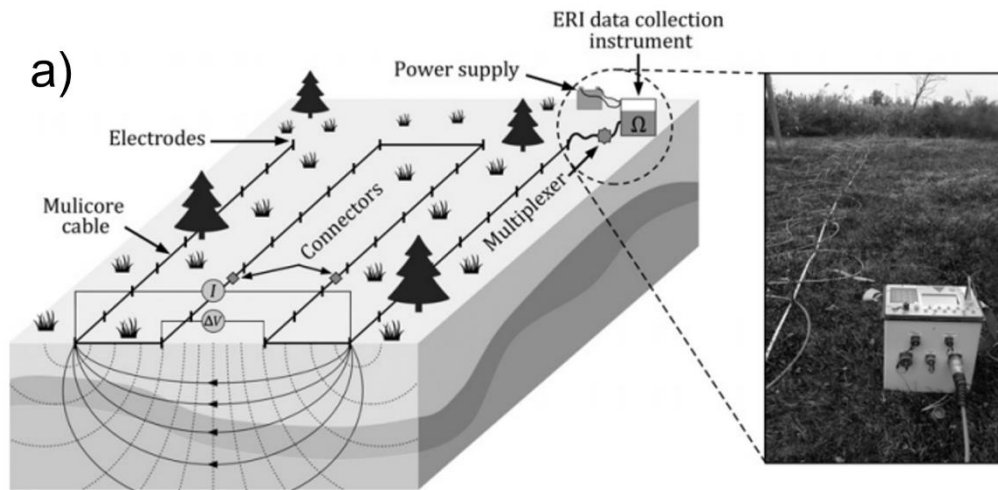


**Figure 2.4:** a) Schematic for an ERT survey, showing the electrode setup, potential and current electrodes ( $\Delta V$  and  $I$ ), the ERT data collection instrument ( $\Omega$ ) and the electrical current in the ground (Binley & Slater, 2020). b) Array types for ERT surveys, where  $K$  is a geometric factor,  $a$  is electrode separation and  $n$  is a factor which changes the size of  $a$  when measurement separation is larger than  $a$  (Rinaldi et al. 2006).

Each array type has a different sensitivity and sensitivity is important for an ERT survey and might influence array selection. Sensitivity can be defined as:

$$sensitivity = \frac{\delta \log(\rho_a)}{\delta \log(\rho)} \quad \text{Equation (2.1)}$$

where  $\rho_a$  is apparent resistivity and  $\rho$  is true resistivity. Sensitivity can help provide estimations for depths of investigation, where a threshold for cumulative sensitivity (*e.g.* where over 70% sensitivity exists) can define the depth of investigation (Binley & Slater, 2020).

Resistivity is sensitive to porosity, clay content, pore water conductivity (Binley et al., 2015), moisture content (Fargier et al., 2014) and temperature (Hayley et al., 2007). Hence, ERT can observe changing ground conditions from changes in water content from rainwater influx or variation of groundwater chemistry and temperature. Alongside this, ERT has the ability to successfully distinguish between lithologies, giving bedrock depth, and can give information on slip plane geometries and hydrogeological conditions (Chambers et al., 2011; Chen et al., 2022).

ERT has been one of the most common methods used on embankments for identification of seepage through the detection of conductive regions, which could indicate the presence of water, and seepage could be inferred through identification of such zones if it can be distinguished from other variables which may influence results (Loperte et al., 2016). (Akhmetov et al., 2020).

One problem with ERT is the 3D effect (Figure 2.5), in which proximal, but off-survey, resistivity distributions can influence the model resistivity values directly beneath the ERT line (Fargier et al., 2014; Hung et al., 2019; Hojat et al., 2020; Norooz et al., 2021) under a 2.5D assumption. Consequently, several inversion algorithms have been developed to constrain such effects on inversions (Bièvre et al., 2018; Cho et al., 2014a; Fargier et al., 2014). However, replicability of claimed advantages of such algorithms, such as Fargier *et al.*, (2014)'s model to account for geometric effects, have been disputed (Bièvre et al., 2018). Such 3D effects may cause petrophysical relationships to break down when interpreting 2D surveys, and it can lead to more generalised petrophysical models for 3D data (Zhang & Revil, 2015). 3D effects can arise from factors such as topographic effects, heterogeneous geology and features of anomalous resistivity nearby, such as a buried pipeline. In a river embankment setting, a key source of a 3D effect is likely to be the river. Furthermore, a river of variable stage (water level) and/or fluid electrical conductivity (*e.g.* from tidal influence) may lead to temporally variability of such 3D effects. The structural geometry of such embankments, dams in particular, are likely to be heterogeneous and complex, with different infills, bedrock

geologies, services and filter membranes which may cause 3D effects and inaccurate resistivity distributions. Modelling of the impacts of 3D effects on an embankment dam and the ability to detect defects in the core, showed that dam related 3D effects are likely to produce erroneous resistivity distributions and an inability to detect seepage zones (Norooz et al., 2021).

Laboratory (scaled physical model) experimentation has been used by Hojat *et al.* (2020) to explore the 3D effect induced by rivers. Their experiment involved filling a plexiglass tank, containing a scaled model of a river levee, with water. Surveys were undertaken at various water levels to represent seasonal variations in water level and a significant 3D effect was induced by the water body. Through this they observed changes in apparent resistivity to true resistivity ratios with different electrode spacings. It was shown that the 3D effect is larger with increased electrode spacings, because of greater depths of investigation inducing larger

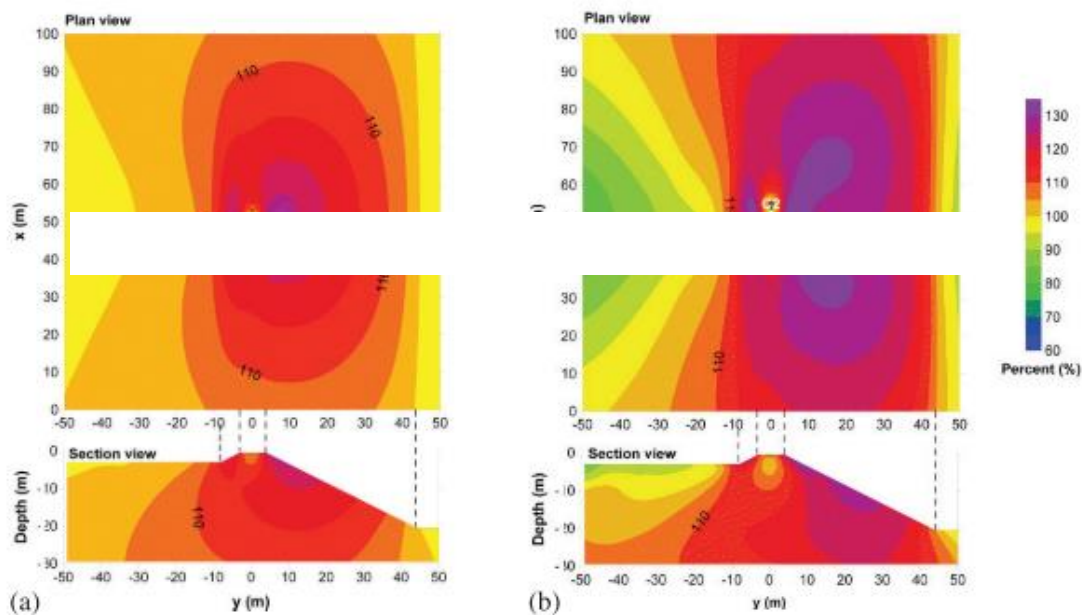


**Figure 2.5:** Distortions of potential distribution caused by the dam's topographic structure for a) a pole-dipole array and b) a dipole-dipole array. The model involved simulating a homogeneous embankment, where the results show percentage variation from the resistivity due to topography (Cho *et al.*, 2014).

sensitivities at depth and hence greater coverage that is potentially affected by adjacent resistivities (Hojat *et al.*, 2020). Further synthetic modelling showed that 3D effects have the potential to decrease with further increase of electrode spacing, as a decrease in shallow resolution will result in the source of the 3D effect having smaller impact on neighbouring data (Hojat *et al.*, 2020) when the source has a fixed position. The 3D effect varies with

seasonality, where the most severe 3D effects are induced in winter, predominantly at greater depths below the surface (Tresoldi *et al.*, 2019).

#### *2.3.1.1 Time-lapse ERT*

The ability for time lapse ERT to monitor temporal and seasonal changes in the subsurface enables improved understanding of subsurface variations due to effects of changes in porosity, moisture content, chemical composition of pore fluid, temperature and mineralogy (Carey *et al.*, 2017). This has promoted use of continuous monitoring systems. Such minimisation of repeat manual surveying, through automation, has allowed data acquisition to be controlled remotely (*e.g.* Daily *et al.*, 1992; Chambers *et al.*, 2014; Butler & Boulay, 2020). The British Geological Survey (BGS) has developed the Proactive Infrastructure Monitoring and Evaluation (PRIME) system, which enables monitoring at high spatial and temporal resolutions at near real time, creating the ability to give early warnings of failure (BGS, 2021b; Whiteley *et al.*, 2021). PRIME is powered by 10 W solar power and can assess changes in resistivity induced by moisture content variation (Holmes *et al.*, 2020; Holmes *et al.*, 2022), infer ground movement from identification of electrode movement through time (Wilkinson *et al.*, 2016) and joint electrode movement-resistivity inversions enable it to assess internal conditions (Boyle *et al.*, 2017; Loke *et al.*, 2018). Developments of other monitoring systems like PRIME (Pellicer *et al.*, 2012; Carey *et al.*, 2017; Butler & Boulay, 2020), have enabled time-lapse ERT to be monitored continuously over the long term (Hilbich *et al.*, 2011). This enables such systems to monitor geotechnical parameters, geohazards and groundwater processes (BGS, 2021b).

Greater quantification of seepage through an embankment can be acquired through time-lapse monitoring, in which temporal variation can be detected, giving a more detailed understanding of the progression of seepage phenomena and structural heterogeneities can be separated from changes due to changes initiate by potential seepage (*e.g.* moisture content) (Sjödahl *et al.*, 2008).

#### *2.3.1.2 Recent Developments*

The proliferation of the PRIME system has led to installation of the system worldwide to monitor landslides on natural and engineered slopes, rail embankments and cuttings, dams

and for agriculture (BGS, 2021a). Use of Time-lapse ERT for monitoring landslides, with robust association of resistivity with temporal variation in rainwater and groundwater content has been observed, and integration of other data has demonstrated successful use for assessing ground conditions (Lapenna & Perrone, 2022). Time-lapse ERT has also been employed successfully to monitor the evolution of hydrocarbon contamination, with dynamic assessment of changes in water content, temperature and biodegradation with progression of an oil plume (Nazifi et al., 2022). Time-lapse ERT has been used for several other purposes, including monitoring for other contaminants (*e.g.* saline intrusions and mining waste), volcanology and changes in permafrost through time, with over 75% of studies occurring in the last decade (Dimech et al., 2022). This shows the potential and applicability of time-lapse ERT for monitoring dynamic changes in large scale infrastructure, such as dams. However, it is impossible to generalise the results for all geological and geomorphological situations, meaning thresholds for slope instability is currently unachievable, and petrophysical models are not always able to be made for more reliable assessment (Lapenna & Perrone, 2022).

The importance of validating data has led the continued pursuit of petrophysical relationships between ERT and geotechnical data. The use of Archie's law has been used to investigate relationships between resistivity and porosity for applications, such as monitoring tailings contamination (Canales et al., 2020), temperature and saturation with Waxman-Smiths models for landslide analysis (Holmes et al., 2022) and pollutant concentration for analysis of contamination over time (Shao et al., 2022). Further progression has been made in terms of multiphase analysis (*e.g.* Canales et al., 2020) of petrophysical relationships which is important because unconsolidated sediment is of different phases (*i.e.* solid grains and pore water) (Lapenna & Perrone, 2022). The use of this can further support interpretations of what changes in resistivity represent and can be readily applied for monitoring seepage in dams, where moisture content and signs of slope instability are paramount for monitoring purposes.

### ***2.3.2 Induced Polarisation (IP)***

IP (Figure 2.6) is a technique that measures the ability of a material to be polarised by an injected electric current (Binley et al., 2015), which accumulates or redistributes ions in a material (Telford et al., 1990). IP is undertaken using two current electrodes and two or more potential electrodes, as with ERT (Revil et al., 2012). The chargeability measured by IP is



primarily sourced from chemical energy and can be measured, in the time domain, from the decay in voltage following interruption of an electric current (Telford et al., 1990). It can therefore be assumed that chargeability occurs along the charged grain boundaries or at pore throat interfaces (Binley et al., 2015). As such, it is not reliant upon pore connectivity, unlike other conductivity methods, but results may not be pronounced with current instrumentation due to weak polarisation characteristics of some geologies (Slater et al., 2014; Binley et al., 2015). Polarisation of the material is linked to presence of electrically chargeable minerals (e.g. clays, metallic minerals), which leads to polarisation due to impedance of an electrical current from an accumulation of ions at the mineral-solution interface, as well as membrane polarisation from clay minerals due to their net negative charge attracting positive ions from the electrolyte (Sharma, 1997). Minerals with high chargeability include ferrous minerals and clay deposits, where the latter can be used for detecting seepage in embankments (Martínez-Moreno et al., 2018) and can monitor the signature of the infill, given the common use of clay for infill and core. Alongside time domain measurement, IP can be measured in the frequency domain, where 100 Hz represents a typical practical upper limit for frequency readings due to associated interference from electromagnetic induction above this limit in the field (Revil et al., 2012). However, IP may be preferable given its capability to assess the time taken for the electrical polarisation to return to equilibrium (*i.e.* its relaxation time) (Binley et al., 2015).

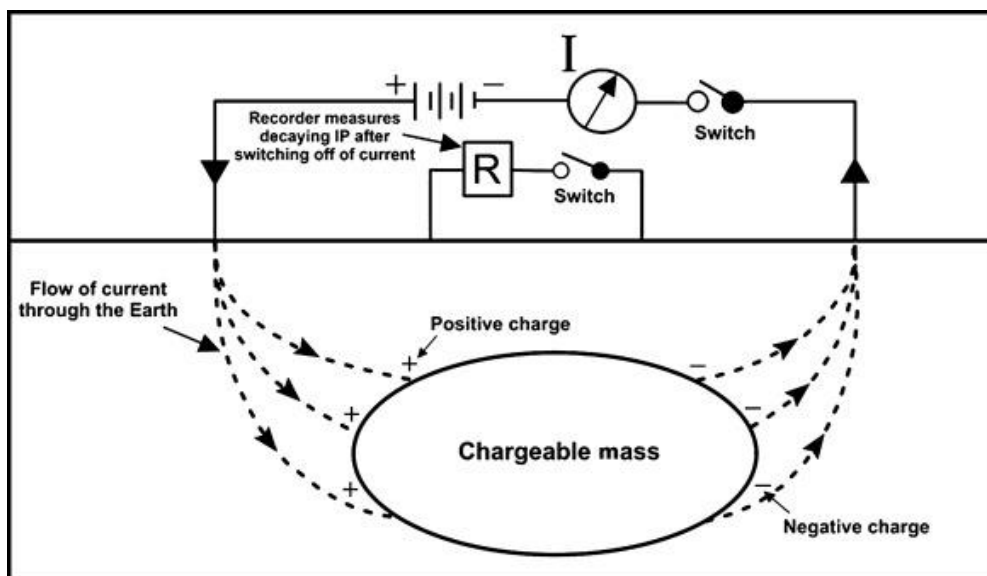


**Figure 2.6:** : The principles of IP, showing the injection of current from two current electrode, the two potential electrodes and the charges resulting from a chargeable mass in the ground (Gandhi & Sarkar, 2016).

IP is limited by the possibility of capacitive coupling with its wiring and noise induced by electromagnetism (Robinson et al., 2008), alongside difficulties in interpretation (McLachlan et al., 2017). IP requires more time consuming surveying than ERT, which hinders it for standalone surveying where time is limited and distances to be surveyed are large, but it may give an advantage over ERT for monitoring given ERT's insensitivity to variance between conduction from electrolytic composition and surface conduction (*e.g.* from clays), unlike IP (Vagnon et al., 2022).

#### *2.3.2.1 Recent Developments*

Use of IP has so far been relatively limited on water retaining structures, but some studies have utilised this for assessment (Martínez-Moreno et al., 2018; Ahmed et al., 2020; Akhmetov et al., 2020). Many ERT systems, including for time-lapse, have the capability to undertake IP surveys and further studies have looked at the real and complex conductivity and related relaxation time to permeability in sand deposits (Ma et al., 2022), as well as use of 3D IP for monitoring landslide deposits where landslide formation was linked with increased water content, areas of high permeability and highly plastic clay (Revil et al., 2020). Other studies have applied IP for biogeological purposes, including monitoring plant and tree structures and root intake (Kessouri et al., 2019).

#### *2.3.3 Self Potential (SP)*

SP involves the passive monitoring of the electric current generated by the flow of ions by electrokinetic, thermoelectric, electrochemical or mineral processes (Sharma, 1997). Electrokinetic coupling arises from the uneven distribution of ions in a liquid transferred through a porous media, creating a potential difference (Bolève et al., 2011). For identifying leakage paths, the ability of SP to detect flow gives it a distinct advantage over other geophysical methods, and has been used to identify mineshafts (Pringle et al., 2008). SP results in an ability to detect flow because the surface of mineral grains are typically negatively charged, creating an excess of electrical charge in the vicinity of the mineral-solution interface (the electrical double layer) (Leroy & Revil, 2004). The mobile part of the electrical double layer is transported by the flow of water and this produces an electrical

current proportional to the Darcy velocity (Bolève et al., 2011). From the polarity and magnitude of the electrical field produced by the streaming potential, direction and flow velocities can be inferred (Revil & Jardani, 2010). SP surveying can be undertaken using the leapfrog method and fixed base method, where the former involves moving an array of a fixed length across the survey area reading, and the fixed base method involves a fixed location for one electrode and movement of the other electrode with the progression of the section (Figure 2.7) (Wang et al., 2018). SP surveys have been commonly used due to their economic benefits and comparatively simple apparatus for use in the field, allowing rapid surveying (Sentenac et al., 2018), but masking by noise can make surveys difficult to interpret (Gupta & Roy 2007).

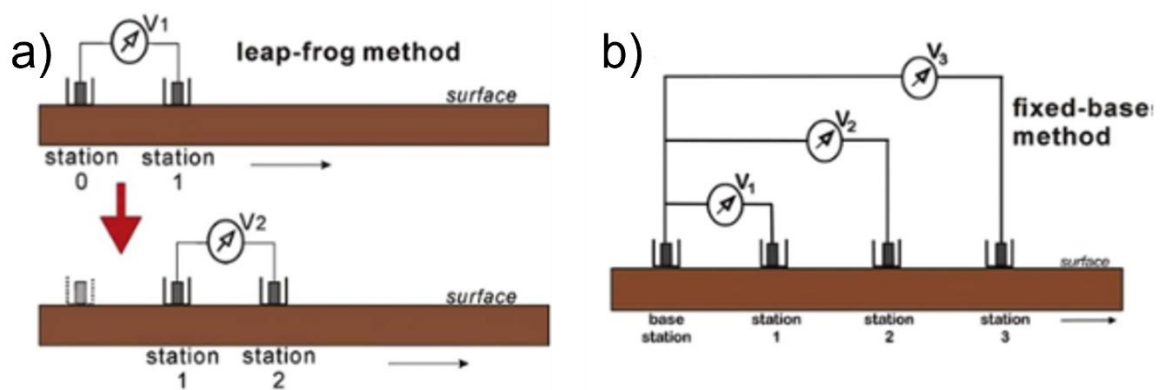


**Figure 2.7:** The different arrays for self-potential surveying, where a) is the leap-frog method and b) is the fixed base method (Wang et al., 2018).

Injection of a tracer can allow monitoring of anomalies in SP, as with other methods, where the tracer is expected to generate an associated SP anomaly which is distinctly different to background levels (Bolève et al., 2011). For example, injection of a salt tracer allows tracking of seepage paths through time, facilitating monitoring of its progression (Bolève et al., 2011). In a dam or embankment, contours of equipotential for an SP survey should be parallel, meaning any distortions give indication of seepage pathways developed or developing (Gallas, 2020).

### 2.3.4 Seismic Surveying

Seismic surveying (Figure 2.8) involves the recording the arrival of refracted and/or reflected seismic waves using a geophone array (Dunbar et al., 2017). Thus, variations in velocity of the refracted or reflected wave between layers can be used to infer characteristics of the sub-surface (Telford et al., 1990). Body (P and S) waves and surface waves have been utilised for the purpose of evaluating the integrity of embankments (Dunbar et al., 2017). The use of P and S waves gives benefits through their ability to be correlated to geotechnical parameters like Poisson's ratio, due to the linkage with elastic stiffness, giving an assumption that seismic velocity responds directly to shear strength and soil stiffness (Cardarelli et al., 2014).

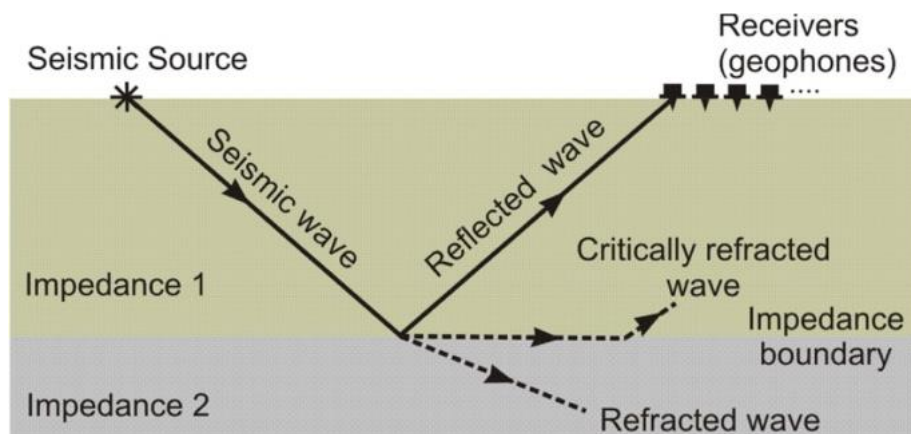


**Figure 2.8:** A seismic survey showing the reflection and refraction of waves from a layer boundary (such as the water table or bedrock-soil interface). Geophones can be used to detect the reflected and refracted waves from a source (Hunter et al., 2022).

Seismic surveying suffers from interpretation difficulties, processing noise for a realistic survey (e.g. multiples) and time taken to process, especially for reflection surveying. Moreover, accurate calculations of wave velocities and layer depths are hard to estimate and geometric and velocity structures can cause misinterpretations of subsurface features (Taner et al., 1970).

Seismic surveying has been used for the monitoring of slope failure due to variations in seismic impedance within the landslide body (Pappalardo et al., 2018). It is therefore suggested that this method could be undertaken for understanding the possibility of potential slope failure within an embankment. Seismic surveying has also been used to successfully

visualise the subsurface and identify seepage paths (Wang et al., 2018). Combining seismic surveying with ERT can generate a better, more reliable characterisation of dam characteristics and erosion (Sazal et al., 2022).

#### *2.3.4.1 Active and Passive Seismic Surveying*

Active seismic surveying for near surface geophysics involves generating a source, by means of, for example, a hammer or weight drop, that will release seismic waves that are detectable by geophones (Dunbar et al., 2017). Multi-channel analysis of surface waves (MASW) is increasingly being used because surface waves often have greater depth resolution than body waves in refraction surveys (Cardarelli et al., 2014), they can produce higher amplitudes of energy, they are suited for use of non-invasive geophone arrays and can be readily correlated to shear modulus, because shear-wave velocity increases in a relationship with material rigidity (Dunbar et al., 2017).

Passive monitoring is also used for seismic reflection, refraction and MASW surveying (Planès et al., 2016; Baglari et al., 2018), where this involves use of an ambient noise source capable of generating seismic waves of sufficient magnitude to be detected by geophones. In selecting geophone array locations, it is important to align geophones with the source in order to ensure coherent noise across the section (Planès et al., 2016). Sources of ambient noise in embankments are typically external factors, like traffic (Planès et al., 2016). Noise emitted from water release after reservoir level reduction and earthquakes can also provide passive sources (Kim et al., 2021). This may provide useful information for the monitoring of water retaining structures due to the direct linking between leakage and noise generation, increasing reliability of interpretation. However, such sources may not generate strong enough amplitudes for surveying. In either case, source location needs to be known in order to filter noise and to ensure that ambient noise is constructional to the tomogram (Planès et al., 2016).

#### *2.3.4.2 Recent Developments*

Seismic surveying has been used to detect seepage from active surveying or from seepage within the embankment itself, if noise is sufficient (Bièvre et al., 2017), allowing identification

of leakage paths through embankments, where drops in seismic velocity correspond to formation of sand boils and piping initiated by seepage (Planès et al., 2016).

The development of processing frameworks and improved equipment for seismic surveying has enabled greater use of passive surveying (Antonovskaya et al., 2019). This enables greater quantification of potential seepage, which can be associated in conjunction with other methods. Several recent studies have used seismic surveying in conjunction with electrical methods to jointly assess the geological and hydrological structure of embankments (Rahimi et al., 2019; Golebiowski et al., 2021; Sazal et al., 2022; Vagnon et al., 2022).

### *2.3.5 Electromagnetic Induction (EMI)*

Electromagnetic induction in the frequency domain involves the generation of a primary field within a coil and induction of electrical currents perpendicular to the primary field within the ground, which can be detected using a receiver in the coil (Sharma, 1997). In time domain EMI, transient electromagnetic (EM) pulses are generated and the primary field is immediately ceased, allowing measurement of decay of the secondary field induced in the ground (Figure 2.9) (Sharma, 1997). Frequency domain EMI involves the generation of a primary magnetic field by an electrical current, where both are in phase. Eddy currents in the ground are induced by the electromagnetic force and generate a secondary magnetic field which can be used to infer properties from the out-of-phase components (McLachlan et al.,

2017). The conductivity of the medium, electromagnetic frequency and coil spacing between transmitter and receiver dictates the depth of investigation (Michalis & Sentenac, 2021).

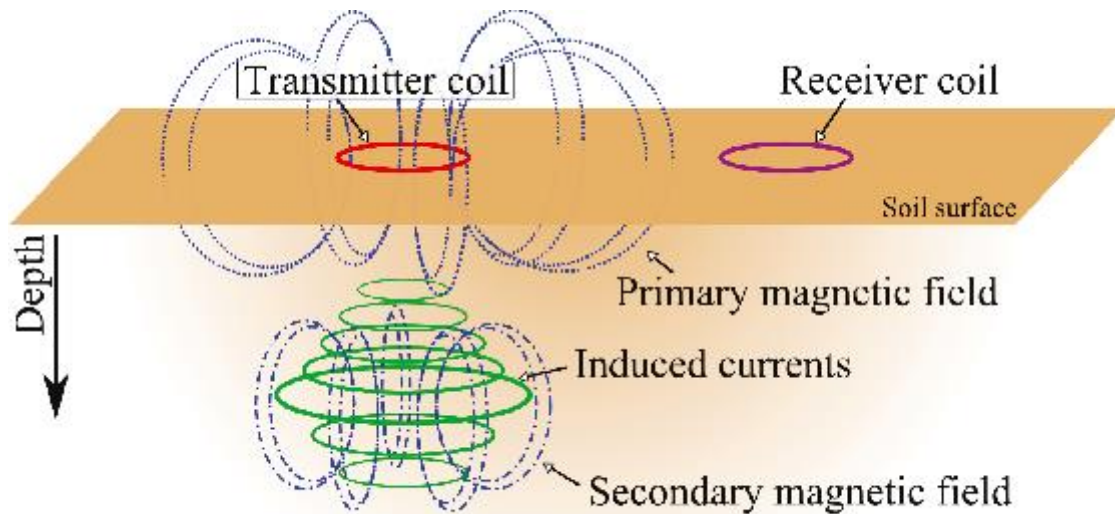


**Figure 2.9:** Principles of an EMI survey, where a transmitter coil generates a primary magnetic field, which induces eddy currents and a secondary magnetic field. This is then detected by the receiver coil (Mester, 2015).

EMI can be used for identifying conductive bodies, which could refer to clay or water, so they can be applied to identification of seepage paths and monitoring of internal structure of an embankment (Sentenac et al., 2018). Modern frequency domain EMI instrumentation can extract data from several depths simultaneously, using multiple secondary coils (McLachlan et al., 2017). This gives them greater suitability for the potential assessment of internal features of interest within water retaining structures and potential use for waterborne surveys. Whereas ERT, IP and SP involve insertion of electrodes into the ground, EMI involves no direct contact with the ground, meaning that it is truly non-destructive, which may be of benefit.

EMI may present a cheap and rapid reconnaissance survey to estimate conductivity, but is limited by an insensitivity to resistive features (Huitzil et al., 2022) and an assumption that the low induction number (ratio of the coil spacing to skin depth) is valid, which is not the case for very conductive media or high conductivity contrasts (Lavoué et al., 2010). Moreover, EMI is less suited for time-lapse analysis given its manual operation and that common instrumentation does not have the same depth of investigation or flexibility in survey design for optimised depth of investigations as ERT.

#### 2.3.5.1 Recent developments

Like other geoelectrical techniques, EMI has seen increasing use for agricultural, civil engineering, archaeology and groundwater assessment (Everett & Chave, 2019). Some studies have applied EMI for assessing water retaining structures (Adams et al., 2021; Davydov et al., 2021), though are fewer than ERT. There is a growing understanding into the stability and increased use of calibration with ERT data, which has enabled greater use for hydrogeophysical purposes (Lavoué et al., 2010; Boaga, 2017), and surveys are more commonly using data filtering and inversion to improve results (McLachlan et al., 2017).

#### 2.3.6 Electrical Current Imaging

Electrical current imaging can be used to survey for potential leaks from the detection of an electrical current flowing through a medium, where this was pioneered to monitor waste leakage through geomembranes due to the insulating layer forming a contrast above and below the geomembrane (Parra, 1988). Electrical current imaging uses two potential electrodes to generate an electrical current in a horizontal orientation, which differs from ERT because ERT involves measuring current in vertical and horizontal orientations (Lee & Oh, 2018). Electrical imaging can be used to detect leakage in embankments through measuring the potential difference between two electrodes located at opposite faces of the structure (Lee & Oh, 2018). There are three principal methods in which surveying can be undertaken for identifying leakage (Figure 2.10), where leakage can be analysed from distortion of the electric field, as caused by currents flowing through a conduit (*i.e.* a leakage path) (Lee & Oh, 2018). The movement and distribution of electric current is analogous to flow of water, therefore flow-field fitting can be employed to fit flow fields of seepage to identify leakage paths (Meng et al., 2019).

Electrical current imaging has had success in identifying small leaks which may give the technique advantages over ERT, because resistivity contrast variations may not be detectable in ERT (Binley et al., 1997) and previous successful use in identifying features of leakage in concrete dams and contamination pathways could indicate potential for detecting seepage in earthen water retaining structures.



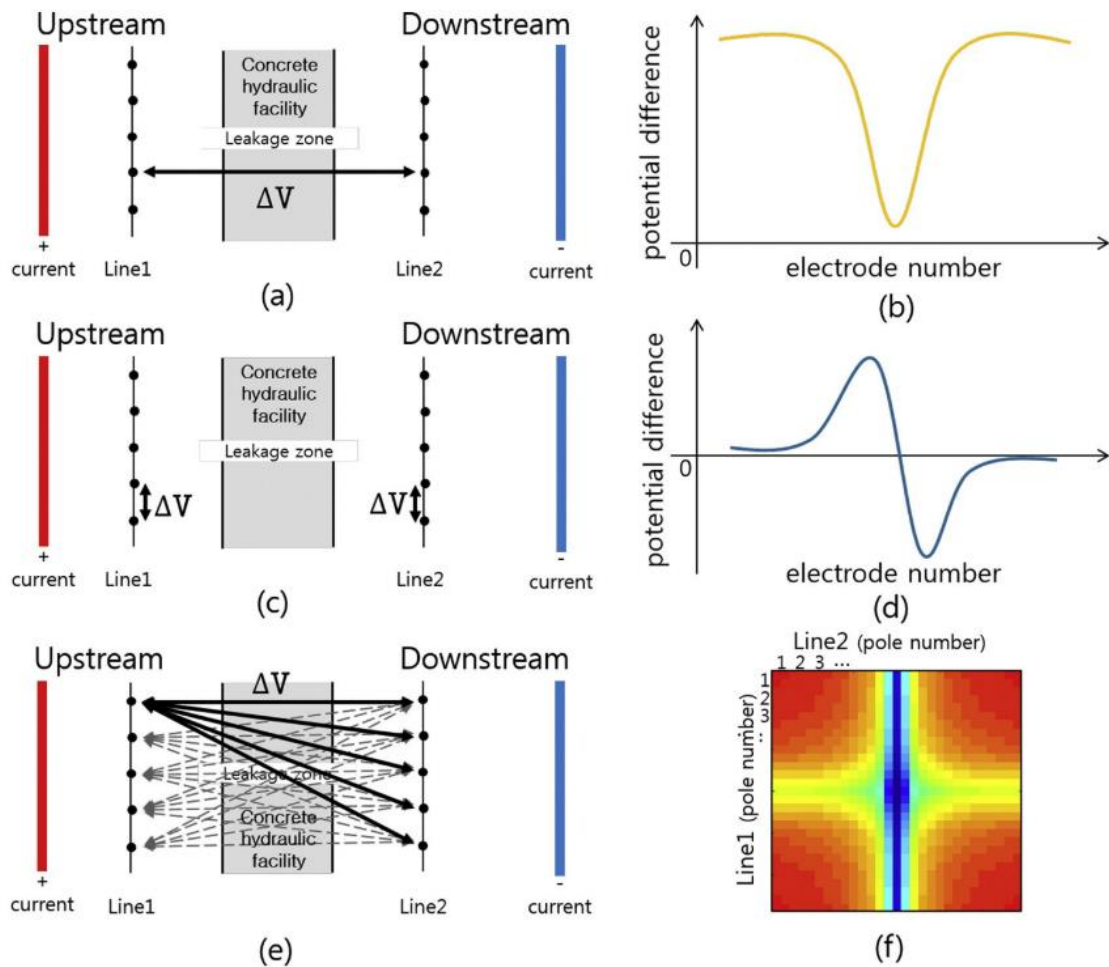


**Figure 2.10:** Three methods of utilising electrical current imaging along an electrode array. Where a) is a cross potential array, which measures the differences in potential across singular upstream and downstream poles and b) is its associated plot. c) is a direct potential array, which measures the potential difference between adjacent electrodes in each line and d) is its associated plot. e) is a D-lux array which measures the potential difference between all the upstream and downstream poles and f) is the resultant matrix, which is similar to a tomogram. The blue and red lines represent positive and negative potential electrodes (Lee & Oh, 2018).

### 2.3.7 Magnetometric Resistivity (MMR)

Akin to electrical current imaging, MMR involves injection of an electrical current, generating a magnetic field, as measured between two magnetometers (Jessop et al., 2018). Modern usage of MMR has been primarily focussed around the company, Willowstick, where the aims of MMR are to utilise the conductivity of the pore fluid alone to identify leakage (Kofoed et al., 2014), due to sensitivity of MMR to a current concentrated in a conductive body (Jessop et al., 2018).

The horizontal resolution achievable with this method is between 0.25 m and 0.5 m for 1 m spacing of magnetometers (Kofoed et al., 2011), enabling verification with vertical boreholes provided the leak is intercepted at the predicted depth, and depths of investigation of 100 m have been reported (Kofoed et al., 2014), where depth resolution is likely to be around 10% of target depth. MMR has better abilities to detect features below a conductive overburden, which would interfere with data from electrical current imaging (Edwards et al., 1978).

### ***2.3.8 Ground Penetrating Radar (GPR)***

GPR (Figure 2.11) is an electromagnetic technique which typically uses 10-1000 MHz EM waves to image the shallow strata of the ground from the propagation and attenuation through the subsurface (Sharma, 1997). GPR can detect variations in the dielectric properties of the subsurface (Sharma, 1997), which enable it to readily detect contrasts generated by voids, but it is highly attenuated by conductive material, such as clay. This makes it difficult to use in earthen water retaining structures, which are often clay-rich (Antoine et al., 2015). Propagation of waves are driven by a transmitting antenna and waves are backscattered from interfaces between electromagnetically contrasting media, which are then detected by a receiver array (Loperte et al., 2016). Like EMI, the technique is truly non-invasive when not emplaced in boreholes, and its high resolution enables it to distinguish between features at shallow depths (Sharma, 1997). GPR is mostly measured in the time domain, but larger bandwidth frequency domain models are available (*e.g.* Bi et al., 2018). The receiver antennae can collect data using common midpoint, fixed offset and other gathering techniques (Pringle et al., 2003).

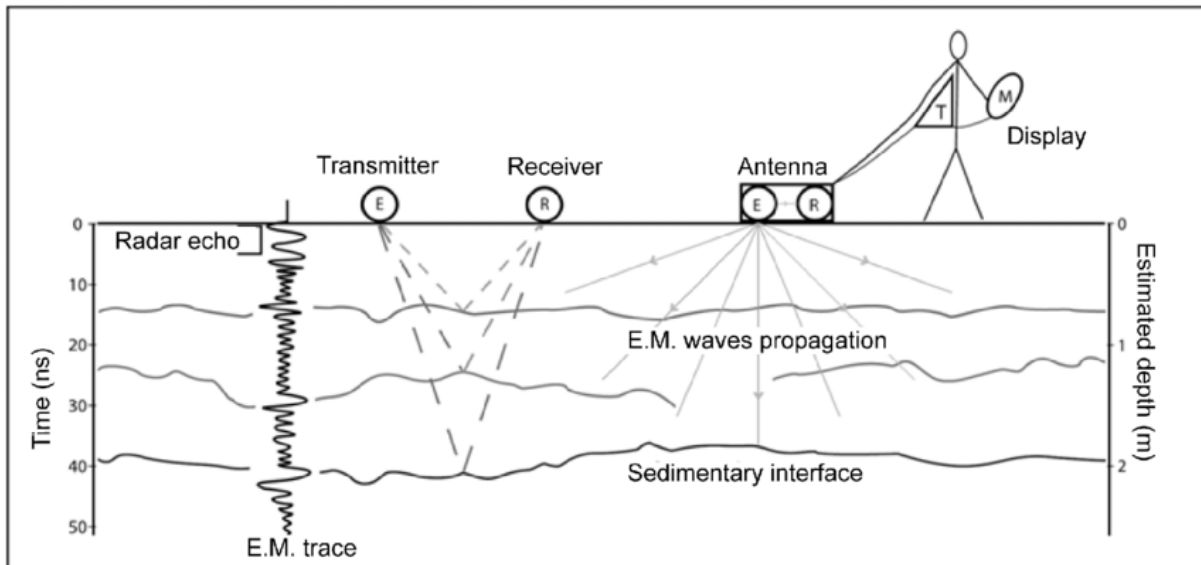


**Figure 2.11:** Schematic representation of a GPR survey, showing the transmission of the waves and detection by a receiver, as well as a 1D electromagnetic trace, with high amplitude signals at layer boundaries (Lavigne et al., 2013).

GPR can be used in ground-coupled and air-coupled approaches, where the latter provides access for more inaccessible locations and faster acquisition, but is more prone to noise and inability to visualise data (Vilbig, 2013). Typically GPR requires different antennae for different frequencies, but more modern step-frequency or 3D GPRs can be used to probe different depths (Gopalakrishnan et al., 2017). GPR can also be used in boreholes, using vertical radar profiles with antennae at different depths, as well as along vertical sections (*i.e.* cliffs) for better identification of layer boundaries (Pringle et al., 2003).

### 2.3.9 Distributed Temperature Sensing (DTS)

Temperature can be used to assess for potential seepage within embankments. In low to non-existent flow, the temperature distribution in the upper section of the subsurface varies seasonally in accordance with air temperature, whereas in high flow velocities, temperature variation is lower and dominated by advection (Bersan et al., 2018). Therefore, temperature variations could be indicative of sub-surface conditions. DTS is a relatively new technique which has had increasing use within geophysics for hydrogeological purposes, following the increased development of optical fibre sensors since the 1980s (Yosef et al., 2018), allowing large scale monitoring of embankments, where previously temperature had only been utilised locally (Schenato, 2017). This can be used to monitor for spatial variation over large scales, allowing potential identification of areas effected by leakage. Distributed optical fibre sensors

detect temperature variations through means of Rayleigh, Raman and Brillouin scattering of electromagnetic radiation (Boyd, 2008). In Rayleigh scattering the sensors detect environment dependent propagation effects from attenuation, polarisation, rotation or phase interference, and in Raman or Brillouin scattering, the sensors correlate the intensity of the scattering to temperature (Schenato, 2017). DTS can be undertaken using active or passive means, where active sensing involves heating the cable and observing the subsequent temperature decrease to identify flow rates and passive sensing measures the natural variability in temperature for temporal analysis (Bersan et al., 2018). Passive monitoring is preferable due to lower cost and effort, but active means may prove useful if variations in the temperature gradient are minimal (Schenato, 2017). Emplacing the optic fibre cables involves burying the cable in the soil, in a narrow trench or under the surface of the downstream slope, where it should be installed lengthwise at an embankment, at the upstream face for water tightness control or at the downstream face or face for seepage monitoring (Schenato, 2017). Increasing seepage rates (Bersan et al., 2018) leads to temperature decreases (Chen et al., 2018). Seasonal temperature variation at depth is usually minimal (varying between a few degrees Celsius), unless a filtration flow is present, causing more pronounced temperature variations at depth (Schenato, 2017).

There has been a growing use of DTS for monitoring embankments (Figure 2.12); Bersan *et al.*, (2018) used it to assess for backwards erosion and seepage in a levee, where internal erosion patterns have been determined based upon whether heat advection or conduction is dominant. In advection dominant scenarios, potential erosion can be determined using the thermal front velocity to calculate the distance that this front travels along a seepage path, where this can be monitored over time to detect and observe seepage, as well as to calculate seepage rates. Alternatively, non-uniform temperatures towards the base can indicate erosion, where temperature variation in the foundation and pipes indicate advection dominance and variation in pipes alone indicates conduction dominance (Bersan et al., 2018). DTS has also been applied successfully in dams, where temperature variations from fluid flow have been detected and inferences of seepage can be made from linkages between the reservoir and potentially leaking water (Yosef et al., 2018). For instance, the associated thermal processes accompanying the advection of groundwater flow enables DTS to detect

variations in temperature from seepage (Bersan et al., 2018), as seepage will typically involve cooler water temperatures infiltrating at depth (Yosef et al., 2018).

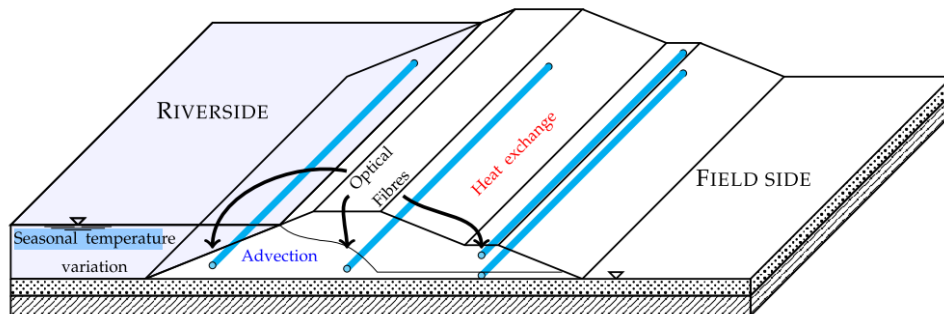


**Figure 2.12:** The use of DTS for monitoring seepage through an embankment. The optical fibres used for DTS can be emplaced riverside, landside or underneath the embankment to monitor temperature associated changes which might arise from the water body (Schenato, 2017).

#### 2.3.9.1 Recent developments for distributed optical fibre sensors (DOFS)

DTS and the use of other distributed optical fibre technology has been described as being technologically revolutionary, due to the number of sensory points compared to single-point contact technology (Schenato, 2017). The lack of interference from electromagnetism, lightweight nature, ability to sense multiple parameters, multiplexing and remote automation capabilities (Schenato, 2017) makes DOFS an attractive technique. These advantages, coupled with decreasing costs have led to further usage and development (Bersan et al., 2018), and the distributed nature of monitoring makes DOFS highly applicable for use in dams and levees, where geographical extent is high, ground conditions may be harsh and high spatial density is required (Schenato, 2017). However, DOFS (Figure 2.13) could be used to measure other physical domains, such as pressure or strain (Schenato, 2017). Distributed pressure sensing, however, is unproven in accuracy, resolution and dynamic range for it to be confidently used for assessment (Schenato, 2017). Distributed acoustic sensing (DAS) has had more success, but requires high spatial resolution and sensitivity (Schenato, 2017). However, it has been used in embankments to detect deformations caused by soil movement (Kihara et al., 2002).

Back-scattered light signals, arising from inhomogenities in the fibre, are used to detect strain measurement, as induced by seismic sources (Ning & Sava, 2018). DAS is more spatially resolute and cost efficient than use of geophones, leading to greater preference for surveying

(Ning & Sava, 2018) However, DAS is limited to measurements of axial strain and methodologies have been developed to extract multicomponent data from axial strain measurements (Ning & Sava, 2018). Difficulties have arisen in achieving analyses windows which can account for seismic wavelengths smaller than such windows (Ning & Sava, 2018), which has led to recent progress in instrumentation to overcome such problems. One such example is use of helical fibre sensors (Ning & Sava, 2018) and optimised survey designs containing more than one fibre at preferential pitch angles have been shown to be suitable for obtaining multicomponent data at short wavelengths (Ning & Sava 2018).

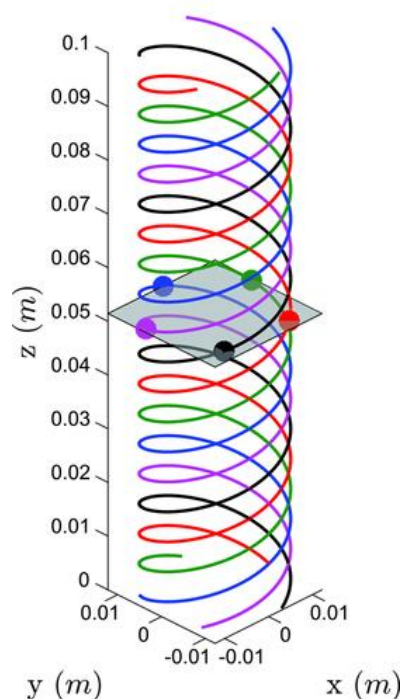


**Figure 2.13:** A representation of a helical fibre sensor of DOFS cables for sensing strain. The horizontal plane, and dots on it show how each cable is placed at an equidistance (Ning & Sava, 2018).

### 2.3.10 Numerical Modelling

When creating a spatial representation of the subsurface using geophysics we can use forward modelling. This is often developed prior to geophysical surveying to give a hypothetical model of the subsurface, so that survey design can be aided, comparisons can be made between observed and synthetic data, and an estimation can be made for the most appropriate technique for surveying (Jones et al., 2014). Forward modelling can also be used to assess reliability of interpreted data, where consistency between the result and forward model gives greater confidence, and as a guide to aid data interpretation. An example of

where forward modelling can be used to aid geophysical design is using it to investigate the effects of electrode array type for ERT. This approach can help selection of a suitable array for minimal artefacts in the inversion (Carey et al., 2017) and to estimate if targeted features are likely to be detected with the geophysical technique (Pringle et al., 2012).

While forward modelling computes a theoretical response from given parameters, inverse modelling develops a model from a set of parameters that is consistent with the data (Binley, 2015). Inversion of geophysical data typically involves modelling spatial variations of one property (Figure 2.14); joint inversions are undertaken for geophysical techniques that are sensitive to multiple properties (Agostinetti & Bodin, 2018). Modelling can be undertaken stochastically or deterministically. Stochastic modelling can provide estimates of the uncertainty in model parameters (resistivity in the case of ERT) and can offer more reliable estimates of the global minimum in an inversion, however, they are computationally demanding, which can limit the size and dimensionality of the problem they are applied to. Deterministic methods are more easily applied to complex and highly parameterised 2D and 3D models, though they only output one single solution (Rosas-Carbajal et al., 2014).

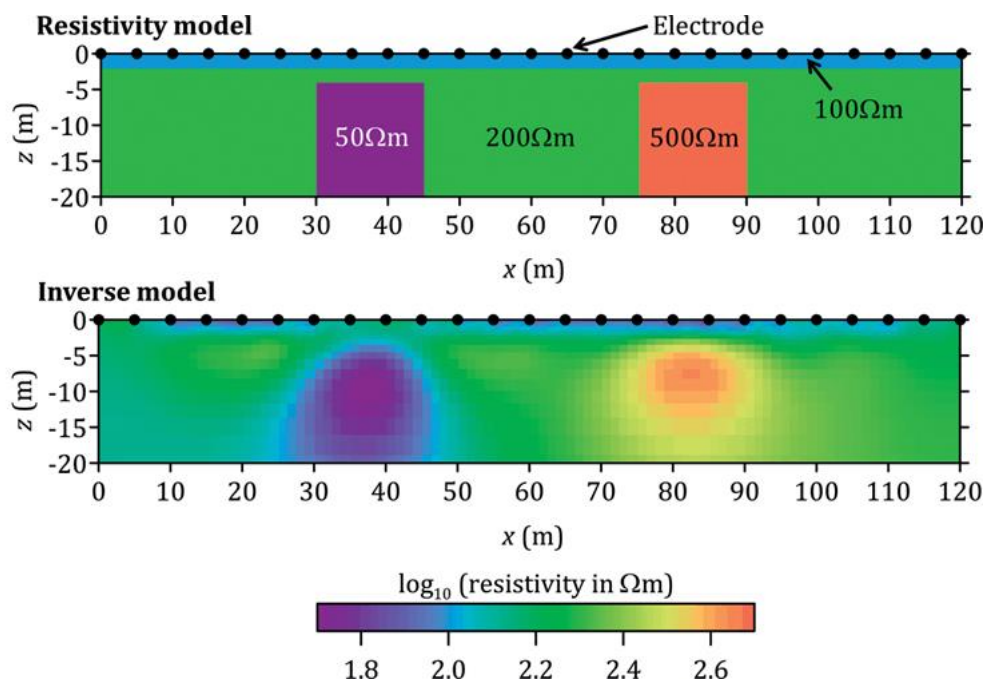


**Figure 2.14:** Inversion of a synthetic 2D model, showing the resistivity model, with assigned resistivity values for the forward model, and the output of an inversion for the model (Binley & Slater, 2020).

For time-lapse inversion, a reference model is chosen as a baseline for inversion. The baseline dataset is inverted and following datasets are inverted using this as a reference model (Jouen et al., 2016). Such inversions focus upon temporal variation from one parameter and use temporal changes within the geophysical parameter to visualise changes (Kemna et al., 2002). Typically, inversions from standalone and time-lapse surveys employ spatial smoothness constraints, but they may not be coherent with the local geology (Hermans et al., 2016). The principle role of such constraints is to stabilise the inversion process, but they also effectively introduce *a priori* information, e.g. creating smoother, more geologically reasonable, images (deGroot-Hedlin & Constable, 2002). As such, alternatives have been sought, such as blocky inversions (Hermans et al., 2016), which create more geologically coherent tomograms in areas with sharp resistivity changes, but fail to create robust representations of resistivity variation where resistivity changes are gradual (Loke et al., 2003). Such inversion models can be constrained by inputting known variables from external sources, which do not require regularisation and increase reliability of the model. However, this approach may be constrained to more homogeneous settings due to complexities in heterogeneous settings decreasing reliability of the data (Hermans et al., 2016). To assess model validity, it is important to report error models associated with the inversion, where reciprocal error models (deviation between results from measurements using the same electrodes, but with alternate potential and current electrodes) are more suited than stacking errors (an average of the stacks from data collection equipment) due to the associated higher errors in the inversion (Tso et al., 2017).

Several computer software for processing of ERT data have been developed and used for assessment of water retaining structures. RES2DINV (Loke, 2022) has commonly been used for processing (Wilkinson et al., 2010; Ikard et al., 2012; Martínez-Moreno et al., 2018; Jodry et al., 2019; Sazal et al., 2022). However, development of open-source software, such as ResIPy (Blanchy et al., 2020), has enabled more accessible inversion software for use on ERT.

Other techniques require processing. GPR can be processed using software, such as REFLEX-w (Sandmeir, 2023) and GPRPy (Plattner, 2020) to ensure the arrival times start at 0 ns, filter noise to make target hyperbolae more pronounced, removal of any 'ringing' effects from repeated wavelets, bandpass filters to remove low-amplitude signals and to employ other techniques to enhance clarity of the data (Pringle et al., 2012). GPR data can then be



presented as singular slices over a given transect or as a combined selections of slices from a 3D survey to visualise the subsurface in both lateral orientations at different depths. EMI data can be processed and inverted using the software, EmagPy (McLachlan et al., 2021) and several packages exist for processing seismic surveying for stacking the data, deconvolution and migration of stacked wavelets. Such software include RadExPro (RadExPro, 2023), VISTA (SLB, 2023) and REVEAL (Shearwater, 2023).

Further studies have explored numerical modelling for assessing the validity of the geophysical model produced, given external factors (*e.g.* topography) can influence geophysical results (Fargier et al., 2014; Bièvre et al., 2017). This shows that the modelling of geophysical data can be highly limited by ambiguity, and it is imperative that a greater understanding as to impacts on geophysical data is possible for greater reliability and knowledge as to how such modelling effects occur. Therefore, the following chapters are heavily focused on exploration of how such 3D effects can impact data and whether 3D inversions can help improve visualisation for ERT.

### ***2.3.11 Physical Modelling and Geophysical-Geotechnical Relationships***

It is necessary for geophysical contrasts to be interpretable as hydrogeological or geotechnical differences within the subsurface. To make a reliable assessment using geophysics, it is important that uncertainties are minimised as much as possible so that solutions are not non-unique. Physical modelling has allowed the generation of relationships. ERT is sensitive to temperature (Hayley et al., 2007), which may be needed to be accounted for if moisture content variations are the primary monitoring variable. With temperature, there is an associated approximate 2% decrease in conductivity for every 1°C increase (Pellicer et al., 2012), but vegetation may cause localised temperature differences (Zumr et al., 2020) which may affect temperature data if gathered from another part of the site. Various methods have been used to account for effects induced by these variables, including characterisation of uncertainties on the quantities of interest, which aims to predict and constrain uncertainty in the targeted parameter (*e.g.* resistivities associated with a contamination concentration in pollution monitoring), given a set of inputs from a multivariate parameter (Linde et al., 2017). Also, normalisation techniques have been utilised for the reduction of topographical or reservoir effects (Fargier et al., 2014).

Linking geophysical features to geotechnical parameters can further constrain data, such as by connecting geophysical variations to features identified from geological cross sections (*e.g.* Martínez-Moreno et al., 2018) or borehole data (*e.g.* Loperte et al., 2016). The use of multiple geophysical data sets, structural approaches and petrophysical modelling have been used to quantitatively assess interpretation of geophysical models (Zhang & Revil, 2015). For example, studies have correlated resistivity to water tension (Descloitres et al., 2008), dielectric permittivity to water content and IP to interconnected pore space (Slater, 2007). Such modelling techniques have been commonly performed by empirical means, but there have been attempts to model mechanistically to give greater predictive abilities (Revil, 2012).

ERT data can be empirically shown to be related to gravimetric moisture content through a Waxman-Smits model and physical experimentation, where samples taken from a field site are progressively wetted and associated resistivity measurements are taken (Figure 2.15) in a temperature controlled environment (Chambers et al., 2014). From data extracted from the field, such as on a railway embankment at East Leake, United Kingdom (Gunn et al., 2018), there are demonstrable strong relations between resistivity changes and changes in the dynamic moisture distribution. When coupled with weather data, such resistivity changes can be related to seasonal effects and can be used to determine whether moisture content variations are primarily associated with effective rainfall. For instance, moisture content variations which are larger than expected values from increased effective rainfall data may indicate ingress of water from other sources, such as seepage from nearby surface water bodies. Moisture content, and resistivity, can be related to shear strength, where decreased moisture contents are associated with increased shear strength, and a drop in shear strength at the transition between drying and wetting events correspond to increased resistivity values from soil fabric deterioration (Hen-Jones et al., 2017).

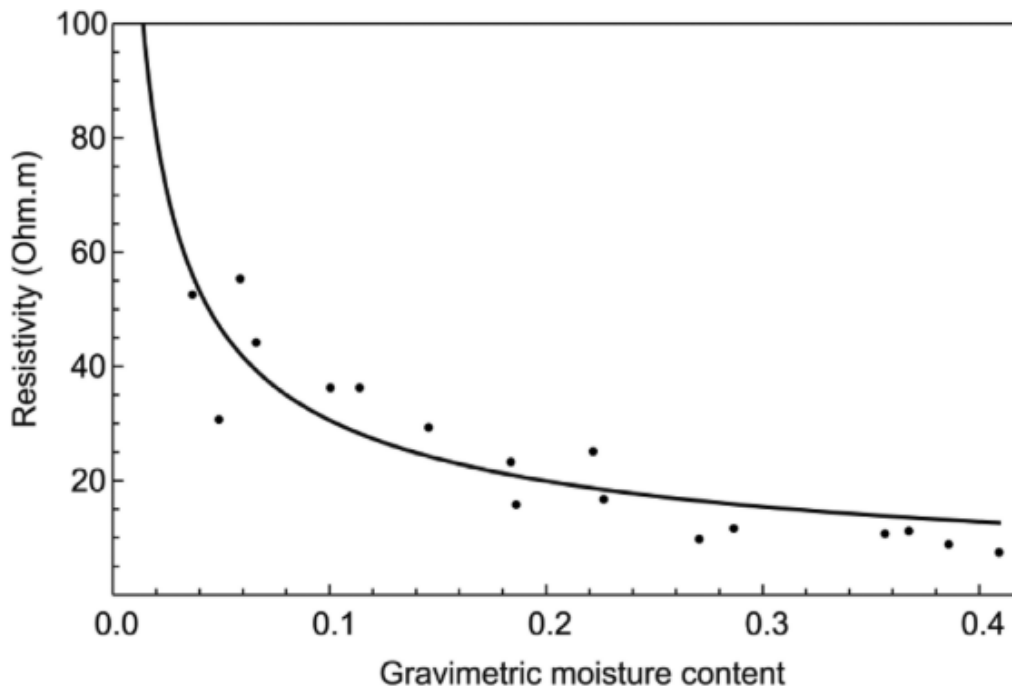


**Figure 2.15:** Resistivity variations from increased gravimetric moisture contents from laboratory analysis of samples of the Whitby Mudstone Formation taken from a railway embankment near Nottingham (Chambers et al., 2014). This shows the relationship which can be derived from field samples, which can be later used to validate moisture induced changes on resistivities from ERT surveys.

Relationships between electrical and hydraulic parameters vary in different contexts. For instance, in clay rich freshwater there is a negative correlation between electrical and hydraulic conductivity due to effects arising from pore surface conductivity, as a result of clay minerals forming a surface charge, while saline water forms a positive correlation due to increased salinity leading to increased conductivity (Purvanca & Andricevic, 2000).

Common moduli used to characterise soil stiffness include the shear modulus and Young's modulus, where the shear modulus is the ratio of shear stress to shear strain and Young's modulus is the ratio between uniaxial stress and strain, giving a measurement of the soil's stiffness (Jones & Ashby, 2019). In terms of relating this to seismic data, both moduli are considered to be a function of total stress and seismic velocities are defined by soil density and their elastic moduli (Uhlemann et al., 2016), allowing for assessment of ground response to the stresses acted upon it from seismic data. The elastic moduli are related through Poisson's ratio and this can give structural information related to the subsurface, as it could discriminate between boundaries of two different formations with different degrees of water

saturation (Uhlemann et al., 2016). This can then lead to cross correlation between two different geophysical data sets if they are both sensitive to moisture content (*e.g.* between seismic surveying and ERT), further increasing reliability.

Physical modelling of embankments has been undertaken to simulate geophysical surveys on a manageable and reduced scale. For example, a scaled embankment was modelled with a fluctuating water level to observe changes in resistivity between water levels (Hojat et al., 2020). Further experimentation monitored the development of seepage with ERT and seismic surveying (Maalouf et al., 2022). Outside of geophysics, further experimentation has been undertaken to model the development of erosion and breaching pathways in dams (Zhu et al., 2011) and levees (van Beek et al., 2010), using different slope angles, geometries, construction material and water flow rates (Xiangang et al., 2018). However, limitations in geophysical experimentation exist. The time for erosion and seepage to develop may be too rapid for identification by ERT, if single channels are adopted (thus lengthening survey time), but may yield extra information of internal structure with seismic surveying (Maalouf et al., 2022). Care must be taken to avoid interference in the data from the experimentation, such as containers where the experiment is taking place (Hojat et al., 2020).

## 2.4 Discussion

### *2.4.1 Characterisation of Degradation within Water Retaining Structures*

Geophysical techniques have had an increasing range of application for determining the hydrological and geotechnical properties of investigated sites in differing contexts (Binley et al., 2015). Geophysical methods have been applied in a number of embankment studies (Table 2.1), where focus has been predominantly on seepage and surface cracking (Lin et al., 2018). It is common practice for two or more geophysical methods to be used in combination for reliability (Sentenac et al., 2018), alongside potential use of numerical modelling, remote sensing or geotechnical methods (Loperte et al., 2016; Almadani et al., 2018; Bièvre et al., 2018; Oliveira et al., 2023). Section 2.3 discussed the various geophysical techniques used to monitor water retaining structures; this section will summarise how the erosional processes discussed in section 2.2 can be evaluated with geophysical methods

**Table 2.1:** Selected studies on water retaining structures using various geophysical techniques, including the geological context of the setting in which the investigation was undertaken.

Embankment Type	Embankment Name	Methods Used	Fill Composition	Author
Dyke	Canal de Roanne a Digoin Dyke, France	Seismic surveying, ERT	Clay, silt and gravel	Bievre et al., 2017
Dyke	Unnamed, France	ERT	Alluvial sands and clays	Fargier et al., 2014
Experimental reservoir dam	Landao Creek, Canada	DTS	Gravel and clay	Chen et al., 2018
Fishpond dam	Podvinak, Czechia	ERT	Compacted Earth	Zumr et al., 2020
Hydroelectric dam	Paranoa, Brazil	Seismic surveying	Rockfill	Guedes et al., 2023
Landslide dams	Miyoshi, Aktani, Kuridaira and Terano, Japan. Kol-Tor, Kyrgyzstan	Seismic surveying, SP	Various	Wang et al., 2018
Experimental levee	Ijkdijk, Netherlands	DTS	Clay with sand foundations	Bersan et al., 2018
Experimental levee	Ijkdijk, Netherlands	Ambient seismic monitoring	Clay with sand foundations	Planes et al., 2016

<b>Table continued</b>	<b>2.1</b>			
Experimental levee	Ijkdijk, Netherlands	Ambient seismic monitoring, SP	Clay with sand foundations	Rittgers et al., 2015
Levee	Saint Firmin, France	GPR	Sand, gravel and clay, underlain by clayey filling material with chalk nodules	Anotine et al., 2015
Levee	Loire embankment, France	ERT	Silty-clayey sand	Jodry et al., 2019
Levee	Thongumbald, United Kingdom	ERT	Clay	Jones et al., 2014
Levee	Wood River, USA	ERT, Seismic surveying	Clay with a sand core	Rahimi et al., 2018
Moraine dam	Unnamed, USA	ERT, SP	Till	Moore et al., 2011
Reservoir dam	Unnamed, France	ERT, SP	Clay and alluvium	Boleve et al., 2011
Reservoir dam	Unnamed, Italy	ERT, Seismic surveying	Clay	Cardarelli et al., 2014
Reservoir dam	Yedang, South Korea	Seismic surveying	Unnamed	Kim et al., 2021
Reservoir dam	Monte Cotugno, Italy	GPR, ERT	Conglomerate	Loperte et al., 2016

<b>Table 2.1 continued.</b>				
Reservoir dam	Negratín, Spain	IP, ERT	Clay and conglomerate overlain by silt and gravel	Martinez-Moreno et al., 2018
Reservoir dam	Mugdock, United Kingdom	EMI, ERT	Clay	Michalis et al., 2016
Reservoir dam	Som-Kamala-Amba, India	Resistivity, SP	Earthen body with quartzite and schist foundations	Panthulu et al., 2001
Reservoir dam	Carl Blackwell, USA	ERT, Seismic surveying	Alluvium	Sazal et al., 2022
Reservoir dam	Vitineves, Czechia	ERT, EMI, SP	Silt and clay	Sentenac et al., 2018
Reservoir dam	Hällby, Sweden	ERT	Sand with a till core	Sjödahl et al., 2008
Reservoir dam	Unnamed, Undisclosed country	DTS	Compacted Earth	Yosef et al., 2018
Reservoir dam	Unnamed, Kazakhstan	SP, IP	Loam	Akhmetov et al., 2020
Tailings dam	Unnamed, Brazil	ERT	Compacted rock and clay core	Arcila et al., 2021
Tailings dam	B1, Brazil	ERT	Rockfill and clay	Oliveira et al., 2023

Geological conditions, in which seepage zones may be located, can be assessed with seismic surveying or ERT. For instance, the presence of a leakage zone within weathered material was noted due to anomalous lows in shear wave tomography at a dyke in France (Bièvre et al., 2017), and ERT undertaken at Mugdock Dam in Scotland allowed differentiation between layers of superficial and bedrock geology (Michalis et al., 2016).

The presence of surface cracks and burrows have been commonly detected with GPR, from the detection of voids, due to the high contrasts associated in dielectric permittivity (Sentenac et al., 2018). Desiccation cracks and other voids caused by surface erosion have been monitored using ERT, as air filled cracks in soil have conductivities of zero (Rhoades et al., 1989), thus creating resistivity contrasts with the soil and pore water, allowing for potential detection in ERT. Observations of erosional features with GPR may provide a useful tool for identifying locations where seepage might develop.

The often instantaneous effect of overtopping (Dunbar et al., 2017) makes it hard to detect before potential failure and difficulties in identifying pre-failure signals of overtopping, may make geophysical monitoring for it impossible. However, given the tendency of overtopping to initiate erosion, which may later lead to failure, geophysics could be employed post-overtopping to monitor the embankment's integrity.

Geophysical approaches can detect potential failure planes in the subsurface due to the formation of potential fluid pathways, (Kušnirák et al., 2016), where permeability contrasts exist on either side of the plane, allowing detection of a flow using techniques like SP. Monitoring lithological variations, which may control landslide morphology, and moisture content variations may identify potential slope instability in engineered slopes using ERT (Bièvre et al., 2015). Monitoring for sub-surface cracking could be used to assess the potential for slope failure in an area where slope instability is of risk (Chen et al., 2018). GPR has been utilised for analysis of slope instability due to its ability to generate two dimensional representations of the sub-surface and its capability in successfully recording physical parameters of the soil which can be correlated to landslide features (Popescu et al., 2016).



### *2.4.2 Applicability of Geophysics*

As discussed, geophysics has been a common tool for producing 2D or 3D models, which give spatial or volumetric information on the subsurface, as compared to surface observations or discrete intrusive geotechnical sampling (Michalis et al., 2016). The assumption made is that geophysical data and models can provide subsurface information from which useful hydrogeological and geotechnical parameters can be inferred, due to associations between them. In other words, the geophysical data collected for every measurement should relate to a similar property or state that could have been acquired through geotechnical investigation.

A major strength of geophysics, in terms of monitoring for water retaining structures, is that many techniques are sensitive to the detection of water or flow of water, and hence can be used as a proxy for internal variations which may lead to failure (Fargier et al., 2014; Moore et al., 2011). Also, the use of continuous monitoring systems, such as PRIME, allows monitoring of temporal variations. Geophysical methods may be advantageous for monitoring, as intrusive geotechnical methods can only every sample a small proportion of the subsurface, while geophysical methods can monitor spatial variations and complement temporal monitoring from geotechnical instrumentation (Chambers et al., 2014).

Results to date have been encouraging, as evident through the volume of research which has been undertaken on this topic. One such example of a petrophysical relationship is the creation of an electrokinetic coupling with groundwater flow, in which variations in moisture content and presence of voids allows interpretation of seepage paths with techniques like SP, ERT (Figure 2.16) and GPR (Bolève et al., 2011; Fargier et al., 2014; Sentenac et al., 2018).

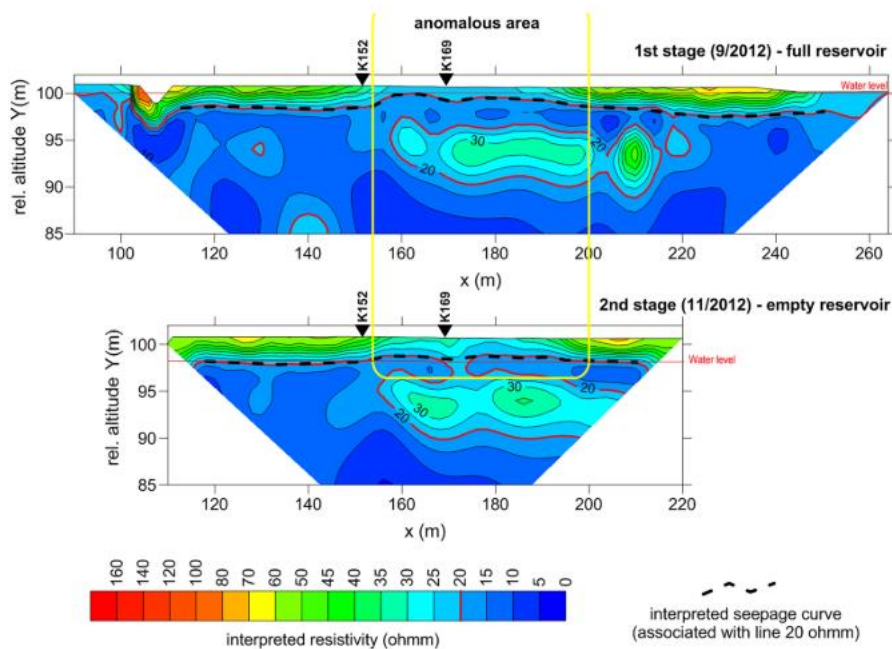


**Figure 2.16:** An example of an ERT inversion showing a decrease in resistivity through an embankment, which has been interpreted as seepage (Sentenac *et al.*, 2018).

The transport of tracers in real time can give estimations of hydraulic conductivity and location of seepage paths (Bolève *et al.*, 2011). Through numerically modelling seepage paths and comparing the models to measured data, Bolève *et al.*, (2011) showed an association between the SP and distance from tracer injection point. For example, in Bolève *et al.*, (2011)'s study, the estimated hydraulic conductivities from the numerical model correlated well with the tracer experiment, but this is only feasible if mobile clay minerals are present in the leakage path, due to consistency between the hydraulic conductivity and a high charge per unit volume. Also, the ability of SP to detect seasonal variation in groundwater movement through time-lapse monitoring makes it useful for slope stability analysis (Chambers *et al.*, 2011).

With ERT being sensitive to moisture content variation, it may only be applicable in conditions in which seepage is associated with fluctuating moisture content. Where seepage occurs with low changes in moisture content, ERT may not be able to distinguish subsurface variation. Geoelectrical techniques that are sensitive to conductivity (*e.g.* EMI, SP) may not be suitable in areas where extreme conductivities may be present, such as in areas of high salinities,

where relevant subsurface conditions may be obscured by effects from the highly conductive feature. In frequency domain EMI, depth penetration may be hindered by electrically conductive upper layers, since current preferentially flows through conductive layers (Sentenac et al., 2018).

### *2.4.3 Differences in Application of Geophysics between Different Water Retaining Structures*

Geophysics has been used on several different water retaining structures (see Table 2.1). However, dams and river embankments are of different scales and serve different purposes. Therefore, geophysical surveys may need to consider different contextual information depending on the type of embankment structure.

#### *2.4.3.1 Geophysical Monitoring of Tailings and Reservoir Dams*

Due to the economic considerations, legacy construction history, higher loading frequencies and potential for greater catastrophic failure, dams have more stringent design standards than other water retaining structures (Dunbar et al., 2017). Therefore, it is critical that weaknesses developed in dams are detectable through monitoring procedures. Impermeability of dams, due to the clay core, can cause underseepage in permeable bedrock; therefore backward erosion piping can be a common failure mechanism which can cause dam failure (Planès et al., 2016). The core is vital to uphold the dam's structure and to act as an impermeable barrier to reservoir water, and since seepage erosion weakens the core (Sjödahl et al., 2008), it is important to gather data from this region to assess for leakage. Seepage phenomena will develop initially in the upstream slope, before they propagate to the downstream side (Planès et al., 2016), so geophysical monitoring should be able to detect effects within the upstream side first.

Dams have abrupt elevation changes, therefore topography highly influences data collected from the embankment slope (Lin et al., 2018). Surveying is usually applied based on a line of equidistant electrodes, for ERT or IP, parallel to the longitudinal direction, such as the crest (Fargier et al., 2014). Topography would need to be accounted for during the inversion process.

Other dams, besides reservoir dams, can form water barriers and have different characteristics. Natural dams can form when water courses are impeded by a structure, such as a landslide or moraine. Tailings dams are built in stages (Arcila et al., 2021), have a higher risk for public safety (Arcila et al., 2021; Guedes et al., 2023) and are more prone to failure, due to more frequent raisings of water levels and weaker infill typically formed from mine residue (Oliveira et al., 2023). All dams can be monitored using the same, cross-applicable, techniques as anthropogenic dams (Moore et al., 2011; Wang et al., 2018).

Types of dam failure linked to internal degradation are summarised in Table 2.2.

**Table 2.2:** Summary of failure mechanisms for dams, their causes and effects.

Failure mechanism	Description	Cause and effects
Overtopping	The rising of water over the dam crest.	Rising water level with rainfall, most pronounced with poorly vegetated slopes. Once overtopping occurs, the water will erode the embankment.
Piping	Formation of erosional channels by internal erosion.	Water moving through the embankment and gradual erosion of the embankment. This includes removal of fines and will lead to the formation of water seeping through the embankment.
Slope failure	Collapse of embankment slope.	Failure of the slope due to increase in pore pressure or reduction in shear strength of the embankment material.
Animal and vegetative activity	Degradation due to roots or burrowing.	Animal activity can form burrows and plants can form cracks with their roots, leading to potential slope failures.

#### *2.4.3.2 Geophysical monitoring of Levees, Dykes and Flood Embankments*

Geophysical monitoring of dams and river embankments are similar, but scale and size differences create important differences during the monitoring process and the interpretation stage (Dunbar et al., 2017). Levees, dykes and flood embankments do not necessarily contain an impermeable core, as dams do, so water flow may be more continuous through the structure. However, embankments often comprise clay (Sentenac et al., 2018); therefore they are likely to be impermeable and have electrically conductive areas. Dams are usually constrained to a narrow valley, but embankments by water courses can spread for several kilometres, thus potential seepage can flow through an area of embankment over greater distances (Dunbar et al., 2017). Consequently, in applying geophysics it may be required to monitor longer stretches of embankment than in dams, and a reconnaissance survey may be beneficial to identify possible embankment locations for monitoring (Dunbar et al., 2017). The smaller size of these embankments compared to dams may influence results, in techniques like DTS, due to the lower hydraulic loads, smaller size of embankment, and the internal temperature distributions do not correlate to the assumptions made for dams (Bersan et al., 2018).

#### *2.4.4 Uncertainties and Limitations in Geophysics*

Though geophysical applications have been readily applied for use on water retaining structures, challenges still exist in resolving reliability of measurements with petrophysical relationships, as well as providing direct information about hydrogeological conditions of the subsurface (Binley et al., 2015). To attain reliable and accurate data, it is essential that uncertainties within geophysical data acquisition are addressed. Technique limitations have been discussed above, so will not be focussed on in this section.

##### *2.4.4.1 Modelling*

A primary uncertainty in modelling geophysical data is the inherent non-uniqueness of inversion (Michalis et al., 2016). Obtaining a realistic inverse model for a data set can therefore be difficult given the potential for many different solutions for one problem to the limits of accurate data (Hoffman & Dietrich 2004). A unique inverse solution requires

continuous and accurate measurements, and this is restricted by the finite number of data points, such as electrodes able to conduct an ERT survey (Loke *et al.*, 2013). Smoothing can reduce precision of interface location and high contrast heterogeneities smaller than the model cell size may not be detected (Loke *et al.*, 2013) when compared to blocky inversions. However, the gradual change in resistivity across a profile may make smooth models more desirable (Hermans *et al.*, 2016). When inversions involve coupled parameters, joint inversions are used (*e.g.* joint inversions between petrophysical parameters, hydrological variables, structural information, such as using known depths to lithology for constraining seismic inversion, *etc.*) (*e.g.* Linde & Doetsch, 2016).

Geophysical techniques can be used to provide estimations of lithology from characteristic values of the geophysical parameter (*e.g.* Palacky, 1987), but property ranges between lithologies commonly overlap, and salinity, temperature and moisture content makes confident interpretations difficult (Loke *et al.*, 2013). Therefore, it is important to have logging data, in situ testing data (*e.g.* Russell & Barker, 2010; Sungkono *et al.*, 2014) and/or physical testing data (*e.g.* Almadani *et al.*, 2018) to aid interpretation (Loke *et al.*, 2013). Petrophysical models have been developed to constrain lithology and geophysical interpretation, but such methods are not applicable to all lithologies (Zhang & Revil, 2015). For instance, the permeability-porosity model developed by Revil and Cathles is only valid for clay-sand mixtures, provided the clays are not layered or laminated (Revil & Cathles III, 1999; Zhang & Revil, 2015). Other associated issues regarding data aliasing and temporal smearing (where subsurface changes are not negligible during survey time) may be present due to the time intervals involved (Singha *et al.*, 2015).

Electrical-hydraulic relationships have difficulties being replicated with field data, as compared to laboratory experimentation, because of differences in the orientation between hydraulic pathways and electrical currents. Hydraulic information is obtained from horizontal flow from pumping tests and electrical currents are obtained from vertical electrical soundings (Purvance & Andricevic, 2000). Difficulties arise because a constant ratio of anisotropy between longitudinal and transverse orientations is required, which may not be applicable in strata of variable pore size distributions (Purvance & Andricevic, 2000). Secondly, sample volumes for the modelled area are assumed to be the same throughout

monitoring, which may not be the case if packer or flowmeter tests have been undertaken, and this can cause flawed interpretation (Purvance & Andricevic, 2000).

#### *2.4.4.2 Site Specific Considerations*

When surveying embankments, it is important to consider site specifications in focus. Levees may be longer in length than dams and are therefore less likely to have constraints on array sizes. Conversely, in constrained areas, electrode spacing may need to be reduced, limiting the potential depth of investigation. With geophysical techniques, such as ERT, there is a trade-off between resolution and depth of penetration, where wider spacing gives greater depth, but poorer resolution and vice versa (Sharma, 1997). Therefore, when identifying potential weak zones in an embankment it is crucial to have an estimation of survey locations, so that a suitable array choice can be made.

Consideration is needed for the resolution possible from the geophysical method. Smaller embankments may make it difficult for some surveying methods, like seismic surveying, to achieve a suitable resolution to detect features of interest (Bièvre et al., 2017). Injection of tracers to aid with interpretation may cause ecological and environmental concerns (McLachlan et al., 2017) through their effects on drinking water or habitats, and thus their use may not be possible. Climatic conditions can influence data and may be difficult to quantify, such as cases where snowmelt and precipitation infiltrate embankments and affect results (Moore et al., 2011).

For monitoring embankments, non-invasiveness may be of importance: DTS and ERT, for example, can require trenching for emplacement (Schenato, 2017). Optical fibres need to survive hostile environments over a number of years, and there are few case studies which attest to their survivability (Schenato, 2017). Also, insertion of electrodes in geoelectrical surveying is minimally invasive, so insertion must be undertaken carefully to ensure minimal ground disturbance.



#### *2.4.5 Routes for Future Development of Geophysical Applications for Water Retaining Structures.*

This thesis will focus on improving understanding of the use of ERT on water retaining structures. Further discussion on the development of other geophysical techniques for this purpose will be given in chapter seven.

Significant challenges remain for using and interpreting ERT. Globalised petrophysical relationships are still poorly understood and experimental setup for laboratory experimentation to monitor progression of erosion is difficult to optimise (Maalouf et al., 2022). Coupling methods (where the geophysical parameter can be related to a petrophysical relationship that is used in the inversion) are being increasingly used (Bièvre et al., 2018; Norooz et al., 2021; Moreira et al., 2022), but are hindered by large computation time and model optimisation, and 3D effects can influence data and obscure key detail. This research aims to improve our understanding of what 3D effects occur in dam or river embankment settings, and whether use of 3D inversions can improve upon 2D inversions which may be more affected by such effects. 2D inversions are still being used (Turki et al., 2019; Arboleda-Zapata et al., 2022; Ekwok et al., 2022; Trottet et al., 2023), including for embankments (Jodry et al., 2019). This thesis will build upon previous research that has explored the 3D effect on embankments (Cho et al., 2014; Hojat et al., 2020; Norooz et al., 2021), and will explore the use of synthetic modelling to evaluate the result of potential 3D effects from the water body and internal structure. The research will focus on whether the embankment structure and environment can induce a 3D effect in an ERT survey along the embankment, whether this is strong enough to distort model resistivity values, and what can be done to mitigate the effect. This will examine typical features of an embankment, including the water body level and resistivity, the internal structure and presence of off-centre structures in what are heterogeneous environments. Alongside this, the research will examine the ability of 3D inversions and inversions with use of crosslines to improve upon 2D inversions for embankment settings. This will also have a focus on time-lapse ERT data to determine the temporal impacts of 3D effects and how this can distort 2D and 3D inversions.

## 2.5 Summary

With increasing precipitation anticipated with climate change and the aging of many water retaining structures, it is important to understand the integrity of such embankments in order to identify internal problems before catastrophic failure occurs. Such embankments commonly breach due to the impact of water, be it through seepage causing internal erosion or a rising phreatic zone leading to overtopping. Ever improving software and technological capabilities has seen an increase in geophysical methods, which have successfully imaged variations in embankments associated with changes in the internal hydrogeological conditions, allowing detection and monitoring of potential leakages. Common techniques which have been utilised for this purpose have been ERT, SP and seismic surveying, while DTS represents a growing field which may be used in conjunction with more conventional methods to help confirm the presence of seepage. Such methods can be undertaken in 3D, using timelapse methods, in order to give a more detailed representation of the subsurface over time, enabling tracking of any deterioration over time. While such techniques must be used with caution, due to problems with non-uniqueness or uncertain correlation with petrophysical models, research into this area is ongoing. The use of several different geophysical and remote sensing methods to detect seepage successfully demonstrates the applicability of geophysics to this issue, and with increased improvements needed in numerical modelling, inversion and correlation between methodologies there is an opportunity to further increase the benefit of using geophysics to monitor the integrity of water retaining structures.

## 3.0 RESISTIVITY IMAGING OF RIVER EMBANKMENTS: 3D EFFECTS DUE TO VARYING WATER LEVELS IN TIDAL RIVERS

### 3.1 Introduction

This chapter aims to build upon previous investigations of 3D effects in ERT data due to an adjacent water body, as detailed in chapter 2. The work here focuses on the tidal influence of a synthetic river on ERT data obtained from surveys on a crest of a flood defence embankment. Synthetic models simulating varying water levels and salinities, for a homogeneous and heterogeneous embankment, are used to investigate the relationship between measurement and survey design and 3D artefacts, for the purpose of identifying improved ERT deployment approaches for tidal embankment monitoring. Previous research has produced contrasting conclusions regarding the relationship between electrode spacing and the magnitude of the 3D effect (*e.g.* Hung *et al.*, 2019 and Hojat *et al.*, 2020). Therefore, further synthetic numerical modelling is used to help confirm the effect of electrode spacing on the magnitude of 3D effects present from a tidal river adjacent to an ERT array.

Alongside synthetic modelling, time-lapse ERT monitoring from the Hadleigh Marsh field site on the Thames estuary, United Kingdom is used to illustrate potential 3D effects in ERT applied to flood defence monitoring. The series of modelling experiments applied to a synthetic river embankment are used for comparison. Recommendations are offered on approaches to mitigate the 3D effect, including survey design recommendations and application of methodologies during inversion.

The synthetic models were developed and analysed to explore three variables: the effect of a change in distance between the river and the electrode array; the change in river electrical conductivity (representing a change in salinity); the electrode spacing used for the survey. Through the models, the nature and severity of the 3D effect resulting from changes in salinity and water level can be understood and therefore methods to mitigate the impact can be made. In embankments with greater crest heights, a larger electrode spacing may be chosen to achieve greater depth penetration. Therefore, different electrode spacings have been

modelled to determine potential impacts of a 3D effect where a different electrode setup may be selected for this survey scenario.

## 3.2 Synthetic Numerical Modelling

### *3.2.1 Methodology*

To quantitatively assess the impact of the 3D effects resulting from tidal variations (river water level and resistivity) on 2D ERT data parallel to a watercourse, two synthetic modelling scenarios (Appendix B) were designed to simulate a decreasing river level with a waning tide. In both models an electrode array, consisting of 48 electrodes at 1 m spacing, was simulated along the embankment, parallel to the watercourse (Figure 3.1). The embankment crest was 3 m wide, and the array was situated at the midpoint of the crest width. The riverside slope angle was  $14^\circ$  and the river had a maximum width of 27.8 m. In the associated finite element mesh, the modelled river extended for 101 m beyond the first and last electrode in the orientation parallel to the array. This ensured that the river was sufficiently long to reduce boundary effects or influences on the data from resistivity contrasts between the end of the river in the mesh and the background region (Binley & Slater, 2020). Topography was included in the inversion, in order to account for its influence on the ERT data (Fargier et al., 2014; Bièvre et al., 2018). Scenario one involved a homogeneous embankment, while scenario two included a clay core of differing resistivity to explore the impact of such heterogeneity. The embankment geometry is shown in Figure 3.1.

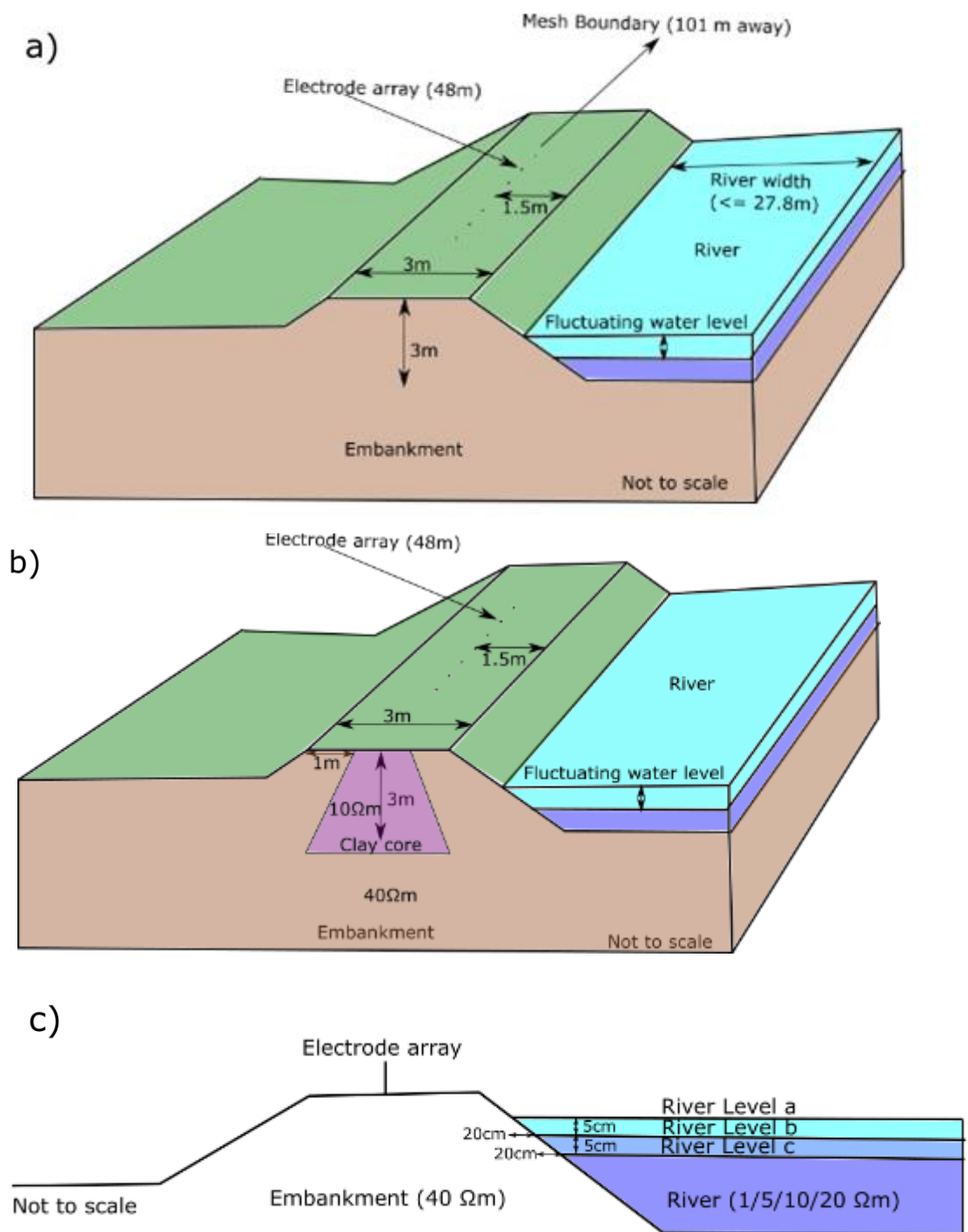


**Figure 3.1:** Geometrical representations of the synthetic model problem. a) The layout of the embankment, river, and electrode array orientation for the homogeneous model. The electrode array is located parallel to the river and is situated at the centre of the embankment crest. b) The heterogeneous model, including the clay core. c) A 2D cross sectional image of the synthetic embankment, showing the adjustments to river geometries with each model and modelled river resistivities, representing salinity changes.

Utilising the mesh generation software Gmsh (Geuzaine & Remacle, 2020), a 3D unstructured finite element mesh was generated, allowing creation of regions representing the river, embankment and clay core for scenario two, each of which can be assigned specific resistivity values. The fineness of the mesh was ensured to be 25% of electrode spacing at the surface, grading down to a spacing equivalent of the electrode spacing 10 m from the electrode array (vertically and laterally). The mesh graded further, to 250 m towards the mesh boundary. Once the mesh was generated and resistivities were assigned to the river, embankment and clay core, the ERT code R3t (Binley & Slater, 2020) was used to compute a forward model for a specific scenario. R3t was used, instead of 2D modelling software, due to the ability of a 3D modelling set-up to incorporate external features (*e.g.* a river) into the model. Once the forward model was complete, 2% random (Gaussian) noise was added to the resultant apparent resistivities. Following this, the data were inverted in 3D, in order to simulate an inversion of ERT data with an adjacent river which could potentially induce anomalous artefacts in the inversion. The inversions for all models incorporated the 3D geometry of the embankment, enabling topography to be accounted for, reducing the 3D effect associated with this. Each inversion utilised smoothness-constrained (*i.e.*  $L_2$  norm) regularisation.

Wenner, Schlumberger and Dipole-dipole array configurations were modelled, in order to determine the likely impact of a 3D effect based on array configuration. For this, using a river level of 2.95 m at 1.7 m distance from the electrodes, models were run with electrode sequences corresponding to each configuration and synthetic measurements could then be compared. From this, the electrode configuration with the most severe 3D effect was selected for subsequent modelling. For all electrode configurations, an  $a$  spacing of 1 to 4 m was selected, where  $a$  spacing is the distance between measurement electrodes. The Schlumberger array had an  $n$  of 1 to 9 and the Dipole-dipole configuration had an  $n$  of 1 to 9, where  $n$  is a factor multiplied to  $a$  spacing to determine the distance between the current and potential electrodes.

The homogeneous river embankment was assumed to consist of a clay fill, representing a common construction material for embankments. The assumed resistivity of the embankment was taken to be 40  $\Omega\text{m}$ , based on typical resistivity values for clay (Palacky, 1987). The second modelling scenario consisted of a more conductive clay core, set at 10  $\Omega\text{m}$ , with a more resistive 40  $\Omega\text{m}$  infill, to test for effects of heterogeneity in a set-up

representative for such embankments. The water in estuarine environments is typically brackish (Sandrin *et al.*, 2009), so models included ranges of resistivities typical of more brackish water and freshwater, 1, 5, 10 and 20  $\Omega\text{m}$ , the latter representing freshwater rivers with some tidal influence (Palacky, 1987). In addition, modelling procedures were repeated for different electrode spacings to observe the effect of spacing on the associated 3D effect from a tidal setting.

To study the effect of changes in river level, the finite element mesh was adjusted for a given river level; the modelled river level was decreased by 5 cm vertically and the river front was retreated 20 cm laterally per model scenario (Figure 3.1b), which represented a waning tide. The initial conditions were a river that was 1.7 m from the electrode array, at a river height 5 cm lower than the crest elevation (Figure 3.1). For each river level, four separate forward models and inversions were undertaken, where river resistivities were assigned as 1, 5, 10 and 20  $\Omega\text{m}$  for each scenario, in order to account for varied river salinities. Once the inversions for each modelled river salinity were completed for the given river level, the synthetic river level was decreased, and models were run as before. From this, resistivity values underlying the electrode array could be obtained, allowing comparison between models as to the magnitude of the 3D effect with changing water level and river salinities. The process described was repeated for every reduction in river level until there was no observed change in resistivity underlying the ERT array from a 3D effect after inversion for all modelled river resistivities.

Table 3.1 details each modelling scenario and the variation in parameters modelled.

**Table 3.1:** Modelling scenarios tested for the synthetic numerical modelling, and associated parameters assigned for each modelling scenario.

<b>Modelling Scenario</b>	<b>River level (m) (Embankment height: 3m)</b>	<b>River resistivity (<math>\Omega\text{m}</math>)</b>	<b>Electrode spacing (m)</b>	<b>Embankment Infill resistivity (<math>\Omega\text{m}</math>)</b>
Alternating river level	2.95, 2.9, 2.85, 2.8, 2.75, 2.7, 2.65, 2.6, 2.55, 2.5, 2.25	1, 5, 10, 20	1	40
Alternating river salinity (resistivity)	2.95, 2.9, 2.85, 2.8, 2.75, 2.7, 2.65, 2.6, 2.55, 2.5, 2.25	1, 5, 10, 20	1	40
Electrode spacing	2.95, 2.25	1	1, 2, 4	40
Heterogeneous embankment	2.95, 2.75, 2.5, 2.25	1, 10	1	Core – 10 Other infill - 40

### 3.2.2 Synthetic Modelling Results

#### 3.2.2.1 Array Configurations

The results for the synthetic modelling of Wenner, Schlumberger and Dipole-dipole arrays, using the homogeneous embankment model, are shown in Figure 3.2. This comparison simulates using the maximal river level, using 1  $\Omega\text{m}$  as a river resistivity, in order to demonstrate the maximum possible impact of a 3D effect from each array type.



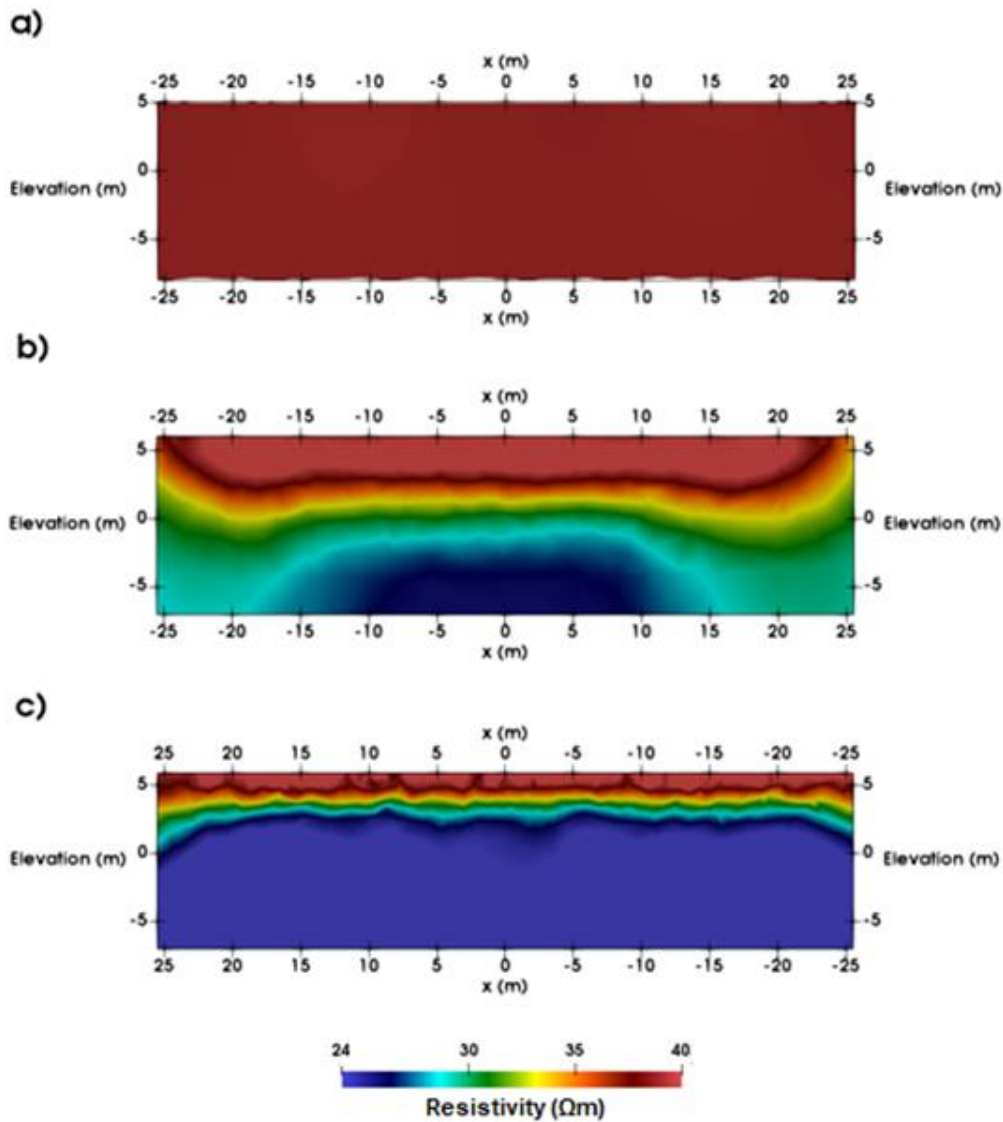


**Figure 3.2:** ERT inversions, showing the 3D effect resulting from differing array types, where the inverse image represents the synthetic subsurface resistivity distribution directly beneath the electrode array. a) Wenner configuration. b) Schlumberger configuration. c) Dipole-dipole configuration. For each configuration the river is 1.7 m from the embankment, the river is 0.5 m below crest height and the river's apparent resistivity is 1 Ωm. The apparent resistivity of the embankment is 40 Ωm. In each image the embankment height is 5 m.

As shown in Figure 3.2, the resistivities for the Dipole-dipole array (Figure 3.2c) are more affected by a 3D effect than the other array configurations, suggesting a greater lateral (off-plane) sensitivity for this array. For the Wenner array (Figure 3.2a), with a spacing of 1 m, there is unlikely to be any significant 3D effect, but it may be more of an issue if greater electrode spacings are selected for a survey. The Schlumberger array (Figure 3.2b) shows influence from a 3D effect induced by the river, but with poorer model resolution compared with Dipole-dipole. Therefore, for the purpose of the further synthetic modelling a Dipole-dipole array has been selected because of the greater apparent sensitivity to off-plane effects.

### *3.2.2.2 Distance of River from Electrode Array*

Selected inversions taken from the different modelled river levels were chosen for assessing the resistivities directly underlying the ERT survey for both modelling scenarios. For each model in the homogeneous embankment scenario, the embankment resistivity is 40  $\Omega\text{m}$ , so significant deviation from this, which gives greater error than expected from noise alone, is inferred to be a 3D effect, induced by the modelled river. Likewise, for the heterogeneous model, the clay core resistivity is 10  $\Omega\text{m}$ , with a 40  $\Omega\text{m}$  background resistivity for the remainder of the subsurface, meaning deviations from this represent influence from a 3D effect. Figure 3.3 is a representation of the resistivities at various depths beneath the ERT array for the synthetic models, showing the resistivities for each modelled water level.

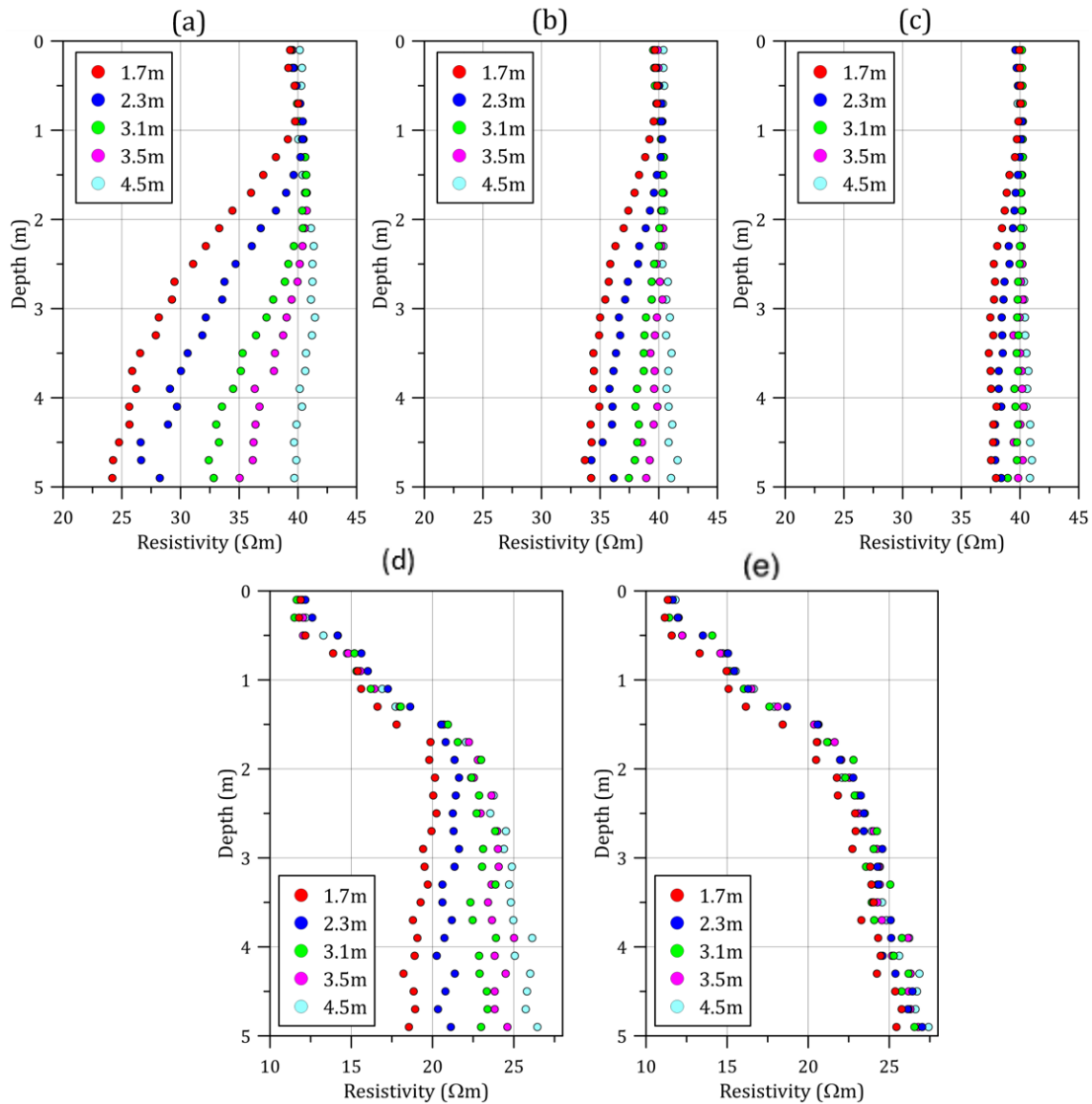


**Figure 3.3:** Profiles of resistivity variation below the synthetic ERT array for different river levels in different modelled river resistivities. The river is a) 1  $\Omega\text{m}$  and the model is homogeneous, b) 5  $\Omega\text{m}$  and the model is homogeneous, c) 10  $\Omega\text{m}$  and the model is homogeneous, d) 1  $\Omega\text{m}$  and the model is heterogeneous, e) 10  $\Omega\text{m}$  and the model is heterogeneous. The models associated with a river of 20  $\Omega\text{m}$  are not shown, due to the lack of distorted resistivities underlying the electrode array for all distances of river to electrode.

From the models, as is evident in Figure 3.3, there is a distinct effect on resistivities located at greater depths below the ERT line, while at depths less than 1 m, the effect is negligible. As expected, the effect is more severe where the river is closer to the electrode array, with less pronounced distortions to resistivity with decreasing river level. For the most proximal river level in the homogeneous model, estimated resistivity values can reduce by approximately 15  $\Omega\text{m}$  at depths of 3.5 m below the array when the river is least resistive. The magnitude of the effect reduces until the river reaches 4.5 m from the electrode array, where the resistivities

approximate to  $40 \Omega\text{m}$  for every modelled river resistivity (i.e. there is no 3D effect). Slight discrepancies in the trend with depth are likely impacts of adding 2% noise to the apparent resistivities prior to inversion. The noise does not obscure the trend in the models, indicating that anomalous resistivities from the inversion can be ascribed to the 3D effect induced by changing river levels or salinities, as opposed to random background effects, in a real-life scenario where noise will be present.

In the heterogeneous models (Figure 3.3d and 3.4e), with decreasing river level there is no obvious associated trend in resistivity at depths less than 1.5 m, indicating that resistivity variation is driven by influences from the embankment and 2% added Gaussian noise, not effects from the river. This contrasts with depths below 1.5 m, where the resistivities are noticeably less resistive with higher river levels, more proximal to the electrode array. As with the homogeneous model, this indicates that the 3D effect from the river is more pronounced with depth, using a 1 m electrode spacing, and embankment heterogeneity does not obscure such a trend in 3D effect.

#### *3.2.2.3 River Salinity*

The plots in Figure 3.3 also show a distinct reduction in resistivity with increased modelled river salinities for both a homogeneous and heterogeneous embankment. It is evident that from Figure 3.3 that the trend of the resistivities for modelled river levels is less steep with increased river resistivity. The effect is most pronounced for the modelled river salinity of  $1 \Omega\text{m}$ , with a clear decrease in resistivity at depth when the river is proximal to the electrode array. When the modelled river is  $20 \Omega\text{m}$ , negligible 3D effects are seen. This indicates that a significant 3D effect in river embankments will be most prominent in estuarine environments where water is likely to be brackish. With higher modelled resistivities for the river, which represent freshwater environments, the associated 3D effect is negligible across all river levels. In conditions like this, freshwater is unlikely to induce an impact (provided the array is far enough away from the water body) and a 3D effect would be limited to estuarine or coastal environments.

As a decrease in salinity also reduces the magnitude of the 3D effect in the heterogeneous scenario at depths shallower than the base of the modelled core, it indicates that the bulk of the induced 3D effect, at shallow depth, arises from changes in river level and associated

resistivity. However, for all models the resistivity does not trend towards the modelled value of 40  $\Omega\text{m}$ . This is likely a result of the embankment heterogeneity and modelled clay core values above influencing resistivity values at greater depth.

#### *3.2.2.4 Electrode Spacing*

Plots of resistivities underneath the ERT array for different electrode spacings are shown in Figure 3.4. The river resistivity is set at 1  $\Omega\text{m}$  and selected distances of electrode array from the river (1.7 m and 3.5 m) are shown for comparison. The plots show the effect of electrode spacing of the electrode array, utilising the same mesh characteristics for each associated model. It is evident that with increased electrode spacing there is an associated decrease in resistivity at the ERT array. For an electrode spacing of 4 m, marked decreases of resistivity to 25  $\Omega\text{m}$  are present at shallow depths when the river is most proximal, whereas this is not the case for electrode spacings of 2 m. The results from electrode spacings of 1 m are not shown in the Figure, because resistivities are marginally higher, and similar in trend to 2 m spacing. This indicates that for large surveys with very large electrode spacings there will be significant 3D effect at the ERT array at all depths, which would obscure any underlying features which may be present underneath the embankment when the river level is most proximal to the electrode array. This suggests that for smaller electrode spacings the higher resolution and the shorter influence distances from the river help reduce the 3D effect, especially at shallow depths.

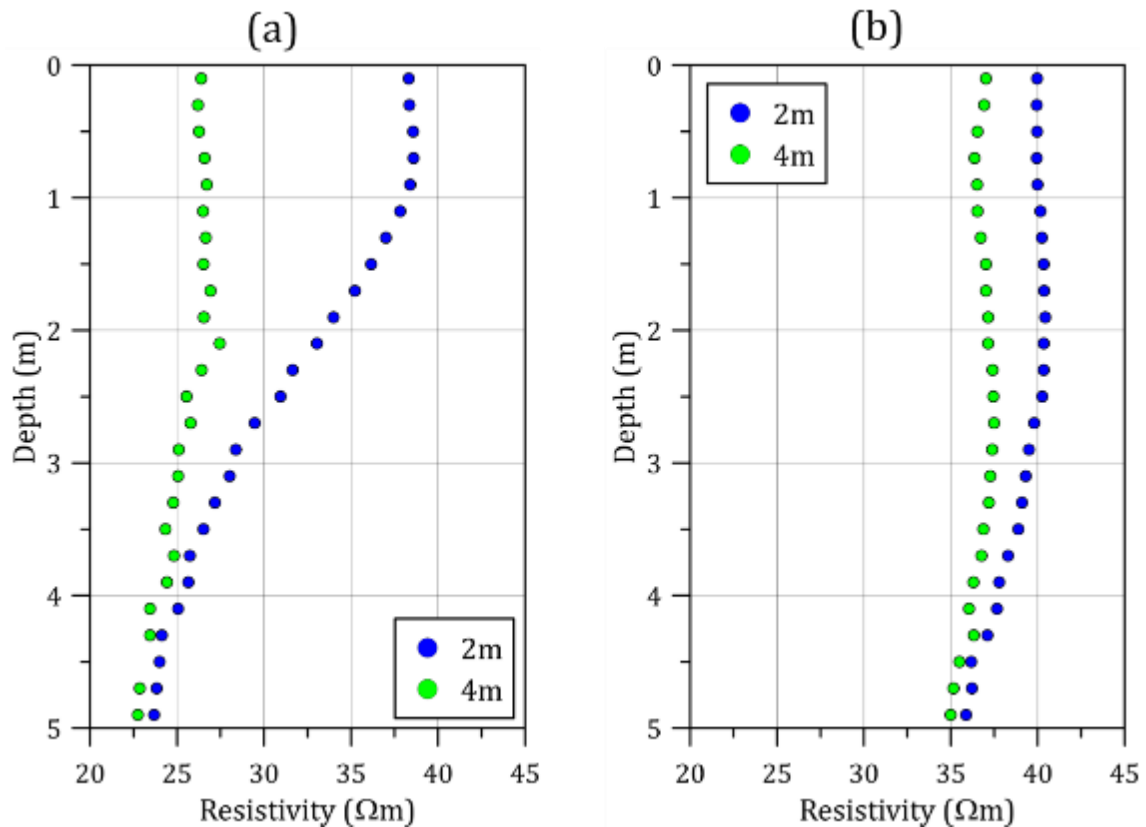


**Figure 3.4:** Resistivities directly underneath the modelled ERT array across the embankment crest, showing resistivity across depth below surface, for different electrode spacings. a) When the river is 1.7 m from the electrode array. b) When the river is 3.5 m from the electrode array.

### 3.2.2.5 Embankment Heterogeneity

Resistivities for the modelling of the more heterogeneous embankment, consisting of clay core, are represented in Figure 3.3d and e. Resistivity values proximal to the surface, in the region of the 10 Ωm clay core, varied between 11 and 13 Ωm. This indicates that the 40 Ωm infill modelled for the rest of the embankment has a weak influence on resistivities at shallow depth. Therefore, embankment heterogeneity and complexity are potential sources of a 3D effect, which may influence interpretation of data.

Resistivities at depth, below the clay core, do not trend towards the set value of 40 Ωm, levelling out at 25-30 Ωm. This is likely due to embankment heterogeneity and weak measurement sensitivity at depth: resistivities in the region below the clay core are influenced by the resistivity assigned to the core.

Overall, trends in resistivity between the homogeneous and heterogeneous models are similar, with decreasing resistivities at depth with declining river levels and salinities.

### 3.2.2.6 Sensitivity Distribution

As outlined in Binley and Slater (2020), there are a number of image appraisal methods available for assessing an inverse model. The computational demands of calculating a model resolution matrix is often prohibitive for 3D problems, and so a cumulative sensitivity approach (see Binley and Slater, 2020) is adopted here. Figure 3.5 shows a cumulative sensitivity distribution (produced by R3t) for the synthetic modelling, using 1 m electrode spacing, for when the river level is at its lowest. It can be seen from this that there is measurement sensitivity within the region of the river, indicating that a 3D effect can be detected by the array for this and all other scenarios, where the river will be more proximal to the array.

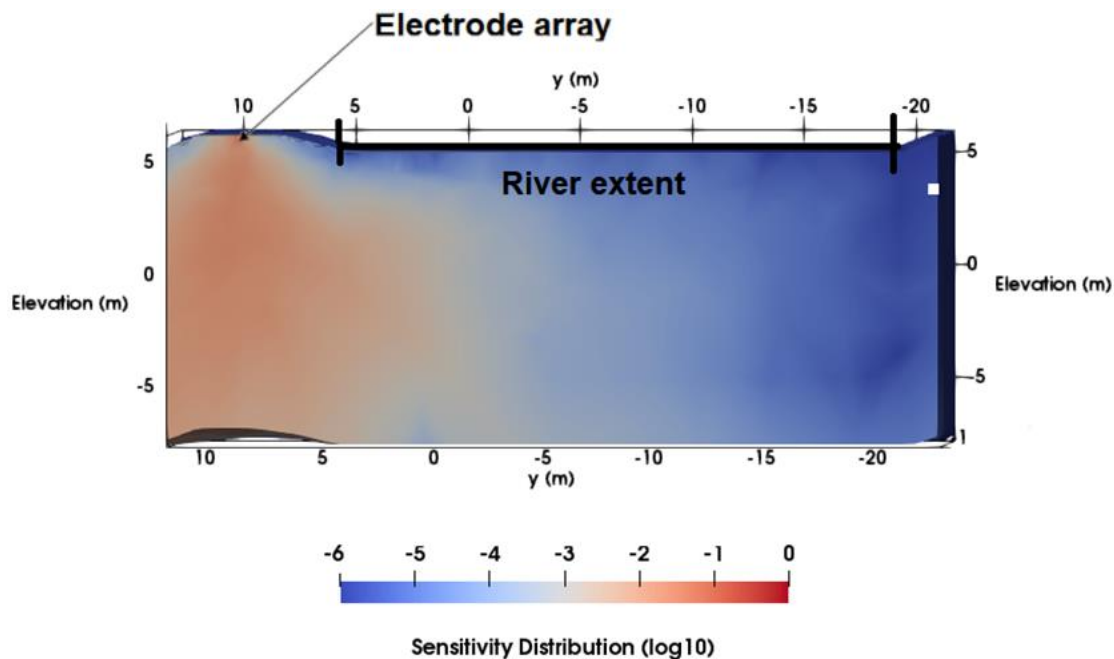


**Figure 3.5:** Cumulative sensitivity distribution for the synthetic model outputted from R3t, including an outline of the river region and electrode array for where the river is at its furthest. This sensitivity map is cropped half-way across the mesh, in the direction perpendicular to the embankment, to show how sensitivity is distributed. The electrode array is located at 9.5 m in the y orientation.

### 3.3 Hadleigh Marsh, Essex, United Kingdom

The Hadleigh Marsh embankment (Figure 3.6) is approximately 4 km long and 65 m wide (Essex County Council, n.d.). The embankment serves as a flood defence on the northern margin of the Thames estuary, and is situated on an eroding coastline (Brand & Spencer, 2019). The present embankment consists of a historic clay embankment, which was subsequently raised in the 1980s using household and commercial landfill waste, capped with puddled clay (Brand & Spencer, 2019). Historical maps suggest that an embankment has existed since the 19<sup>th</sup> century. Current embankment construction predates required legislation for records of such embankments to be kept, so comprehensive details of waste composition are unknown (Secretary of State, 2002). Hadleigh Marsh is situated in a SSSI (site of special scientific interest), it is a marine protected area (Brand & Spencer, 2019) and is within the bathing water zone of influence catchments for eight public beaches along the Thames (Smith et al., 2014). Therefore, it is imperative that the integrity of the embankment is maintained to a suitable standard, so that waste material and leachates do not contaminate the local environment.

Geophysical characterisation was undertaken at Hadleigh Marsh to reveal embankment structure and moisture-driven processes within the asset that could be related to tidal forcing, contaminant transport and slope stability. To facilitate long-term monitoring, an automated ERT measurement system, referred to here as PRIME (Holmes *et al.*, 2020), was installed at the site. The system enables near-real-time ERT data collection and has been powered by batteries charged by a solar panel, with remote operation and data retrieval achieved through a 4G telemetric link. The system was attached to five linear electrode arrays, with two orientated approximately parallel to the estuary front and three perpendicular (Figure 3.6). ERT surveys on all electrode arrays were generally acquired once every three days for each line from the April 2017 to present. The electrodes spacings were 2 m, utilising dipole-dipole measurement configurations with  $a$  spacings of 2 to 8 m and  $n$  in the range of 1 to 7. Where an  $a$  spacing is the current and potential dipole sizes and  $n$  is the current and potential dipole separation.





**Figure 3.6:** Layout of the PRIME array at Hadleigh Marsh, Essex, where L1-L2 are ERT lines parallel to the river front and P1-P3 are ERT lines perpendicular.

Time-lapse ERT data from the site were inverted to visualise changes in resistivity with differences in tides, using ResIPy (Appendix B) (Blanchy *et al.*, 2020). Initial inversions primarily focussed on 2D inversions of line L2 (Figure 3.6), which was the closest line to the estuary and for which the greatest 3D effect due to tidal influence was expected. Inversions of P1-P3 were also undertaken. As with the synthetic model, it is approximately parallel to the river course, but is not located on the embankment crest. The 2D time-lapse inversions were undertaken using the difference inversion method (LaBrecque and Yang, 2001). A 3D inversion was also undertaken, incorporating all ERT lines as a means of addressing whether anomalies present in line L2 from a 2D inversion were a result of 3D effects on 2D data. Tidal information taken from the nearby Sheerness tidal gauge (obtained from the British Oceanographic Data Centre) provided the tidal ranges across the year, and was used for selection of data for time-lapse analysis based on the tidal cycle. For each time-lapse inversion, a period of low tide was selected for the reference model, corresponding with a

period of low tide, and the time-lapse inversion continued until the next high tide occurred. Several tidal cycles were selected for separate time-lapse inversions, taken at different dates in the year, in order to help assess the seasonal impact.

### *3.3.1 Hadleigh Marsh Results*

To explore the potential 3D effect of the River Thames on 2D ERT data at Hadleigh Marsh, 2D inversions were undertaken on the most proximal line to the river, L2, and the intersecting orthogonal lines, P1-3 (Figure 3.6). Representative inversions of L2 are shown in Figure 3.7, taken from the start of a waxing tidal cycle for their respective time cycle and as such represent the initial tidal minimum. In order to demonstrate the tidal nature of any associated 3D effects, a subsequent time-lapse inversion was undertaken when tides were increasing, where the data from Figure 3.7 were used as a reference dataset, and any changes have been related to these tidal variations. Figure 3.8 shows the results of the time-lapse inversion.

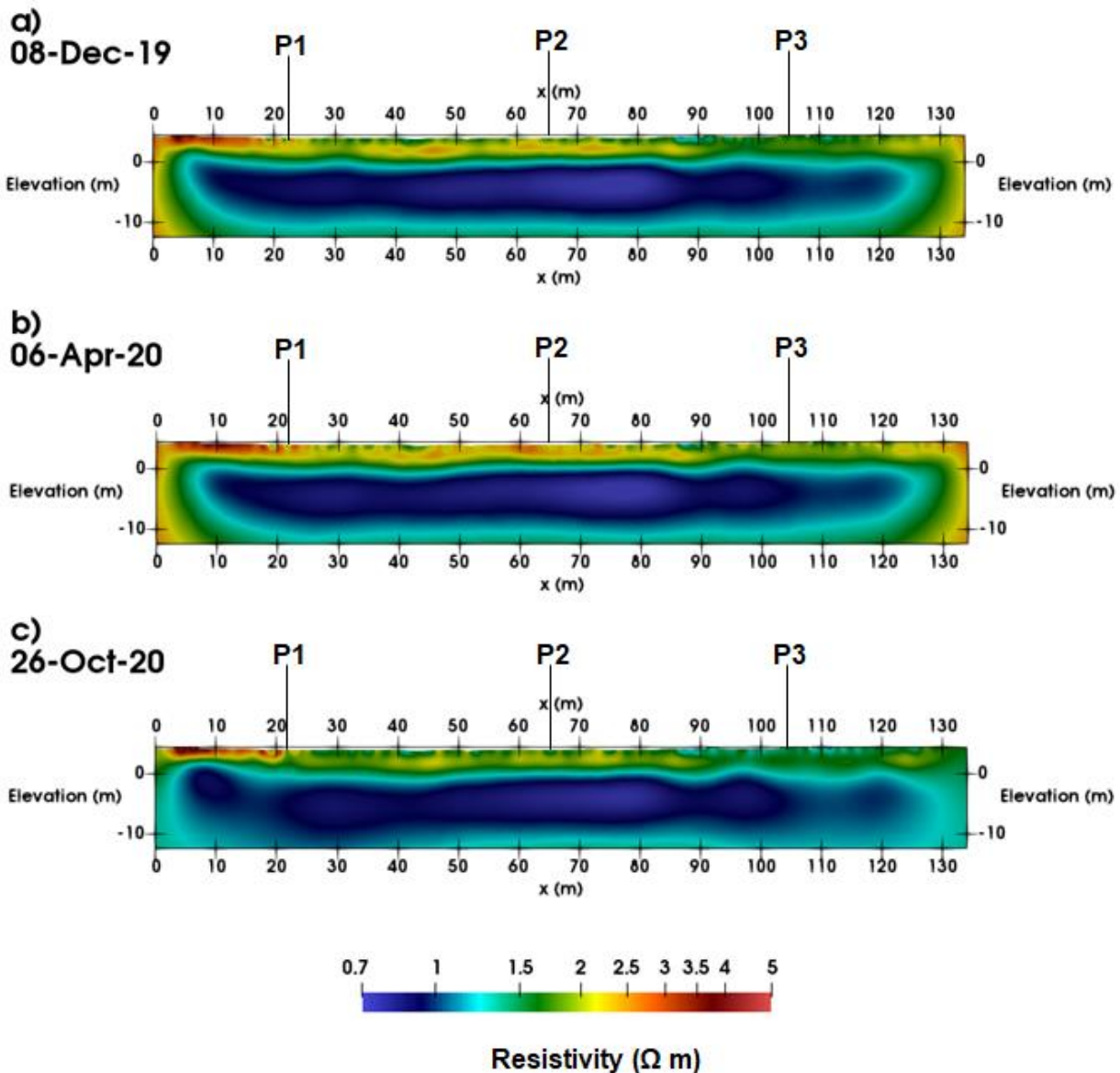


**Figure 3.7:** 2D inversions of the ERT data taken from L2 at Hadleigh Marsh (see Figure 3.2) where each inversion represents the start of a tidal cycle, where it is at a tidal minimum. a) A reference inversion from 08-Dec-19 (water level 1.08 m). b) 03-Apr-20 (water level: 1.65m). c) 26-Oct-20 (water level: 1.35 m). Water levels were taken from at the nearby Sheerness tidal gauge, so water levels are not directly representative of Hadleigh Marsh, but are analogous.

The reference inversions for all data sets shown in Figure 3.7 indicates a conductive subsurface adjacent to the river, where resistivity values are typically less than 10  $\Omega\text{m}$ . However, the upper 2 m is slightly more resistive than at greater depths. It is possible that this is a feature of this section of the embankment (such as drier conditions), or an effect of prior weather conditions, where greater depths are likely to be more saturated and therefore less resistive. However, a 3D effect resulting from a river is likely to induce a conductive feature at depth, as evident in the synthetic modelling, where decreased resistivities are present at depths below 2 m from the surface. This may explain the trends observed, creating

difficulties in the reliability of interpretation. In order to observe changes due to a 3D effect induced by tide, time-lapse inversions have been shown at different points in the tidal cycle, where water level was higher than in the reference inversion.

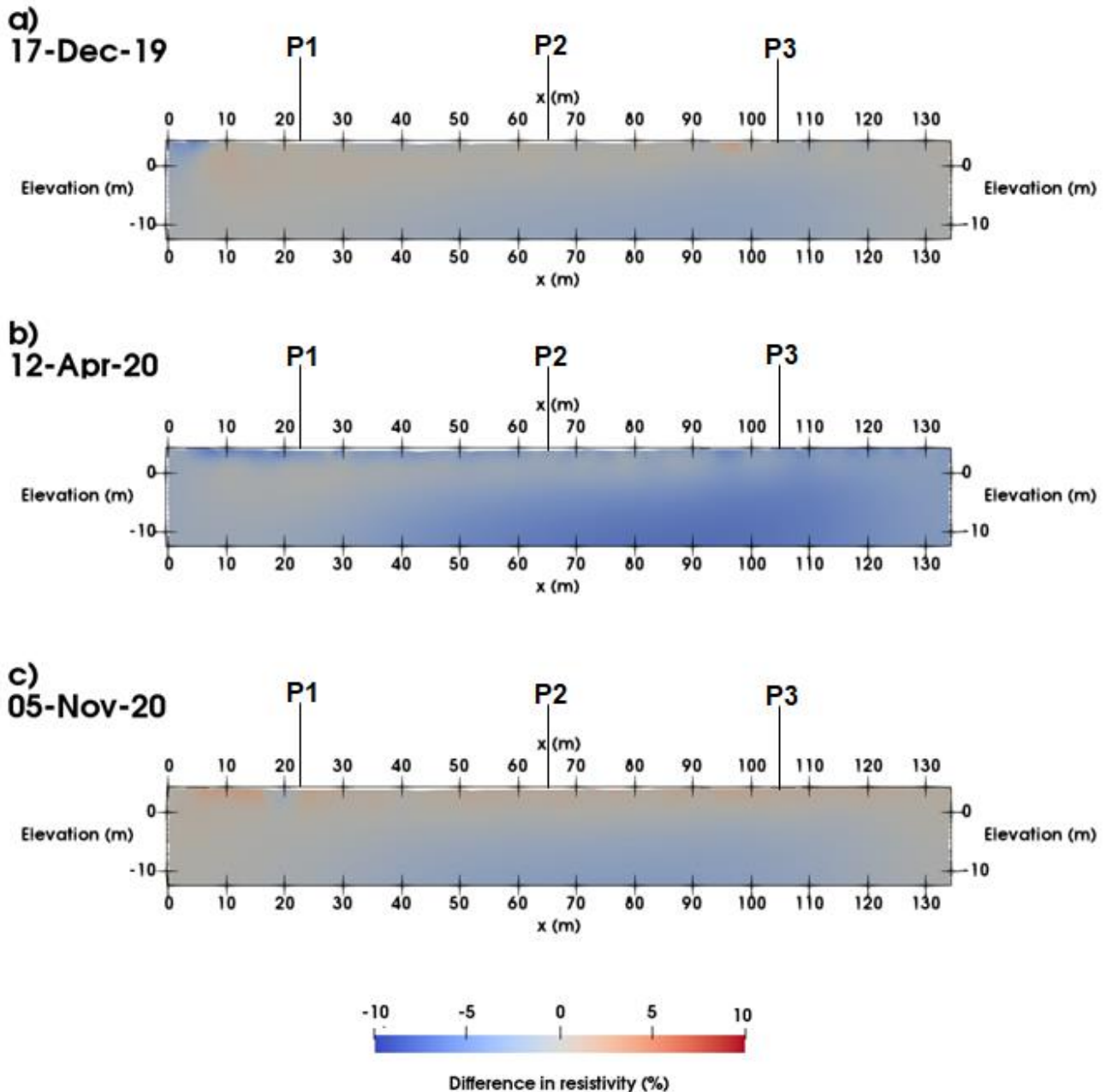


**Figure 3.8:** 2D difference inversions for L2 at Hadleigh Marsh. Each difference inversion shown corresponds to the reference inversion of the same letter shown in Figure 7. a) 17-Dec-19 (water level: 5.64 m, reference inversion: 03-Dec-19). b) 12-Apr-20 (water level: 5.75 m, reference inversion: 03-Apr-20). c) 05-Nov-20 (water level: 5.47 m, reference inversion: 26-Oct-20). Water levels were taken from Sheerness tidal gauge, so water levels are an analogous correspondence to Hadleigh Marsh.

The difference inversions for L2 show generally small changes in resistivity from the start of the tidal cycle to a time of high-water level. In most inversions a decrease in resistivity of

greater than 5% is noted from depths lower than 5 m for approximately 80 m across the embankment to the left of the section. This is potentially an effect induced by the proximal river, where higher tides are inducing a stronger 3D effect at depths where potential 3D effects are noted in the reference inversions. This part of the section is most proximal to the river (Figure 3.6), which gives weight to this interpretation. However, due to the low magnitudes, other lateral effects or over/underfitting of data cannot be ruled out. At shallow depths resistivity variation is not significantly affected by tidal action. Overall, the data shows some potential impact at depths, which may correspond to a 3D effect from the river. The April 2020 dataset shows the greatest decrease in resistivity through time, likely due to the ground being less saturated, meaning resistivity contrasts between river and ground beneath the electrode array will be larger.

2D inversions of P1-3 (Figure 3.9) are generally more resistive than L2, which is assumed to be a result of the landfill infill, with less resistive anomalies close to the river Thames. Subsequent time-lapse inversions of P1-3 (Figure 3.10) show an overall increase in conductivity, assumed to be a result of infiltration from rainfall due to the presence of rainfall in the days following the December reference inversion.

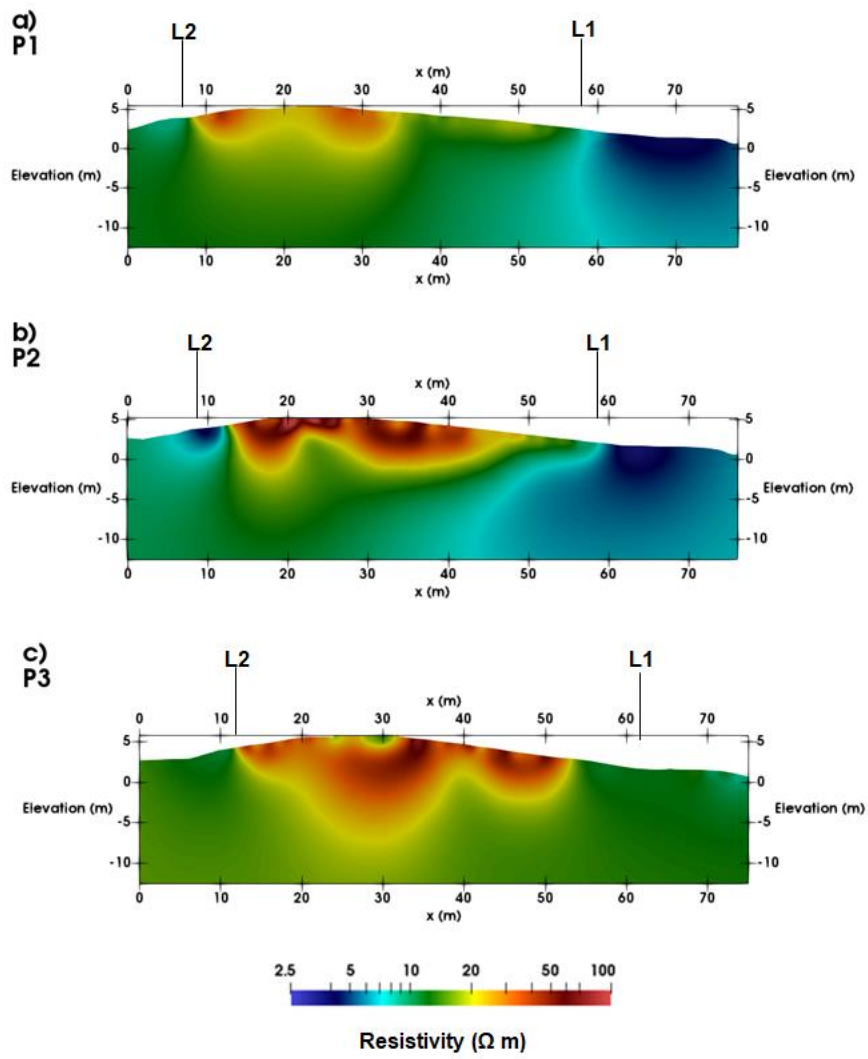


**Figure 3.9:** 2D inversions of lines P1-P3 on 08-Dec-19. a) Line P1. b) Line P2. c) Line P3. The array type used for all measurements was a dipole-dipole array.

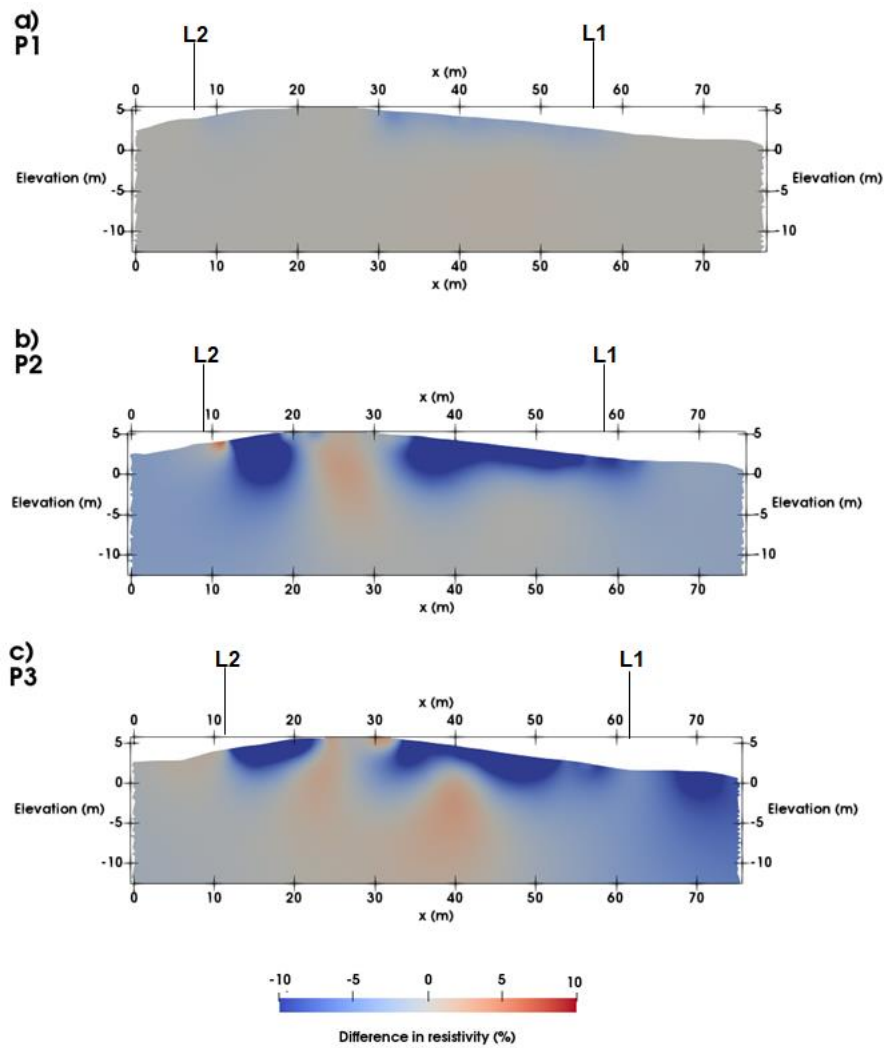


**Figure 3.10:** 2D difference inversions of lines P1-P3 on 08-Dec-19. a) Line P1. b) Line P2. c) Line P3.

Data from all five electrode lines (see Figure 3.6) were utilised in a 3D time-lapse inversion for each tidal cycle at Hadleigh Marsh. Several inversions were run for various tidal cycles across the PRIME monitoring period at Hadleigh Marsh (08-Dec-19 to 17-Dec-19); Figure 3.11 shows a fence diagram of a selected reference inversion for the ERT, at low tide.

08-Dec-19

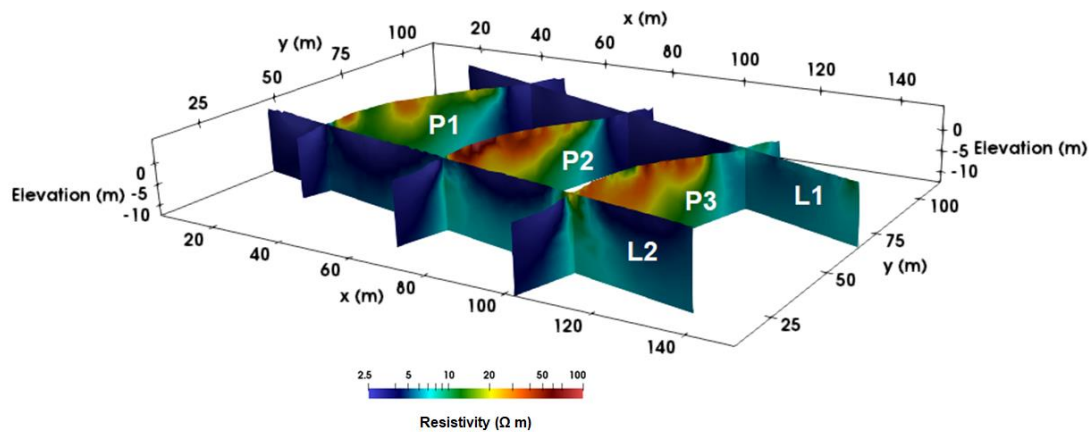


**Figure 3.11:** 3D reference inversion for Hadleigh Marsh, taken from the beginning of the tidal cycle (08-Dec-19), where the maximum tidal ingress is lowest. L2 is adjacent to the River Thames.

The 3D inversion shows a general consistency in resistivity across each ERT line for the December 2019 dataset. The perpendicular lines, P1-P3, are generally resistive, with similar magnitudes to their 2D inversion counterparts (see Figure 3.9). Whereas L1 and L2 are less resistive than P1-3, which is believed to be influence from the Thames adjacent to L2 and the watercourse located adjacent to L1. The region of lower resistivity at depth in L2, observed in the 2D inversions in Figure 3.7, is not present in the 3D inversion. This implies that it might be a 3D effect that is resolved in a 3D inversion. Through incorporation of the more resistive P1-P3 and L1, the result is a more representative inversion. The general consistency between resistivities through lines, indicates that the 3D inversion is able to provide a more reliable representation of the subsurface without influence of a 3D effect. However, the regions in the 3D model between lines P1-3 are associated with low levels of resolution due to the large line spacings, and are therefore not displayed in Figures 11 and Figure 3.12, discussed below). Correlation of resistivities within the inversion, mitigating against such 3D effects, is believed to occur where the orthogonal lines cross (i.e. at the intersection between L2 and P1).

To further identify potential changes with a tidal cycle, the results of a 3D difference inversion is shown in Figure 3.12. The results reveal a distinct change in resistivity at shallow depths. In the 2D inversions and synthetic modelling it was noted that artefacts induced by the 3D effect were present at depth. The 3D inversions do not show a significant change in resistivity at equivalent depths. Therefore, with a similar resistivity distribution to 2D time-lapse inversions and reduced artefacts in lines proximal to the river, it has been suggested that the 3D



inversions are able to successfully visualise subsurface conditions with some mitigation of the 3D effect.

**17-Dec-19**

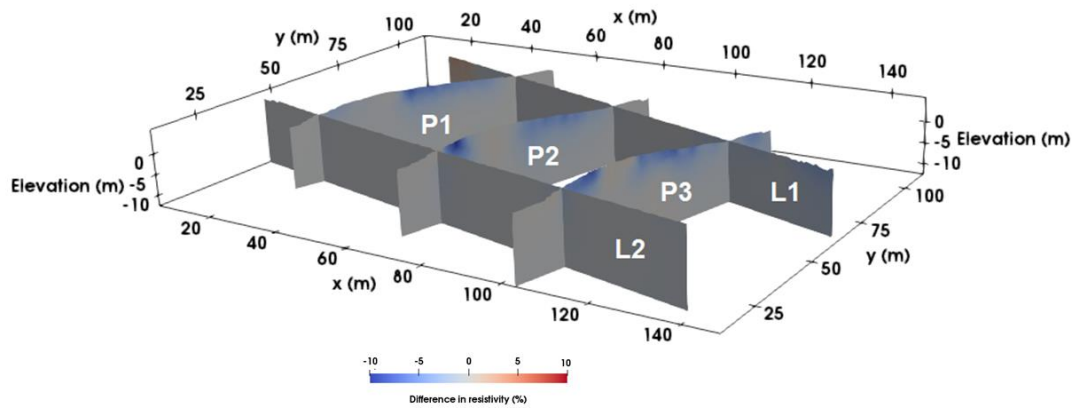


**Figure 3.12:** A 3D time-lapse inversion for Hadleigh Marsh (17-Dec-19), using Figure 11 as a reference, taken from a time period where the maximum tidal height was at its peak. L2 is adjacent to the River Thames.

## 3.4 Discussion

### 3.4.1 Synthetic Numerical Modelling

The synthetic modelling explored the effects of changing river salinity and river level upon resistivities beneath an ERT array. For a scenario of a clay embankment with a homogeneous resistivity of  $40 \Omega\text{m}$ , it has been determined (for the given geometry) that there are unlikely to be any noticeable effects when the river is 4.5 m away from the electrode array, and 0.75 m below crest height (for the geometry of this particular model). Within this limit, resistivity will be decreased at greater depths than 2 m underneath the electrode array where electrode spacings are 2 m or less. The nature of the homogeneous embankment is highly idealised, as it is unlikely that a real embankment will be homogeneous, and the trend and magnitude of affected resistivities are highly impacted by the given parameters. For instance, if the embankment resistivity is higher, higher resistivities from the modelled river would likely induce an effect and the resistivities modelled in this case study could create a greater resistivity contrast. Consequently, the trend of resistivity at depth could be more severe and noticeable at river levels deeper and further away from the electrode array than in this synthetic model. In a more coastal environment embankment resistivities will likely be

smaller than that of the synthetic model (40  $\Omega\text{m}$ ). However, modelling a larger embankment resistivity enables more universal applicability, such as for tidally influenced rivers, where river salinity will be low, and to enable comparison between freshwater and saltwater settings.

The second modelling scenario, with a clay core incorporated into the embankment, provided an opportunity to assess the effect of heterogeneity within the embankment on the 3D effect in the ERT inversions. As with the homogeneous embankment, there was a distinct increase of resistivity at depth with higher river levels, closer to the electrode array. Therefore, the increased heterogeneity modelled within the embankment does not obscure the 3D effect associated with the river at shallow depths. However, embankment heterogeneity influences the inverted model at greater depths, resulting in modelled resistivities from deviating from the true values.

Resistivities of the river have a large influence on the magnitude of the 3D effect. For less resistive river waters, such as brackish conditions typically associated with estuaries, there is likely to be a pronounced 3D effect. In contrast, the higher freshwater resistivities induced negligible 3D effects on the synthetic ERT survey. This highlights the need to be aware of potential 3D effects, particularly in estuarine environments, and a need to account for such when working with data obtained from these environments. Freshwater river fluctuations are less likely to induce a 3D effect in environments similar to the synthetic model. However, natural embankments will be more complex, comprising a greater range of resistivities, where elevated water saturation will likely decrease resistivities in the embankment close to the river. This is more difficult to model for generation of 3D effects in a generalised manner, or to differentiate the influence of the two contributing factors (river water level change and changes in soil water content). A heterogeneous model was developed, but no single synthetic modelling scenario can capture the complexity of a real embankment.

Real resistivities of an embankment will vary over a scale of centimetres and the composition may be highly varied and form irregular layers. The range of resistivities for typical embankment infill, including clay infill can be higher or lower than what was modelled (Palacky, 1987), so with more resistive infill freshwater may induce a 3D effect with larger ranges in values.

River geometries for the synthetic model have been assumed to be close to the crest height at its peak. Many rivers will be at lower depths and further lateral distances to the electrode array in many survey settings, which could mean they are beyond any influence zone to the ERT data. As such, this shows that for many cases it will be unlikely that large artefacts will be induced in the ERT data, arising from river level fluctuations, and that this study represents a more extreme scenario (*e.g.* rising water level after a storm event). However, the highly variable nature of a real-life setting to the synthetic model means that there may be some contexts where a 3D effect is likely, due to a strong resistivity contrast between embankment infill and river or highly saline water. Therefore, it is suggested that river levels with the tide and anticipated resistivities of the river and local geology are known for the survey, in order to enable an estimation of whether a 3D effect is likely.

Electrode spacings of 1 m, 2 m and 4 m were modelled in our synthetic study. It was noted that there is a steep decrease in shallow resistivity with increased electrode spacing, due to the lower resolution at shallower depths, resulting in a greater influence zone for the river to impact data. A larger depth of penetration with increased electrode spacing will enable a 3D effect to be reliably detected at greater depths below the electrode array. Resistivities resulting from 1 m or 2 m spacing give similar values, but electrode spacings of 4 m give marked distortions in resistivity, including at shallow depth. This suggests that when shallow resolution is poorer, there is greater influence from the river as a 3D effect when there are fewer resistivity values at shallow depths beneath the ERT array. All electrode spacings show some distortion in resistivity at greater depth.

### ***3.4.2 Hadleigh Marsh, Essex, United Kingdom***

The analysis of inversions at Hadleigh Marsh indicate the potential for a 3D effect to influence data and potentially mislead interpretation through artefacts being introduced to the data. The most notable is a feature of abnormally low resistivity located at 2 m depth in survey line L2 when inverted in 2D. This corresponds to observed regions of lower resistivity in the synthetic modelling study, caused by the river. With increased maximum tide height during the month, as observed in the time-lapse inversions, there is a decreased resistivity at depth in the area of L2 closest to the river. This suggests that the anomalous region of lower resistivity in L2 is probably a 3D effect resulting from the river, which could incorrectly be

interpreted to be a region of saline water beneath the array instead. At high tide, resistivities are over 5% less resistive at depth than low tide. Therefore, sites with pronounced tidal ranges will experience greater potential 3D effects, and sites which are more resistive will see greater resistivity contrasts between artefacts induced by a 3D effect and the embankment resistivity, potentially leading to a greater degree of misinterpretation. When data are inverted in 3D there is no noticeable conductive region at depth in L2, indicating that 3D inversions could rectify the observed 3D effect in L2 and that incorporating a 3D inversion scheme could aid interpretation of ERT data in tidal settings.

Previous research on an off-centre pipeline had inferred that electrode spacing is unlikely to alter 3D effect magnitudes (Hung *et al.*, 2019), whereas laboratory experimentation and synthetic modelling of different electrode spacings with a change in water infiltration had suggested that increased electrode spacings would increase the 3D effect until shallow resolution had decreased substantially (Hojat *et al.*, 2020). The synthetic modelling here indicates with increased electrode spacing there is more severe decrease in resistivity from a 3D effect, supporting that electrode spacing does alter 3D effect magnitudes. It is therefore suggested that where the suspected source of a 3D effect is larger than the survey, electrode spacings are kept to a minimum feasible level for survey requirements to reduce a 3D effect on surveying at shallow depths, if the survey is to be inverted in 2D.

A summary of the key outcomes from this chapter is found in Table 3.2.

**Table 3.2:** Summary table for the aims and outcomes of the synthetic numerical modelling and Hadleigh Marsh ERT.

Aim	Outcome
Effect of river level on synthetic numerical model.	3D effects present with river proximal to the electrode array, until 1.5 m distance. River level fluctuations can induce a 3D effect on ERT.
Effect of salinity on synthetic numerical model.	3D effects present for 1-10 $\Omega\text{m}$ modelled rivers. Saline conditions in rivers likely to induce a 3D effect in ERT.
Effect of electrode spacing on synthetic numerical model.	Pronounced 3D effects using electrode separations of 4 m compared with 1 or 2 m separation.
Effect of embankment heterogeneity on synthetic numerical model.	Addition of a core to the model caused more complex resistivity pattern. Resistivity values below the core were not as representative of the true model when compared to a homogeneous model. Internal structure can cause 3D effects.
Presence of 3D effect in inversions from Hadleigh Marsh.	2D inversions of ERT at Hadleigh Marsh showed 3D effects in an electrode line closest to the River Thames, with pronounced effects in time-lapse ERT. Such effects were reduced in 3D inversions, suggesting this might be a useful method for mitigation.

### 3.4.3 Recommendations

To account for such issues when they are expected, it is suggested that 3D ERT inversions are undertaken where the survey locations are proximal to a river. The Hadleigh Marsh dataset demonstrated the possibility for 3D effects to be an issue. 3D inversions can incorporate the

full embankment geometry and also the resistivity of the adjacent water course. A 3D inversion would reduce the potential artefacts resulting from a 3D effect linked to the river, as observed at Hadleigh Marsh. Ideally, this would involve a 3D ERT survey geometry, which would allow greater restriction of resistivities across the embankment area. However, time and geometrical constraints may prevent a true 3D ERT survey. Utilisation of a 3D inversion scheme across all lines at Hadleigh Marsh reduced the 3D effect, suggesting that this suppressed 3D effects from 2D inversion, and previous research indicates that incorporating 3D coverage of potential measurements suppresses the 3D effect (Sjödahl *et al.*, 2006). In contrast, with a singular ERT line in the synthetic model the 3D effect is noticeable. Therefore, to constrain 3D effects, the survey should ideally incorporate more than one line in a series of arrays which cross-cut each other across the survey region and can then be inverted using a 3D approach.

If designing a time-lapse ERT set-up, it is recommended that a reconnaissance survey is undertaken for design of the time-lapse system, where several surveys are run during the day at different times, and with more than one survey line, to account for the effect of distance from river. This will enable interpretation of how any 3D effect present varies with tide across the day and survey distance from the river, for optimal survey design for later time-lapse monitoring. From the interpretation of the reconnaissance survey, electrode arrays can be located outside of areas with suspected 3D effects present and survey times set for when the tide is forecast to be low, although this will clearly limit to potential to monitor the integrity of the barrier under such events. For surveys close to a river that could create 3D effects, survey design should ideally include several arrays, which are proximal to each other and provide orthogonal coverage of the area. Such surveys, coupled with recognition of the river feature in any forward modelling, will allow fully 3D inversions to be carried out, eliminating 3D effects due to the watercourse.

### 3.5 Summary

A synthetic modelling exercise was developed to assess the change in 3D effect associated with changing river levels, salinities, and electrode spacings for a homogeneous and heterogeneous embankment. From this, there is a clear 3D effect induced with river resistivities associated with a more brackish water, indicating that estuaries are likely to

induce a 3D effect on proximal surveys. The 3D effect is noticeable at river distances less than 4.5 m in lateral distance and 0.75 m in vertical height from the electrode array and embankment crest height, respectively. Therefore, a significant 3D effect is most likely where ERT surveys are taken on the riverside flank of an embankment and are unlikely to be impacted where surveys are taken on the landward side. Specific boundaries for where a 3D effect from a tidal river may be influential are controlled by embankment geometry, the local geology and water content and it is suggested that local conditions are considered for each survey, since the 3D effect may have a greater or smaller influence distance for different scenarios.

Using time-lapse inversion data taken from tidal cycles at Hadleigh Marsh and modelling of a synthetic embankment, the impacts of the 3D effect have been identified and evaluated, where the nature of the synthetic model has guided interpretation of a presence of the 3D effect at the site and given assessment to whether a 3D effect from tidal action is likely to be experienced in ERT surveys. At Hadleigh Marsh there was an associated resistive low in the inverted model adjacent to the Thames, at depths equivalent to observed 3D effects in the synthetic modelling and areas most proximal to the river, indicating that there is a likelihood that a 3D effect is impacting the data. With greater resistivities, such effects will be more distinguishable and the anomalous resistivities may lead to misinterpretation. This shows a need to address 3D effects resulting from estuaries, which has been explored further in synthetic modelling to assess likely extents of a 3D effect in this environment.

Electrode spacings of 2 m or less in survey sequences have been suggested (for the geometry studied here) to minimise the potential influence from the river to the ERT survey at shallow depths. Alongside this, it is recommended that 3D ERT surveying is set up on the riverside of an embankment to reduce artefacts from the water body with a greater degree of resolution in the inversion. If this is not possible, it is suggested that several linear ERT arrays are used (e.g. parallel and/or orthogonal survey lines), which can be inverted using a 3D scheme to reduce potential 3D effects. This study highlights the potential for a 3D effect to be induced in estuarine environments, due to the likely saline water and potential high resistivity contrasts.

Embankments are likely to be more heterogeneous than the models in this study, meaning that effects may vary in real life, given resistivities will be more variable through an

embankment. Also, embankment geometries, sizes and slope angles will vary, so the results from this model cannot be directly applied globally. However, they demonstrate the potential of 3D effects impacting results in flood embankments along tidal rivers or estuaries, indicating that this needs to be considered for ERT surveys.

Future work in this field will involve modelling of more complex embankment compositions and means of reducing any 3D effect. Research involving mathematically determining the extent of likely influence for a range of given parameters (*e.g.* embankment infill resistivity, number of layers, river resistivity) could enable specification for survey design, giving boundaries for survey design as to where 3D surveying may be necessary to mitigate potential 3D effects. Investigation of more complex embankment geometries could be developed to account for 3D effects in other embankment settings. Also, normalisation techniques could be developed to reduce the influence of a proximal river, as Fargier *et al.* (2014) and Bièvre *et al.* (2018) have utilised for reducing topographic induced artefacts.



# **4.0 ACCOUNTING FOR RESERVOIR AND INFRASTRUCTURAL EFFECTS AT THE MACTAQUAC DAM, NEW BRUNSWICK, CANADA: A CASE STUDY MODELLING IMPACTS OF CONCRETE STRUCTURES AND RESERVOIR ON ERT DATA**

## **4.1 Introduction**

Electrical resistivity tomography (ERT) has potential use for monitoring of dams because of its sensitivity to porosity, clay and water content (Fargier et al., 2014), pore water conductivity (Binley & Slater, 2020), alongside geological variation (Chambers et al., 2014), allowing monitoring of internal conditions and interpretation of any potential seepage, settlement or risks of slope failure. However, ERT is limited by non-uniqueness within the models (Michalis et al., 2016), 3D effects caused by off-line features of anomalous resistivity being mapped onto an inversion as artefacts (Cho et al., 2014; Hung et al., 2019; Hojat et al., 2020), and ability to discern stratigraphical boundaries within the inversion in complex stratigraphy - all of which may lead to obscuration of results and incorrect interpretations of the subsurface.

Embankment dams share common features between them, which may cause interpretive difficulties including the presence of a reservoir and heterogeneous stratigraphy. Dams are complex structures, comprising the reservoir, embankment infill, core, filters, drainage, and presence of infrastructure, such as roads along the crest, sluiceways, concrete abutments and associated wingwalls. These may induce 3D effects within, where proximal features of atypical resistivity outside the footprint of the electrode array may influence the apparent resistivity measurements, creating conductive or resistive artefacts. A common source of a 3D effect in dams would be the reservoir (Sjödahl et al., 2006; Cho et al., 2014;). In terms of a dam, such artefacts may be misidentified as seepage pathways or incorrect interpretations of the dam features. Given the structural complexity of dam settings it is unlikely that an inversion is going to accurately represent the resistivity distribution of the subsurface. This

chapter will therefore focus on addressing whether the presence of complex internal structure (*e.g.* a concrete abutment) will impact ERT data and need to be accounted for, along with whether changes in resistivity in a water body will have an impact on ERT data, including temporally. Finally, it is aimed to determine whether internal features of interest (*e.g.* a seepage zone) can be detected with ERT if such 3D effects from structural complexity and the water body are present.

In this research, a case study taken from Mactaquac Dam, New Brunswick, Canada, was used to assess whether the infrastructure (*i.e.* an abutting concrete structure) and reservoir are likely to influence resistivities in the inversion, so it can be determined whether the presence of such features need to be accounted for and understood when interpreting ERT data in dam settings. This was done through synthetic ERT modelling of the site, using several different modelling scenarios to account for the presence of concrete, temporal effects in water level and resistivity, the ability to detect a zone of concentrated seepage (represented by a region of contrasting resistivity) and comparisons between 2D and 3D inversions. Further comparisons were made with field data taken from the Mactaquac site to infer whether such effects may be of pertinence for processing ERT measurements of the dam.

## 4.2 Mactaquac Dam

Mactaquac Dam (Figure 4.1) is a 500 m long embankment dam, with a vertical span of 58 m from crest to foundation (Conlon & Ganong, 1966; Tawil & Harriman, 2001; Butler et al., 2023), located along the River Saint John, 20 km upstream from Fredericton, New Brunswick and has been operational since 1968 (Butler et al., 2019). The dam is part of a 660 MW hydroelectric facility for NB Power (Butler et al., 2019; Yun et al., 2022) and is a rockfill embankment dam, comprised of fine to medium grained greywacke, very fine grained slate and a clay-till core (Yun et al., 2022). A local highway runs along the crest onto a concrete sluiceway structure abutting the north end of the dam (Yun et al., 2022). An alkali-aggregate reaction within the concrete is causing it to expand, crack and otherwise degrade over time, and various methods of mitigation have been undertaken since 1985 (Gilks et al., 2001).



**Figure 4.1:** Mactaquac Dam. a) The location of Mactaquac Dam within Canada and its more localised location in New Brunswick, Canada (45.95°N, 66.87°W) (Google Earth, 2023). b) An annotated photograph captured of Mactaquac Dam, showing the features of the dam and the area where the ERT survey is located (modified from Butler & Boulay, 2020).

An experimental geophysical monitoring programme has been established to assess potential seepage from the reservoir through the region where the embankment abuts the concrete. In late 2013, a fibre optic distributed temperature sensing (DTS) cable was installed in a

borehole drilled into the concrete immediately adjacent to its interface (Butler et al., 2019). This DTS system remains in use, monitoring seasonal temperature variations, along with anomalies assumed to be caused by preferential seepage at certain depths (Yun et al., 2022). Electrodes for self-potential measurements were also installed (Ringeri et al., 2016). These electrodes and others, 123 in total, were subsequently re-purposed for time-lapse ERT surveying. As shown in Figure 3.2, most are arranged in five parallel lines, starting at the downstream toe of the embankment, running up its slope and across its crest (buried beneath the road). Each of lines 1 – 5, spaced 5 m apart, includes 24 electrodes at a nominal spacing of 3 m. Three additional electrodes on Line 0 (L0) provide improved sensitivity close the top of the concrete abutment that dips below the embankment (Figure 4.2).

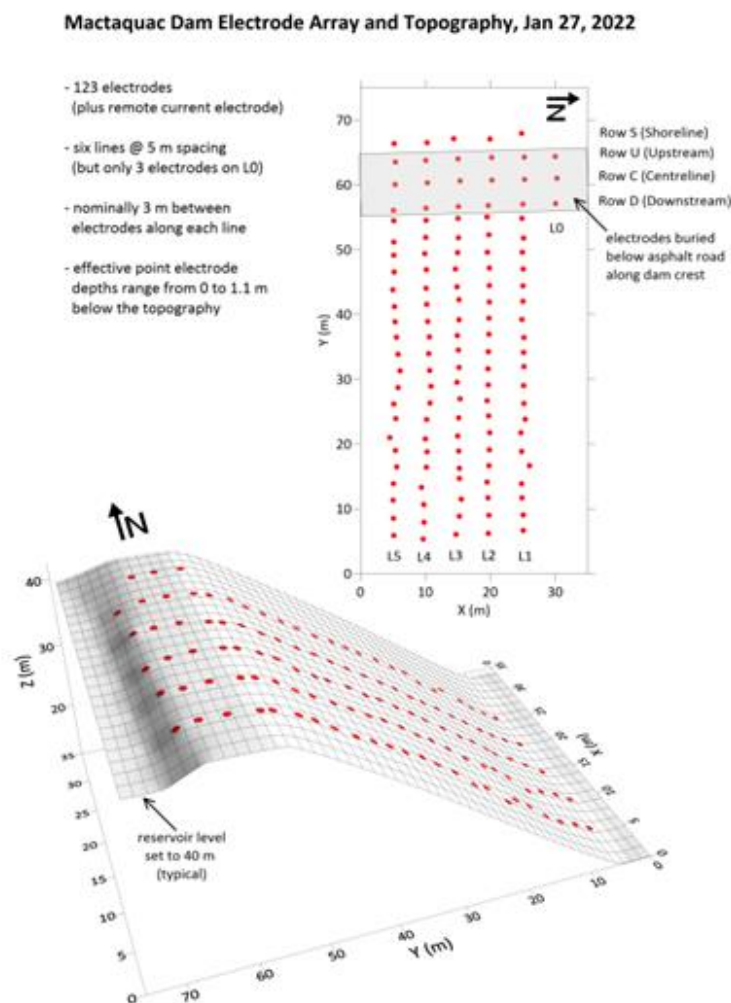


**Figure 4.2:** Electrode layout, as of 2022, for Mactaquac ERT monitoring, showing the 5 principal lines (L1-5) and L0. The concrete wingwall is found to the north, while the headpond is westward from the survey (Butler, 2022).

Assessment of the DTS data revealed a prominent surface and a subtle deep temperature anomaly that was associated with seepage through the concrete and disconnected from the embankment (Yun et al., 2022). Temperature modelling, based on coupled flow of seepage water and heat, indicated that the deeper anomaly is confined to a zone in the embankment, but it was uncertain whether concentrated seepage for the shallow anomaly was linked to the concrete, embankment rockfill or concrete-rockfill interface (Yun et al., 2022; Butler et al., 2023). Previous modelling of self-potential (SP) data suggested a foundation seepage, but did not exhibit clear response to any seepage along the concrete-core interface (Ringeri et al., 2016).

Modelling of seepage based on DTS data could not give a reliable interpretation of seepage through the concrete-embankment interface (Yun et al., 2022). Therefore, any suggestion of seepage-based resistivity changes in the rockfill is not reliably supported by previous Mactaquac investigations. ERT monitoring was therefore initiated in an attempt to determine whether the shallow DTS anomaly extended into the core. Recent results suggest this to be the case (Butler et al., 2023).

The full monitoring array, including the crest electrodes needed for sensitivity in the dam's central clay-time core, became active during summer, 2021 and remains in operation at the time of writing (Danchenko & Butler, 2022). A low power (10 W) single channel resistivity meter (Lippman "4point light 10W"), is used to collect a survey autonomously each night. Power is provided by a 100 W solar panel connected to a 12 V, 52 Ah lead acid battery (Boulay, 2021). The electrodes include 30 lead-lead chloride electrodes previously used for SP monitoring, and 93 subsequently installed stainless steel electrodes, which were made relatively long to minimise high contact resistances expected in the rockfill (Boulay et al., 2020). The electrodes installed in the slope were 0.9 m long, while those in the crest were 1.2 m long and were emplaced ~0.3 m depth below the road surface. The time-lapse ERT setup has been in use since 2019 (Danchenko & Butler, 2022; Butler et al., 2023). ERT data are acquired daily, at night when ambient noise levels from the generating station tend to be lower and more stable. Apparent resistivities from each quadrupole are typically averaged over periods of 4 – 7 days (avoiding days with significant rainfalls) with outlier values (i.e. exceeding ~1.5 standard deviation) excluded. The data from 5-10 days were then used in a difference inversion to visualise changes with time. The ERT measurement scheme utilised a

pole-dipole array predominantly to maximise depth of investigation (Boulay and Butler, 2021), with some Wenner and dipole-dipole measurements added predominantly for shallower depths and to permit collection of reciprocal data, allowing analysis of errors for data quality. The pole current electrode was located approximately 500 m from the survey area. The surveys were undertaken in a true 3D orientation, with measurements along and perpendicular to the electrode lines.

ERT monitoring has identified strong changes in resistivity over time (exceeding 50%) within the core up to 8 m below surface – a depth range consistent with the shallow anomaly observed in previous DTS monitoring. The changes in the core lag behind comparable changes in the resistivity of water (where changes in water resistivity are linked to snowmelt and temperature) in the headpond with time lags on the order of 5 days (Danchenko & Butler, 2022; Butler et al., 2023;). Strong temporal variations in resistivity are also observed (predominantly behind the core) in response to road salt runoff in the winter, and washout of this salt over the following spring and summer (Danchenko & Butler, 2022). Boulay (2021) noted the presence of anomalously low (and temporally variable) resistivities at 15 – 20 m depth in the (presumably) unsaturated rockfill behind the core adjacent to the concrete abutment and hypothesized it could be a consequence of headpond water leaking into the region through fractures in the alkali-aggregate reaction (AAR)-affected concrete. However, the concrete itself is known to be of low resistivity (possibly due to both rebar along its face and the AAR reaction products (Flores et al., 2015; Chopperla & Ideker, 2022), raising the prospect that the low resistivities imaged in adjacent rockfill could be a 3D artefact. It has been observed that in embankment settings, distortions in the expected resistivity do occur because of the presence of heterogeneous stratigraphy within the embankment (Ball et al., 2022), which indicates the potential for the concrete wingwall to induce such an effect.

## 4.3 Synthetic Modelling

### 4.3.1 Methodology

To quantify the effect of the concrete and reservoir on Mactaquac Dam inversion results, a synthetic model of the dam was generated, and divided into separate regions representing the headpond, Saint John River, core, concrete wingwall, rockfill below the headpond level

(labelled as wet rockfill), and rockfill above the water table (labelled as dry rockfill) (Figure 4.3). These regions were set to allow the assignment of different resistivities for use in the synthetic modelling.

The model geometry of the site (*e.g.*, embankment and concrete structure shapes, headpond and river levels and depths) was prepared through use of an AutoCAD representation of the dam, coupled with photography, site diagrams, known topographic coordinates for points along the structure and measured coordinates of the electrodes. The model was extended out to approximately 500 m laterally and vertically from the survey lines, as to not violate boundary conditions. A representation showing the relevant features for the synthetic model is displayed in Figure 4.2. The entirety of the concrete structure is not represented in the model to reduce complexity; the concrete structure extends further below the headpond on the upstream side of the dam and to the north, along the crest, but concrete in those regions was considered unlikely to induce significant effects on the survey based on previous experience in modelling 3D effects associated with water-retaining structures (Ball et al., 2022). For example, the concrete diversion sluiceway noted in the site photo (Figure 4.1) was not represented due to the complexity of this structure in model design, with a lack of necessity due to its distance away from the survey. Also, the concrete was assumed to be homogeneous to reduce complexity. Likewise, the clay core was not extended along the whole embankment, as it would be in reality, to reduce unnecessary complexity and computation time in areas of low interest. Instead, it was extended just 18 m southward from L5 – a distance considered sufficient to capture the vast majority of its influence on modelled apparent resistivities.

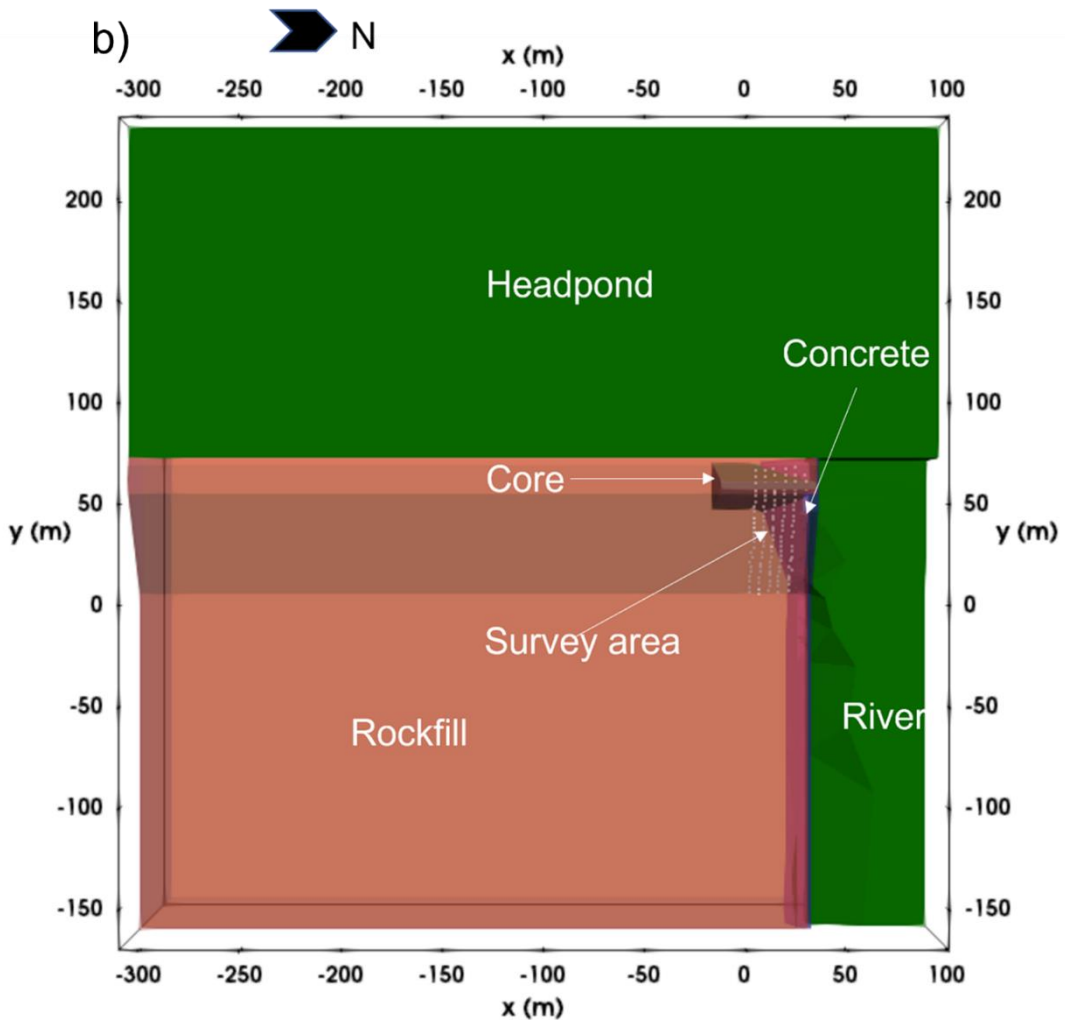
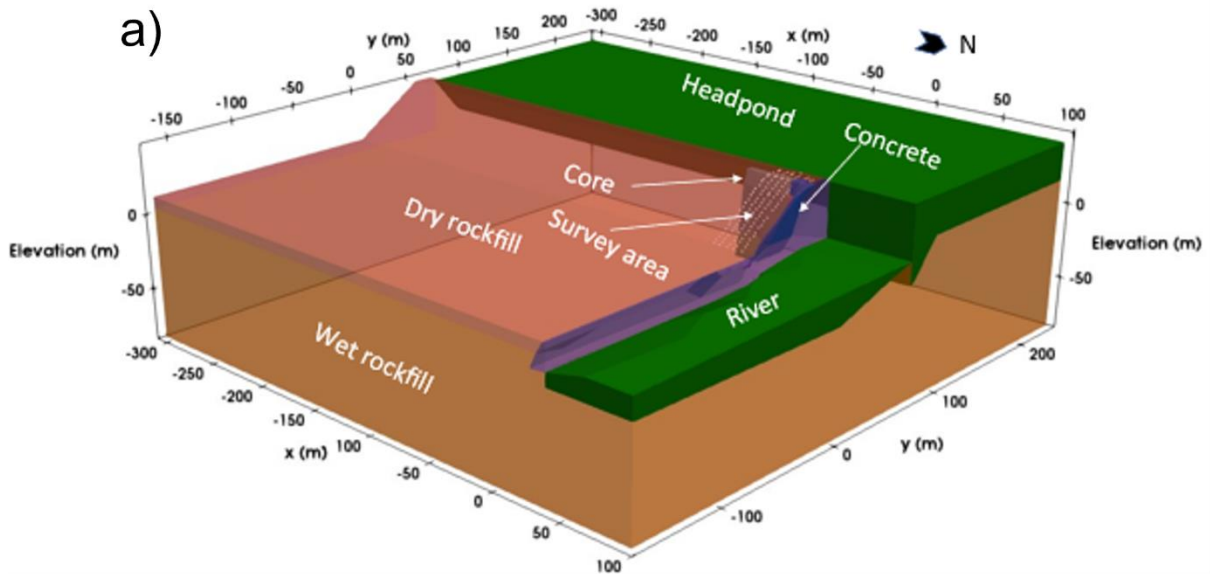
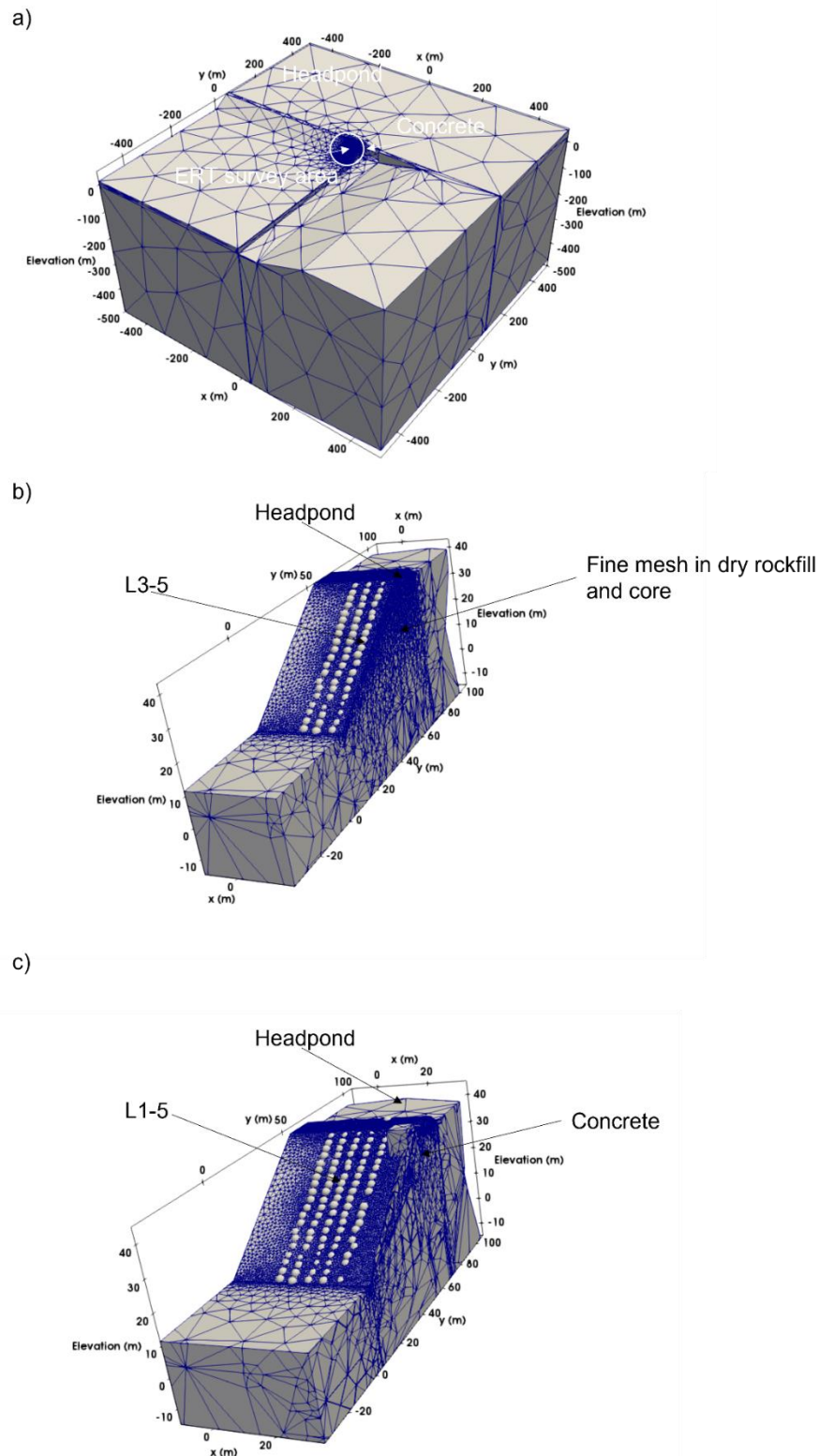


**Figure 4.3:** A model showing the different resistivity zones incorporated into the synthetic model, as well as the ERT survey area. a) Sub-vertical view of the model. b) Aerial view of the model.

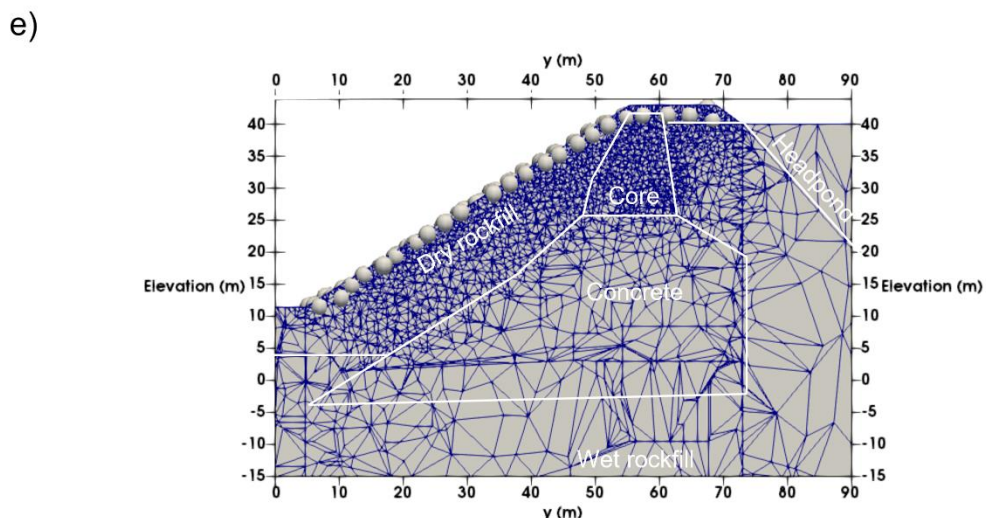
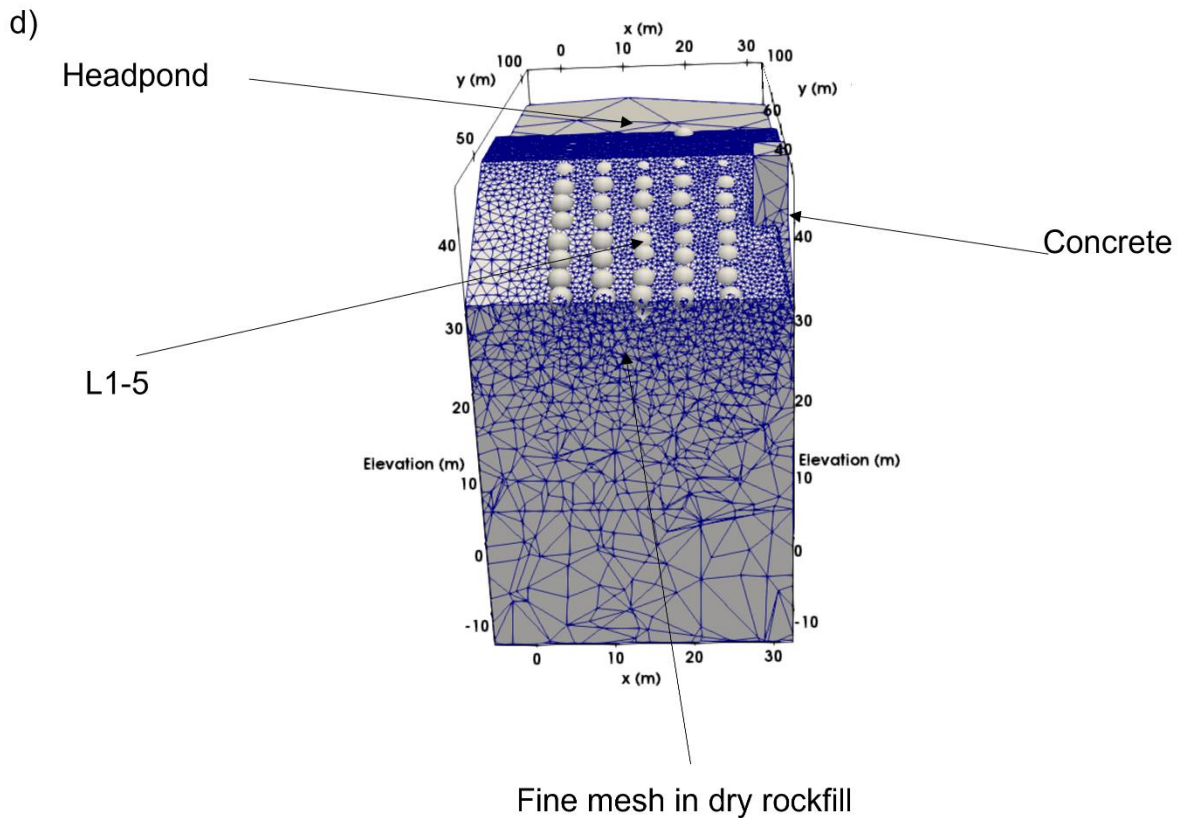
The model design was transformed into a 3D unstructured finite element mesh for use in modelling with the mesh generation software, Gmsh (Geuzaine & Remacle, 2020). The mesh



replicated the geometry of the model shown in Figure 4.3. The characteristic length for the mesh at surface was modelled at approximately one quarter of the electrode spacing to ensure fine discretisation for synthetic modelling of the resistivity data. This included the majority of the modelled core and rockfill in the survey area, and the mesh gradually coarsened to the mesh boundary. The fine mesh region extended to 18 m southward from the survey area within the embankment, and 10 m northward within the adjoining concrete structure. Fineness in the mesh was ensured to permeate to depths of approximately 20 m to allow good coverage within the area at which the ERT has good sensitivity (i.e. the upper 20 m), where a characteristic length of 4-7.5 m was used below 30-40 m to the base of the core and concrete for a gradual coarsening. A characteristic length of 250 m was used along boundary nodes where fine discretisation was less necessary and the boundaries were set at approximately 500 m from the survey area to ensure no boundary effects were present. Representations of the mesh can be seen in Figure 4.4.



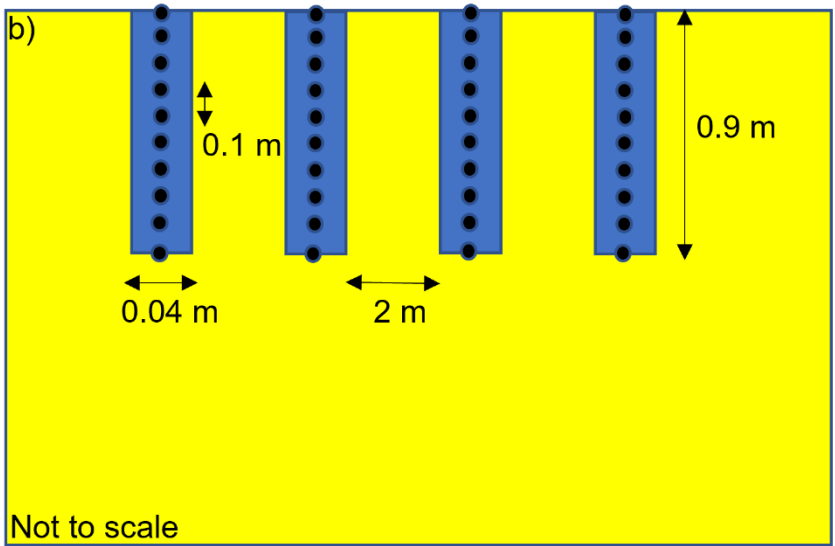
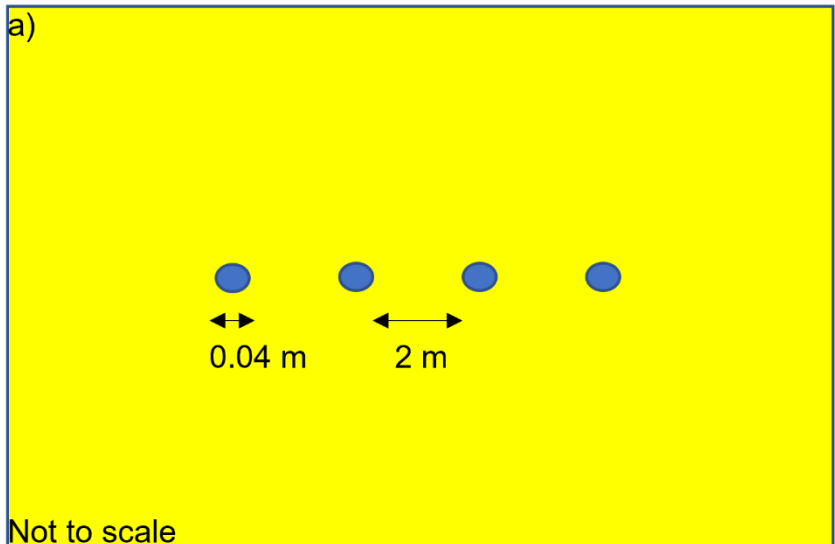
**Figure 4.4:** Representations of the mesh used for the synthetic modelling at Mactaquac Dam. a) An image of the entirety of the mesh. b) Representation of the mesh extracted from within the ERT survey. c) Representation of the mesh showing the entire survey area and concrete wingwall. d) Representation of the mesh, showing the mesh below each major line used in the ERT survey. e) A 2D slice of the mesh underneath L1.





**Figure 4.4** continued.

Before modelling, the optimal coordinate for point location for each electrode was determined, in order to account for the length of the electrodes, i.e. non-point behaviour. It has been shown that for ratios of electrode length/spacing greater than 0.2, representing an electrode as a point source at the top of the electrode, as commonly assumed in ERT modelling, is likely to be invalid (Rucker & Gunther, 2011; Verdet et al., 2018). At Mactaquac Dam, the electrodes on the embankment slope are 0.91 m (3 ft) long, extending from surface

to ~0.9 m depth. The spacing is nominally 2-3 m, with one outlier case of ~2 m. Under the road on the crest of the dam, the electrodes are 1.22 m (4 ft) long, extending from ~0.2 to 1.5 m depth with an electrode spacing of 3-4 m. This gives an electrode length/spacing ratio of ~0.3 for both, meaning that a point source on surface is invalidated. Therefore, following Verdet et al. (2018), a synthetic model was generated for evaluating the optimal depth to emplace a point which is equivalent to that of a line electrode (Figure 4.5).



 Cylinder representing a line electrode.  
 Point within cylinder used as a point source for a forward model.

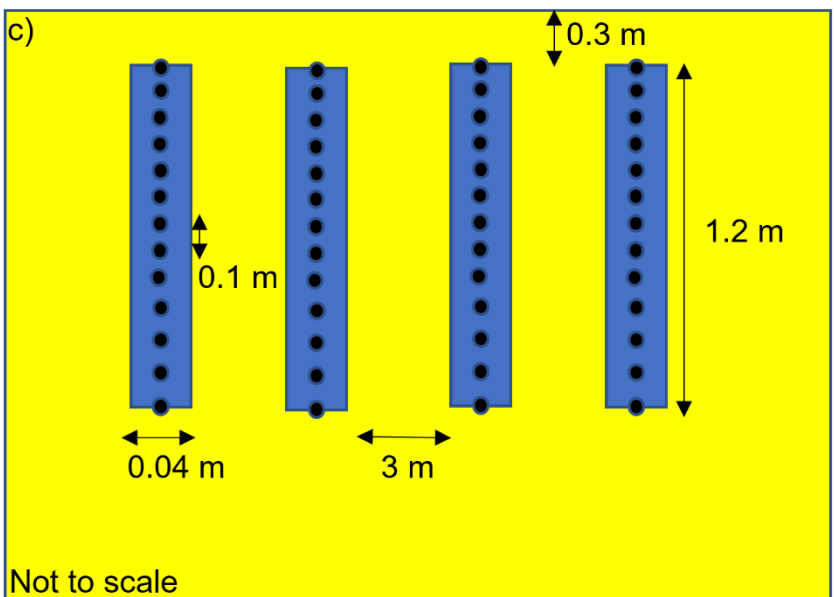
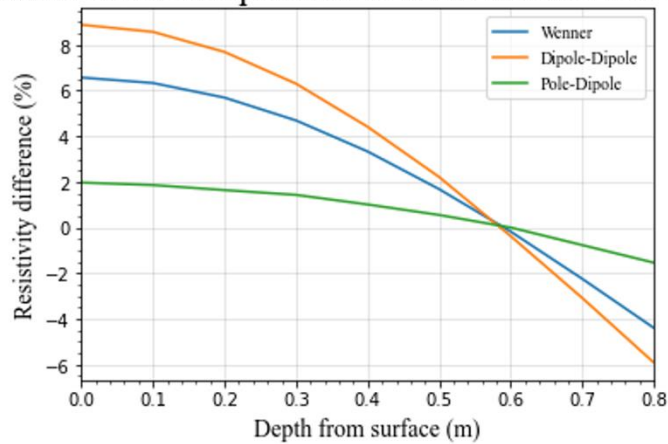


**Figure 4.5:** Electrode layouts for determining the most appropriate depth for a point source. a) Aerial view of a surface array. b) Cross section of a surface array. c) Cross section of a buried array.

Modelling for the optimal position of a point source used four electrodes for the embankment slope and crest, replicating their respective lengths, widths, burial depth and spacing. Electrodes represented as highly conductive cylinders within the mesh, were compared with the point electrode approximation at increments of 0.1 m depth (Figure 4.5). For the initial model, the cylinder was modelled as a hyper-conductive region at  $0.0001 \Omega\text{m}$ , within a  $100 \Omega\text{m}$  background. A forward model was then run to calculate the apparent resistivity using the uppermost points emplaced in the cylinder for the model. The models were then run with a homogeneous resistivity of  $100 \Omega\text{m}$  across the model, with the point electrodes' depths increased by 0.1 m within the cylinder for each subsequent forward model. The resulting apparent resistivities were then compared between the models for the homogeneous models and the models with a hyper-conductive cylinder for each forward model (Figure 4.5), to determine the depth at which apparent resistivities are equal (Figure 4.6). This is inferred to be the point at which a point source for an electrode is valid in comparison with a line source (Rucker & Gunther, 2011; Verdet et al., 2018). Wenner, dipole-dipole and pole-dipole measurements were used to replicate the measurement scheme used at Mactaquac Dam, in order to determine the optimal position for a point source along an electrode for each array type.

- a) Identification of the optimum depth for a point source where apparent resistivities from a point electrode is equivalent to a line electrode for a surface array



- b) Identification of the optimum depth for a point source where apparent resistivities from a point electrode is equivalent to a line electrode for a buried array

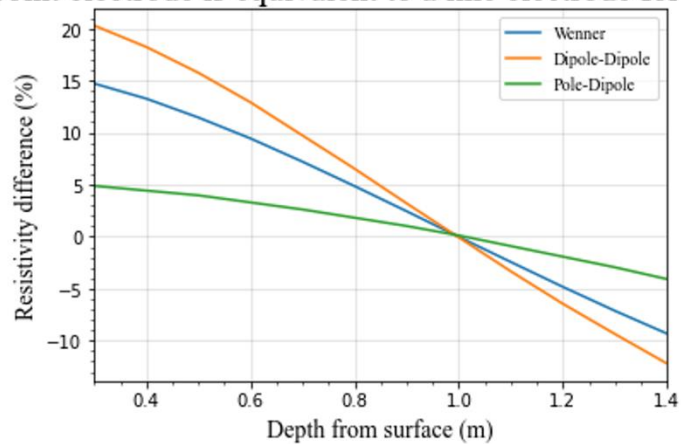


**Figure 4.6:** Differences between apparent resistivities calculated for point electrodes in a homogeneous half-space and those calculated assuming the electrodes were hyper-conductive cylinders for a) a surface electrode array and b) a buried electrode array at Mactaquac Dam.

From the resultant simulations (Figure 4.6) it was determined that a point source was valid at 61% of the electrode length for the electrodes on the slope and 66% of the electrode length for the electrodes on the crest. Differences in value are attributed primarily to the fact that the tops of the crest electrodes were buried 0.3 m below surface. This is similar to what has been reported in previous studies, where similar models produced valid assumed point sources at 60% (Rucker & Gunther, 2011) and 73% of the electrode length (Verdet et al., 2018). Therefore, as the coordinates provided for each electrode represented the top of the electrode, these points were modified to the point on the electrode where a point source would be valid for the main synthetic modelling problem. Alongside this, the point sources for electrodes inserted into the slope had to be rotated by  $53.8^\circ$  in accordance with the approximately  $36.2^\circ$  slope angle (Figure 4.7), as they were inserted orthogonally to the slope

and the modelling for the optimal electrode point depth involved a flat topography for simplicity.

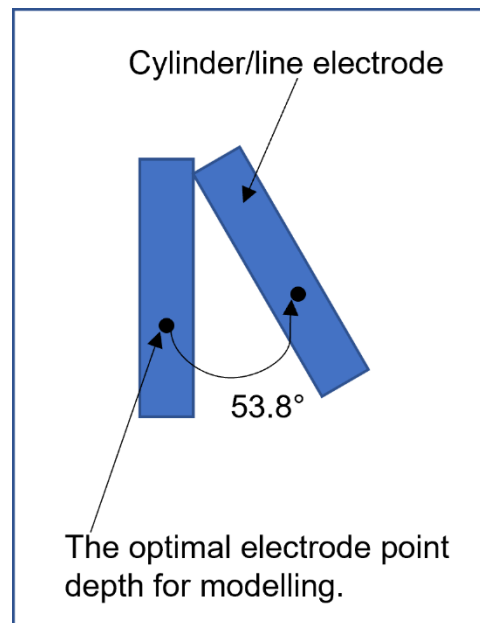


**Figure 4.7:** Rotation of the optimal electrode point depth from the flat topography of the model to the correct location along the Mactaquac Dam slope, which was approximately 36.2°.

After determining the appropriate effective point electrode point depth, the models could then be run after assigning appropriate resistivities for each modelling scenario to be run. Then, a forward model was used for each scenario, using the ERT code R3t (Binley & Slater, 2020). 2% random (Gaussian) noise was added to the apparent resistivities produced for each forward model. The data were then inverted in 3D, using R3t, incorporating the dam geometry to simulate an inversion with the structural facets present at Mactaquac Dam, to determine whether induction of artefacts by these features is likely or a realistic resistivity distribution is achieved. A smoothness-constrained (i.e. L2 norm) regularisation was used for each inversion.

To simulate the effect of a concrete wingwall on an inversion, several models were run using different assigned concrete resistivity values for comparisons of the magnitude of any effects induced by the concrete. Borehole logging measurements in the concrete abutment adjacent to the core have shown resistivities varying spatially from ~10 – 90  $\Omega\text{m}$ , with most measurements in the 45 – 75  $\Omega\text{m}$  range (pers. comm., K.E. Butler). In addition, the resistivity is expected to vary seasonally with the concrete's temperature and with the resistivity of



water from the headpond moving through it. Therefore, the concrete resistivity was changed by 3  $\Omega\text{m}$ , ranging from 45 to 75  $\Omega\text{m}$ , between models, generating 11 models in total. Further models were run with concrete resistivities of 10, 250, 500 and 1000  $\Omega\text{m}$  (Diab et al., 2011; Oleiwi et al., 2018) for comparisons with cases representing other dams where the concrete resistivity is higher than that at Mactaquac Dam, due to factors such as lack of alkali-aggregate reactions (Chopperla & Ideker, 2022), varied salinity and rebar concentration.

The effect of the headpond on ERT data was evaluated considering changes in water resistivity of 50 – 250  $\Omega\text{m}$ , comparable to those observed within an annual cycle, and considering a range of observed river (headpond) water levels. To investigate the former, difference inversions were undertaken using 50  $\Omega\text{m}$  as a reference model, with increments of 50  $\Omega\text{m}$  in the headpond for subsequent models. The wet rockfill resistivity was also modelled to vary proportionately with the headpond resistivity, employing a formation factor of 5.

When monitoring dams for their serviceability it is important that any potential seepage can be detected by the techniques used for monitoring. As the core represents a low permeability region for water flow, it is likely that water content within the core will have a reduced input from the headpond. Hence, the resistivity changes from the headpond to an intact core would vary gradually, while for a seepage zone in the core, the headpond water would advect more rapidly into the zone and resistivity changes in the core would have a shorter time lag from the headpond. Concentrated seepage through part of the core can decrease its resistivity as a consequence of bringing in headpond water that is warmer or has higher total dissolved solid (TDS) content than the water currently saturating the core. Additionally, for sufficiently high seepage rates, internal erosion of fine particles could decrease the resistivity if the additional porosity is filled by water that is less resistive than the fines. Alternatively, resistivity would be expected to increase if water entering from the headpond was colder, or had lower TDS, or if the fines (e.g. clay particles) removed by internal erosion were more conductive than the water.

Considering one of the scenarios outlined above, a 5 m vertical span region of increased seepage was used to determine whether the inversion can identify a region of anomalous resistivity in the core. In this scenario, it is envisaged that this zone has been degraded (i.e. by internal erosion) and represents a concentrated seepage (or 'leakage') zone with a higher moisture content. To account for this, the concentrated seepage zone within the core was

modelled at 25  $\Omega\text{m}$  to provide a distinct difference from the 50  $\Omega\text{m}$  core where no excess seepage zone was present. A difference inversion was then undertaken using a homogeneous, 50  $\Omega\text{m}$  core, for the reference model. The seepage zone was developed for different models at different depths (5 and 10 m below surface) to test the ability of the inversion to resolve such a seepage zone (Figure 4.8) considering sensitivity reductions with depth.

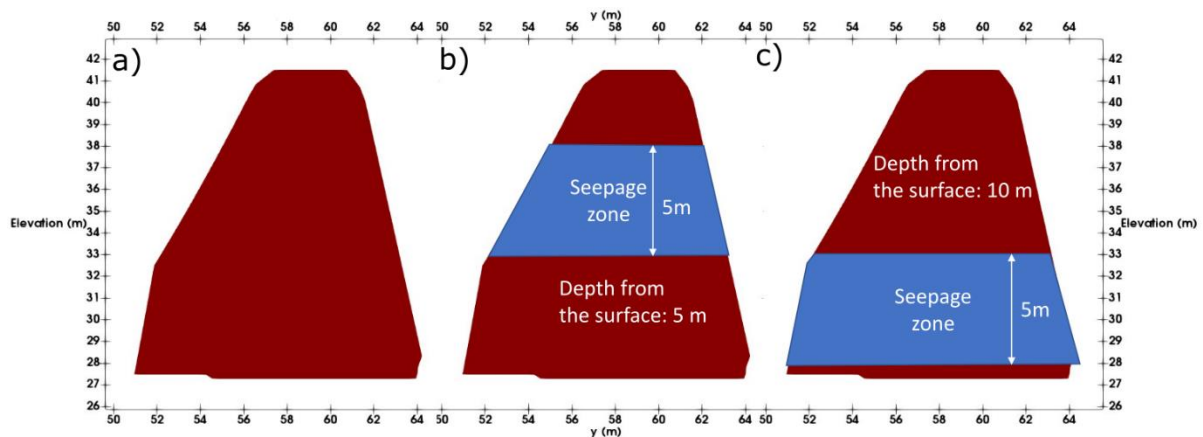


**Figure 4.8:** A cross section of the dam core beneath L1, showing a) a homogeneous core as used for most models, b) a shallow seepage zone and c) a deep seepage zone. Note that the crest of the dam lies 1.5 m above the top of the core.

The resistivities assigned for each modelling scenario are given in Table 4.1 and the layout is given in Figure 4.4.

**Table 4.1:** Resistivities assigned for each region in the model for each scenario the synthetic models were applied for.

Scenario	Concrete resistivity ( $\Omega\text{m}$ )	Headpond resistivity ( $\Omega\text{m}$ )	Core resistivity ( $\Omega\text{m}$ )	Wet rockfill resistivity ( $\Omega\text{m}$ )	Dry rockfill resistivity ( $\Omega\text{m}$ )	Seepage zone resistivity ( $\Omega\text{m}$ )
Modelling the effects of concrete.	10/45/48/51/ 54/57/60/63/ 66/69/72/75/ 250/500/1000	100	50	500	2000	-
Modelling the effects of the headpond.	60	50/100/150 /200/250	50	250/500/ 750/1000/ 1250	2000	-
Modelling the effects of a seepage zone.	60	100	50	500	2000	25/75

Further 2D inversions along L1 were completed for comparisons between 2D and 3D modelling to examine whether 3D modelling can present a more realistic image of the subsurface than 2D modelling. It has been suggested that 3D modelling may be able to present a representation with fewer artefacts, and therefore of higher reliability for interpretation (Ball et al., 2022). The 2D inversions utilised the same array types and measurement specifications as the 3D survey, but with only electrodes used in L1 (plus the remote current electrode) and were inverted with R3t for a 2D survey, because of its ability to incorporate off-centre features into the model, which may induce a 3D effect.

## 4.3.2 Results

### 4.3.2.1 Effect of the concrete wingwall on resistivity imaging

The inversions for assessing the impact of the concrete wingwall on ERT are shown in Figure 4.9, where the concrete resistivity was set to 60  $\Omega\text{m}$  in this example. The image is shown as a 2D slice from the true model.

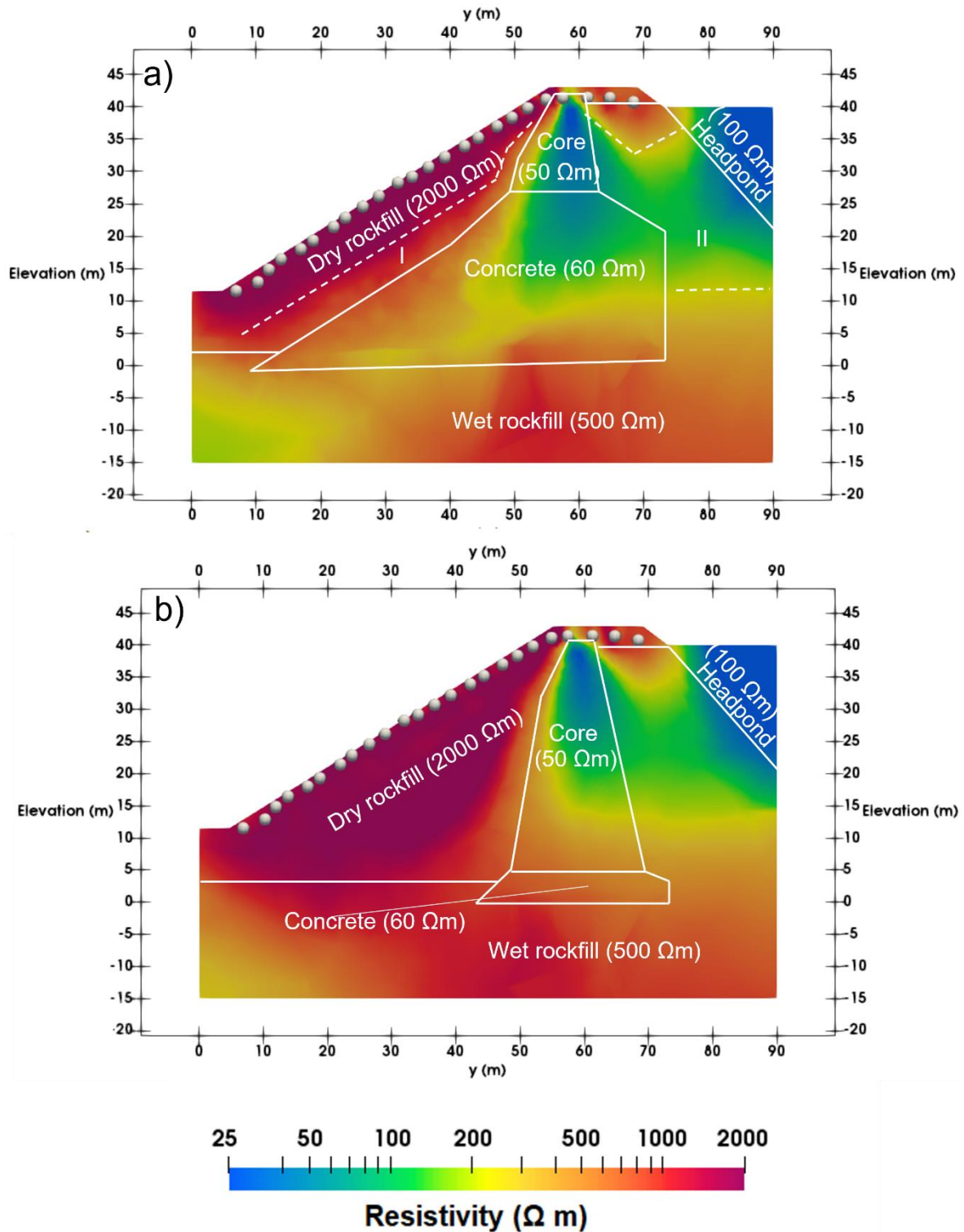


**Figure 4.9:** 2D slices of the 3D forward model and inversion of Mactaquac Dam with the concrete wingwall at 60  $\Omega m$ , where the slice is taken from a) L1 inversion, including zone I and zone II, where zone I is a feature of lower resistivity above the concrete-dry rockfill boundary and zone II is a feature of lower resistivity between core and headpond. b) L3 inversion. Overlays of the true model sections and resistivities are shown in white.

Figure 4.9 shows examples of inversions from the Mactaquac Dam synthetic data, when the concrete wingwall was modelled at 60  $\Omega\text{m}$ , for different lines along the survey. The values for the other regions in the dam are given in Table 4.1. Figure 4.9a shows a vertical slice through L1 - the line of electrodes closest to the concrete wingwall. There is a clear region of low resistivity in the core and shallow concrete below the dam crest, but no clear distinction between those two regions as a consequence of their similar resistivities (50 and 60  $\Omega\text{m}$  respectively).

Underneath L1, the concrete downslope from the crest is more resistive than modelled. However, these resistivity values from the inversion are 1000  $\Omega\text{m}$  lower than the 2000  $\Omega\text{m}$  at which the dry rockfill was assigned in the forward model, and reductions in resistivity within the rockfill are present above the concrete-core boundary. The concrete resistivities are not the values assigned for the forward model because the sensitivities are lower than in the overlying rockfill, and smoothing constraints enable the high resistivities from the rockfill to influence the resistivity values within the concrete. There is an associated reduction in resistivity in the approximately 5 m span of rockfill immediately above the concrete wingwall, as indicated in Figure 4.9, due to the presence of the concrete wingwall. This is likely to guide interpretation, where the reduced resistivity might be misinterpreted as a region of wetter ground, where seepage might be present. This shows that, in an inversion, resistivities will likely be reduced in a resistive layer adjacent to a conductive one and resistivities increased in a conductive layer adjacent to a resistive layer.

By way of contrast, on L3 (Figure 4.9b), which is 10 m farther away from the concrete wingwall on surface, the dry rockfill resistivity remains high to much greater depth, reflecting a lack of influence from the more distant concrete. The resistivities present in the dry rockfill adjacent to the core are reduced, however, as it the case on L1. For each inversion the low resistivity associated with the core appears slightly off-centre - shifted upgradient towards the lower resistivity wet rockfill region.

The resistivities of  $\sim 25\text{-}50$   $\Omega\text{m}$  recovered for the headpond region, for all three lines in Figure 4.9, are lower than the value of 100  $\Omega\text{m}$  that was assigned to it. This is interpreted as influence from the core and concrete structure which intersects with the headpond in close proximity to L1 and L3. The wet rockfill upgradient of the core is also imaged with resistivities significantly lower than the 500  $\Omega\text{m}$  assigned to it, as outlined in Figure 4.9d (region II). This

is likely due to the lower sensitivities in the margin of the survey, adjacent to regions of higher sensitivity in the less resistive core and concrete, which is likely influencing resistivities recovered in the wet rockfill region.

All of these features show that an inversion at Mactaquac dam, unconstrained by any prior information apart from the topography, will have inherent difficulty in representing a complex subsurface due to multiple factors: (i) the presence of the adjacent electrically conductive concrete structure, which dips below the survey area; (ii) the similarity between resistivities of the core and the concrete; and (iii) the effects of model smoothing constraints (L2 norm regularization in this case), particularly in regions of low sensitivity such as the headpond and wet rockfill upgradient of the core.

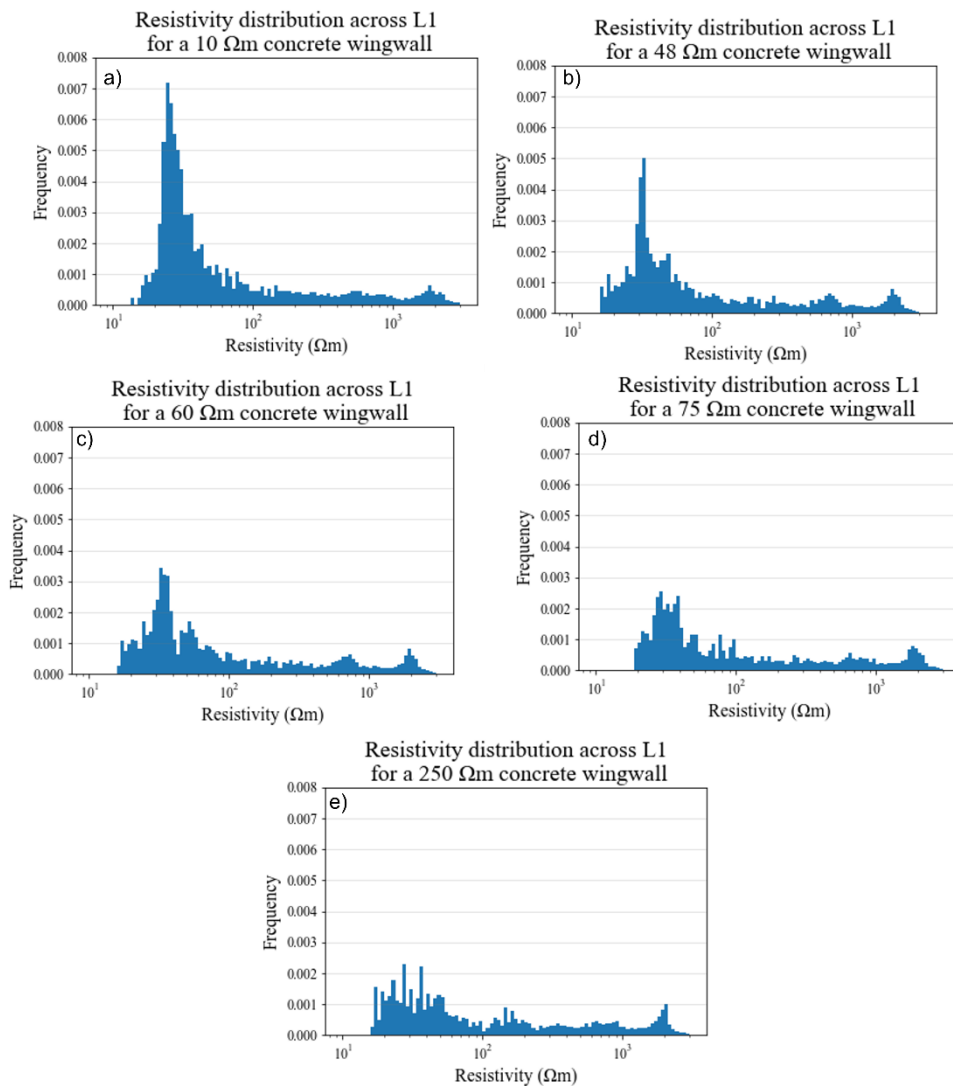


**Figure 4.10:** Histograms showing the resistivity frequency across the ERT survey area to a depth of 40 m below the surface for a concrete wingwall modelled at a) 10 Ωm b) 48 Ω c) 60 Ω d) 75 Ω and e) 250 Ω, while the core, rockfill and headpond are the same resistivity for each model.

The impact of changing concrete resistivity on the results is summarised in Figure 4.10 in the form of histograms showing resistivities distributed across model cells underneath L1, where variation from the concrete was expected to be the strongest. These were achieved through filtering by sensitivity, where sensitivities less than 0.001 were excluded from the results, due to an assumption that they would be less affected by the electrical current. It should be noted that with varying element volumes across depth there will be a bias towards the uppermost regions of the mesh. Therefore, any interpretation is based on the trend in resistivity change between models, and not the magnitude. When the concrete wingwall is modelled at low (i.e. less than 100  $\Omega\text{m}$ ) resistivities, as at Mactaquac Dam, there is a large frequency of low resistivities. A resistivity peak is visible in the histograms due to a high frequency of low resistivities in the core and concrete regions. For the 48  $\Omega\text{m}$  concrete model there is a peak in resistivities at approximately 30  $\Omega\text{m}$ , with a normalised frequency of 0.008 while for the 60  $\Omega\text{m}$  concrete model the peak in resistivity has a normalised frequency of 0.007. For a 75  $\Omega\text{m}$  model the peak in resistivity has a normalised frequency of 0.005 and the 250  $\Omega\text{m}$  model has no meaningful peak in resistivity. There are high concentrations of resistivities that are lower than modelled, which is likely a compensatory effect from the concrete adjacent to the area. For a 10  $\Omega\text{m}$  model there is no significant difference between the resistivity distribution from the 45  $\Omega\text{m}$  model except that the peak in resistivity distribution is of a larger magnitude. This indicates that the low resistivity in the core-concrete region is likely to be larger for lower concrete resistivities modelled. However, for concrete resistivities higher than the expected concrete resistivity at Mactaquac it may be easier to differentiate between core and concrete given an appropriate colour scale.

There was no identifiable trend observed for the higher resistivities (approximately 80  $\Omega\text{m}$  and above) in the histograms for all models. Similar frequencies in resistivity were present across models, with any variation being indiscernable from noise.

#### *4.3.2.2 Effect of headpond resistivity changes on resistivity imaging*

The synthetic modelling also considered how changing the headpond resistivity affected the inversion results. The modelling examined at how a headpond resistivity change from a 50  $\Omega\text{m}$  summer baseline (Figure 4.11a) to a 250  $\Omega\text{m}$  spring maximum, with 50  $\Omega\text{m}$  increments, affected the ERT inversion. The wet rockfill was also assumed to vary, following a linear



relationship between fluid and bulk resistivity (a formation factor of 5 was assumed). The reference model for a difference inversion to assess changes with headpond resistivity variation is shown in Figure 4.11a. The resultant difference inversions, for the cases where the headpond is 100 and 200  $\Omega\text{m}$ , respectively, are shown in Figure 4.11b and 4.11c. The difference inversion was used to show how seasonal variations in headpond resistivity could potentially lead to variability within the resistivity, by means of a 3D effect, through such temporal variation.

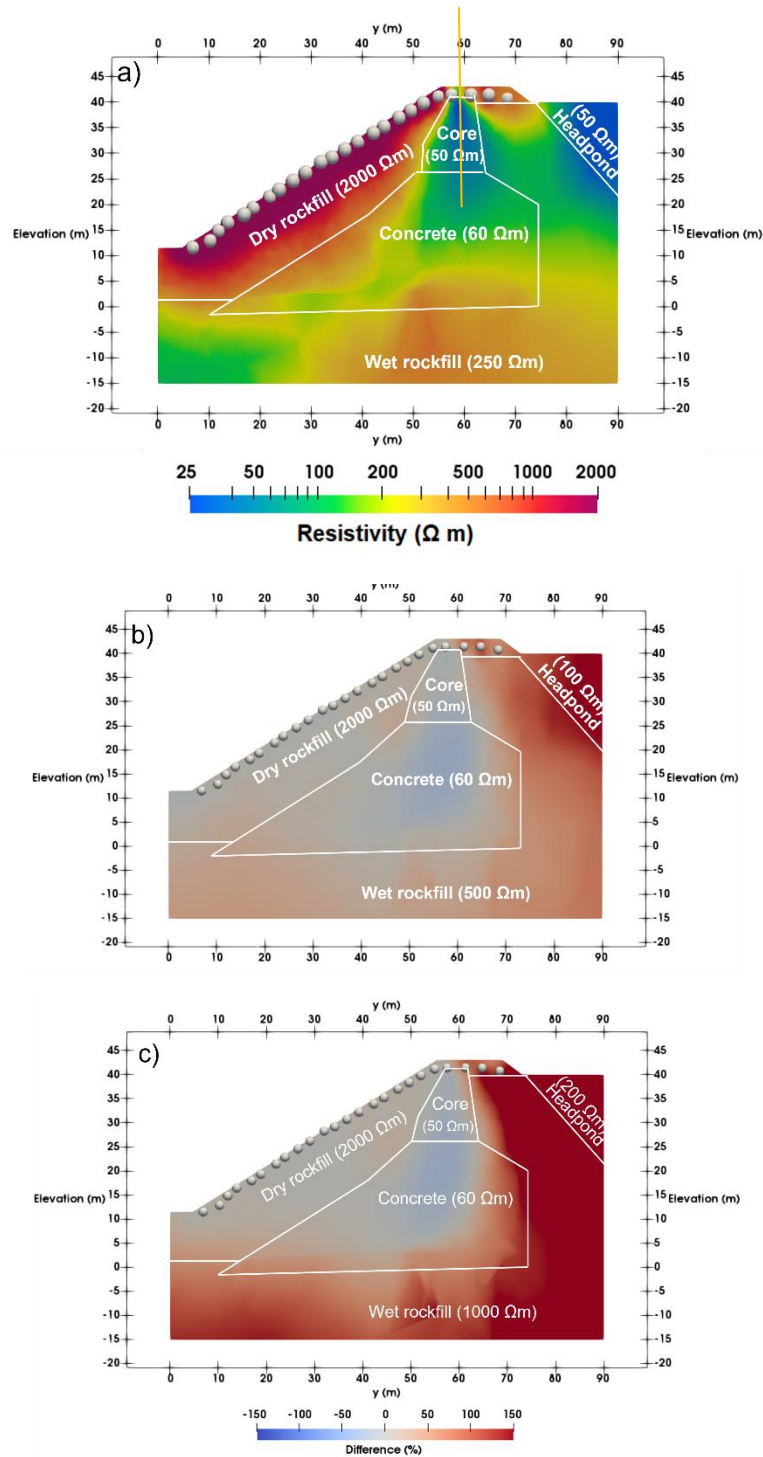


**Figure 4.11:** Difference inversions from Mactaquac Dam taken from a reference model where the headpond was 50  $\Omega\text{m}$  and the wet rockfill was 200  $\Omega\text{m}$ . a) The reference model used in the difference inversion. The difference inversions used a headpond and wet rockfill resistivity of b) 100 and 500  $\Omega\text{m}$  and c) 200 and 1000  $\Omega\text{m}$ . The core was modelled at 50  $\Omega\text{m}$ , the concrete 60  $\Omega\text{m}$  and dry rockfill 2000  $\Omega\text{m}$  for each model. The values assigned to each region in the forward model is shown in brackets. An orange line has been added to a) to show the section used in Figure 4.13.

The inversions in Figure 4.11 show a clear increase in resistivity towards the headpond and area of wet rockfill close to the river, as expected. There is also an increase in resistivity

towards the upstream boundary of the concrete, especially for a 200  $\Omega\text{m}$  headpond, which may be misinterpreted as a feature resulting from a decrease in water content, even though these inversions have assumed no change in resistivity in these regions. A region of decreased resistivity is also observed in the core and concrete sections. This is likely to be a result of compensation in the inversion from the adjacent resistivity increase in the headpond and wet rockfill. This could lead to false interpretation of increased moisture content in this region, and is likely to cause a bigger source for misinterpretation than the noted increase in resistivities to the margin, due to it covering a larger area in this region.

To quantify the resistivity variation within the core and concrete with a change in headpond resistivity, histograms have been plotted of the resistivity distribution in this area for headpond resistivities of 50, 100 and 200  $\Omega\text{m}$  (Figure 4.12).

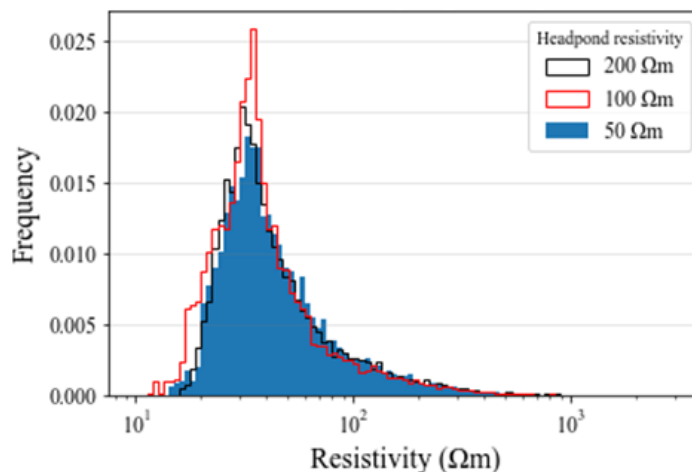


**Figure 4.12:** Histogram showing the resistivity frequency across the core and underlying concrete to a depth of 40 m below the surface for a headpond at 50  $\Omega\text{m}$  100  $\Omega\text{m}$  and 200  $\Omega\text{m}$ .

Histograms showing the resistivities distributed across the model cells within the core and concrete (Figure 4.12) show the range of resistivities observed within the volume of the core and concrete to a depth of  $\sim 20\text{m}$  below surface, based on sensitivity value, as before. This was used to explore the effect of the compensation in the inversion with an increase in headpond and wet rockfill resistivity. As can be seen, there is an increased frequency of resistivity, of around 30-50  $\Omega\text{m}$ , for an increased headpond and wet rockfill resistivity. The approximate normalised frequency for each headpond and wet rockfill resistivity is given in Table 4.2. This shows that with increased headpond resistivity an anomalously conductive artefact is expected in the core and concrete, which could be incorrectly attributed to a seepage-induced change in the core or concrete.

**Table 4.2:** The (normalised) frequency at which 30  $\Omega\text{m}$  occurs in each synthetic model for a change in headpond resistivity.

Headpond/Wet rockfill resistivity	Approximate normalised frequency of resistivities in the model at 30 $\Omega\text{m}$ .
50/250 $\Omega\text{m}$	0.017
100/500 $\Omega\text{m}$	0.021
200/1000 $\Omega\text{m}$	0.025

To further quantify the nature of the low resistivity artefact underneath the core and concrete, attributed to a compensatory effect from higher headpond and wet rockfill resistivities, a representation of resistivity variation with depth has been generated for the associated region (Figure 4.13). A 2D line has also been shown in Figure 4.1a for the location for which these resistivities represent.

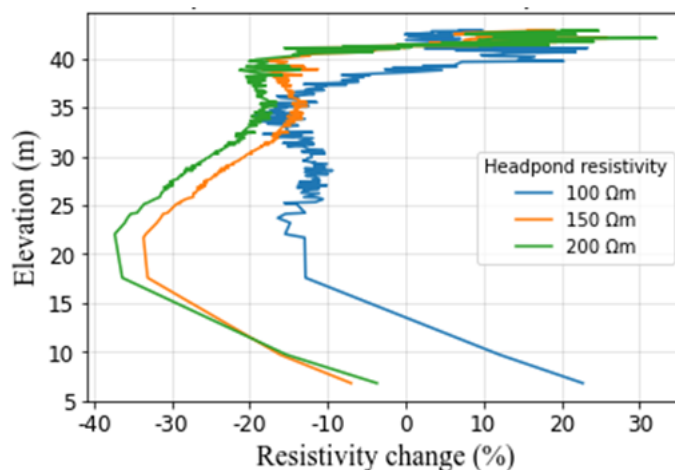


**Figure 4.13:** Variation in the change in resistivity, compared against the 50  $\Omega\text{m}$  headpond reference model, for subsequent time-lapse difference inversions at 100, 150 and 200  $\Omega\text{m}$ .

These results show that for the upper 3m there is an associated increase in resistivity of 0 – 30% across models with different headpond resistivities, assumed to be a 3D effect from the increase in headpond resistivity between models. However, from approximately 40 to 20 m elevation there is a step decline in resistivity up to a 40% decrease for a 200  $\Omega\text{m}$  headpond and 15-20% for a 100  $\Omega\text{m}$  headpond. Below 20 m there is a further increase in resistivity, but it must be noted that sensitivity here is low, so results are likely to be less reliable. The resistivity decrease at depth is more pronounced with a higher resistivity headpond, indicating that the inversion undergoes a greater degree of compensation with a higher

resistivity disparity between headpond and core/concrete. However, the 150  $\Omega\text{m}$  headpond model is more similar to a 200  $\Omega\text{m}$  headpond than a 100  $\Omega\text{m}$  headpond, indicating that the relationship is not linear and more extreme resistivity variations will not necessarily have a more extreme effect.

#### *4.3.2.3 Incorporation of a seepage zone into the core*

A 5 m vertical span seepage zone, with lower resistivity, was incorporated into the core at two separate depths to determine the ability for ERT to detect changes in the inversion linked to this zone of elevated seepage. The resistivity of the seepage zone was set to 25  $\Omega\text{m}$  (half the value assigned to the rest of the core), representing lower resistivity from a higher water content, due to increased moisture content, and with a potentially higher concentration of TDS.

The overall trend in resistivity distribution for both a shallow and deep seepage zone did not differ, visually, from Figure 4.9a, where a homogeneous 50  $\Omega\text{m}$  core resistivity was modelled. However, difference inversions did reveal changes in the expected regions as shown in Figure 4.14 for sections below Line 3.

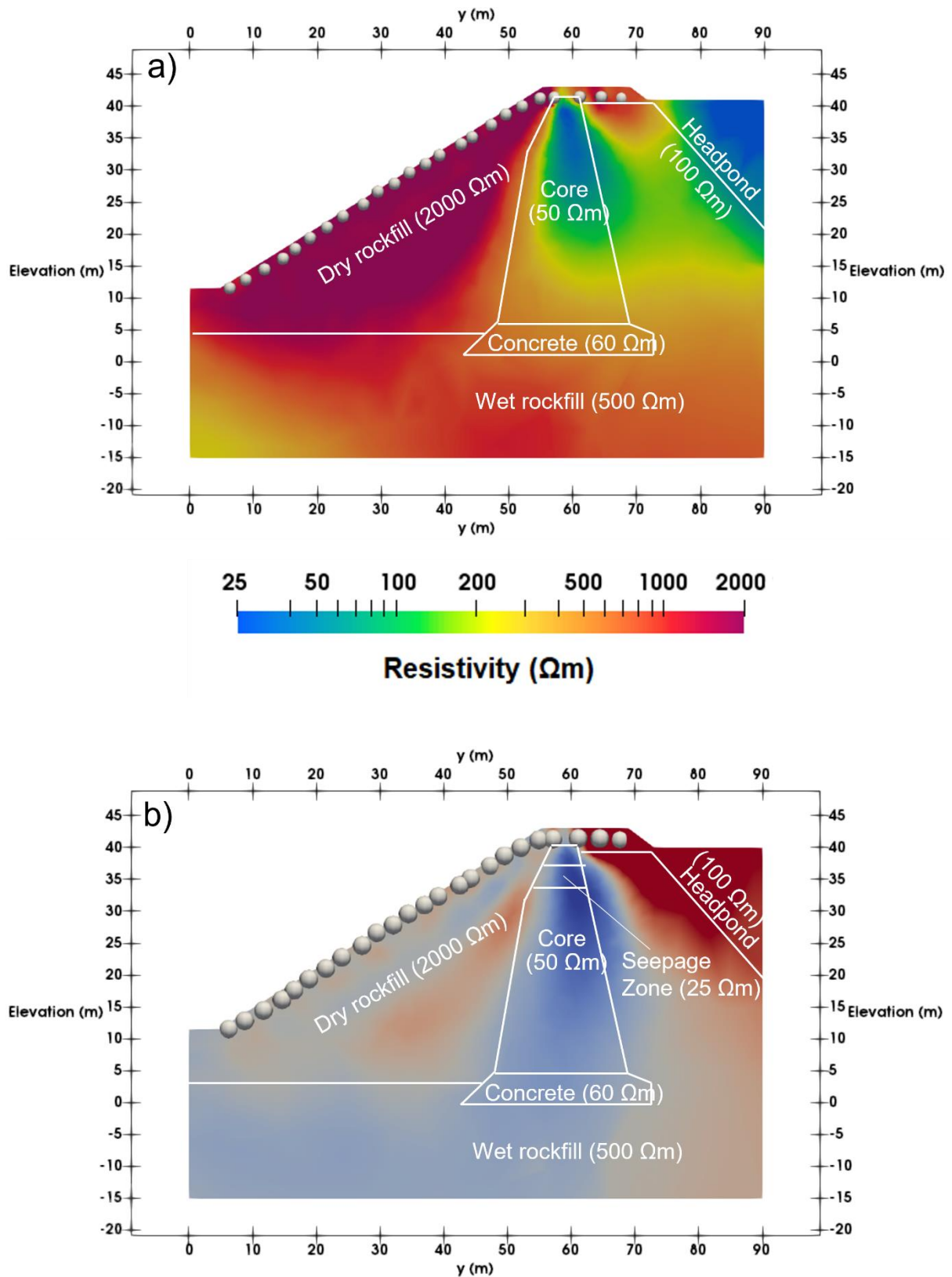


**Figure 4.14:** Inversions from underneath L3 for a) The reference model assuming an intact core, b) an inversion of a seepage zone at shallow depth and c) an inversion of a seepage zone at depth.

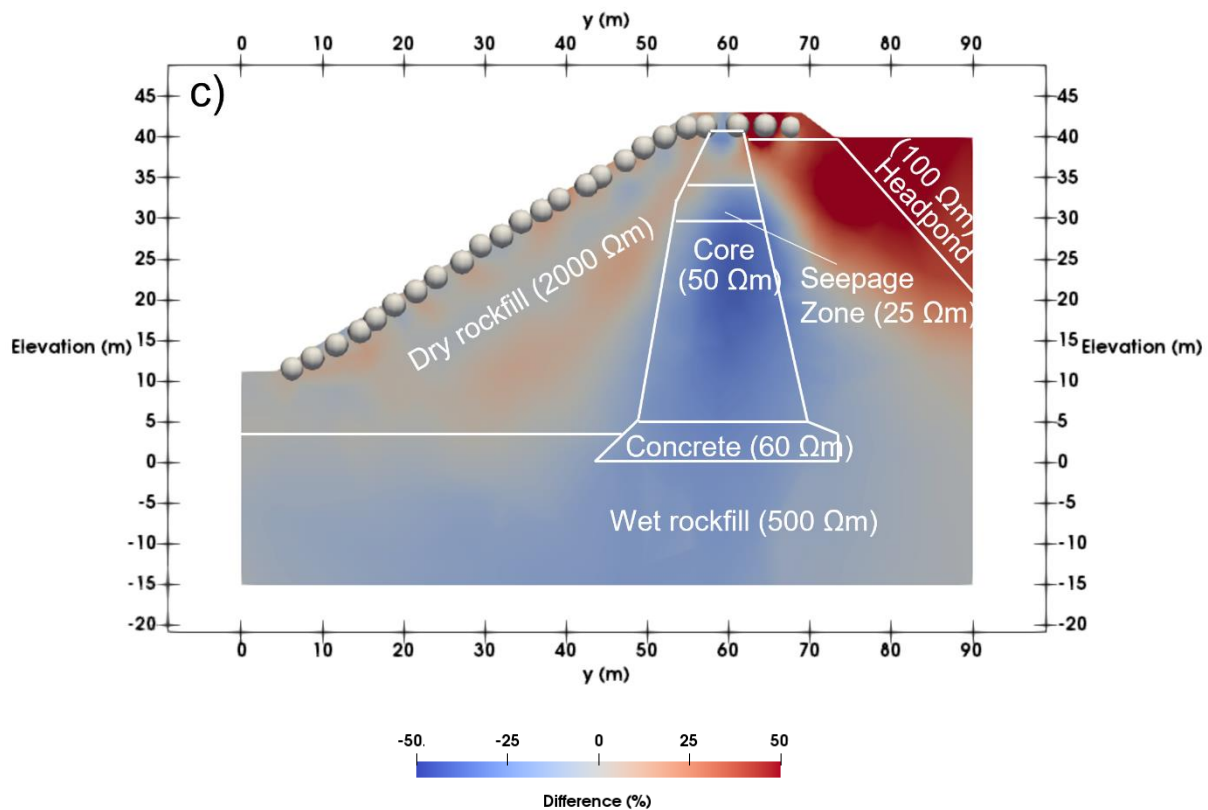


**Figure 4.14** continued.

In the shallow seepage zone (Figure 4.14b) there was a decrease in resistivity by 25 -50%, whereas, for the deeper seepage zone (Figure 4.14c) there is no significant decline in resistivity in the seepage zone. For both modelling scenarios, areas of increased resistivity exist in the dry and wet rockfill and extend into the seepage zone for a deep zone. These are interpreted to be compensatory effects in the inversion. The inability for the inversion to detect a noticeable decrease in resistivity in a deeper seepage zone indicates that, in areas of lower sensitivity, evidence of dam degradation may be missed.

To further examine the ability of the inversion to detect a seepage zone, resistivities have been extracted from the seepage zone across the core for comparison between a homogeneous 50 Ωm core and a seepage zone, and they are illustrated as a histogram in Figure 4.15.

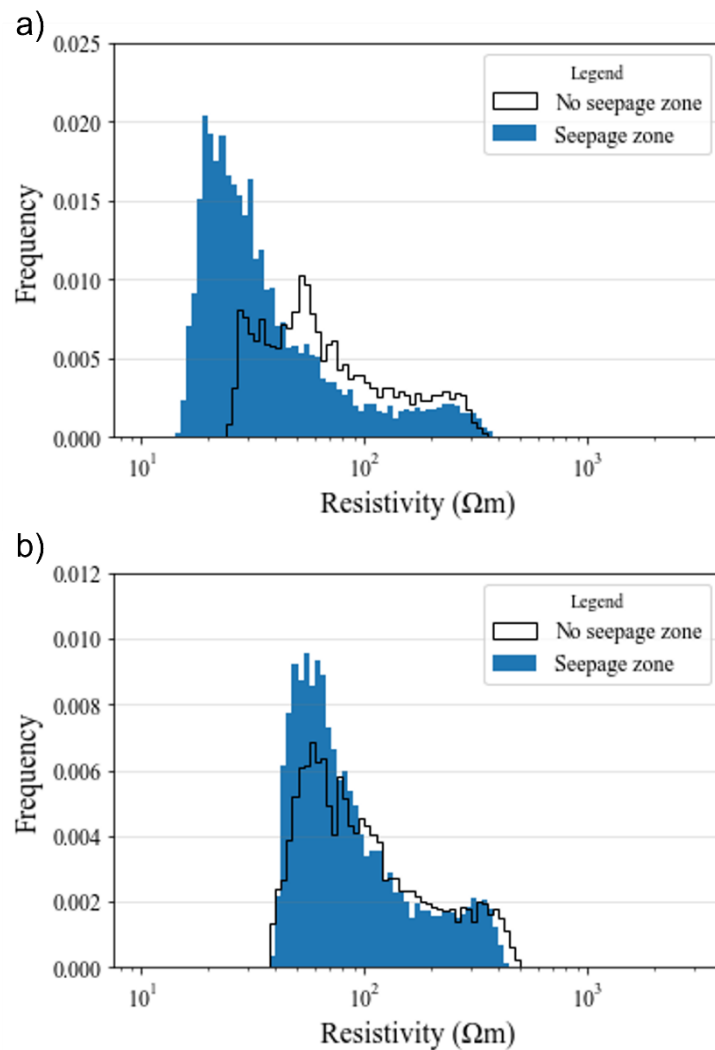


**Figure 4.15:** Histograms showing the resistivity distribution for a seepage zone compared with an intact core for a) a shallow seepage zone and b) a deeper seepage zone.

The resistivities in the histograms for Figure 4.15 were extracted from the seepage zone of the core for both a shallow and deeper seepage zone. As can be seen, there is an evident increase in the proportion of model cells with low resistivities, in the magnitude of 10-30  $\Omega\text{m}$  for the existence of a shallow seepage zone when compared to no seepage zone. Whereas, for a deeper seepage zone, there is a large frequency of model cells with resistivities in the 20-40  $\Omega\text{m}$  range for a model with a seepage zone and no seepage zone. However, for the deeper seepage zone model, there is a more subtle increase in the frequency of resistivities in the model cells between 35 and 80  $\Omega\text{m}$  than with a shallow seepage zone. This indicates that a seepage zone is affecting the resistivities for both models, but is more distinct for a



shallow seepage zone, meaning identification of a seepage zone would be less likely to be made for deeper seepage zones.

#### 4.3.2.4 2D Modelling of L1

2D inversions of L1 (Figure 4.16) were undertaken for comparison with 3D inversion results. The modelling procedure was the same for the 3D model, except it only used electrodes from L1, alongside the pole electrode. This was selected due to it being the most proximal to the concrete wingwall where the greatest resistivity distortions were expected.

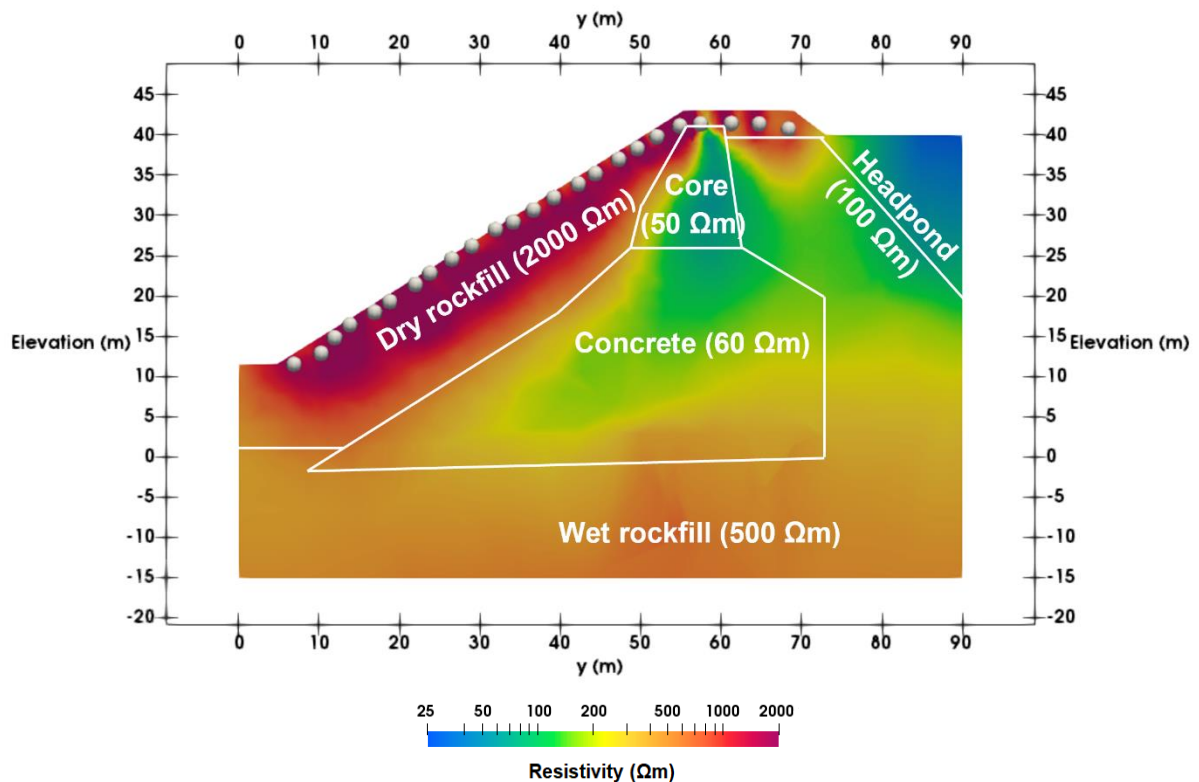


**Figure 4.16:** A 2D inversion underneath L1 at Mactaquac Dam, with the concrete wingwall at 60 Ωm.

The 2D inversion (Figure 4.16) shows a resistivity distribution similar to the 3D model; a region of lower than expected resistivity is present above the concrete-dry rockfill interface, which could be misinterpreted as a water pathway. A higher than expected resistivity is present within the wet rockfill, between core/concrete and the headpond. The core and concrete geometries are observable from the differing resistivities in the inversion. However, the shape of the core region is less defined and is more sinuous in shape. Moreover, the magnitude of

the resistivity in the core is less than that of the 3D model, and the core is more resistive than expected. This is because of the lack of cross-line measurements, which enable greater resolution of the core shape and an assumption that resistivity values remain constant perpendicular to the electrode line, which is not true in a 3D actuality. In contrast, there is a clearer dry rockfill-concrete boundary towards the base of the downstream slope, than in the 3D model. This is likely due to the lack of smoothing and differing resistivities found in L2-5, where the inversion assumes the resistivities present within L1 carry on infinitely in a direction perpendicular to the profile.

## 4.4 Inversion of Mactaquac field data

Prior inversions from Mactaquac Dam undertaken by the University of New Brunswick (Boulay, 2021) were used to compare and understand which artefacts and features identified in synthetic modelling, from the concrete wingwall and headpond, may be of relevance for field data. The data were originally inverted using the 3D ERT software, RES3DINV (Loke, 2022) and the synthetic modelling described above used for comparison to identify where there may be similar features of resistivity within the real data and the synthetic modelling. These features may have been interpreted as seepage from the headpond or an effect of seasonal temperature changes. These comparisons allow the assessment of whether such features could instead be the result of 3D artefacts.

### 4.4.1 *RES3DINV Inversions*

Datasets from June and October 2020 were used for inversion, representing typical summer and autumn conditions (Boulay & Butler, 2021). It should be noted that crest electrodes were not yet emplaced at the time of inversion and, therefore, the images are restricted to the region below the downstream slope of the embankment. An example of the inverted data is shown in Figure 4.17.

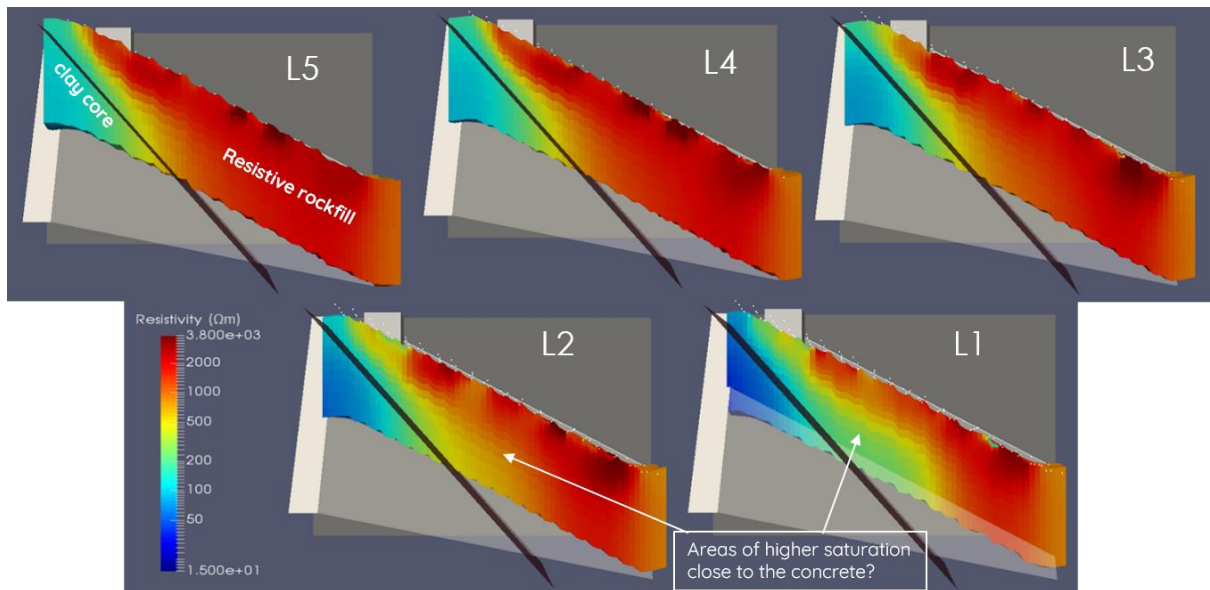


**Figure 4.17:** RES3DINV inversions for Mactaquac Dam showing 2D slices across all the lines. Resistivity images from June 2020, highlighting the decreased resistivities in lines close to the concrete wingwall. These sections extend 19 m below the surface with no vertical exaggeration (Boulay & Butler, 2021).

The inversions show that there is a resistive dry rockfill and underlying lower resistivity core. A reduction of the resistivities has been noted above the core/rockfill boundary. On L1, low resistivities in the deep rockfill stretch downhill, parallel to the concrete wingwall which cuts through the section at about 17 m depth. This was attributed to possible elevated water saturation, resulting from water seeping through the concrete; it was acknowledged that some influence from the adjacent concrete wingwall might be expected but that would fail to explain why the resistivity low does not persist along the whole length of the line which is equidistant from the wingwall. The synthetic modelling presented in Figure 4.9, where resistivities decrease from  $\sim 2000 \Omega\text{m}$  in the shallow rockfill to  $\sim 500 \Omega\text{m}$  at depth (similar to the drop from  $\sim 1500 \Omega\text{m}$  to  $\sim 300 \Omega\text{m}$  seen in the real data inversions) lends credence to the possibility of this being a 3D effect from the concrete. While the modelling does not explain all aspects of the deep rockfill anomaly at Mactaquac (i.e., the anomaly's disappearance below the lowermost third of the slope, nor its seasonal variability), it does illustrate the importance of taking such 3D effects into account when interpreting inversion models from regions of an embankment adjacent to an abutment.

These interpretations do not discount that the resistivity patterns observed may be real. From the synthetic numerical modelling there is no deterministic means of identifying whether the resistivity variations are a result of the concrete or seepage effects. However, the similarity in output shows that an effect from the concrete cannot be discounted, so any interpretation

of seepage cannot rely on a standalone ERT inversion and requires support from time-lapse monitoring of the site, which can resolve ambiguity (Boulay & Butler, 2021) when relating dynamic changes to other aspects, such as rainfall and petrophysical relationships (Chambers et al., 2014). Alongside this, the geotechnical, self-potential and DTS data collected from site are needed to form such reliable interpretations within ERT data (Yun et al., 2022).

## 4.5 Discussion

### *4.5.1 The Effect of the Concrete Abutment*

The synthetic modelling explored the capabilities of the inversion to accurately represent the resistivity distribution of the subsurface in the structurally complex Mactaquac dam setting. The underlying question is: do we need to account for the complexity of the geoelectrical structure of the dam in ERT modelling to provide reliable estimates of resistivity variation in the dam? The presence of several facets within the dam may induce 3D effects, leading to incorrect interpretation of ERT inversions. Previous inversions of field data had indicated the possibility of the concrete and headpond creating distortions within the inversion. Therefore, the synthetic modelling focussed on testing the impact of the concrete and headpond on the data. Investigation of the effects of the concrete structure was done using several models where concrete resistivity was changed, both for values typical of Mactaquac and for a broader range of dam conditions. Modelling the effects of changing headpond resistivity and water level was carried out, along with the exploration of the sensitivity of ERT measurements to synthetic seepage zones within the dam core. The synthetic modelling at Mactaquac accounted for concrete resistivities akin to that expected at the dam, as well as further which are not expected for Mactaquac Dam to compare with a broader range of sites where concrete resistivities may be different. Such instances of differing concrete resistivity may represent a concrete body fully saturated with highly saline water and/or concrete with high rebar concentrations. These more resistive models may represent a less saturated, more impermeable concrete and/or a concrete which has not undergone AAR which tend to lower the concrete resistivity.

Synthetic modelling of the presence of concrete revealed noticeable changes within the inversion. There was a noticeable region of lowered resistivity above the concrete-rockfill

boundary, which was interpreted as an effect from the concrete, given that inversion lines further away from the concrete had a more resistive subsurface. Therefore, it can be said that the presence of concrete will distort the resistivities within an inversion where it is proximal to electrode lines. At Mactaquac Dam, there were noticeably lower resistivities, of approximately 1000  $\Omega\text{m}$ , around this region, where seepage from the concrete had been interpreted, giving the potential for misinterpretation. This approximately 1000  $\Omega\text{m}$  region extends into the concrete, which should be less resistive, meaning accurate interpretation of the location of a concrete-dry rockfill boundary is impossible. This is caused by a smoothing effect from the model and large resistivity disparity between layers, which has been shown to affect resistivity, such as in a case study where a low resistivity clay core distorted the resistivities of the layer below (Ball et al., 2022). Coupled with this, a region of lower than anticipated resistivity has been observed in the wet rockfill, adjacent to the core and concrete in all lines, which has been attributed to influence from the core and concrete (where concrete is proximal) in a region of low sensitivity. Such low sensitivity means that the lower resistivities of the core and concrete will influence the resistivities to a greater degree in the wet rockfill region.

It should be stated that the results observed are specific to Mactaquac Dam alone. Other dams will have different subsurface geometries and compositions which will affect the resistivity distribution and how these will distort resistivities across the inversion. However, the factors which have caused a distortion in resistivity at Mactaquac Dam are not unique. While other dams may not have concrete or concrete of the same resistivity, since concrete is highly variable and may have different levels of water saturation, AAR and rebar concentration, the problems with smoothing, sensitivity and resistivity contrasts affecting other layers will still exist. Problems may be lessened in dams when the expected resistivity contrasts will be minimal, but dams are highly heterogeneous structures. Besides concrete, rockfill and a clay-till core, other dams may contain different infill compositions across the dam, a rock abutment, geotechnical membranes, different geologies for dam foundation and water resistivities. All of which are likely to be highly varied and cause potential distortions of resistivity in an inversion. Therefore, when designing ERT arrays on dams it is highly recommended that a thorough desk study is completed prior to survey design, where the survey considers the likely effects from 3D effects and a complex internal structure. Ideally,

the ERT survey should extend into the headpond/reservoir to allow greater sensitivity for edge effects on the dam and to visualise the slope on both sides of the dam.

#### *4.5.2 The Effect of Headpond Resistivity*

Increases in headpond and wet rockfill resistivity induced an expected increase in resistivity within each respective region. This also induced 3D effects within the concrete region, where increased resistivities were noted close to the boundary between these regions and the wet rockfill. However, more pronounced decreases in resistivity in the core-concrete region were present, increasing in magnitude with increasing headpond and wet rockfill resistivity, which could lead to a false interpretation of a wetting core. Therefore, it is imperative that ERT monitoring of dams considers the reservoir resistivity, because changes in resistivity is likely to drive such changes underneath the crest, where focus on seepage will be precedent. This is of high importance for areas with highly variable water resistivities throughout the year, such as at Mactaquac Dam, where snowmelt will drastically alter the resistivity.

Changes in headpond resistivity may therefore influence the resistivity. However, primary changes will be from resistivity changes within water bodies and water level variation is unlikely to cause significant effects when surveys are sufficiently far from the water body. Previous research had indicated that water level does impact the data when ERT surveys are proximal to the water body (Ball et al., 2022), so other surveys would need to potentially account for water level if the electrodes are more proximal to the water body (e.g. if there were electrodes on the headpond side of the crest at Mactaquac Dam).

It must be noted that these models assumed a linear relationship between fluid and bulk resistivity. This is likely to be overly simplistic, where wet rockfill resistivities are likely to be influenced by other factors, such as TDS, which may perturb the linearity of the relationship. Therefore, such effects may be less or more pronounced depending on the seasonality of the survey, since TDS content increases with colder conditions (e.g. an increase in the use of salt for the roads may be transported into the subsurface), and such values from the model cannot be used as a direct comparison to real inversions. However, they do indicate the potential for headpond resistivity to affect the data, given such varied resistivities are expected at Mactaquac Dam and in other sites.

### *4.5.3 Incorporation of a Seepage Zone*

The effect of incorporation of a low resistivity seepage zone of anomalous resistivity was examined, considering two different 'disturbed' zones. Difference inversions indicated a decrease in resistivity within a shallow seepage zone, but it was less distinguishable for a deeper seepage zone. However, when looking at resistivities extracted from within the core, and plotted as histograms, it is evident that there are subtle differences in the distribution of resistivities for both scenarios, though of a lesser magnitude for a deep seepage zone. With the existence of a seepage zone there is an increase in distribution of the lowest resistivities observed, when compared with a model with no seepage zone in the core over the same volume. This indicates that there is a resistivity variation with the seepage zone, which is unlikely to be visible over a colour range which covers the entire spread of resistivities, but one which may be evident with more quantitative analysis. This demonstrates the use of extracting resistivity values from regions of interest for quantitative analysis to help with interpretation of features which may otherwise be missed. It also shows that seepage zones in highly sensitive regions of the inversion may be detectable with structural complexity, but the ability to detect such lessens as sensitivity declines.

A summary Table for the results of the synthetic numerical modelling is given in Table 4.3.

**Table 4.3:** A summary table, outlining the key findings of the modelling aims for Mactaquac Dam.

Model Aim	Outcome
Testing whether the concrete abutment resistivity impacts the ERT.	There was a noticeable reduction in resistivity above the core-dry rockfill boundary attributed to influence from the concrete in the inversion. This might cause misinterpretation as a seepage pathway.
Testing whether headpond resistivity, and changes in headpond resistivity, impacts ERT.	Headpond resistivity induced expected changes in the wet rockfill region. However, a compensatory effect was evident in the core region, where decreased resistivities were noted with increasing headpond resistivity. This may cause misinterpretation of increased water content.
Testing whether a modelled seepage zone within the core can be identified, despite potential 3D effects.	A seepage zone was modelled through the core at two different depths. The seepage zone was not noticeable in an inversion, but quantitative analysis of the resistivity distributions showed a decrease in resistivity associated with the seepage zones, especially for a shallow zone.

#### 4.5.4 Comparison of the Synthetic Numerical Models to Inversions at Mactaquac Dam

Previous research had indicated the potential for 3D surveys to better represent inversions, without 3D effects, than 2D inversions (Ball et al., 2022). The 2D inversions for Mactaquac Dam were able to represent a varied resistivity distribution across the survey in a relatively similar manner as the 3D inversion, where a region of lowered resistivity above the core-dry rockfill boundary was present and there was a lower resistivity core-concrete region. However, the shape of the core is less distinct and magnitude of resistivity lower, due to an



assumption of infinitesimal 2D resistivities. While a 2D inversion can sufficiently represent the subsurface geometry, this indicates that a 3D inversion is preferable, because an accurately represented region of the subsurface (e.g. the core) with a representative resistivity is vital for any interpretation. Less distinct shapes and resistivities are likely to cause misidentification of any seepage zones, an estimated size or shape of the seepage zone and potentially distinctive resistivities associated with the seepage zone.

It must be stated that there are several assumptions made to carry out the synthetic modelling. It has been assumed that each resistivity zone is of homogeneous resistivity, which is unlikely. A concrete wingwall, especially one with AAR is unlikely to be homogenous in terms of its resistivity. It is known, from field observations, that there is a vertical temperature gradient in the concrete, implying that the resistivity will vary with depth. These would cause localised variations in resistivity, but it is believed that the effects of this are likely to be minimal, as the temperature variation will only be 2% per 1°C and temperature variability will decline relatively gradually with depth. Moreover, seasonal variations in temperature are likely to change resistivity through time for each aspect of the subsurface at shallow depth. Alongside this, TDS may infiltrate the subsurface and will affect resistivity, seasonally. Capturing a realistic model which accounts for the dynamism of resistivity changes with temporal variations is therefore difficult. The modelling results, therefore, will not necessarily capture the full range of resistivity variation. However, they represent potential effects which may be evident even with a more dynamic resistivity regime. The subsurface temperature at Mactaquac can fall below 0°C, which means water will be frozen for the winter period. Frozen ground will have different geoelectrical and geotechnical properties than ground saturated with water. The models used were developed under the assumption that the groundwater is a fluid and therefore cannot represent cases where parts of the subsurface are frozen.

#### *4.5.5 Recommendations*

The results of the synthetic modelling at Mactaquac Dam show that it is imperative that ERT surveys in dams of high structural complexity are carefully undertaken. It is highly likely that ERT inversions will be contaminated with artefacts from 3D effects resulting from the local geometric features and a lack of differentiation between regions of similar resistivity, meaning potential misinterpretation of subsurface geometry. This can lead to incorrect

structural interpretation and misinterpretation of subsurface processes. However, previous research with SP and DTS and the use of time-lapse resistivity monitoring validates some of the ERT interpretations (Ringeri et al., 2016; Yun et al., 2022), which adds credibility to the results and are vital, given the ambiguity present from ERT modelling at Mactaquac Dam, as the synthetic modelling has shown.

It is therefore suggested that a priori information of structural features present within a dam, including coordinates of any feature with potentially anomalous resistivity, water levels, water resistivity and other relevant geophysical information, are gathered. Therefore, this can be related to the model, so the correct geometry of the internal structure can be visualised in the model and evidence can exist for potential effects on the data as caused by structural complexity. Alongside this, it is recommended that resistivity values are extracted from the inversion, and plotted graphically, to observe effects over time to potentially identify resistivity changes which may not be observable within an inversion. For example, the effect of adding a seepage zone was not clearly evident in the inverted resistivity image, although a comparison of resistivity histograms from inversion with and without the modelled seepage zone did reveal differences. Using such could allow the interpreter to identify subsurface changes which may not otherwise be observable due to small resistivity contrasts.

## 4.6 Summary

Mactaquac Dam is a hydroelectric dam in New Brunswick, Canada, which has a high degree of structural complexity in the vicinity of the ERT survey area, including a concrete wingwall, headpond, clay-till core and a rockfill. Inversions of real datasets had revealed potential seepage pathways close to the concrete wingwall and resistivity variation close to the headpond. Prior to this study, it had been suggested that 3D effects from the headpond and the presence of concrete could be distorting the resistivities leading to false interpretations. Therefore, a synthetic modelling program was undertaken to test the effects on the inversion from the presence of concretes, over a range of resistivities, the effect of a changing water level, as well as a change in headpond resistivity with the seasons. Finally, a seepage zone of anomalous resistivity was incorporated into the core to test the ability of the inversion to identify zones of anomalous resistivity with such structural complexity present.

It was observed that the presence of concrete affected the resistivities across every synthetic model. At lower concrete resistivities there was a noticeable 3D effect from the concrete on the downstream slope, where resistivities were reduced in the dry rockfill, which may otherwise be recorded as seepage. Also, structural reconstruction of the core-concrete boundary is difficult due to the similar resistivities present. Increases in headpond and wet rockfill resistivities will cause a decrease in resistivity within the core and concrete as a means of an inversion compensation. A seepage zone was evident when comparing changes in the resistivity distribution within the core for a core with a seepage zone and one without. This was true for both modelled seepage zone depths, though it is less obvious for a deeper seepage zone. Therefore, it has been suggested that it is important to analyse the resistivity data quantitatively, and statistically, and not rely on inversion imaging alone for interpretation.

While the model demonstrates the impact of the headpond and concrete abutment, the model has not been able to capture the full complexity of the ground conditions, due to the complexity required for modelling. The temporal and vertical variations in resistivity, due to temperature, will likely have an impact on the nature of 3D effects at the site, but including them in the model, realistically, is challenging.

It has been suggested that for interpreting ERT in such settings it is important to acquire all a priori information possible for interpretation, including coordinates and elevations for structures (i.e. concrete wingwalls) which may cause distortions in resistivity, so that any interpretation can be made with a more comprehensive interpretation. 3D inversions are preferable to 2D inversions, due to their ability to recover more representative resistivities and correct geometry of subsurface features. Future work could look at methodology to reduce such effect for a more reliable interpretation. This research has demonstrated that it is vital to be cautious when interpreting dams and other environments with high structural complexity, and that the geophysical data needs to be supported by geotechnical data, other geophysical data and petrophysical relationships for the best interpretation.

## **5.0 COMPARISON AND ASSESSMENT OF 2D AND 3D INVERSIONS FOR DETERMINING THE MOST APPROPRIATE INVERSION, FROM BARTLEY DAM, BIRMINGHAM, UK.**

### **5.1 Introduction**

Bartley Dam is an earthen embankment dam situated in the south of Birmingham, UK. The internal structure of Bartley dam is heterogeneous, consisting of several elements, including the embankment fill, core, filters, drainage and services. Previous chapters and research have indicated that 3D surveys have the potential to improve the reliability of the inversion; this study will focus on a more quantitative assessment of whether 3D inversions sufficiently represent a more realistic and reliable inversion at a complex dam setting of Bartley Dam, United Kingdom.

Bartley Dam has regularly experienced seepage since construction and has undergone several programmes of grouting to mitigate the problem (Birmingham Water Department, 1931). Despite remedial work, seepage has continued. ERT monitoring has therefore been undertaken to illuminate the internal conditions at Bartley Dam, and temporal variation across seasons. However, the heterogeneous nature of the site may hinder 2D inversions at Bartley Dam (Water, 1931). Therefore, this site has been used to compare and evaluate the performance of 2D and 3D resistivity imaging in the context of a structurally complex dam setting. Time-lapse monitoring enables greater estimation of the impact of 2D versus 3D modelling with temporal variation, where dynamic changes in the subsurface may lead to a distortion of the resultant difference inversions, allowing for greater assessment of any better capabilities of 3D modelling. 2D modelling along smaller scale embankments have produced poor quality results, due to topographic and other 3D effects, where application of a custom geometric factor, which does not assume an infinite flat half-space, to normalise for topographic variation can potentially improve results (Bièvre et al., 2018). This study will focus on the ability of 3D modelling to account for such effects in larger scale embankments (i.e. dams)

This particular study has therefore focussed on determining whether subsurface processes, such as seepage, present at Bartley Dam can be detected by ERT surveying. It has been hypothesised that changes in ground conditions are driven by an increase in water content from rainfall, changes in reservoir level and/or steady state flow of water through the dam. Therefore, the study aims are: (i) to provide greater understanding of the respective hydraulic drivers of subsurface resistivity changes, (ii) determine whether a 3D inversion model can better (and more reliably) determine the resistivity pattern of a singular inversion and (iii) determine whether 3D inversions can improve upon 2D inversions for time-lapse modelling. The ERT will be used in conjunction with geotechnical data for the site for support of resultant interpretations and to determine whether the resultant models are realistic.

## 5.2 Bartley Dam, Birmingham, United Kingdom

Bartley Dam (Figure 5.1) is an approximately 20 m high, 600 m long earthen embankment dam, with an associated reservoir which extends to 18 m depth (Barnes, 1927), and was built for storage of potable water for the city of Birmingham. Bartley Dam is situated close to a housing estate. A small stream emanates from the base of the dam running in a north-easterly direction to the housing estate (Figure 5.2), indicating the risk of flooding, with associated risk to infrastructure and human life, if a large volume of water is able to pass through the dam upon failure. Therefore, it is crucially important that structural integrity of the dam is maintained – for which monitoring of the structure plays a key role in targeting maintenance and remedial activities. The crest of the dam has a road running across, in between the downstream and upstream flanks (Figure 5.1). Drainage and electrical services underlie the dam.



**Figure 5.1:** Location of Bartley Dam, circled, within Birmingham and the United Kingdom ( $52.43^{\circ}\text{N}$ ,  $2.00^{\circ}\text{W}$ ). The numbers correspond to the photograph locations for Figure 5.2 (Google Earth, 2023).



**Figure 5.2:** Photographs taken from Bartley Dam during site visits and investigations, showing residential areas adjacent to the dam.

The dam overlies marl, which was used for infill, alongside sandstone beds of 6 m thickness (Birmingham Water Department, 1931) (Figure 5.3), where the geology forms an arched anticlinal feature (Barnes, 1927). The sandstone is heavily fractured and provides a potential seepage pathway beneath the dam, hence the sandstone has been grouted since construction (Birmingham Water Department, 1931). The concrete core was emplaced into the underlying geology, where the crest of the sandstone anticline had been excavated to a depth of 25 m below the surface (Barnes, 1927). However, seepage has still occurred and it has been hypothesised that two separate seepage pathways have developed through fissures within the sandstone which were not identified during construction, or subsequently, and hence remain ungrouted (Kofoed et al., 2014).

Bartley Dam has been monitored through its history to understand seepage patterns and embankment conditions. Exploratory boreholes were drilled at construction and initial remedial measures against seepage (Birmingham Water Department, 1931) and further boreholes with a series of piezometers were installed across the embankment in 1988. A large

concentration of boreholes were drilled above the sandstone bedrock, to monitor for suspected seepage through this stratum. Outlets, such as drains, gauges and v-notch weirs, have been used to monitor flow of water from the reservoir through the dam. Further piezometers, a weather station and temperature probes to 5 m depth were installed in 2020, allowing greater estimations as to the presence of seepage, associations with rainfall and general embankment conditions.

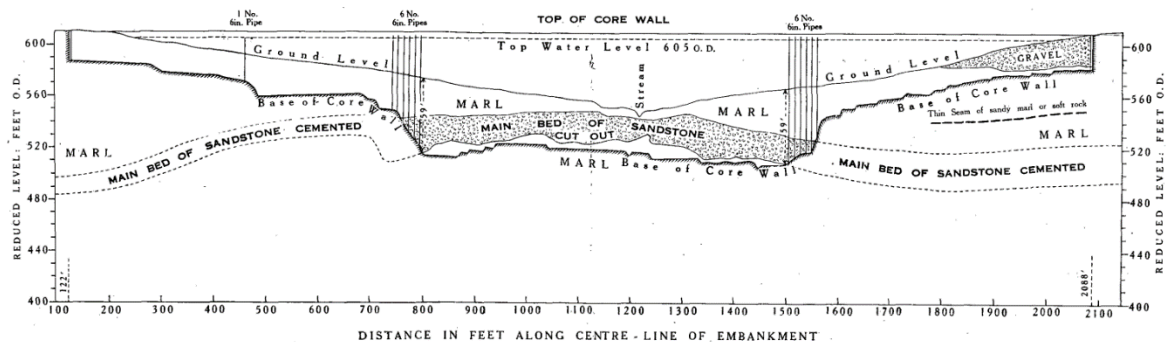


**Figure 5.3:** A cross section of Bartley Dam, taken from underneath the crest, showing the underlying geology, including the sandstone anticline and geology excavated during construction (Birmingham Water Department, 1931). As can be seen the geology is of an interbedded marl and sandstone, where the anticlinal crest has been removed.

Geophysical methodologies have been used to aid determination of subsurface hydrological conditions for the purpose of understanding the nature of any seepage present. A magnetometric resistivity survey, using the Willowstick instrument, was undertaken in 2014 and identified potential seepage pathways through the dam via fractures in the sandstone (Kofoed et al., 2014), originating from the north-western flank of the dam. Subsequently, a time-lapse BGS PRIME ERT system was installed in 2020, following initial reconnaissance ERT and EMI surveying in 2019. This monitoring system was developed to help visualise temporal changes through the seasons and how this might impact any seepage through the dam, in conjunction with the geotechnical data.

The Prime system is connected to two 252 m long lines, consisting of 126 electrodes each at 2 m spacing (Figure 5.4). The measurement scheme utilises a dipole-dipole array type and has an  $a$  spacing of 1-4 and an  $n$  spacing of 7. A further set of 4 electrodes was installed at 0.5 m spacing for the potential of refinement in the model within a region of interest, where seepage pathways were suspected. All electrodes were buried at the surface, in a shallow (less than 0.15 m) trench, are approximately 0.25 m long and are comprised of stainless steel.



The small electrode size compared to electrode spacing indicates a point source assumption is valid (Rucker & Gunther, 2011) and this could be used for subsequent inversions without any adjustment. Reciprocal measurements were collected for each survey to allow for error estimation and assessment of data quality, and two sets of measurements for each line were run daily.



**Figure 5.4:** Location of the two major electrode lines, Line 1 and Line 2, at Bartley Dam. The map also shows a rubble drain, a piezometer (POR30-A) and two boreholes (SP08SW194 and 214) used for acquiring water flow rates, water levels and geological information.

The site at Bartley Dam represents a structurally complex setting, with several underlying services and infrastructure for monitoring dams. Moreover, concrete has been widely used in areas of services, creating several resistivity contrasts and potential 3D effects. As previous chapters and research indicates, the presence of off-centre features and high structural complexity can induce artefacts and cause unreliable data interpretation (Ball et al., 2022).

## 5.3 Methodology

The initial modelling of Bartley Dam focussed on 2D inversions of Line 1 and Line 2 across several time periods of the year. It was hypothesised that significant variation in resistivity, in which a seepage zone may be more visible, would occur with either rainfall or reservoir level variation, due to increased water content originating from the reservoir. Therefore, it was decided to assess the change over time by using on-site and local weather, piezometer, and reservoir level data (see section 5.4.1) as a means to guide dates selected for an inversion scheme. It was decided that the inversion scheme would be set for when reservoir level was relatively low and run until the next peak in reservoir level was reached. These time periods would also include dates where significant rainfall was present, and these were highlighted for analysis, especially during a short-term static reservoir trend. Analysis of short-term periods of high rainfall and static reservoir level, and increased reservoir level but no rainfall, allowed assessment of whether rainfall or reservoir level played a significant role in resistivity variation throughout the inversions. The dates selected for inversion are shown in Table 5.1. To ensure that the results would be reliable, a data quality scheme was undertaken to assess statistical parameters for reciprocal errors and contact resistances over time (see section 5.3.1).

**Table 5.1:** The selected date ranges for the inversion scheme at Bartley Dam, showing the range in reservoir level and maximum in effective rainfall for the given dates selected. Reservoir levels were acquired from gauges present at the dam and rainfall data was acquired from Birmingham Weather Station.

Date range	Reservoir level (m)	Effective rainfall peak (mm/day)	Total Rainfall (mm)
03-Jun-2020 to 23-Jun-2020	183.49 to 184.34	15.62	27.77
17-Aug-2020 to 08-Sep-2020	183.07 to 184.37	23.43	6
09-Nov-2020 to 01-Dec-2020	183.54 to 184.11	7.41	27.92
25-Mar-2021 to 22-Apr-2021	182.98 to 183.69	4.9	6.76

Initially, a single inversion was run for a reference dataset for assessment of the quality of the inversion data, before a more intensive difference (i.e. time-lapse) inversion was run. Each inversion used the 2D inversion code, R2 (Binley & Slater, 2020) after generation of a 2D mesh using the mesh generation software, Gmsh (Geuzaine & Remacle, 2020). The mesh (Figure 5.5) used a mesh fineness of a quarter of the electrode spacing (2 m) close to the electrodes and gradually coarsened towards the mesh boundary, which was set at 500 m from the electrodes to approximate infinite boundary conditions. The inversion utilised a smoothness constrained (i.e. L2 norm) algorithm. Once the inversion was trusted to give realistic results for the site, a difference inversion was performed using R2, with the difference inversion method of (LaBrecque & Yang, 2001). These were then run for every date range given in Table 5.1 for both lines Line 1 and Line 2.

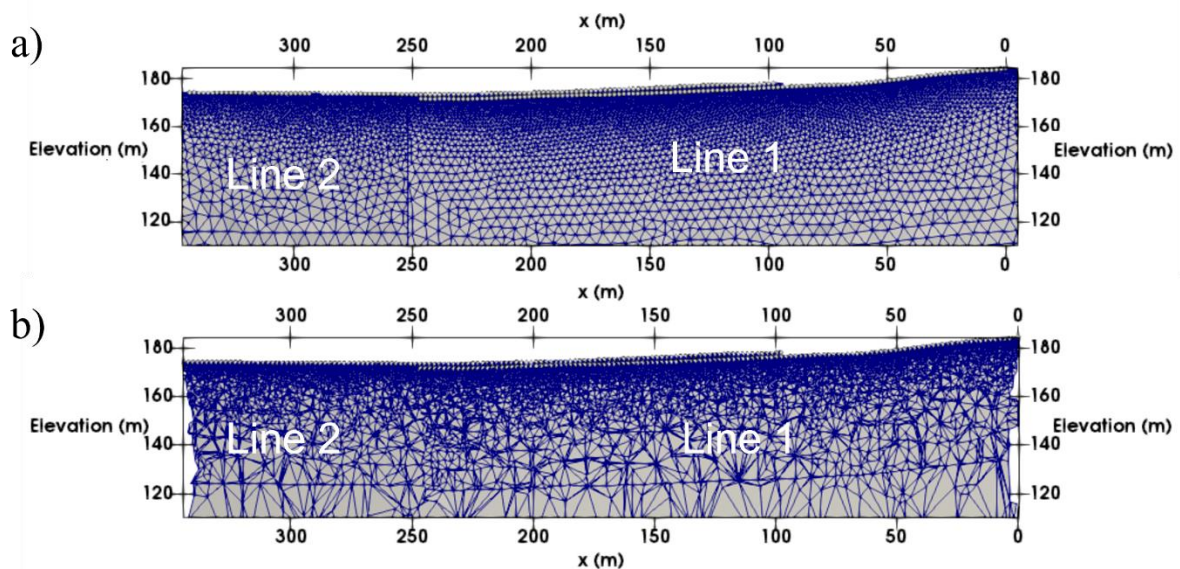


**Figure 5.5:** The uppermost section of the mesh for a) a 2D model and b) a 3D model at Bartley Dam.

Subsequently, 3D models were run for selected datasets to compare between inversion results. This utilised the 3D inversion code R3t (Binley & Slater, 2020) and used the same inversion parameters as before (e.g. it was smoothness constrained) and the mesh characterisation was the same as 2D (Figure 5.5a), except scaled to 3D. Initial single inversions were run to ensure that the inversion was satisfactory. Following that, difference inversions, using the same method as in 2D modelling, were undertaken for selected dates.

For comparing the results between 2D and 3D models, graphical representation of resistivities beneath Line 1 and Line 2 was created for a quantitative assessment between datasets. These were done in the form of histograms, to visualise the resistivity distribution within model cells underneath each electrode line, alongside graphical plots showing resistivity change between 2D and 3D models. To estimate the effects of reservoir level and rainfall, resistivity monitoring results were compared with the piezometric and flow data.

An electromagnetic induction (EMI) survey of the site was completed in February 2022 for the purposes of validating ERT models, visualising ground conditions beyond the electrode lines and to observe any evidence of variations within ground conditions from a separate method. The EMI used a GF Instruments CMD Explorer using the horizontal coplanar orientation. The survey was carried out by walkover and transections were undertaken parallel to each other, upslope, and at approximately 3 m separation.

### *5.3.1 Data Quality Control*

To ensure that the selected time-series data sets were suitable for reliable assessment, contact resistances (Figure 5.6) and reciprocal errors (Figure 5.7) for the Bartley Dam dataset were assessed for electrode lines Line 1 and Line 2. For the contact resistance, the first, second, and third quartile are shown to demonstrate the spread of the contract resistances where this was used over an average because the data may have been skewed by large outliers which may indicate poorer overall data quality than actuality. Contact resistances should be low (i.e. less than 5 k $\Omega$ m) to ensure the standard deviation of the measurements is low. Assessing the contact resistances therefore allows an additional data quality check, where contact resistances of 5 k $\Omega$  or greater are assumed to be of poor quality. The median reciprocal error has been used across separate pseudo depths below ground surface to visualise variation from hypothetically identical survey results in areas of differing sensitivities (Figure 5.7).

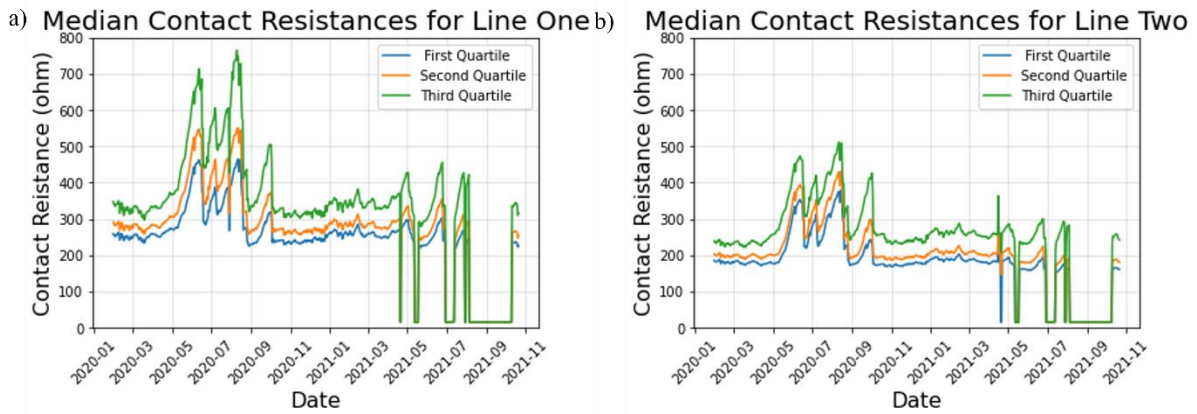


**Figure 5.6:** Contact resistances for a) Line One and b) Line Two from January 2020 to October 2021.

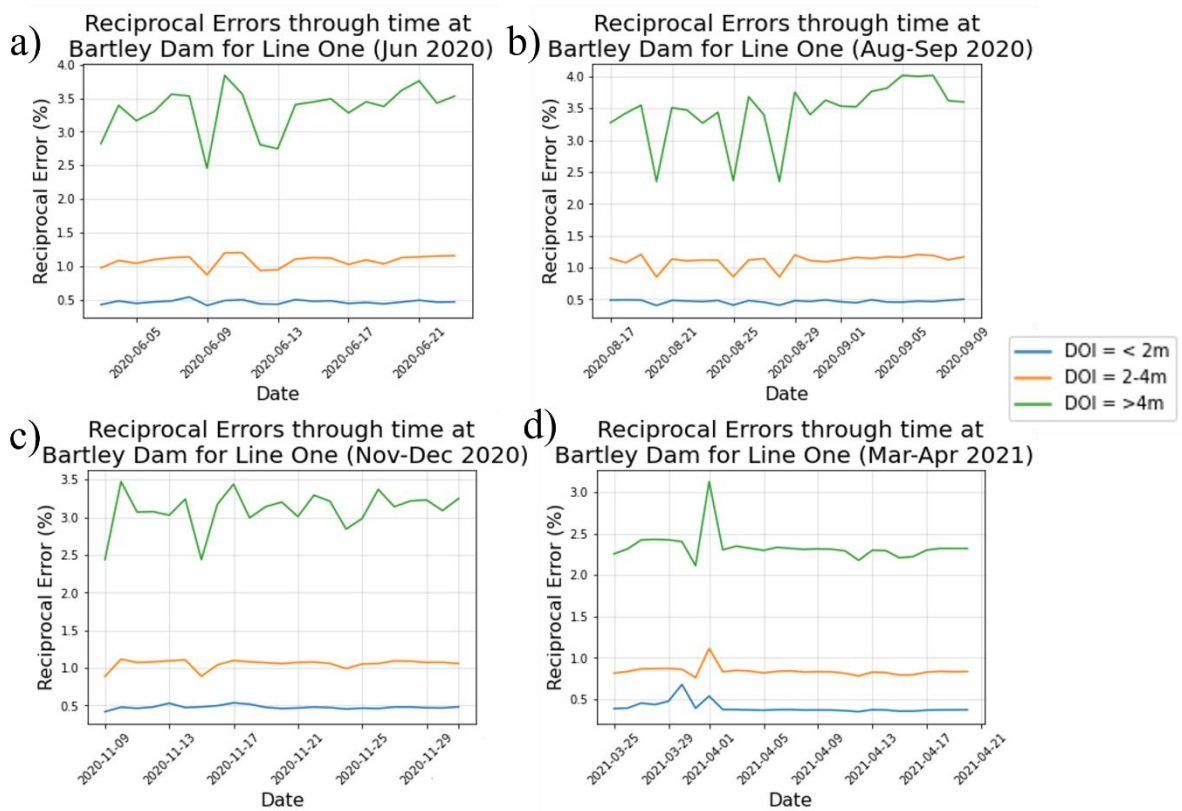


**Figure 5.7:** Median reciprocal errors from Line 1 for the selected datasets for time-lapse analysis. a) June 2020, b) August-September 2020, c) November-December 2020 and d) March-April 2021. Line 2 has not been shown due to similar behaviour to Line 1 for all selected dates.

The results from the data quality check described above show that for the time periods selected the overall data quality is good. The reciprocal errors are all 4% or less for all depths indicating minimal variation between surveys. Contact resistances within all quartiles in the survey, for both lines, are below 5 k $\Omega$ , indicating satisfactory conditions. The majority of the survey data have contact resistances less than 1 k $\Omega$ , except for the third quartile, which has a maximum of approximately 0.8 k $\Omega$  approximately in Line 1. The majority of the variation

occurs in the spring-summer months for both lines, due to drying ground, and the contact resistances are higher for Line 1 than Line 2 because of more gravelly ground conditions.

It should be noted that in late April 2021 regular anomalously low contact resistances, towards 0 k $\Omega$ , and high reciprocal errors were reported, occurring recurrently over several months until January 2022. This was due to a suspected system fault resulting from a lightning strike nearby. Therefore, no data from this time range were used for analysis. The dates selected cover a period of 11 months through different seasons, which is deemed to be sufficient for assessing any changes in resistivity with different temporal ground conditions.

## 5.4 Results

### *5.4.1 Geological and Hydrological Data*

To ensure a reliable interpretation of the ERT data at Bartley Dam it is important to understand the hydrological and geological data obtainable from site, through piezometers, gauges, drainage, weather stations and geological site investigation. These sources were used for assessment of hydrological conditions during the time-lapse ERT monitoring for identification of associated changes within the ground, enabling more reliable interpretation of resistivity changes within the ERT, such as that which may be linked to seepage. The associated piezometer (POR30-A), flow drains/gauges (rubble drain) and boreholes for geological logging are shown in Figure 5.4. Results for the selected dates for ERT are shown in Figures 4.8 and 4.9, showing the water levels and flow rates across relevant time periods selected for ERT analysis. The effective rainfall data are shown alongside relevant results for added contextual information.

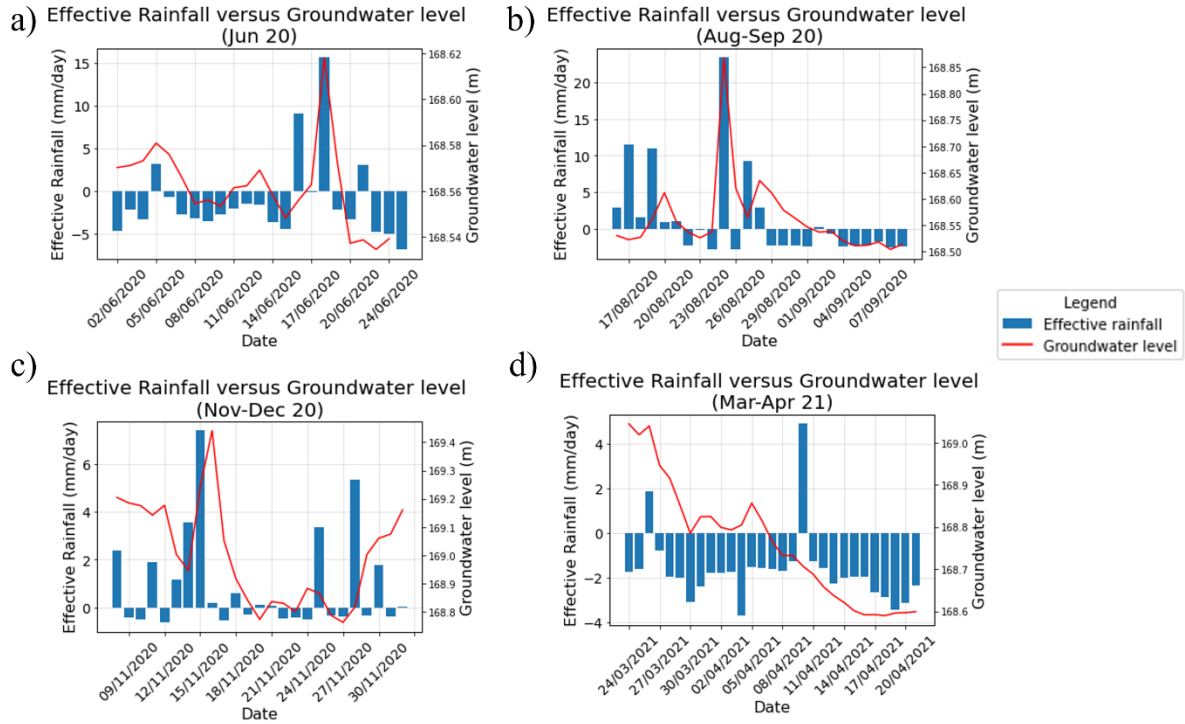


**Figure 5.8:** Groundwater levels compared with effective rainfall for the dates selected for time-lapse analysis. a) June 2020, b) August-September 2020, c) November-December 2020 and d) March-April 2021.

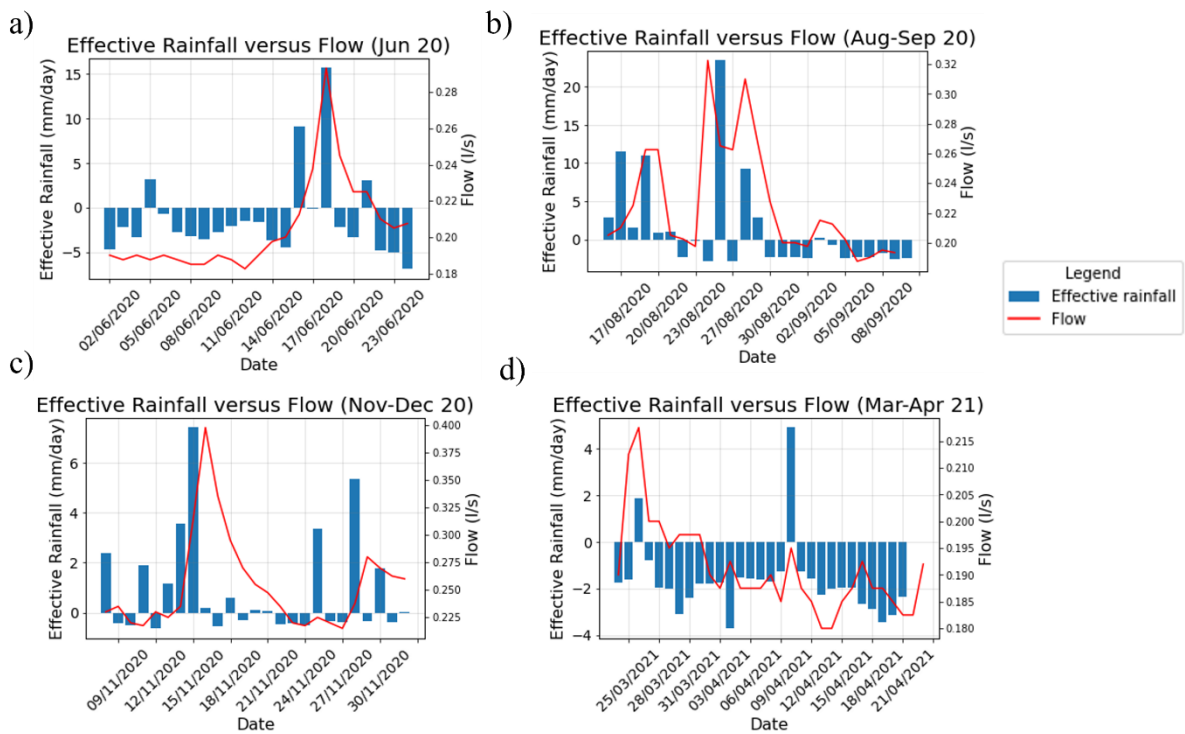


**Figure 5.9:** Flow rates compared with effective rainfall for the dates selected for time-lapse analysis. a) June 2020, b) August-September 2020, c) November-December 2020 and d) March-April 2021.

The piezometer data in Figure 5.8 show the water levels over the period of each respective period selected for time-lapse monitoring. For all time periods it is clear that rising water level is strongly associated with rainfall. For example, there is a 20 cm water level rise in the water level in POR30-A on 18-Jun-2020 after 15 mm effective rainfall event on that day and a 70 cm water level rise on 15-Nov-2020 after 7 mm effective rainfall on 14-Nov-2020. The peak in groundwater level rise often occurs on the same day as the rainfall event, although there is sometimes a lag of one day, as was the case for the 14 November 2020 rainfall event. This is to be expected, given groundwater levels will have an associated lag time following rainfall and the piezometer data being represented as a daily level, meaning any rise in groundwater would not necessarily be recorded on the same day as the rainfall event if the event was late in the day. These were then used as a basis for analysis with time-lapse inversions, where dates after immediate rainfall could be used for comparison with a reference model where conditions were drier.

A clear link between groundwater level and rainfall is evident (Figure 5.8). However, there are times when there is an unclear association between rainfall and water level. From 25-Mar to 20-Apr 2021 there is no apparent rise in the water level in POR30-A after high rainfall. Instead, there is an associated variation in water level which coincides with the reservoir level. For example, on 26-March 2021 the water level is 169.05 mAOD and the reservoir level is 182.96 mAOD. By 20-Apr-2021 the water level is 168.6 mAOD and the reservoir level is 183.64 mAOD, and the reservoir level has a generally inverse relationship to the piezometric water level in between these dates. From this, it has been suggested that with a decrease in reservoir level, the water flowing from the reservoir can permeate through the embankment, raising water level in the piezometers. The effective rainfall was the lowest for this dataset (25-Mar to 20-Apr 2021) out of all analysed datasets, meaning input from rainfall was less likely to offset changes from reservoir levels. Therefore, it has been hypothesised that reservoir level may have a controlling factor on water level alongside rainfall, and seepage may be evident with such reservoir and rainfall induced changes. The selected dates for time-lapse ERT analysis utilised this information, where each time-lapse focussed on a rising reservoir level with dates of rainfall in between, allowing monitoring of changes which may be related to these factors. Monitoring of drains and gauges for the flow of water revealed a similar response to rainfall, helping to verify the groundwater response to rainfall, which might help indicate any seepage



effects in relation to the weather conditions. As can be seen with comparisons to rainfall events for the selected dates (Figure 5.9), a rainfall event typically increases flow of water through the embankment by 0.2 to 0.4 l/s. A lack of significant flow of water through the embankment suggests that reservoir level may have an effect on the flow of water through the embankment, as opposed to just weather.

Geological logs from past site investigations (Soil Mechanics, 1989) were used for generating an understanding of the subsurface stratification, which can then be related to the ERT data and to verify the resistivity distributions which have been attributed to the geology. This can then validate whether 3D inversions can produce more realistic representations than 2D. Relevant geological logs (Figure 5.4) have been represented with the inversions for comparison between resistivity and the geological stratification at Bartley Dam.

#### *5.4.2 2D Inversions*

The June 2020 reference model for used for its associated time-lapse dataset is shown in Figure 5.10. The reference models for the other time periods do not differ significantly from this inversion, so all features described below apply for all datasets. Two simplified geological logs have been shown and marked on the inversion for comparison between the resistivity and geological data.

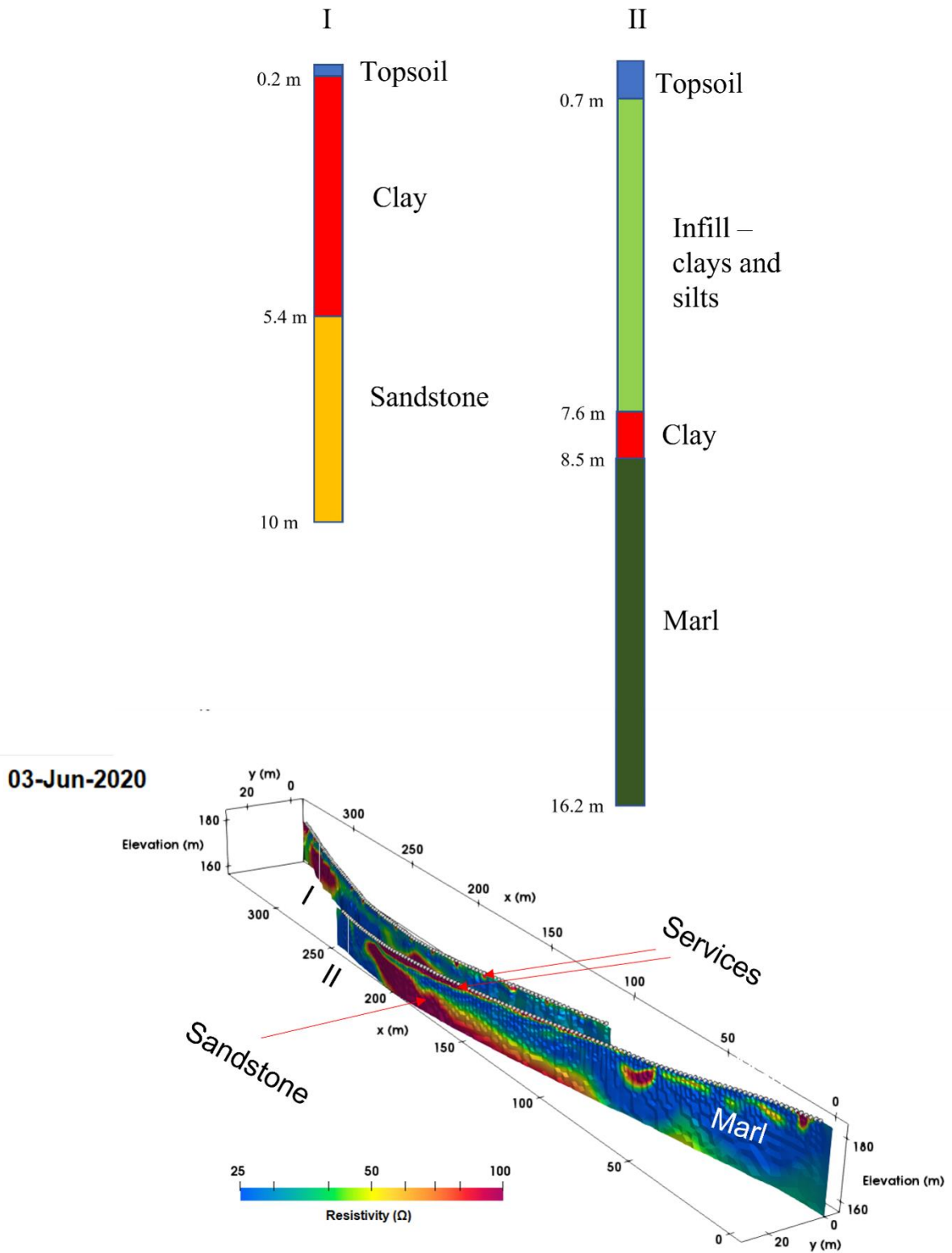
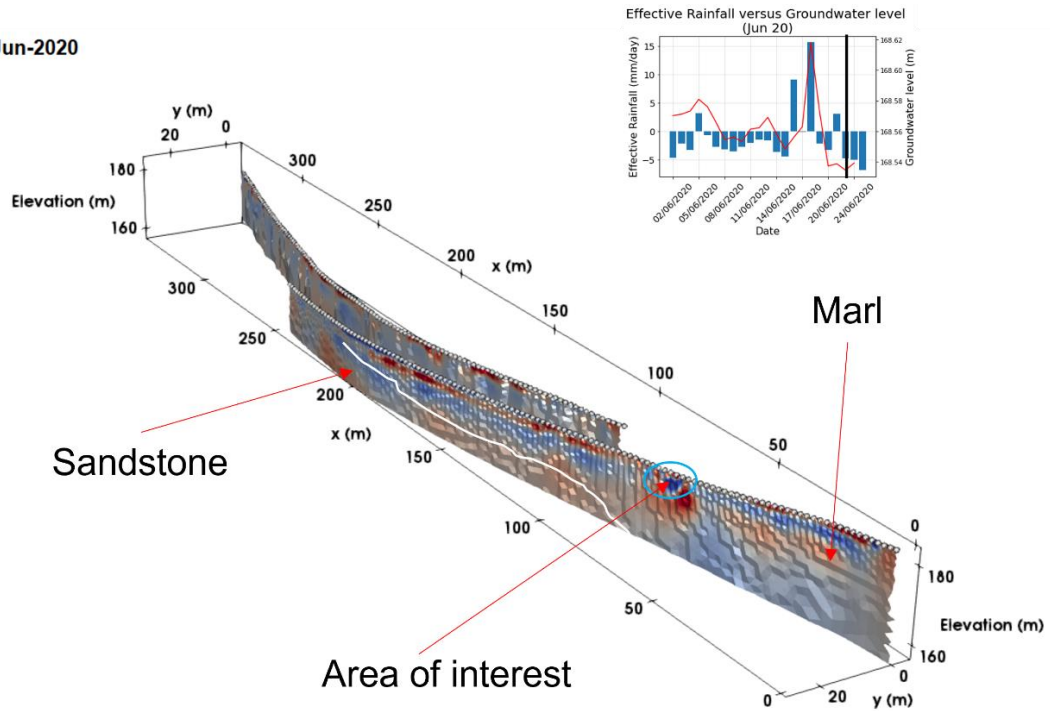


**Figure 5.10:** Reference model for the June 2020 dataset, taken from 03-Jun-2020. Nearby geological logs are indicated by I and II, where I is SP08SW214 and II is SP08SW198, as indicated in Figure 5.4.

The 2D inversions of the June 2020 reference model are shown as a fence diagram of both lines Line 1 and Line 2 with representative borehole logs included for comparison. The 2D inversions show clear 75-150  $\Omega\text{m}$  resistive features at 10-20 m depth, between 200 and 250 m in Line 1 and Line 2, as well as 300-325 m in Line 2, which are associated with the sandstone (based on the borehole logs). The less resistive ground in between is consistent with the presence of marl, which tends to have a resistivity of 20-40  $\Omega\text{m}$ . Geological logs indicate the presence of overlying clay infill, which is not apparent in the inversion. However, site information indicates the infill was sourced from the marl (Birmingham Water Department, 1931), so resistivity contrasts between the marl and infill are unlikely. Further 150  $\Omega\text{m}$  resistive anomalies are found strongly at the surface between 100 and 250 m in Line 1 and are believed to be a result of concrete for services. Such shallow features are evident in Line 2 at approximately 20 m spacings and relate to drainage. An ovoid feature of 100  $\Omega\text{m}$  is present in Line 1 at 2-5 m depth between 70 and 80 m laterally and is a large service for drainage. While there is sufficient similarity between Line 1 and Line 2 for related geological units, there is a presence of highly resistive features at shallow depth (i.e at 140, 160, 180, 200 m along Line 2) which may be artificial and better resolved in 3D modelling.

Difference inversions from the reference model for each selected date range with a are shown in Figure 5.10. The difference inversions chosen for visualisation were selected due to them being after rainfall events or at reservoir highs, and the reference model for each inversion is given in the caption.

a) 23-Jun-2020



b) 26-Aug-20

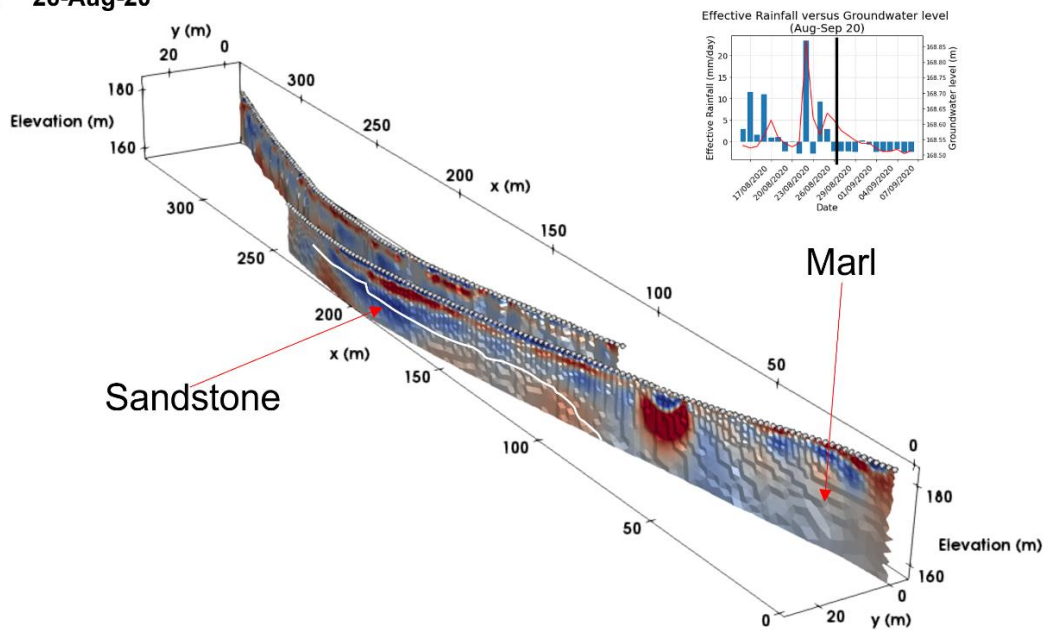
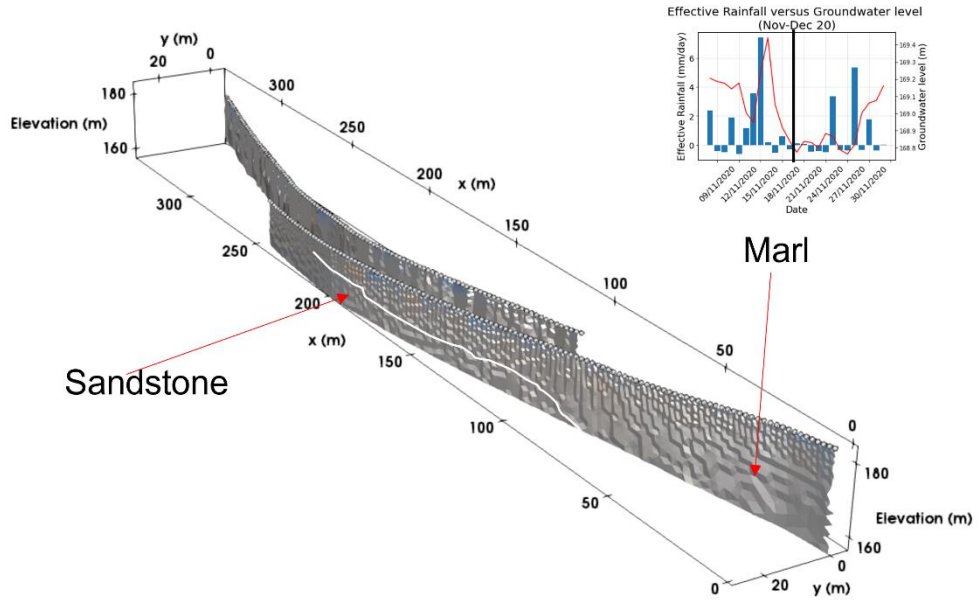


**Figure 5.11:** Difference inversions from the four selected time periods after periods of reservoir level increase and/or rainfall. a) 23-Jun-2020, reservoir level: 184.34 m (reference: 13-Jun-2020, reservoir level: 183.49 m), b) 26-Aug-2020, reservoir level: 184.37 m (reference: 17-Aug-2020, reservoir level: 183.07 m), c) 17-Nov-2020, reservoir level: 184.11 m (reference: 09-Nov-2020, reservoir level: 183.54 m), d) 20-April-2021, reservoir level: 183.69 m, (reference: 25-Mar-2021, reservoir level: 182.98 m). For each model a timestamp is shown along the graph with groundwater level and effective rainfall. A blue circle in a highlights a region of interest (drainage) interpreted from the inversion.

c) 17-Nov-20



d) 20-Apr-21

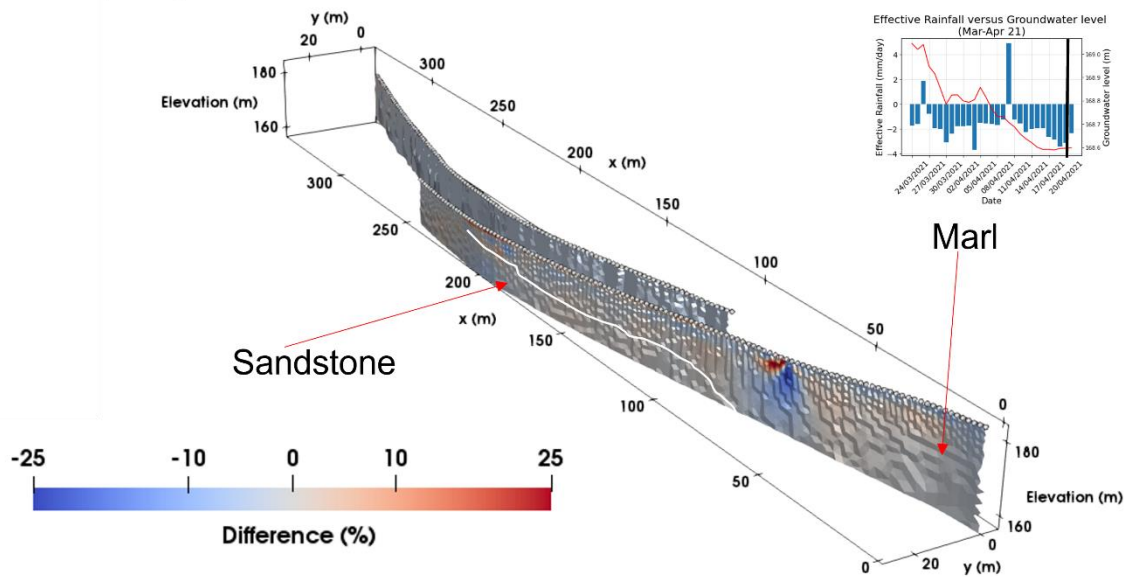


Figure 5.11 continued.

The difference inversions show a strong increase in resistivity at shallow depths where there is a high likelihood of 3D effect resulting from the concrete services, so any interpretation here will be unreliable. After an increase in effective rainfall, as evident in Figure 5.11a there is a distinct change in the resistivities one or two days after the rainfall event. A 10-25% decrease in resistivity is present at 2-10 m depth, typically, and is associated with the marl

layer. There is a strong decrease in resistivity beneath the service at 70-80 m in Line 1. However, this service is suspected to be two drains, with a metal shaft present, so 3D effects are likely and with one electrode line it is going to be hard to interpret correctly. It should be noted that reservoir level was relatively static between 19 and 23-Jun-2020, indicating that reservoir level is unlikely to have an effect on the resistivity for this time period and such changes can potentially be inferred as an effect of effective rainfall.

When looking at the 01-Dec-20 dataset, which was taken from a time after minimal rainfall and high reservoir levels, the magnitude of any resistivity change is small. There were small, localised decreases in resistivity, of 5-10% variation, in areas which were observed to have a decreased resistivity after rainfall. This suggests a potentially minor effect from steady-state flow through the dam. Moreover, the changes predominantly effect Line 1 over Line 2, whereas when rainfall has increased, changes appear to affect both lines. Alongside this, there is some degree of data striping present in the resistivity, where there are alternating decreases and increases in resistivity, due to 3D effects and sensitivity.

The service identified at 70-80 m has strong changes in resistivity compared to the rest of the inversion. Underneath this there is a feature of opposite polarity which has a strong magnitude of change in resistivity. This has been interpreted as a potential seepage pathway, but it could be a compensatory or overfitting effect in the inversion, and the striped nature of the resistivity variation, indicates that such interpretations may be influenced strongly by artefacts. This, coupled with the lack of correlation between Line 1 and Line 2 with reservoir level variation alone, indicates that any interpretation of a 2D dataset may well be influenced strongly by inversion effects (e.g. 3D effects). However, a link between reservoir level and seepage is unlikely given the low changes in magnitude, which may be artefacts. Changes in resistivity with time have been quantitative analysed through calculating the change in resistivity from the June 2020 reference model within the difference inversions for this dataset, in the area of interest circled in Figure 5.10a and compared with groundwater level (Figure 5.12).

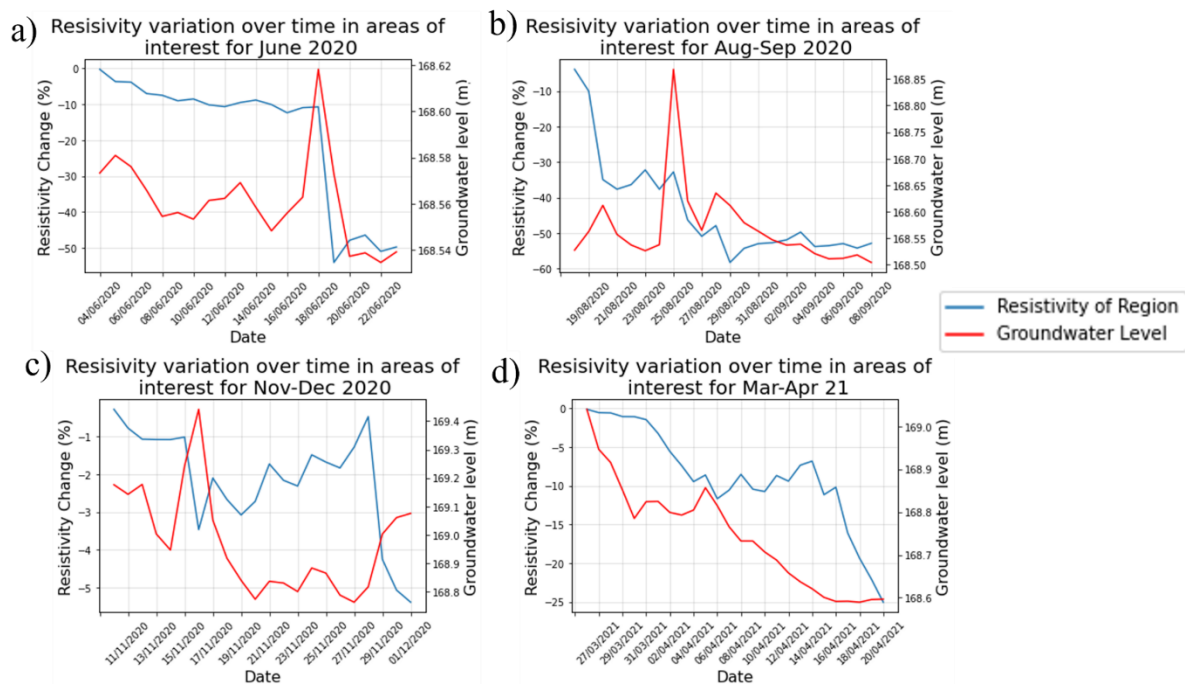


**Figure 5.12:** Resistivity variation in the area of interest, as indicated on Figure 5.11, through time, showing how resistivity varies with groundwater level. a) June 2020, b) August to September 2020, c) November to December 2020, d) March to April 2021.

The change in resistivity in Figure 5.12 for the area surrounding the area of interest shows an overall decline in resistivity from the reference model over time. It is evident that there is a strong inverse association between groundwater level and the change in resistivity. For example, there was a 40% decrease in resistivity with a 6 cm increase in groundwater level on 18-June-2020. A rainfall event (Figure 5.9a) on 18-June-2020 had a significant impact on groundwater level and resistivity, following another rainfall event two days prior. The shallow nature of this low resistivity feature, linked with rainfall, indicates that such changes may be a result of rainwater percolation. This resistivity decrease is in the area associated with seepage (Kofoed et al., 2014) and the presence of resistivity variation linked with groundwater level shows the capability for seepage to be identified. A further low resistivity feature is present at approximately 5 m below surface, at 50 m on Line 1. However, such detail at greater depth is less certain due to the poorer sensitivity. It should be noted that groundwater levels do not correspond to the location of the region of interest, which may indicate why high resistivity variation may occur with low groundwater level changes.

The same trend of a decline in resistivity with an increase in groundwater level is noticeable throughout, especially for November to December 2020. However there are discrepancies,

such as in August 2020, when a steep decline in resistivity is observed from 18 to 20 December. This coincides with a rainfall event (Figure 5.8b), as does the drop in resistivity from 28 March 2021 (Figure 5.8d). This shows that resistivity variation at Bartley Dam can be linked to water content, and changes in resistivity can be inferred as to be potentially a result of seepage or rainfall, depending on depth of the anomaly and correlation with groundwater level or effective rainfall.

### *5.4.3 3D Inversions*

3D inversions, including both Line 1 and Line 2, were then run to determine whether this would better represent the subsurface changes with time-lapse monitoring, and correct potential overfitting and compensatory effects that may be present in the 2D inversions. A June 2020 reference model is shown in Figure 5.13 and analysis of subsequent difference inversions has been undertaken to observe how resistivities within the inversion vary temporally when compared to the 2D time-lapse dataset for June 2020.



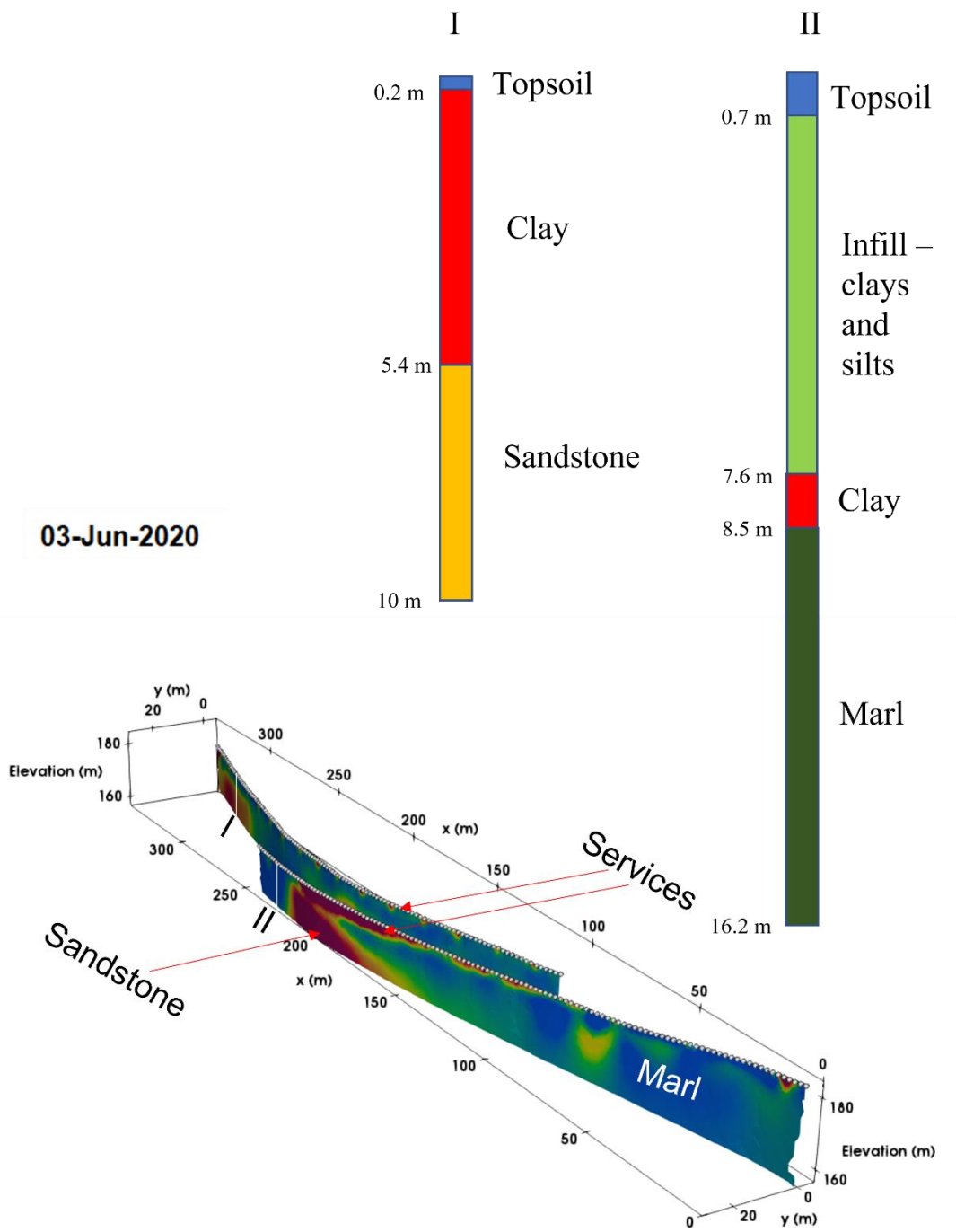


**Figure 5.13:** A 3D reference model for 03-June-2020. This is the equivalent dataset for the 2D model shown in Figure 5.10, where the same borehole logs are shown.

The 3D inversion generated a similar subsurface model to that of the 2D inversion. The resistive sandstone and less resistive marl persist in similar locations, shallow services are still detected and the observed resistivities for each region is of a similar magnitude to the 2D inversion. However, the depth to the interpreted sandstone beneath Line 1 is shallower (between elevations of 175 and 250 m, as opposed to between 100 and 250 m in the 2D

inversion). A 2D inversion assumes infinite continuation of resistivities orthogonal to the array, and this enabled greater influence of the high resistivity sandstone on the 2D inversion. Whereas, with a 3D inversion, the interaction between Line 1 and Line 2 more likely allows the inversion to estimate a more reliable resistivity of the subsurface underneath both lines. The largest or smallest resistivities will be tempered by interaction between resistivities in the adjacent model cells where resistivities will be of a less extreme magnitude, causing a reduction in the size of the sandstone in this inversion. Alongside this, the resistive service between 70-80 m is of a lower resistivity, by approximately  $25 \Omega\text{m}$ , in the 3D inversion than the 2D model. This indicates a potentially lesser 3D effect on the inversion resulting from this service. The difference inversion of the 23-June-2020 dataset, using the above 03-June-2020 as a reference model, has been represented for comparison between the 2D results from the same date (Figure 5.14).

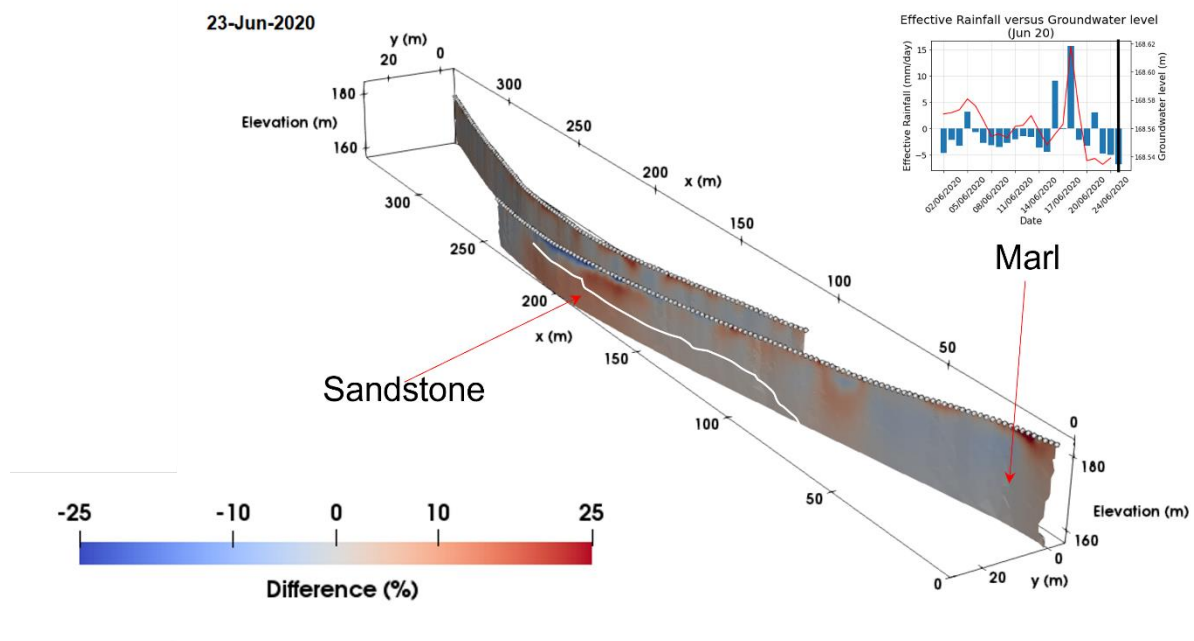


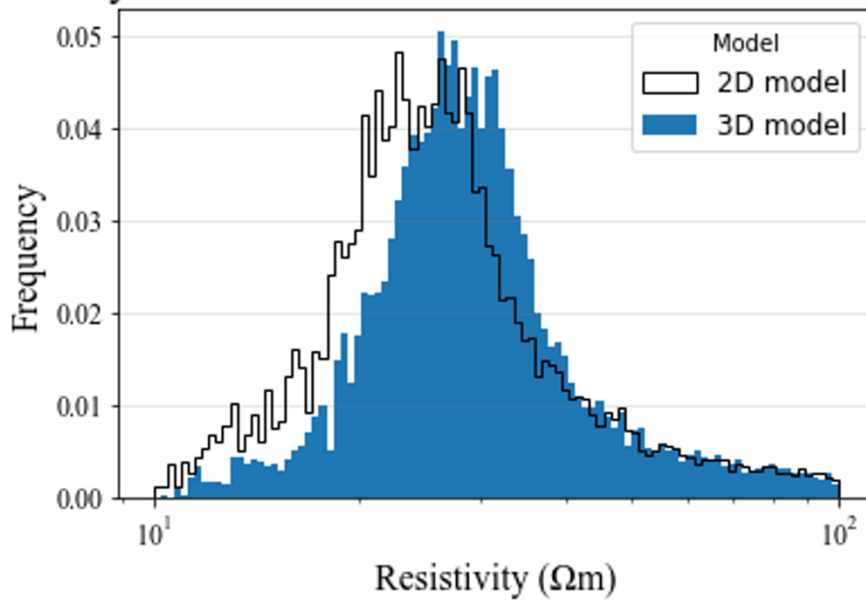
**Figure 5.14:** 3D difference inversion for the 23-Jun-2020 dataset for the corresponding dataset to Figure 5.11a. A timestamp has been shown for the groundwater level and effective rainfall at this time period.

The difference inversion shows some significant variation from the 2D inversions. The overall magnitude of the changes is less extreme for a 3D inversion compared with 2D, with the typical resistivity variation in 2D being up to 50% variation, and towards 10% in 3D. The 3D difference inversions include less of a striping effect than the 2D inversions and more consistent regions of lowered or increased resistivities. For example, the area of lowered

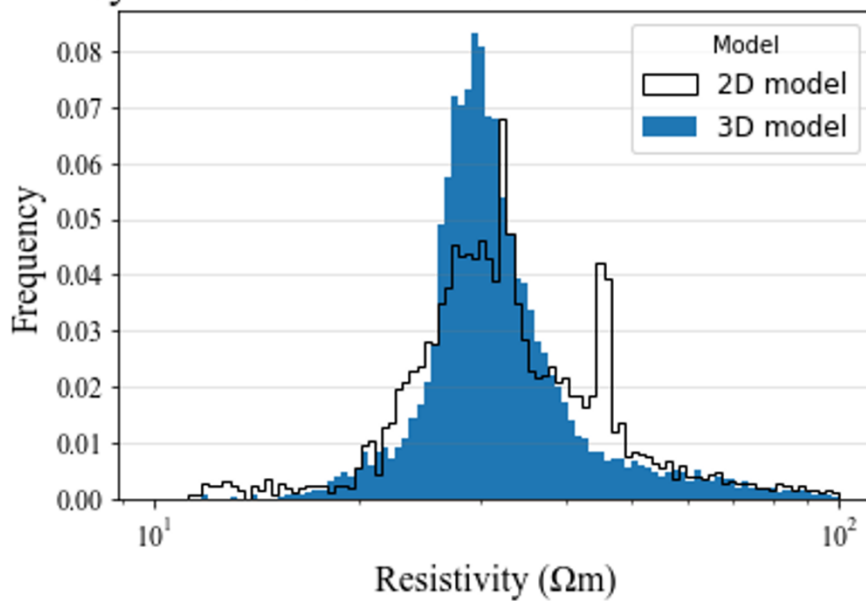
resistivity at 2-5 m does not persist throughout Line 1, as in 2D inversions. These features suggest that the 3D inversion does not suffer as strongly from compensatory or overfitting effects. Therefore, it is easier to identify changes in resistivity which are likely caused by real subsurface processes and variation, such as a strong 20% decrease in resistivity observed for the upper 1-1.5 m between 175 and 250 m on 23-Jun-2020 after a period of rainfall, which is likely to be an effect of rainwater infiltration. The lack of infiltration of rainwater further into the ground is not unexpected given the likely dry ground conditions and inability of water to infiltrate dry ground in June. A decrease in resistivity is also noted at depths below 1 m in Line 1 between 0 and 50 m. This is in the location where seepage was suspected, as discussed in section 5.4.2, and there is a clearer pattern of resistivity decrease extending to 10 m below the surface. This is unlikely to be rainwater percolation at such depth and could be an indicator of seepage, which is rainwater controlled. This shows that 3D modelling has a potentially greater ability to provide more realistic representations of changes over time, than in 2D modelling, and has the potential to give more reliable indication for subsurface processes.

The ERT data from the 2D inversions has been compared with 3D inversions, along areas of interest (Figure 5.11a) to quantitatively assess how resistivities have varied between both modelling scenarios (Figure 5.15).

a) Resistivity distribution underneath L1 for a 2D and 3D model



b) Resistivity distribution underneath L2 for a 2D and 3D model



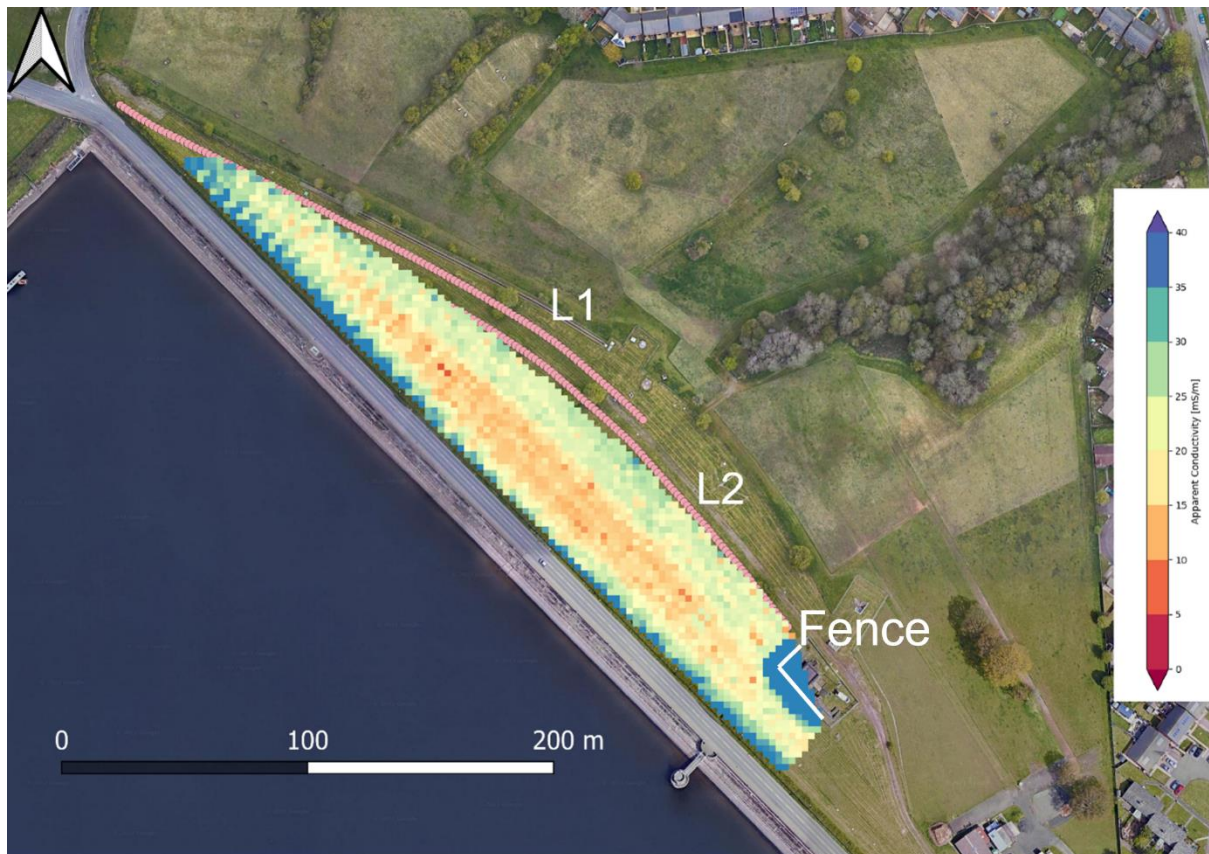
**Figure 5.15:** Histograms showing the resistivity distribution across model cells for the 03-Jun-2020 dataset a) from underneath Line 1 and b) from underneath Line 2 for the upper 20 m.

Figure 5.15 shows a histogram of resistivities distributed over the model cells for a 2D and 3D model for Line 1 and Line 2, beneath each associated electrode line to 20 m below ground level. For Line 1 there is a clear increase in resistivity in a 3D model compared with a 2D model. This shows the impact of a reduced size of the resistive sandstone in the 3D model, compared to the 2D model, and the lower 3D effect associated with the service. Whereas, the 3D inversion for Line 2 shows a more even spread of resistivities across model cells than a 2D

model. There is a higher distribution of resistivities towards  $30 \Omega\text{m}$  and less of an anomalous peak in resistivity at  $40\text{-}50 \Omega\text{m}$ , as with the 2D inversion. This greater spread of data is unsurprising with a smoothness constrained model. Therefore, this indicates that the 3D model has potentially better resolved the inversion at Line 2.

#### 5.4.4 Electromagnetic Induction Survey

In February 2022 an EMI survey was conducted at Bartley Dam to support any ERT findings and observe further trends in the electrical signature of the subsurface, across the site. The survey covered a more comprehensive area than the ERT and as such was used for potential identification of where the trends in the resistivity dataset continue for a larger section of the dam. The results from the EMI are shown in Figure 5.16 as conductivity maps across the area.



**Figure 5.16:** An EMI survey undertaken in February 2022 at Bartley Dam, showing the conductivity map of the subsurface at an estimated 4.2 m depth.

The EMI results show the conductivity trends above the electrode line at Bartley Dam. There is a noticeable feature of low conductivity, at approximately  $10 \text{ mS/m}$  (i.e.  $100 \Omega\text{m}$ ), running

across the site, roughly parallel to the electrode lines. This is a feature associated with Dry ground upslope in an area of gravel infill. Other such features include higher conductivity anomaly at the site's south-western boundary and to the very north-east. These are associated with metal fences bordering the site and an electrical substation respectively. Towards Line 1 the conductivity is of 15-30 mS/m and there are no noticeable features which indicate subsurface variation. The high concentration of services and gravel infill are likely to interfere with the survey and it has therefore not been able to provide further support for any evidence of seepage or geological information.

## 5.5 Discussion

A time-lapse ERT system was installed at Bartley Dam, Birmingham for the purpose of monitoring ground conditions at the site, through the seasons, where seepage had been noted to be occurring. To reliably interpret inversions resulting from the ERT on site it is important that the source of resistivity trends within the inversion and any artefacts present are understood, as are techniques for reduction of such effects. There are several means by which resistivities may be distorted in an inversion, from 3D effects resulting from off-line features of anomalous resistivity, a complex and heterogeneous subsurface inducing abnormal resistivities elsewhere in the survey and under or overfitting of data. If not carefully accounted for in the inversion process such features may cause misinterpretation of data, obscuration of the true resistivity and a lack of trust in the capabilities of ERT to successfully visualise subsurface features. This study was carried out to visualise the difference between 2D and 3D inversions for a resistivity model to understand whether the latter can produce more realistic representations of the subsurface and to determine whether seepage interpretations are likely to be reliable with 2D and/or 3D modelling.

### *5.5.1 Differences Between 2D and 3D Inversions for a Singular Inversion*

The 2D and 3D models showed noticeable differences in how they represented the resistivity distribution at Bartley Dam. While both 2D and 3D inversions were able to generate an overall representation of the subsurface with consistency in the features observed, there were significant variations in the resistivity distribution and changes in resistivity over time which would potentially cause varied interpretation. In a standalone inversion, the 2D inversion

(Figure 5.10) showed underlying sandstone as being tens of metres more expansive than in the 3D inversion (Figure 5.13) and resistivities of some features, especially with likely artefacts, were higher than in 3D inversions. Accounting for 3D topography and interaction between lines in a 3D inversion, enables a more realistic resistivity distribution, causing artefacts to be of a lower magnitude and generating a more realistic geometric shape for observed features. This helps confirm features observed in previous studies (Ball et al., 2022; Bièvre et al., 2018) which indicated that 2D models were insufficient to represent 2D embankments and that 3D modelling has the capability to reduce the magnitude of artefacts in a 2D inversion.

### *5.5.2 Differences Between 2D and 3D Inversions for Time-Lapse Modelling*

Resistivity variation over a time-lapse survey was evident in both 2D and 3D modelling. From observing the 2D inversions there was a region of lowered resistivity, which might have indicated an increase in moisture content, as could be expected with seepage. However, potential overfitting of data meant such results were unreliable. In contrast, the 3D model produced a less overfitted dataset with a more consistent change in resistivity across depth, making such data more believable. The resistivity variation in the 3D model was of a lower magnitude than in 2D modelling, as to be expected with a small change in reservoir level and relatively low effective rainfall during the dates modelled, giving it a greater reliability. The less artefact-vulnerable 3D inversions revealed more reliable changes with reservoir level and rainfall variation, which can lead to greater interpretation of likely subsurface changes over time. A small variation in resistivity is expected, given the small time frame between dates selected for difference inversions, leading to greater credibility for the inversion output of 3D modelling and 2D modelling. The likely cause of such drastic resistivity changes with 2D modelling is likely to be caused by poor sensitivity and 3D effects in an inversion, which are less evident in the 3D model.

### *5.5.3 Accounting for the Presence and Cause of Seepage*

A key question for analysis was whether seepage could be identified at Bartley Dam and what caused any evident seepage. The modelling shows that 3D modelling can potentially identify areas in which seepage is occurring and the seepage is strongly affected by rainfall. From

looking at resistivity variation with the groundwater level, flow and effective rainfall, it is evident that the change in resistivity can be associated with water content. Interpretation of the 3D dataset showed that, resistivity variation linked to rainfall was present at the surface between 100 and 200 m in Line 1 (Figure 5.13) and between 0 and 50 m to a greater depth. The former is likely to be an effect of rainfall percolation, but the latter is potentially a seepage pathway which can be monitored with 3D time-lapse analysis. In contrast, the data contained more noise and striping in a 2D inversion, which obscured such key detail and would create erroneous interpretation. Therefore, any identification of seepage is more likely to be made with a 3D inversion scheme and 2D inversion schemes may be insufficient to detect subsurface changes the interpreter is interested in.

A summary table describing the outcomes of the research aims can be found in Table 5.2.



**Table 5.2:** A summary table detailing key outcomes from the research aims for Bartley Dam.

Aim	Outcome
Comparison of 2D and 3D inversions for a singular inversion.	Both 2D and 3D inversions managed to identify sandstones, marls and services. However, the 3D inversion had more realistic geometries for the underlying structure and reduced 3D effects from services.
Comparison of 2D and 3D inversions for time-lapse inversions.	The 3D inversions showed resistivity patterns which could be related to weather phenomena, and realistic variations in resistivity over the time scale modelled. While the resistivity pattern for 2D inversions were less realistic and likely affected by 3D effects and sensitivity issues. Interpretation from the 2D inversions would likely cause misinterpretation, demonstrating that 3D inversions are more useful for assessment.
The ability for ERT to detect potential seepage pathways and ground conditions reliably.	An area of suspected seepage was highlighted in the 3D inverse model. Decrease in resistivity were associated with increases in groundwater content, giving an interpretation that the resistivity variation observed is linked to water content.

#### 5.5.4 Recommendations

The ERT lines at Bartley Dam were too widely spaced for a true 3D survey with cross-measurements between lines. A true 3D survey would better enhance the capabilities of resolving any 3D effects off-line, giving the potential for more realistic resistivity distributions

and a further reduction in artefacts. The 3D inversions at Bartley Dam have been used solely to validate whether a 3D inversion scheme can produce more reliable models than a 2D inversion scheme. However, these results show that there is a significant improvement in subsurface representation in 3D over 2D modelling with time-lapse analysis. Dams are likely to consist of highly heterogeneous infill and complex subsurface features, with adjacent structures, such as the reservoir, as well as abutments and roads, which are likely to induce artefacts in the data. Therefore, it is recommended that any ERT survey for time-lapse monitoring sited on a dam utilises a 3D inversion scheme to avoid interpretation being biased by unreliable data with a high number of artefacts. A 3D inversion scheme is known to be more computer intensive than 2D inversions, which makes the latter more appealing for those without the resourced needed for a 3D inversion. For example, a single 2D inversion for Bartley Dam took less than one hour, whereas for a 3D inversion took over one day and the running of a time-lapse dataset would take several days, as opposed to several hours in 2D. A 2D inversion is able to capture the overall geometric spread of the resistivities, meaning that the 2D inversion can still be useful for identifying features evident from the resistivity in a standalone inversion. However, 3D inversions should be focused on for any time-lapse analysis, given the lower likelihood of it being able to represent a reliable dataset showing change over time without artefacts.

## 5.6 Summary

Bartley Dam is an earth-fill embankment dam in Birmingham, UK which has documented seepage since construction, in a highly fractured bedrock. Previous remediation has included grouting, but water continuously found new fracture zones to travel down. Subsequent geotechnical and geophysical investigations were undertaken for a greater understanding of the seepage. Such formed a basis for continued monitoring of the dam to observe potential seepage effects temporally and to observe seasonal variation. Commonly, inversions have used 2D modelling due to its more rapid output with a lack of computer intensive software. However, such data is likely to be contaminated with artefacts, resulting from 3D effects and high structural complexities. Therefore, 3D modelling of Bartley Dam, in conjunction with 2D modelling has been used to determine whether 3D modelling can better resolve a resistivity model and understand the causes of any resistivity variation.

The inversions at Bartley Dam for a 2D model and 3D model showed some consistency, including a more resistive sandstone, less resistive marl and services at the surface. However, the sandstone feature was noticeably less expansive in the 3D model, and some services were of a lower magnitude of resistivity. Such features in the 2D inversions may be a result of artefacts and insufficient rendering in the inversion. Significant variation was observed in the time-lapse analysis of the data between 2D and 3D models, where 2D inversions had several artefacts present due to the overfitting of data when observing the change in resistivity from the reference model. In contrast, 3D inversions had a more realistic spread of the data, with fewer artefacts present, indicating that 3D inversions can produce more reliable models than 2D and should be used for all time-lapse ERT surveys on dams. However, a true 3D ERT survey is optimal, where cross-line measurements can potentially generate more realistic resistivity distributions, because a 3D inversion is unlikely to eliminate all artefacts, even if it can reduce them.

3D inversions are still limited by the computational effort required, which may make such inversions less appealing to users, though the benefit as shown here is large. Though 3D inversions have shown promise in visualising ERT over 2D, true 3D surveys are likely to yield more reliable results. However, these are time consuming and may not bring optimal survey times for time-lapse monitoring. It must be noted that different sites are likely to differ significantly, so 3D inversions may not be as beneficial for sites more complex than Bartley Dam. A case study at an embankment at Paull Holme Strays will be assessed in the following chapter for further understanding of how 3D inversions may aid interpretation of embankments over 2D modelling. This will include the use of crosslines, which can build upon the understanding into how a 3D model can improve upon 2D.

# **6.0 A COMPARISON OF 2D AND 3D INVERSIONS, USING CROSSLINES, AT PAULL HOLME STRAYS, YORKSHIRE, UNITED KINGDOM**

## **6.1 Introduction**

The previous chapter considered of the performance of 3D and 2D inversions to monitor an embankment dam with time-lapse ERT. It was determined that 2D inversions could generate a visualisation of the subsurface in a standalone inversion which represented a realistic resistivity distribution, whereas time-lapse monitoring of 2D ERT data provided poor results with artefacts and poor sensitivity. With 3D modelling such artefacts were minimised and resistivity variations linked to potential seepage was better defined. Therefore, further assessment of 2D versus 3D inversions have been used on a tidal embankment at Paull Holme Strays, Yorkshire, United Kingdom to assess whether use of crosslines in 3D inversions can provide a more realistic resistivity image of the subsurface at the site.

As noted previously, the internal structure of small-scale embankments has been poorly resolved in 2D inversions, due to geometric distortion and 3D distribution of resistivities, which invalidate a true 2D assumption (Bièvre et al., 2018). Furthermore, previous synthetic evaluations of ERT for imaging tidal embankments have indicated that surveys will be influenced by 3D effects originating from varying water levels and resistivity with salinity (Ball et al., 2022), as seen in chapter two. Geometric corrections have been used for improving 2D inversions in embankment settings (Fargier et al., 2014; Bièvre et al., 2018), but have found use primarily for topographic variation and cannot account for other 3D effects (Bièvre et al., 2018). It has been suggested that 3D inversions of a 2D ERT measurement using a linear array can resolve some of the 3D effects observed in 2D inversions (Ball et al., 2022), due to moderation of in-line resistivities through interaction with other parallel electrode lines during a 3D inversion.

The focus of this study is on the benefits of using crosslines for inclusion in a 3D inversion, when compared with 2D, to evaluate whether the former can produce more realistic modelling of the resistivity profiles from interaction between electrode lines. On-site data has

then been used to determine the most suitable output from 2D and 3D inversions. The aims are therefore to determine whether use of crosslines in 3D inversions can improve upon 2D inversions and to further investigate whether 3D inversions are more reliable than 2D inversions.

## 6.2 Paull Holme Strays, Yorkshire, United Kingdom

Paull Holme Strays (Figure 6.1) is host to an embankment for flood defence, sometimes referred to as the Thorngumbald embankment (Jones et al., 2014). It is situated 8 km south-east of the city of Hull on the north bank of the Humber estuary (Smith et al., 2016). The current embankment was built in 2003 (VBA, 2014), after the breaching of an older embankment situated closer to the estuary, for the creation of salt marshes for ecological purposes (Dyer et al., 2009). Recent remediation has been undertaken to ensure the embankment is of a sufficient height, and to reduce potential settlement. The embankment is approximately 1500 m long (Smith et al., 2016), 3 to 4 m in height (Čejka & Beneš, 2015) prior to remediation, and protects a nationally important gas works with feeder pipes originating from the North Sea (VBA, 2014). The embankment is constructed from locally sourced alluvial clays, comprising kaolinite and illite, as well as quartz, calcite and dolomite (Jones et al., 2014). There is a 100 m length of the embankment (Smith et al., 2016) which experienced extreme settlement of up to 1.2 m between 2003 and 2014, and this contributed to an overtopping event with flooding in December 2013 (VBA, 2014). The extensive fissuring of the embankment had been noted from 2006 (Dyer et al., 2009) to 2014 (VBA, 2014). Previous borehole logs from site investigations indicate a peat layer within this region of settlement, believed to be a palaeochannel, which may have been the origin of the settlement (Smith et al., 2016; VBA, 2014).

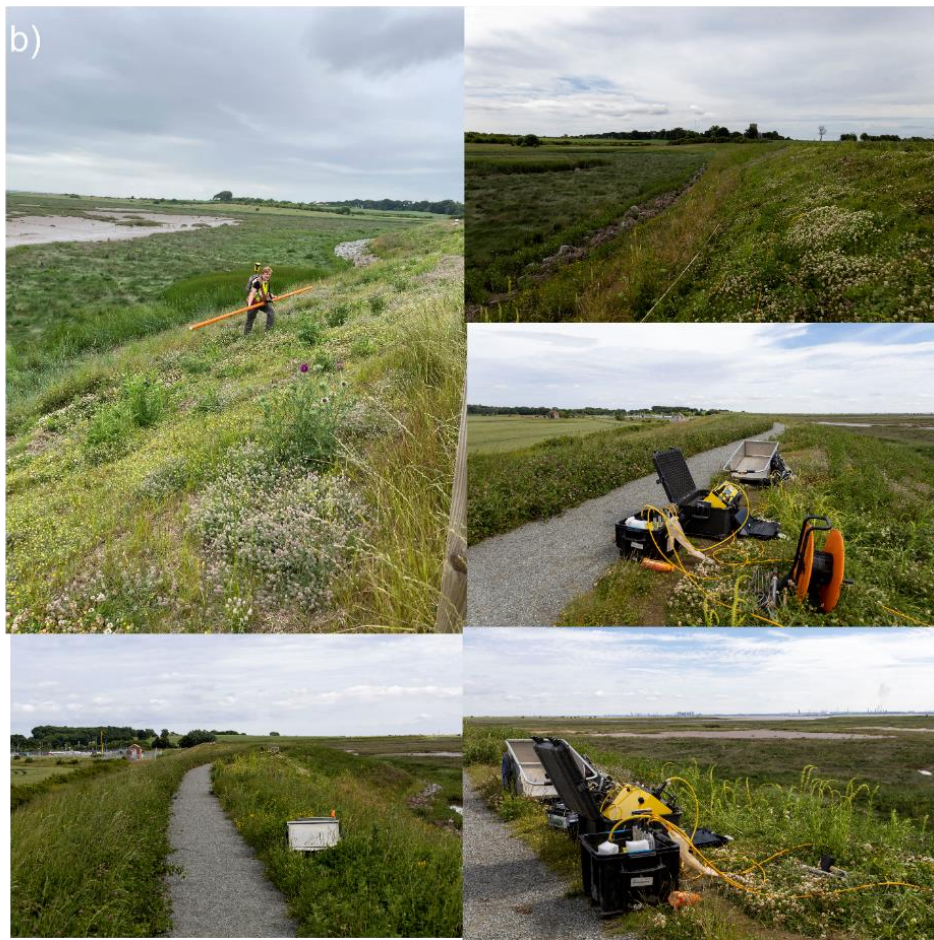


**Figure 6.1:** Paull Holme Strays, Yorkshire, United Kingdom ( $53.71^{\circ}\text{N}$ ,  $0.21^{\circ}\text{W}$ ) (Google Earth, 2023). a) Paull Holme Strays site location, where the area of the embankment surveyed is circled. b) Photographs from Paull Holme Strays.

Previous site investigations focused on several geotechnical investigations, including standard penetration testing, Atterberg Limits, triaxial testing, shrinkage testing, particle size distribution testing and chemical testing for nitrate, sulphate, chloride, magnesium and pH (Smith et al., 2016; VBA, 2014). The testing revealed high settlement levels and that the desiccation of clays was caused by shrink-swell initiated by climatic factors, undrained bearing capacity of the infill exceeded by the applied stresses (VBA, 2014). Previous geophysical exploration had been undertaken to survey the desiccation with electrical resistivity tomography (ERT) (Jones et al., 2014) and a further ERT and electromagnetic induction (EMI) survey for identification of inner structure post-flooding, planning for geotechnical investigation or remediation, and to adjust existing models (Čejka & Beneš, 2015). The results indicated a layer of fracturing up to 1 m below the surface (Jones et al., 2014) and extensive low resistivity features associated with highly plastic clays and peat (Čejka & Beneš, 2015). Several boreholes were drilled for site investigation in 2014 and the results are shown in Figure 6.2.

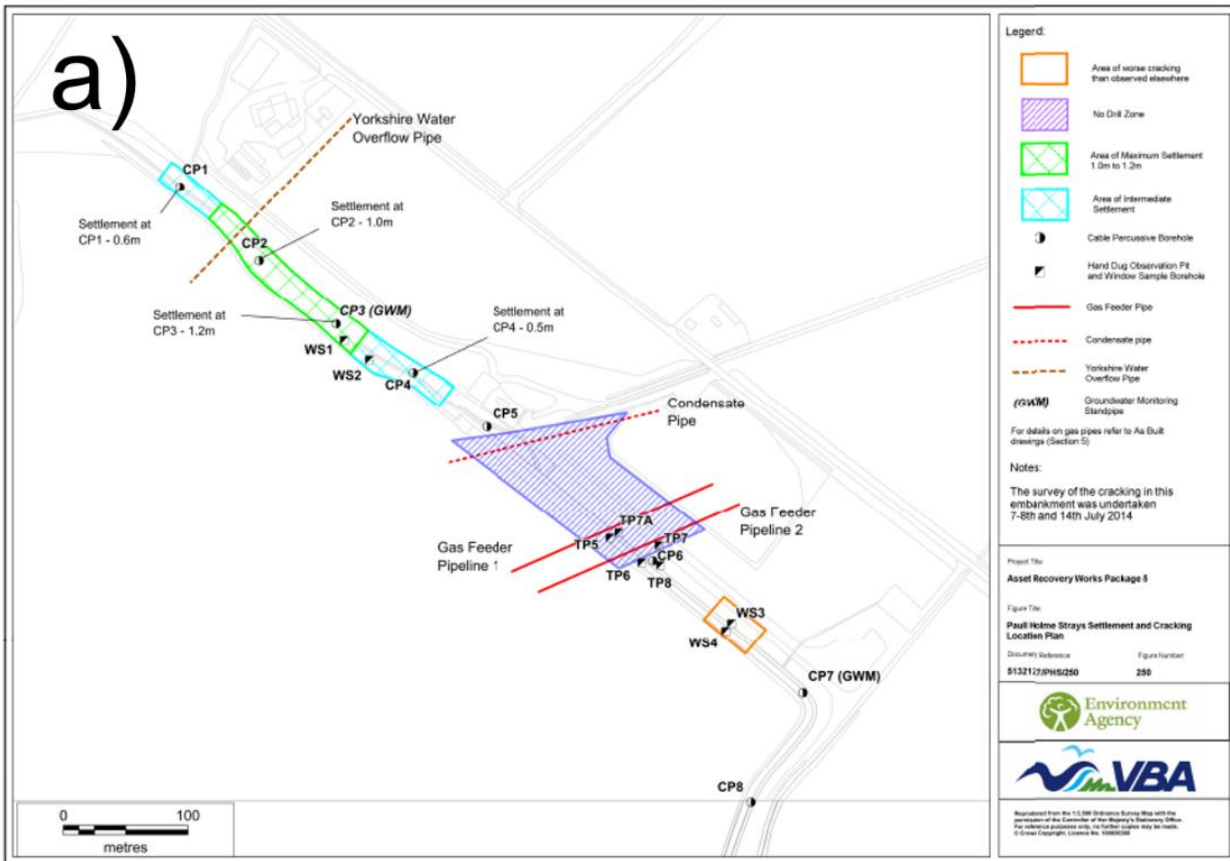


**Figure 6.2:** Geological boreholes drilled at the Paull Holme Strays embankment (VBA, 2014). a) A map of the boreholes drilled. b) Geological borehole logs and interpolation of geology between boreholes. CP1-3 are located within the ERT survey undertaken.



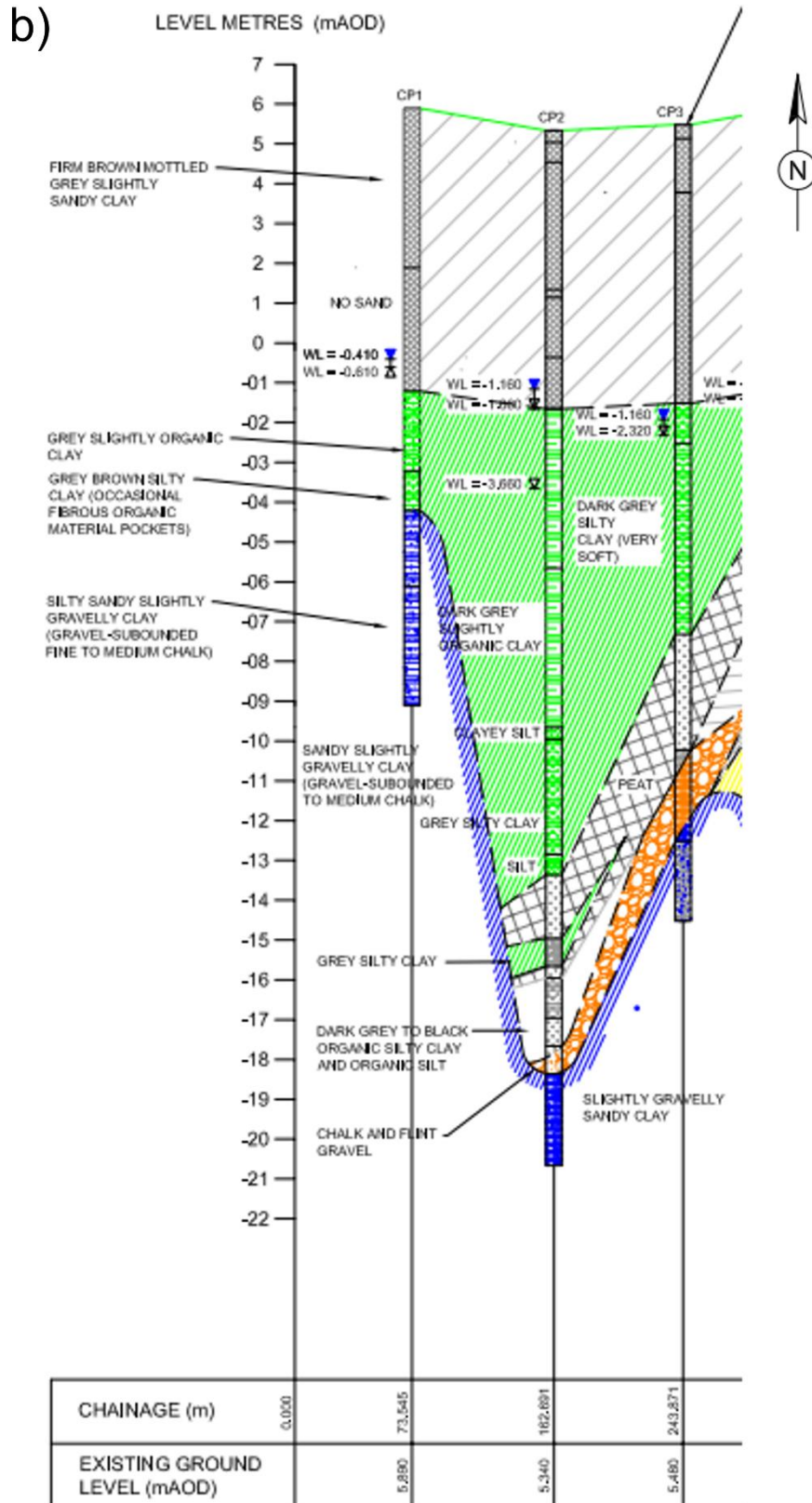


Figure 6.2 continued.

The underlying geology shows that the embankment infill extends to approximately 8 m below surface, which is underlain by silty clays. Between CP2 and CP3 there is a peat layer of 1-2 m thickness which varies from 21 m below surface to 14 m below surface.

The area of the embankment which had experienced high settlement was rebuilt between 2018 and 2021 to restore the embankment to its original height. The clay infill within the embankment core was replaced with lightweight aggregate contained within plastic sheeting, to both reduce any desiccation and reduce load and hence settlement. A geophysical survey consisting of an ERT and EMI survey was undertaken in June 2021, shortly after the embankment remediation was completed, for assessing ground conditions when the embankment was pristine. This could then be used as a reference for any future geophysical surveying to monitor future ground conditions. An EMI survey was also undertaken in October 2019 in a field behind the embankment for estimating the extent of the underlying peat layer.

The Paull Holme Strays site therefore presents an opportunity to determine the suitability of 2D and 3D inversions for monitoring such flood embankments. There are potential sources of 3D effects from the saline ground in the salt marsh, differing geology and topography which may impact 2D inversions, and 3D inversions may be able to mitigate some of these effects, as seen in chapter four. There were no crosslines incorporated into the Bartley Dam embankment, so inclusion of such at Paull Holme Strays allows assessment of their capability to improve inversion results.

## 6.3 Methodology

An initial field campaign to collect geophysical data at Paull Holme Strays was undertaken during June-July 2021, comprising of ERT and EMI. The ERT consisted of three major electrode lines (PHSLT1, PHSC1 and PHST2), with an electrode spacing of 3.5 m, running parallel to the embankment, and with two lines on either side of the crest and one running along the crest (Figure 6.3). These lines were 632m in length (PHST2), 444 m (PHSC1), and a third was limited to 344 m due to ground conditions (PHSLT1). PHSLT1 was located on the toe of the embankment furthest from the estuary, while PHST2 was positioned on the flank of the estuarine side of the embankment, due to difficult ground conditions towards the toe. Eight further crosslines were undertaken perpendicular to the embankment between the start and end of the lines running parallel to the embankment, using an electrode spacing of 1 m. The

EMI survey covered the area of the entire ERT survey and extended into the salt marsh for comparison and validation of the ERT data. The seismic survey was not used in the context of this research, so will not be discussed further.



**Figure 6.3:** Electrode lines used for the ERT survey at Paull Holme Strays, where PHSLT lines are those parallel to the crest and PHSX lines are crosslines perpendicular to the embankment.

The ERT surveys were undertaken using the SuperSting system (Advanced Geosciences, 2023), utilising a dipole-dipole array. PHSLT1, PHSC1 and PHST2 had an associated  $a$  spacing of 1-8 (i.e. 3.5 m – 28 m) and  $n$  spacing of 6, while the crosslines had an  $a$  spacing of 1-4 (i.e. 1 m – 4 m) and  $n$  spacing of 5.

The methodology for comparing 2D and 3D inversions at Paull Holme Strays was similar to that used at Bartley Dam (discussed in Chapter 5). Initially 2D inversions were undertaken of the three lines parallel to the embankment using the R2 software (Binley & Slater, 2020), with the L2 norm smoothness constraint. The finite element meshing software, Gmsh (Geuzaine & Remacle, 2020), was used to generate a mesh (Figure 6.4) for the inversion, using a characteristic length of 0.75 m, coarsening to the mesh boundary, which was set at approximately 500 m away from the electrode line to satisfy infinite boundary conditions.

Topography was added to the mesh for the site, using dGPS coordinates acquired for electrode locations. Before any inversion, filtering of data was needed to remove bad data points, including removing unpaired measurements (i.e. those without reciprocal measurements), negative apparent resistivities, measurements of greater than 50% reciprocal error and then of greater than 20% error after the fitting of a power law error model (Table 6.1). This was necessary due to the poor data quality resulting from the highly saline and conductive ground, causing poor results from low voltages in conductive ground if such were included in the inversion.

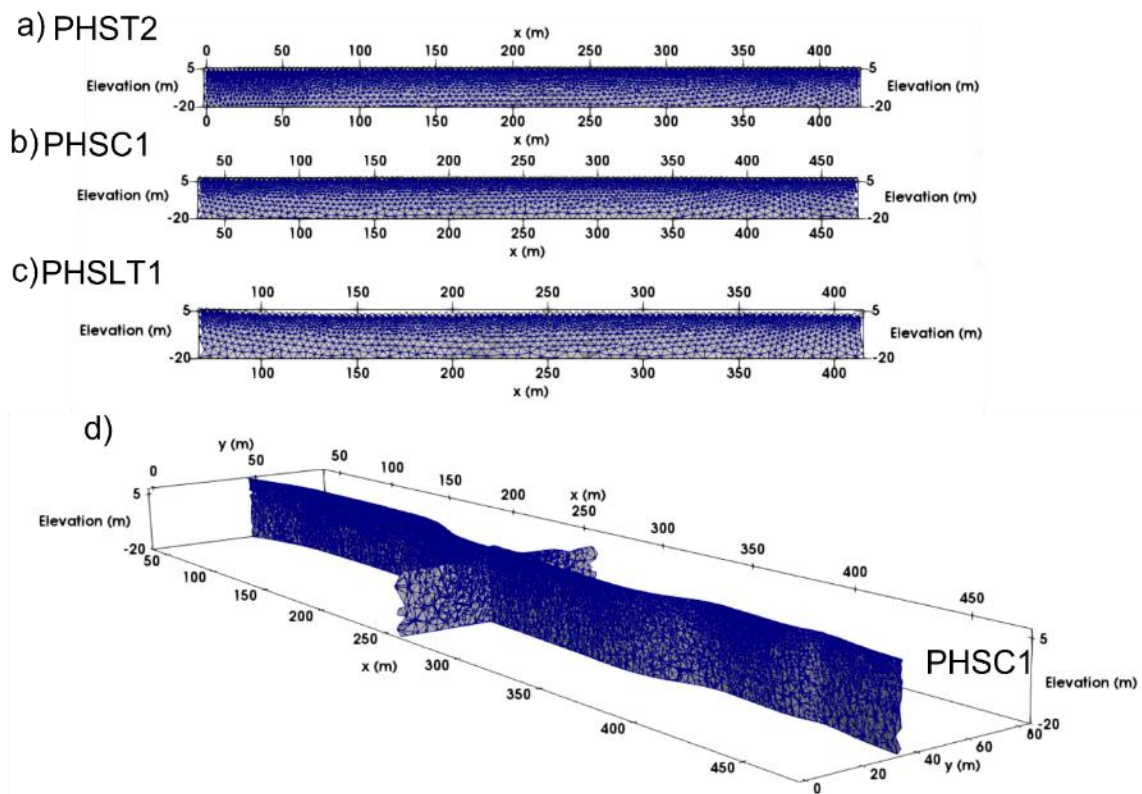


**Figure 6.4:** The mesh for 2D and 3D inversions. a) 2D mesh for PHST2 (10964 elements), b) 2D mesh for PHSC1 (8760 elements), c) 2D mesh for PHSLT1 (6687 elements), d) The 3D mesh through PHSC1 (1362302 elements).

**Table 6.1:** The number of data filtered from each electrode line and percentage unfiltered, used for analysis between 2D and 3D inversions.

Electrode line	Number of measurements	Negative data filtered	Unpaired measurements filtered	>50% reciprocal error filtered	>20% reciprocal error filtered post-error fitting in 3D modelling	Percentage unfiltered (%)
PHST2	12392	727	659	1572	1720	62.2
PHSC1	10085	125	114	248	330	91.9
PHSLT1	7379	664	417	1210	1252	52
PHSX1	2403	29	48	6	8	96.2
PHSX2	3040	28	44	66	34	94.3
PHSX3	1634	0	14	10	36	96.3
PHSX4	1648	38	38	82	56	87
PHSX5	1520	12	12	32	44	93.4
PHSX6	916	1	1	2	6	98.9
PHSX7	2362	0	0	0	2	99.9
PHSX8	2222	5	137	4	6	93.2

The 3D modelling utilised the same methodology as above for data quality assurance and used a characteristic length of 0.35 m, which coarsened towards boundaries set sufficiently far away to satisfy boundary conditions. The topography for the 3D model used a localised digital terrain model (DTM) from 2019 with a 1 m resolution, using Environment Agency acquired LiDAR data (Environment Agency, 2021), and used a spline interpolation for correct electrode location, where the centre of the pixel cell was assumed to be the true value for a coordinate. Alongside the three lines parallel to the embankment (PHSLT1, PHSC1 and PHST2), the eight crosslines were included in the inversion.

The EMI survey used a GF Instruments CMD Explorer with the horizontal coplanar orientation, coil spacings of 1, 2 and 3 m with nominal depth of investigations of 1.2, 2.1 and 4.2 m. The survey was carried out by walkover surveying and transections were undertaken parallel to each other, upslope, and at approximately 3 m separation. The results from this were converted to conductivity maps using the EMI processing software, EMagPy (McLachlan et al., 2021) which were then exported into GIS software for visualising the conductivity distribution across the site.

## 6.4 Results

The results from the inversions have been plotted as resistivity images for both 2D and 3D inversions, alongside histograms to show, graphically, the spread of the resistivity distribution underneath each relevant electrode line. The 2D inversions have focussed on PHSLT1, PHSC1 and PHST2 given their larger size and greater electrode spacing enabling the possibility of larger differences between 2D and 3D inversions. The eight crosslines were included for the 3D inversion. Alongside the ERT, the EMI survey results are shown for comparison between datasets.

### *6.4.1 2D Inversions*

Inversions of PHSLT1, PHSC1 and PHST2 are shown in Figure 6.5, with interpretations marked for internal features identified in the inversion. Figure 6.3 shows the location of the electrode lines used in these inversions.

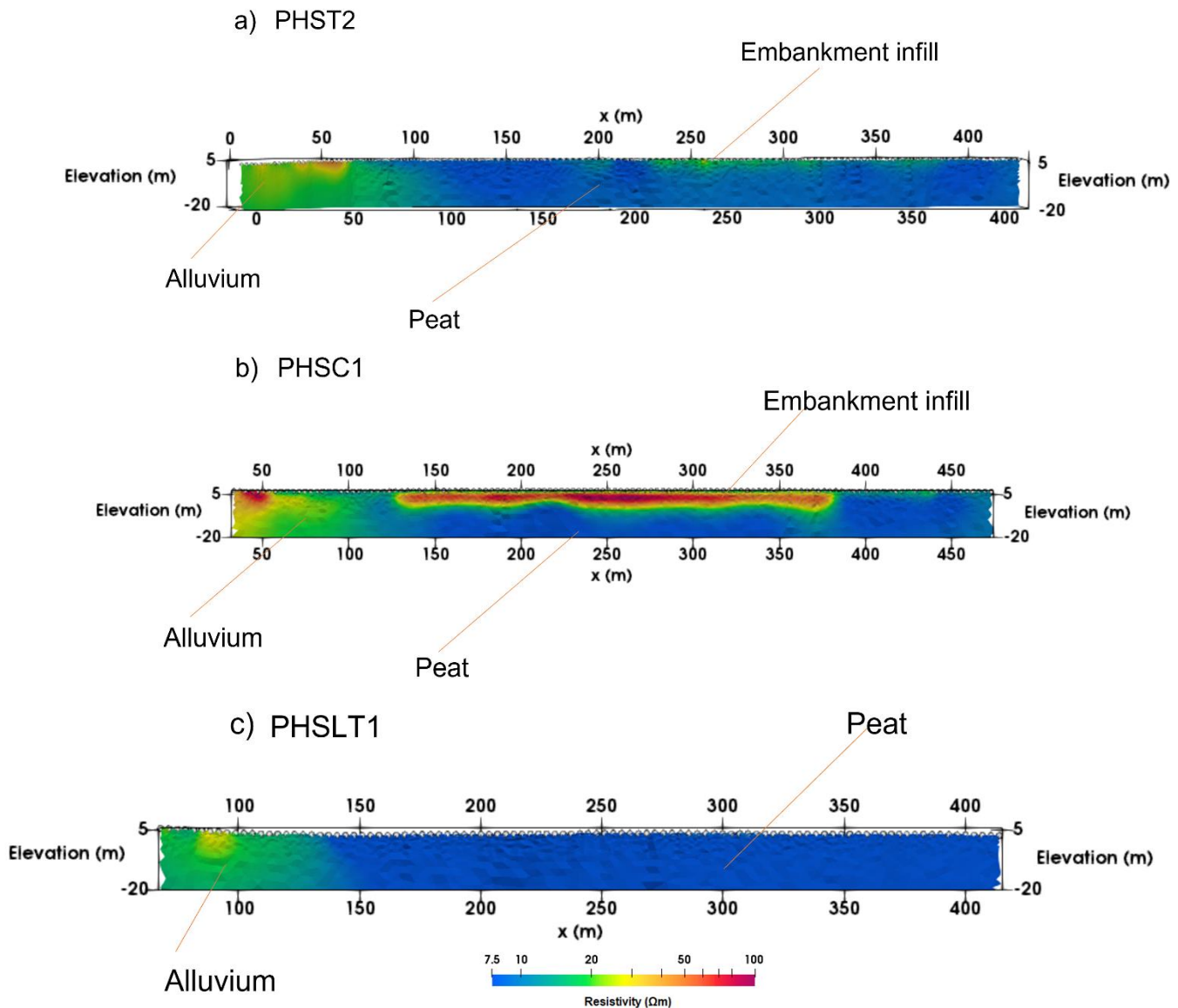


**Figure 6.5:** 2D inversions taken from the three longest lines parallel to the embankment, with a) PHST2, b) PHSC1 and c) PHSLT1. The x,y,z coordinates are the same for each line in the survey and the first line has been plotted from a different orientation due to its non-linear nature.

The 2D inversions show a more resistive feature (35-50 Ωm) between x= 0 and 150 m and a less resistive feature (5-10 Ωm) at x> 150 m, which is consistent between all lines. However, it should be noted that resistivities are low across the survey area, as expected in a saline setting adjacent to a salt marsh and estuary. The inversion shows a clear boundary between the more resistive alluvial deposits expected to the north (leftward on the x axis of Figure 6.5) and the less resistive peat to the south (rightward on the x axis of Figure 6.5). PHSC1 shows a more resistive feature underlying the crest of the embankment, which is interpreted as the

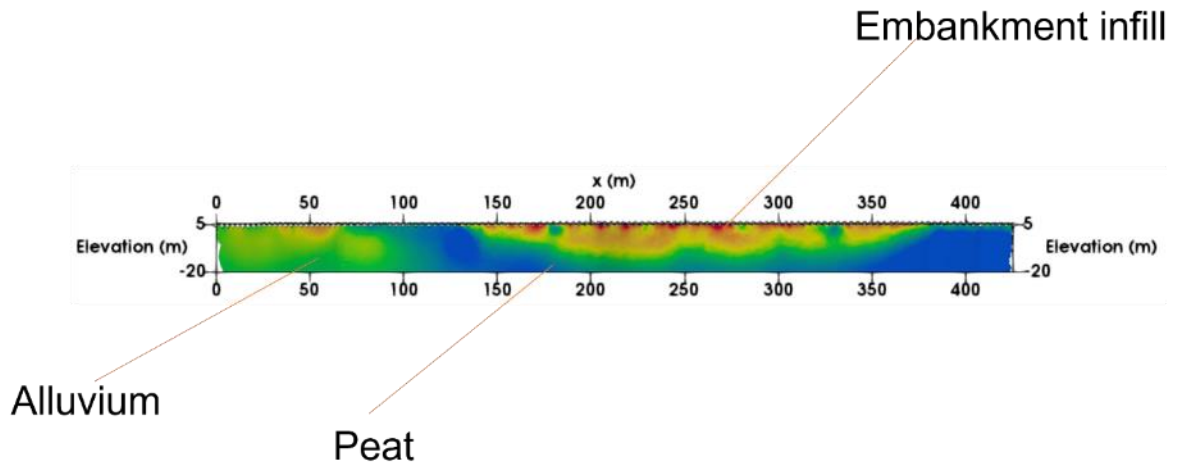
embankment infill, including the lightweight aggregate core. The plastic in which the clay is contained is believed to contribute to the higher resistivity. The low resistivity peat underlies the infill, at 5-10 m depth from surface, and its presence supports the previous interpretation of an extensive peat layer underlying the section with previous settlement observed.

#### *6.4.2 3D Inversions*

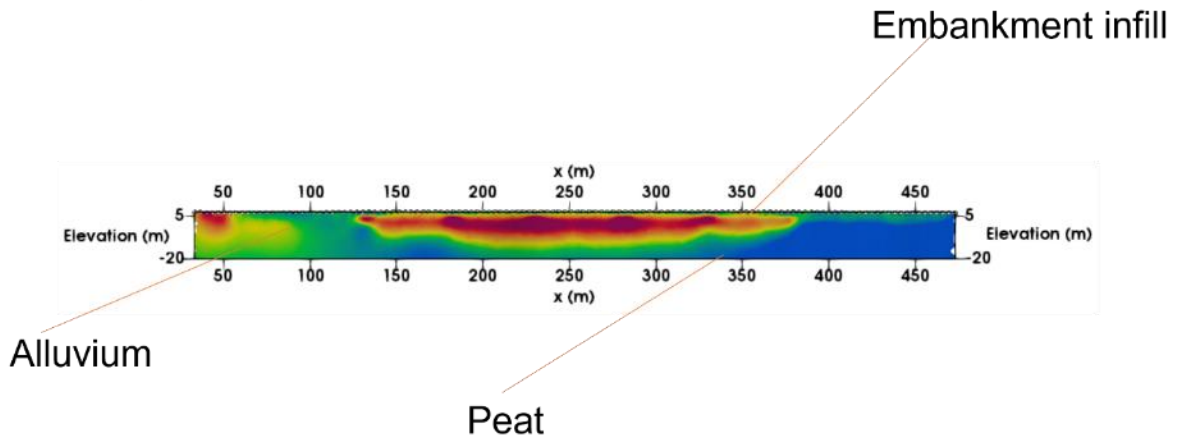
Using the 3D inversion results, vertical sections were extracted along lines PHSLT1, PHSC1 and PHST2 (Figure 6.6) for comparison between the 2D and 3D inversions of these lines.



a) PHST2



b) PHSC1



c) PHSLT1

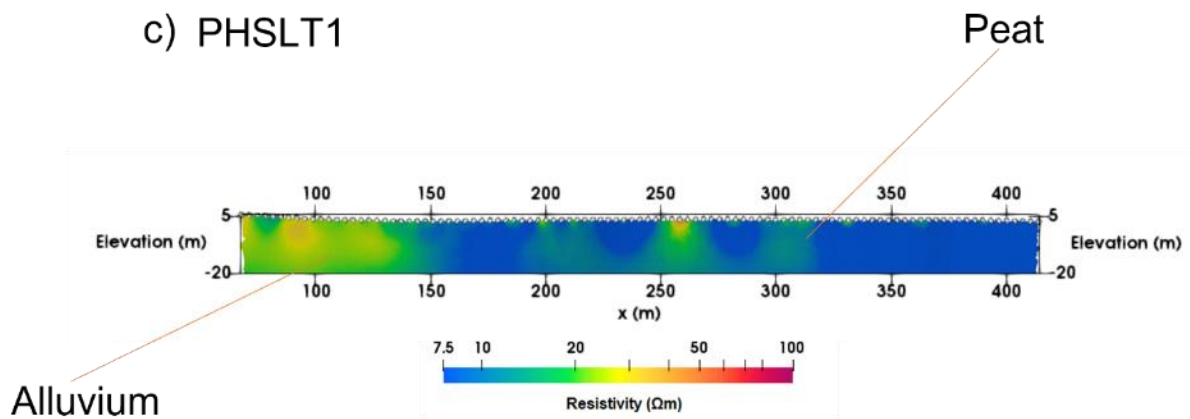


**Figure 6.6:** 3D inversions taken from the three longest lines parallel to the embankment, with a) PHST2, b) PHSC1 and c) PHSLT1. The x,y,z coordinates are the same for each line in the survey and the first line has been plotted from a different orientation due to its non-linear nature.

The 3D inversions for PHSLT1, PHSC1 and PHST2 show a similar overall trend to the 2D inversions in that an alluvium layer is distinguishable from the adjacent peat deposit and the embankment infill. However, there are some clear differences between the 2D and 3D inversions, where the more resistive embankment infill extends to greater depths in PHSC1 and PHST2, and PHSLT1 has more resistive features present. The 2D inversion of PHST2 data reveals a more resistive layer at the very upper surface (to approximately 5 m depth from the surface), but in the 3D inversion the feature extends down to approximately 10-15 m below the surface. Borehole logs (Figure 6.2) indicate that the made ground extends to 5-6 m below the surface, underlain by silty clays and peat, which is at 14-21 m below the surface. The silty clays are akin to the alluvium, so a higher resistivity is to be expected, and smoothing from the resistive core is likely to be present. Therefore, the 3D inversion more accurately captures the depth to the peat layer than the 2D inversion. Features representing the resistive peak in Figure 6.6b (of approximately 100  $\Omega\text{m}$ ) are at approximately 4-7 m below surface, which corresponds to the base of the embankment infill. For PHSLT1, there are resistive features that are not observable in the corresponding 2D inversion (such as at  $x=200$ , 260 and 300 m; see Figure 6.6c). In PHST2, the more resistive feature is continuous for a large section of the line and corresponds well with the resistive infill in PHSC1, but the resistive features in PHSLT1 are not continuous and resemble artefacts. This is evident when comparing them to the location of crosslines (Figure 6.7), which shows that these resistive anomalies are strong at distances further away from the crosslines, perpendicular to PHSLT1. It should also be noted that a high number of data were filtered for PHSLT1 (see Table 6.1), due to poor data quality. Therefore, with fewer data for line PHSLT1, the inversion may have been more readily biased in the 3D inversion by a concentration of higher resistivities in PHSC1. The alluvium appears more resistive in PHSLT1 for the 3D inversion than the 2D inversion, while resistivities are similar for the other two lines in this region for both inversions, indicating that with fewer data present the ability for the line to be strongly influenced by adjacent lines is high. A 3D effect on the 2D inversion from the salt marsh is a potential cause for the shallow depth of the resistive layer for PHST2, where the resistivities may have been influenced by the local, conductive ground in the marsh.

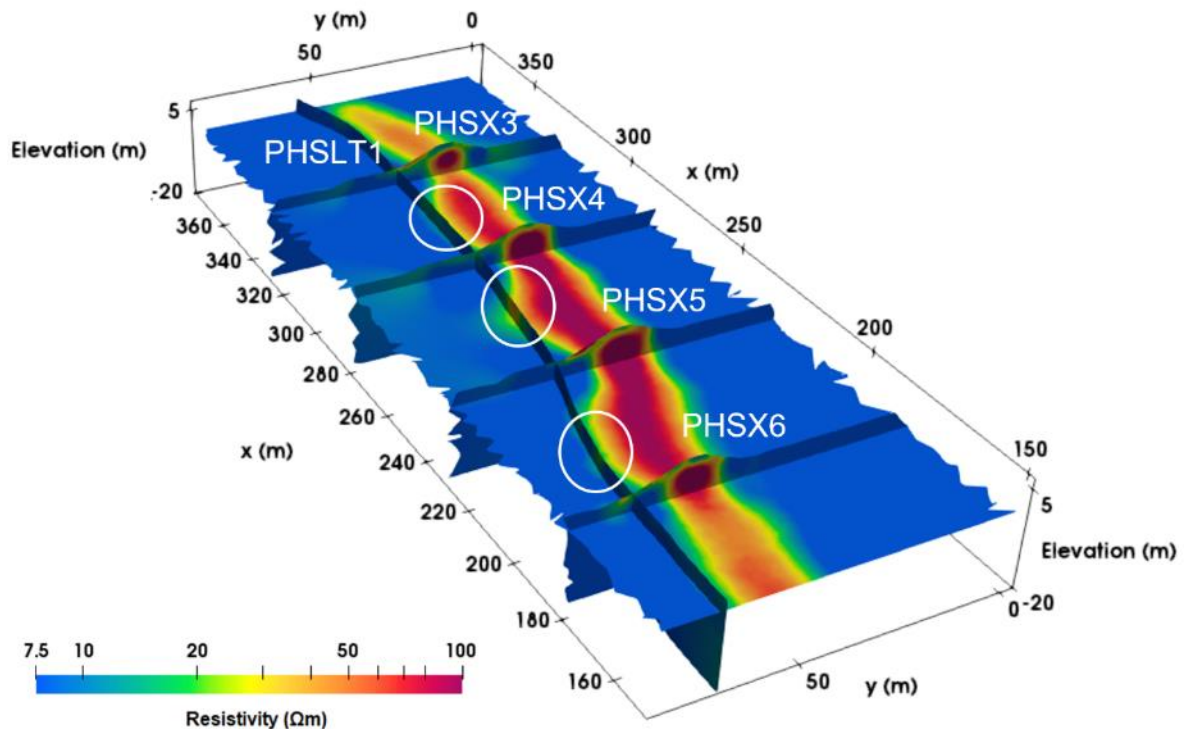


**Figure 6.7:** A fence diagram of the 3D inversion, showing PHSLT1 and selected crosslines for visualising the resistivity interaction between the line and that of the core, where intersections of the core resistivity and PHSLT1 are circled.

From Figure 6.7, it is evident that the anomalous resistivities identified in Figure 6.6c are present at approximately the midpoint between crosslines for PHSLT1. This indicates that these resistive features are most likely an artefact of the inversion from interaction between PHSC1 and PHSLT1. The lack of artefacts close to the position of the crosslines indicates that the inversion can better visualise the true resistivity from interaction between the crossline and PHSLT1, due to interaction between the lines in areas of high sensitivity. Whereas, in PHST2 the resistive feature is consistent across the line (Figure 6.6a). It should also be noted that PHSLT1 is sited off the embankment, while PHST2 is sited on the embankment, meaning that resistivities associated with the infill are expected for PHST2. The resistivity distribution for 2D and 3D inversions have been compared in histograms (Figure 6.8) for a more quantitative analysis of how the inversions differed.

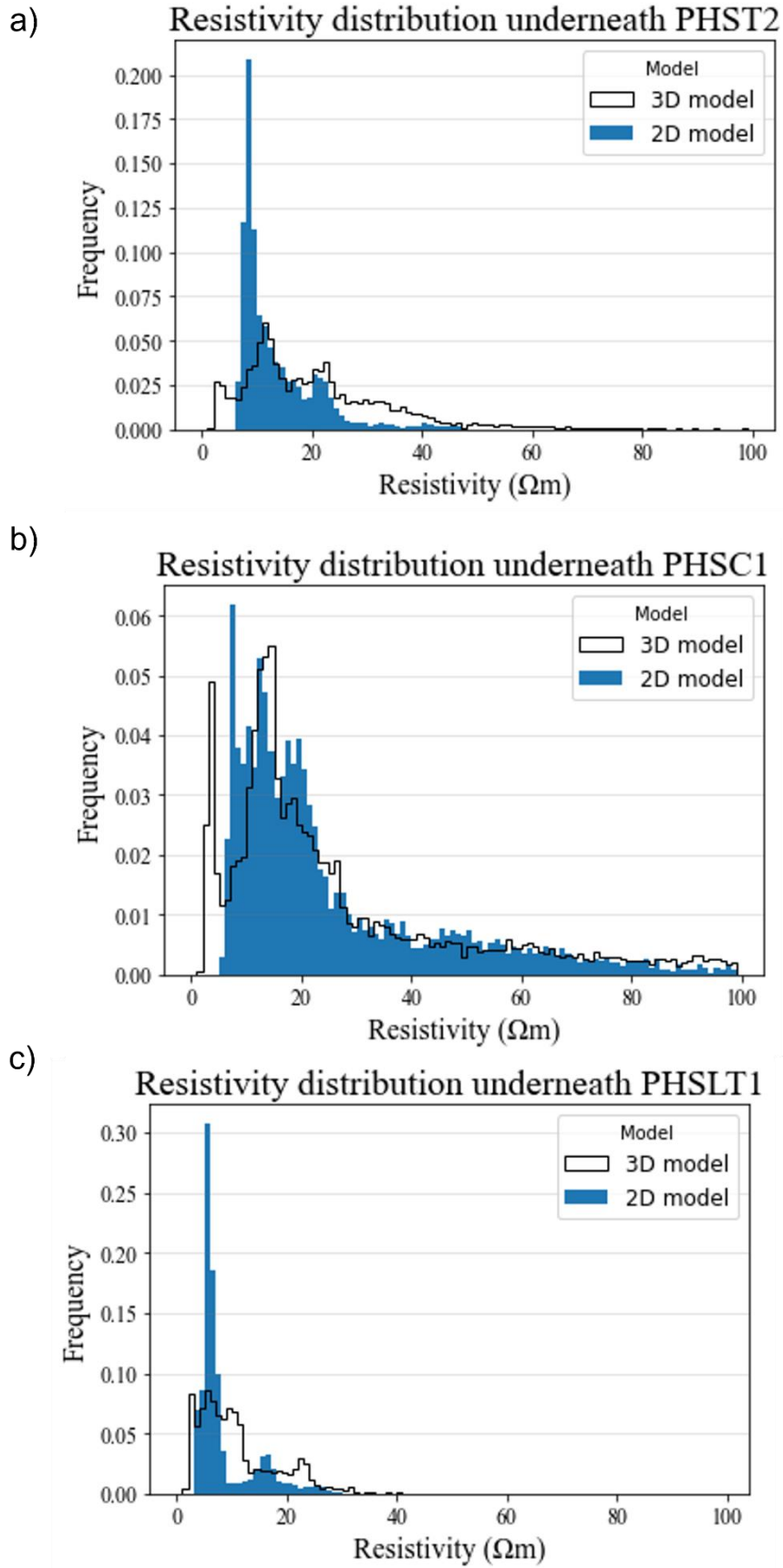


**Figure 6.8:** Histograms showing the resistivity distribution of 2D and 3D inversions underneath each respective electrode line for a) PHST2, b) PHSC1 and c) PHSLT1.

The histograms in Figure 6.8 show the resistivity distribution at Paull Holme Strays underneath PHSLT1, PSC1 and PHST2 to a depth of 20 m below ground surface. It is evident that for PHST2 and PHSLT1 that there is a steep decrease in the distribution of resistivities at 0-15  $\Omega\text{m}$  and an increase in resistivities greater than 20  $\Omega\text{m}$  in the 3D model. This shows how the resistivities in a 3D inversion are higher than their 2D counterparts and are likely being influenced by the more resistive PHSC1 or are more accurately capturing the resistivity underneath the line. For Figure 6.8b, there is more similarity between the 2D and 3D inversion. However, there is an increase in resistivity distribution of resistivities between 0 and 5  $\Omega\text{m}$  and between 15-20  $\Omega\text{m}$ , but a decrease between 5 and 15  $\Omega\text{m}$ , which are likely due to a slightly larger extent of the alluvium and artefacts.

### **6.4.3 EMI**

An EMI conductivity map has been developed from the conductivities collected from site for all depths from the horizontal coplanar orientation (Figure 6.9)

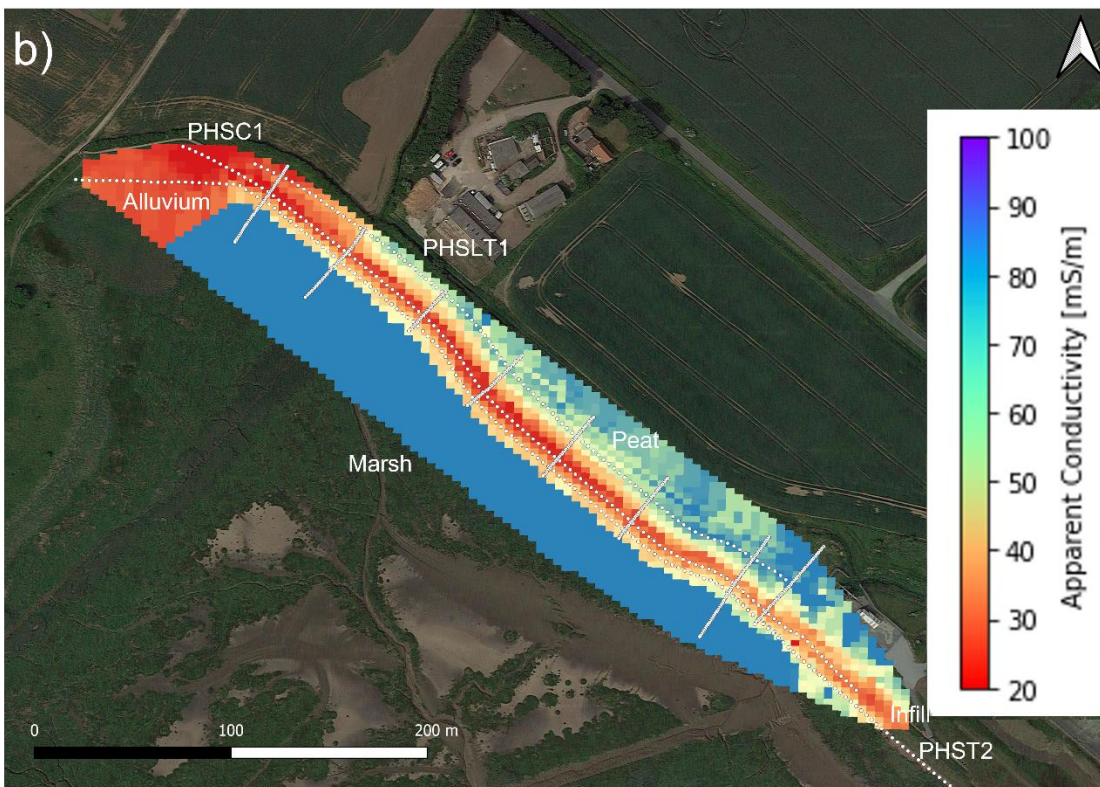
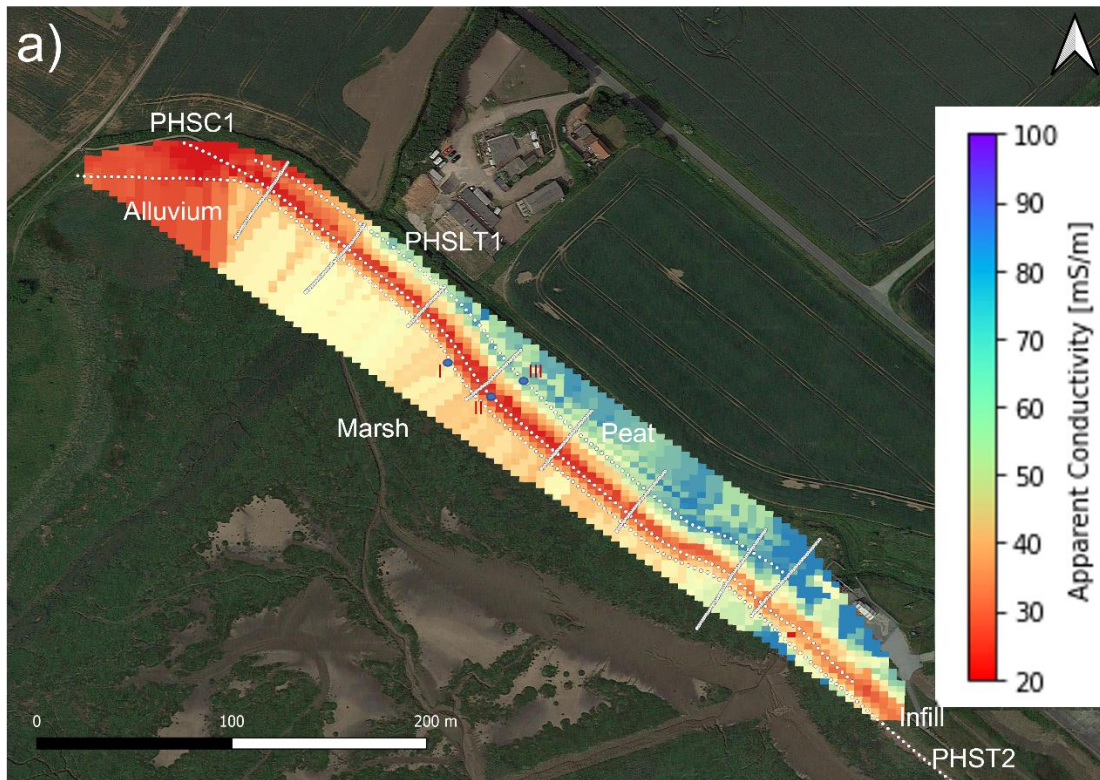


**Figure 6.9:** EMI conductivity map for Paull Holme Strays, encompassing the majority of the ERT survey area and salt marsh. The DOI is at 2.1 m with a coil spacing of 2 m. a) The conductivity with extreme values filtered from the salt marsh. I, II and III show the location of three points used for comparison between EMI and ERT data. b) The conductivity without extreme values filtered from the salt marsh.

The EMI shows a conductivity map from across the survey area and a section of the salt marsh. The salt marsh consisted of a highly conductive (greater than 100 mS/m) region, as can be seen in Figure 6.9b, which was filtered for values higher than 100 mS/m to give a more representative conductivity map (Figure 6.9a). The results from such filtering reveals a similarity to the ERT in that there is a clear boundary between the alluvium and peat, as indicated on Figure 6.9, especially on the landward side of the embankment, which is less affected by high conductivities associated with the salt marsh. The less conductive infill of the embankment is identified with lower conductivities across the embankment crest. Representative conductivities along each electrode line are shown in Table 6.2, taken from the points shown in Figure 6.9a, where they are compared with the resistivities from the ERT. The conductivity along PHST2 is approximately 40 mS/m (25  $\Omega$ m) for the bulk of the electrode line and is like that of the 3D inversion for the same line. This supports the interpretation that the presence of a more resistive infill beneath PHST2 to be real. While PHSLT1 is shown to be conductive in the EMI survey data, at 80-100 mS/m (approx. 10  $\Omega$ m) in the area of the peat, supporting the interpretation of resistive features in the ERT as artefacts.

**Table 6.2:** A comparison between the approximate conductivities from the EMI and ERT for both 2D and 3D models, from selected points along PHSLT1, PHSC1 and PHST2.

Comparison point (Figure 6.9a)	EMI Conductivity (mS/m)	Converted resistivity from EMI conductivity ( $\Omega$ m)	Resistivity from ERT ( $\Omega$ m) – 2D	Resistivity from ERT ( $\Omega$ m) – 3D
I	40	25	15	30
II	20	50	50	50
III	90	11	8	8

## 6.5 Discussion

The Paull Holme Strays site is an embankment adjacent to the Humber estuary which had experienced significant settlement before recent remediation. Geophysical surveying provided an opportunity to characterise the embankment, which included a newly reconstructed section, as a reference for any future monitoring. In addition, this site provided a useful opportunity to further assess the differences between 2D and 3D ERT inversions for

embankment imaging. Synthetic modelling of a tidal embankment had suggested that 3D modelling may better resolve artefacts generated in such an environment, arising from saline water (Ball et al., 2022), and further research at Bartley Dam indicated that 3D inversions can mitigate extreme resistivity trends in time-lapse data caused by 3D effects and overfitting. This study was used to complement past research in examining the differences between inversions along 3 lines parallel to the embankment crest (PHSLT1, PHSC1 and PHST2), which were of varying topography and ground conditions, for assessment of whether a 3D inversion with use of crosslines can better represent the data than a 2D inversion.

### *6.5.1 Use of Crosslines and Comparisons Between 2D and 3D Inversions*

The inclusion of the crosslines in the 3D inversion showed noticeable differences in resistivity distributions from the 2D inversions for PHSLT1, PHSC1 and PHST2. Both 2D and 3D inversions were able to generate a visualisation of the subsurface which corresponded to the geology of the site, with a more resistive alluvium to the north, and a less resistive peat layer to the south underlying the resistive embankment infill and core. However, the resistive infill and core extends to a greater depth in the 3D inversion and to a greater extent laterally, with a more pronounced layer in PHST2, and the alluvium is more resistive in PHSLT1 for a 3D inversion.

The differences between 2D and 3D inversions of data from the Paull Holme Strays site shows the potential benefits and limitations of using a 3D model with crosslines over a 2D model. There was a more realistic representation of PHST2 with a 3D model, given that this line was located above the flank of the embankment, meaning infill is likely to underlie the line. The 2D inversion of PHST2 only shows a thinner, less than 5 m thick, discontinuous resistive layer at the surface and a lower resistivity associated with peat immediately below. Whereas, the 3D inversion showed a peat zone extending to greater depths below the surface, in accordance with previous ground investigations (VBA, 2014). The saline marsh was close to PHST2 as evident in Figure 6.9b, which is characterised by high conductivity. In a 2D inversion, such adjacent features of anomalous resistivity have been shown to influence data as a 3D effect (Cho et al., 2014; Hojat et al., 2020; Ball et al., 2022), and this has been interpreted as a potential 3D effect from the salt marsh. However, the 3D inversion for PHSLT1 is less realistic, with several potential artefacts noted at shallow depths, most prominent in areas between crosslines. Natural variability was evident in the EMI, meaning anomalous



resistivities in the ERT could correspond to that, but the presence of these high resistivity features at the midpoint between crosslines suggests that this is likely to be artificial. This has been caused by biasing of the data in a 3D inversion from the more resistive regions in PHSC1, possibly due to the poor data quality in PHSLT1. A large proportion of data was filtered out in PHSLT1 compared to PHSC1 (see Table 6.1), during the data processing stage, meaning that the 3D inversion had fewer measurements underneath PHSLT1. Therefore, the resistive feature in PHSC1 was able to influence resistivities in PHSLT1. PHST2 also had poorer data quality than PHSC1, so some biased influence from PHSC1 cannot be ruled out, but its similarity to the resistivities of the crosslines and EMI indicates a greater reliability regardless.

This research has demonstrated previous recommendations of using 3D inversions in tidal environments, where known conductive features linked to an estuary or coast are near and shown the benefits of incorporating crosslines to improve 3D modelling. However, filtering of data to account for poor data quality has shown to induce artefacts, resulting from 3D effects associated with adjacent electrode lines, especially when there is a strong contrast in resistivity between lines. High reciprocal errors were prevalent in the Paull Holme Strays ERT data and may be likely across many estuarine and other saline sites, because of the low voltages in conductive areas. This would potentially make a less reliable 3D representation of lines with poor data quality, due to the presence of such artefacts as observed in Figure 6.8b. Therefore, a 2D inversion may be more suitable in some cases for representing the resistivity distribution below ground. Ultimately, it is recommended that when assessing a site, 2D and 3D inversions are run so the interpreter can make a judgement for the best representation of the resistivity, while using supportive information gleaned from geotechnical, hydrological and geological data. If 3D inversions are ignored, the interpretation may be greater influenced by 3D effects from off-line features and overfitting, but in some circumstances, when a high degree of data filtering has been undertaken prior to inversion, the 3D inversion may induce 3D effects itself, as observed at Paull Holme Strays.

A summary of the key outcomes is detailed in Table 6.3.

**Table 6.3:** Summary of the key outcomes of research at Paull Holme Strays, Yorkshire, United Kingdom.

Aim	Outcome
Improve visualisation through use of 3D over 2D ERT	Overall, 3D inversions produced an improvement in visualisation of ERT, with a more realistic thickness of embankment infill in PHST2 than in 2D inversions. However, due to poor data quality and heavy data filtering, artefacts were induced in PHSTLT1 from influence of resistive infill values.
To determine the ability of crosslines to improve visualisation.	Crosslines improved inversion reliability. In PHSLT1, there were no artefacts proximal to where it intersected with orthogonal electrode lines.

### 6.5.2 Recommendations

The use of crosslines can improve model resolution, particularly at the intersections between lines. Further suggestions for mitigation of the issue with poor data quality would be to run further crosslines at small spacings between lines in areas of interest identified in interpretation of original surveying. It was observed that the resistivity for PHSLT1 was more realistic close to the crosslines, where the resistivities in PHSLT1 were likely being more strongly influenced by those in the crosslines than PHSC1. Therefore, a survey with such anomalies suspected should have a more realistic resistivity distribution if more crosslines are used in a further survey. Also, EMI can prove useful for comparing resistivity values and distributions, so should be used alongside ERT to help confirm interpretation. It is imperative that a thorough understanding of the resistivity distribution with 2D and 3D inversions is made before implementing any time-lapse monitoring scheme, to optimise survey design and realise where such 3D effects may be present. Previous chapters have shown the problems with overfitting and 3D effects generated with 2D modelling of time-lapse data, which may distort results and influence interpretation.

## 6.6 Summary

Paull Holme Strays is an earthen, clay-fill, embankment along the Humber Estuary, near Hull in the United Kingdom. After breaching of an old embankment for the creation of a salt marsh in 2003, the newer embankment experienced significant settlement above a peat palaeochannel, until it underwent a remediation programme between 2018 and 2021. Geophysical reconnaissance surveys were undertaken in June 2021, shortly after remediation, to visualise the subsurface during pristine conditions. This included ERT and EMI, which were used to continue assessment over the potential for 3D inversions to better resolve resistivity distributions than 2D inversions due to minimising of 3D effects. The focus being specifically on whether the inclusion of crosslines can improve ERT visualisation.

The 3D inversion showed some improvement for some electrode lines, but induced artefacts in others where there was a strong contrast in filtered data and resistivity contrast. For lines situated on the embankment there was a more realistic size for the resistive feature, associated with the infill and clay core, while in the 2D inversion the infill was of a shallower maximum depth than indicated by site investigations. This helps give evidence for the potential for the use of crosslines in 3D ERT to resolve 3D effects in inversions, such as that from a conductive salt marsh in an estuarine setting. However, poor data quality is possible in highly conductive environments, like tidal embankments, and filtering of data is likely, which could make 3D inversions prone to bias from other lines.

This shows the need for judgement to be made over the suitability of 2D or 3D ERT in such sites where data quality is poor. It is recommended that 2D and 3D inversions are used and an assessment of the data for both scenarios is undertaken to ensure interpretation is reliable. Alongside this, further EMI surveying is recommended and more intensive ERT surveying in areas of interest would be beneficial. Overall, this study demonstrates that 3D ERT inversions can provide a more realistic visualisation, so should be included in ERT surveying, but the interpreter must be aware of limitations from poor data quality and the potential for 3D effects to be induced by interaction from resistivities in adjacent lines which might not be real.

# 7.0 DISCUSSION

## 7.1 Introduction

This thesis comprises four research chapters with a unifying theme of assessing 3D effects associated with ERT surveys of water retaining earthworks (i.e. dams and flood embankments). In particular, consideration has been given to influence of adjacent water bodies and considered ways of improving upon traditional 2D surveying and analysis through the use of 3D modelling and inversion. This chapter discusses how the results from chapters 3 to 6 can be unified to address the overarching research questions identified in chapter 1, i.e.:

- 1. Do ERT models of water retaining earthworks need to account for 3D effects resulting from their contextual environment?**
- 2. Does a 3D inversion produce a better visualisation of the resistivity distribution than 2D inversions, with fewer 3D effects present?**
- 3. How does temporal variation impact upon 3D effects and an ability of 2D or 3D inversions to visualise resistivity?**
- 4. What measures should be taken in survey design and data processing to reduce the impact of any 3D effects?**

The discussion that follows will focus on how each of these questions have been addressed. The findings will then be discussed in relation to the literature to answer how it builds on previous research on the use of geophysics for water retaining structures and addressing 3D effects on ERT. The chapter will then finish with a discussion on where future research could build upon this study to enhance geophysical surveying and monitoring of water retaining structures.

## 7.2 Thesis Outcomes

### *7.2.1 The Impact of 3D Effects on Water Retaining Structures*

The first research question relates to the impacts of 3D effects arising from the context of a flood embankment or dam. Chapter 3 focused on fluctuations of water level and resistivity, due to salinity, in a tidal setting, and chapter 4 focused on a structurally complex dam, with a headpond and a heterogeneous internal structure. The associated synthetic modelling for these chapters was used to observe distortions in resistivity resulting from the suspected source of a 3D effect, when assigning resistivities to embankment regions (*e.g.* water body, core, abutment).

The results from these models demonstrate distortions of resistivity within the inversion resulting from the presence of a 3D effect. Chapter 3 showed that fluctuating water levels and water resistivities, outside of the survey area or line, can influence ERT data and resulting inverse models. These changes in resistivity were compared with a case study from Hadleigh Marsh, in which it was apparent that a 3D effect is present. Chapter 4 provided further evidence of how the water body can impact data, using Mactaquac Dam as a basis for synthetic modelling. Various headpond resistivities were modelled in a difference inversion, which revealed distortions within a time-lapse model, which is discussed further in section 7.2.3.

Chapter 4 also looked at how 3D effects in ERT data can arise from the presence of heterogeneity and internal geometry. By analysing ERT images due to different resistivities assigned to a concrete abutment at Mactaquac Dam, the influence of the concrete structure is apparent. Specifically, there was a noticeable anomalous reduction in the resistivity above the concrete abutment, which corresponds to the patterns of resistivity in the same area within the real inversion, for all modelled resistivities, showing its effect on an inversion. This corresponded to the synthetic modelling (Chapter 3), which included a core, where lower than expected resistivities were present beneath the core, further indicating 3D effects can originate from structural geometry.

The results from the synthetic numerical modelling are not able to provide insight into the magnitude of a 3D effect for a universal set of environments. The nature of embankments

varies considerably, and each dam and flood embankment will have different topographic profiles, composition, water levels, resistivities, resistivity contrasts between different components, and dynamic variation with temperature and rainfall that makes generation of a global model which relates change in resistivity from a source of a 3D effect to the magnitude of the 3D effect impossible. The nature of the 3D effect may also be hard to predict with increasing complexity in internal structure. However, the results from this research do indicate potential impacts of a 3D effect in a dam or flood embankment setting. Therefore, it is suggested that proximity of a water body and internal structure should serve as a consideration for any ERT survey, given the internal structure and water body are likely to induce 3D effects in many contexts. These results support previous research which has suggested a 3D effect resulting in water retaining structures (Cho et al., 2014; Hojat et al., 2020) and have developed upon this to consider other factors besides the water body (*e.g.* internal structure). It is recommended that, for ERT surveys, an interpretation must consider the known geological, geotechnical and hydrological information in conjunction with resistivity for consideration over whether features observed are genuine. The resistivity of the water, water level and proximity to surveys and underlying composition needs to be known for optimal survey location and data interpretation.

The water level (in the water body that the barrier forms an embankment to) is likely to have the most significant effect when proximal to an ERT survey and with increasing electrical conductivity, as shown in chapter 3. Thus, ERT surveys located as far away as possible from the water body may be preferential, where possible. However, some surveys may be commissions in order to monitor the embankment slope on the river/reservoir side, thus resulting in a greater susceptibility to 3D effects. It has therefore been recommended that 3D surveying is optimised as much as possible and use of 3D inversions could mitigate effects, which will be discussed further in 7.2.2. Chapters 5 and 6 showed that the results from 2D inversions are more strongly influenced by 3D effects. The internal structure of a water retaining structure may be a strong source of 3D effects and can be difficult to account for in 2D models and analysis. The results demonstrated here shows how 3D effects are likely to be a significant issue, which may affect ERT in various different settings besides water retaining structures, as observed when monitoring the effect of buried pipelines and the associated 3D effect (Hung et al., 2019).

### *7.2.2 The Applicability of Using 3D Inversions over 2D Inversions to Account for 3D Effects*

The use of true 3D ERT surveying will clearly provide a more accurate assessment of the 3D variation in resistivity. However, such surveys may not be feasible over large water retaining structures due to the significant increase in survey time. Therefore, investigations of whether a 3D inversion of 2D data can mitigate 3D effects that result from conventional 2D inversions have been examined for cases when true 3D surveys are impractical. The ability of 3D inversions to improve upon 2D inversions for reducing an impact from a 3D effect had been suggested and briefly explored in some literature (Cho et al., 2014; Hojat et al., 2020).

3D inversions were able to produce improved representations over 2D inversions, such as at Hadleigh Marsh for chapter 3, where the 3D inversions had fewer noticeable 3D effects than the equivalent 2D inversion. Similarly, chapter 4 showed that 2D inversions did not represent the resistivity distribution as accurately as the 3D inversion, where, for example, the shape of the internal features (*e.g.* the dam core) was not as well recovered in the 2D inversion.

Chapter 5 assessed the ability of ERT to detect suspected seepage, using reservoir level and rainfall data to target analysis of time-lapse inversions of monitored ERT data. This allowed assessment of whether a 2D or 3D inversions could reliably indicate potential changes in resistivity which could be related to seepage. Through this it was determined that a 3D inversion produced a more realistic geometric distribution of the resistivities and reduced artefacts in the difference inversions from 3D effects and sensitivity issues. Further discussion on the temporal nature of the ERT at Bartley Dam will be discussed in section 7.2.3.

The use of crosslines (orthogonal surveys) in a 3D inversion to improve visualisation of ERT over a 2D inversion was explored in chapter 6, which showed a more representative resistivity for embankment infill in a 3D inversion, while 2D inversions were less resistive, potentially as a 3D effect from a saline marsh and low resistivity peat deposits.

Chapter 6 showed limitations of 3D inversions in producing more realistic inversions over 2D models. There were several features of low resistivity noted in one longer line at Paull Holme Strays, at shallow depth, which occurred at the midpoint between crosslines. This was interpreted as a result of the 3D inversion being influenced by a highly resistive core feature

in an electrode line running along the crest, where an adjacent line of poor data quality and highly filtered data was likely strongly influenced by the larger concentration of unfiltered high resistivity values from the line above the crest. However, the ability to represent a more accurate resistivity distribution proximal to the crosslines demonstrates that crosslines can sufficiently aid in the inversion to produce realistic resistivities in lines perpendicular to the crossline, where problems from 3D effects and poor data quality in 3D inversions could be mitigated.

This study shows the benefits of using 3D inversions over 2D inversions, in the right context. Artefacts of anomalous resistivity at Bartley Dam were of a lower resistivity when modelled in 3D. Regular use of crosslines may help in 3D inversions to ensure resistivities in the lines perpendicular are more representative, though it is appreciated time constraints in surveying may be a barrier. Several lines across embankments may help improve the output, with greater interaction between lines in an inversion, moderating anomalous resistivities originating from a 3D effect. However, continued use of (more conventional) 2D inversions are still recommended for use, as a comparison, and may be more representative if there are discrepancies in the amount of data filtered between lines, where the highly filtered line may have strong influences from the larger number of data present in the largely unfiltered line.

### *7.2.3 Temporal Changes and the 3D Effect, and use of 3D Versus 2D Inversions*

The use of time-lapse ERT has increased over the last decade, with the advent of low power systems and increased availability of appropriate computational resources (BGS, 2021). In the context of water retaining structures, it is important to assess how ground conditions change seasonally and with the weather, since increased water content in the reservoir can induce seepage and play an important role in the formation of slope failure. Therefore, it is vital for ERT to be able to accurately assess resistivity changes in the subsurface over time, since such changes may be linked to changes in ground conditions, such as moisture content. As discussed, 3D effects present a challenge through distorting resistivity images, which can lead to misinterpretations or obscured data in difference inversions.

When interpreting the 2D inversions at Bartley Dam in chapter 5, it was difficult to locate potential seepage pathways due to striping in the difference inversion because of sensitivity distribution. This was interpreted to be a result of poor sensitivity at depth and a 3D effect



resulting from a high number of services present. It was noted that changes in resistivity were most prominent after periods of rainfall, which gave some indication as to their causes, but identification of the location of where water was infiltrating was difficult. The 3D inversions were able to produce an inversion with a more reliable change in resistivity from the reference model than a 2D inversion. Areas of decreased resistivity were observed close to the surface, indicating rainwater infiltration, and an area in the vicinity of the suspected seepage pathway also had a decreased resistivity at a greater depth. Resistivities in the area of the seepage area were able to be linked to effective rainfall, showing seepage is likely to be weather related and that 3D inversions can best identify this over 2D inversions.

Temporal variations from headpond resistivity and through identification of a seepage pathway were used to inform the Macaquac Dam synthetic model study. This showed the impact on a difference inversion from a 3D effect. With an increased resistivity of the headpond and region of wet rockfill, there was an expected increase in the change of resistivity within these associated regions. However, there was also a decrease in resistivity in the core as a compensatory effect from the change in headpond and wet rockfill resistivities. These changes in resistivity did not have a direct relationship to the change in headpond resistivity, but decreased with headpond resistivity increase, showing that interpretation of ERT in time-lapse analysis of water retaining structures should account for such potential compensatory effects close to the water body. This builds upon previous research, which has not focussed on time-lapse analysis of a 3D effect, except for controlled experimentation (Hojat et al., 2020).

#### *7.2.4 Mitigation of 3D Effects*

For interpretation of ERT it is important to understand where 3D effects in the inversion may be present, to avoid misinterpretation. It is therefore important to detail what is needed for mitigation or prevention of 3D effects in the ERT. Preventative measures could include optimised survey designs, where electrode arrays are emplaced at a significant distance from sources of a 3D effect (*e.g.* a water body) and timing of the survey to be undertaken when the tide is not at its highest and less likely to induce a 3D effect (Ball et al., 2022). This would require a pre-study, to determine tide times, and reconnaissance survey for identifying ideal survey locations for future assessment and monitoring.

Prevention will not always remove the potential for 3D effects. The complexity of the embankment structure, and necessity to emplace surveys in areas where 3D effects are likely, means that 3D effects could still be an issue. Methods of mitigation could include the use of 3D inversions, as discussed in this this thesis, along with use of crosslines in ERT surveys. Alongside this, the use of inversion algorithms to reduce the 3D effects resulting of topography may help reduce the issue (Fargier et al., 2014; Bièvre et al., 2018), and be expanded to account for other 3D effects in future research. However, use of mitigation for 3D effects are likely to be time consuming; therefore, it may be preferable to include as much preventative measure as possible to reduce processing time.

For the user of ERT it is important to have an understanding into work processes required for undertaking a survey. Therefore, a summary of measures suggested to be undertaken during ERT surveying and processing is given in Table 7.1.

**Table 7.1:** A brief overview of steps needed to be undertaken during an ERT survey at an embankment, with emphasis on ensuring the survey is optimised for a reduction in the 3D effect.

ERT step	Description
Undertake desk study	Research the field site. Gain an understanding of likely geological conditions and the nature of the embankment infill. Alongside this, research what other features are present at the embankment (e.g. abutment, services) and determine the local tide times, if the water body is tidal. Identify areas where may be of interest for surveying.
Reconnaissance survey	If a reconnaissance survey is planned, use the desk study to determine survey locations. Ensure ERT surveys are undertaken across the regions of interest in the embankment and undertake EMI surveys covering the survey area. If it is planned to run a survey close and parallel to the water body, undertake surveys at several distances from the water body to assess whether there is a 3D effect and where the 3D effect is reduced. Bear in mind the effects of tide if the water body is tidal. Process reconnaissance survey data.
Main survey design	From the desk study and reconnaissance survey (if applicable), design an appropriate survey location for the main survey. Information from previous steps should enable optimised locations of surveys where distances from 3D effect sources are known, and the survey is placed in an ideal location for observation of the embankment for its intended purpose.
Main survey	Once survey locations and setup are decided, the main survey should be undertaken or a time-lapse ERT system is installed, depending on the survey purpose.
ERT processing	After undertaking the main survey, or the first sets of data from a time-lapse survey are collected, check the data for quality and filter where necessary. If undertaking analysis of time-lapse, assess data across several initial dates to establish a baseline for inversions.

Table 7.1 continued.	
ERT inversions	Once suitable processing steps have been undertaken, quality has been assured and the forward model has been determined to be suitable, inversions should be undertaken. Ensure that 2D and 3D models are able to be run. The 3D model may present more realistic results than 2D, but the latter is useful to check and ensure model reliability.
Future surveying	The main survey is likely to have electrode arrays across a large region, so future ERT surveying could use a more concentrated survey, which may be a true 3D survey, for identifying features to a greater resolution. This might be undertaken in areas suspected to have issues with a 3D effect to determine the cause. Alongside this, electromagnetic induction (EMI) surveys can be used to corroborate ERT surveys.

### 7.3 The Applicability of the Research Outcomes to the Academic Literature

Other research has been undertaken with regards to the 3D effect in ERT, use of 3D inversions and time-lapse ERT for embankments and other contexts, as summarised in chapter 2. Hojat et al. (2020) used an experimental levee, with ERT, to test for 3D effects arising from the water body. Their results demonstrate an evident 3D effect at depth resulting from the water body and plexiglass container, where the 3D effects showed an amplification of the apparent resistivities by a factor of 1.5-2.7. This thesis has further demonstrated the importance of a 3D effect on such embankments with synthetic modelling at a fieldwork scale and emphasis on the importance of internal structure, besides water level, as discussed above.

Norooz et al. (2021) modelled potential 3D effects for an experimental dam at Alvkarleby, Sweden. Their modelling involved exploring different inversion types (*e.g.* L1 and L2 norm), mesh characteristics and array types and models with and without region control (where regions within the model can be assigned a specific resistivity for an inversion) to determine if hypothetical defects could be identified in ERT. The modelling showed that without region control, 3D effects can arise from the reservoir and obscure important information in the resistivity profile of the dam. In this thesis, modelling of a synthetic defect at Mactaquac Dam

in chapter 5 indicates that changes in resistivity from the emergence of a defect may be difficult to identify from a resistivity image, but could be observed more clearly by quantitative assessment of the distribution of model cell resistivities. This indicates that with prior knowledge of where a seepage zone may be located, quantitative assessment of how resistivity distributions change through time may be able to help identify leakage when compared with the ERT data and other information.

A number of previous studies have focused on the effect of the water level alone as a 3D effect from a water body (Cho et al., 2014; Hojat et al., 2020). The research documented here shows similarities in how the 3D effects from the water level impacted data, including enhanced 3D effects, larger electrode spacing (Cho et al., 2014), though further increases have the potential to reduce the 3D effect (Hojat et al., 2020). This thesis expanded on this with assessment of changing resistivities in the water body, where it was shown that changing resistivities in a water body can have an impact on the resistivity in an ERT array and in time-lapse ERT.

This study has furthered the understanding into the potential for 3D inversions to mitigate against 3D effects using quantitative assessments between 3D and 2D inversions at Bartley Dam and Paull Holme Strays. However, it has also shown potential limitations in their usage due to potential influence between survey lines, as discussed above. Therefore, this thesis has demonstrated the need to be cautious in interpretation. 3D inversions are likely to improve an assessment of a water retaining structure but a 2D inversion and use of other data are needed in case 3D models are unsuitable after a holistic assessment between ERT and other data.

The use of time-lapse ERT has increased in recent years, including continued use of 2D ERT inversions (Jodry et al., 2019), despite the risk of 3D effects present. Jodry et al (2019) incorporated topography into their inversion model to avoid 3D effects from geometric variation. However, this thesis has demonstrated that 3D effects can have a significant impact on time-lapse ERT data. Chapter 5 showed that 2D inversions were not able to sufficiently identify seepage in time-lapse analysis, while 3D could. While this thesis has focused on 3D effects, use of 3D over 2D inversions and time-lapse ERT in a dam or flood embankment setting, the findings are applicable to other case studies where ERT has been of use. 3D effects are ubiquitous and the problems inherent with 2D inversions will exist for other

environments, where time-lapse ERT is being increasingly used (*e.g.* Hilbich et al., 2011; Pellicer et al., 2012; Jouen et al., 2016; Uhlemann et al., 2016; Lapenna & Perrone, 2022; Nazifi et al., 2022).

## 7.4 Future Developments for Geophysical Monitoring of Water Retaining Structures

This thesis has attempted to provide further insight into the 3D effect on ERT data in the setting of a water retaining structure, alongside the use of 3D inversions and time-lapse ERT. While it is believed that the research has increased knowledge of how a 3D effect can impact data in a standalone and time-lapse inversion, in addition to how 3D inversions can improve assessment of resistivity variation, there are still avenues for future research to progress our understanding into this. It is important to note that this thesis primarily focused on ERT, and chapter 2 detailed the various other geophysical techniques which can be utilised on water retaining structures. Therefore, it is important to discuss potential research possibilities for assessment of water retaining structures using other geophysical methods.

### *7.4.1 Future Developments for Understanding the Impacts of a 3D Effect on Water Retaining Structures and how 3D Inversions may Improve Results*

A lot of the research in this thesis was directed to answering whether a 3D effect from the water body and internal structure can impact ERT data in the resistivities in the inversion. As discussed above, it was determined that 3D effects can influence the resistivity and will need to be understood and accounted for in an inversion scheme. However, such modelling of 3D effects made several assumptions for simplicity, which may not be valid in real conditions. For example, the synthetic modelling of Mactaquac Dam in chapter 4 looked at how a concrete abutment impacts resistivity data in isolation. While this demonstrated the potential impact on the resistivity from such a feature, it does not assess 3D effects with temporal variation of geoelectrical properties of the engineered structure. It is, therefore, suggested that further research could focus on examining temporal changes within internal structure in embankment settings. This would involve including temporal variation in saturated and unsaturated ground of varying composition (*i.e.* different regions of the dam) and include depth components where temperatures, and therefore resistivities, differ. This could then

provide a more accurate assessment of how 3D effects could impact data in an embankment setting with changes in ground conditions. The results of such research could then be applied to other scenarios, including synthetic modelling of defects in the embankment. Hydrological modelling could be used to provide estimations of changes in water content with time and through a defect, using known parameters like hydraulic conductivity for providing a synthetic model which accurately represents site data. This could then be assessed with real-life time-lapse data for greater assessment of whether 3D effects impact the data.

This study has focussed on the context of reservoir dams and flood embankments. The research has shown that interpretations of the nature and magnitude of any 3D effect will be constrained by several localised variables which make such interpretations impossible. They can, however, give a general indication for the context of the site being surveyed. To expand the understanding into how 3D effects impact water retaining structures, the impact of 3D effects could be applied to other structures, such as moraine and tailings dams, where different geologies and reservoir characteristics might have different impacts on the resistivities. Moreover, further settings could be explored for potential 3D effects in ERT. Other studies have focused on the impacts of buried pipelines (Hung et al., 2019) and topography (Fargier et al., 2014; Bièvre et al., 2018), but ERT has also been used for agricultural purposes (Turki et al., 2019), the cryosphere (Hilbich et al., 2011), landslides (Uhlemann et al., 2016), archaeology (Carr et al., 2020) and other purposes. 3D effects from the contextual surroundings (e.g. buried services, geology) are likely to affect these cases and further research into how it affects ERT data would be beneficial.

There have been attempts to use geophysical inversions with parameters for petrophysical relationships, though such methods cannot fully incorporate 3D effects (Zhang & Revil, 2015). There have been attempts to account for 3D effects on 2D survey lines numerically (Fargier et al., 2014). However, there are still concerns over the applicability for such methods, due to possible artefacts in data or a failure to account for large scale seepages (Bièvre et al., 2018). Utilisation and development of such methodologies may be beneficial to ensure that 3D effects in 2D surveys are reduced without affecting seepage detection or biasing the data.

Comparisons between 2D and 3D inversions when assessing models for 3D effects is recommended, to continue the understanding over whether 3D inversions can improve visualisation and mitigate 3D effects in standalone and time-lapse inversions. The research in

this thesis indicates that there may be contexts where 3D inversions do not improve data quality and might induce artefacts where data filtering has occurred in one line more than another, as seen in the Paull Holme Strays case study. The use of crosslines constrained the artefacts observed; therefore, further research on the use of crosslines in 3D modelling could be undertaken to verify this.

#### *7.4.2 Future Developments for the use of Other Geophysical Methods for Monitoring Water Retaining Structures*

ERT is not the only available technique for monitoring water retaining structures, as explored in chapter 2, where examples were shown using IP (Martínez-Moreno et al., 2018), EMI (Flores-Berrones et al., 2011), seismic surveying (Cardarelli et al., 2014), GPR (Almadani et al., 2018) and distributed temperature sensing (DTS) (Bersan et al., 2018). Therefore, it is important to discuss the areas in which these studies can be furthered to aid the understanding into the surveying and monitoring of water retaining structures.

There is substantial potential in using DTS in combination with self-potential (SP), due to the sensitivity of both methods to fluid flow. This creates an excellent opportunity to establish further reliability of results obtained by this method in different environmental settings. Further modelling development of temperature to help validate results (Bersan et al., 2018) and to aid interpretation is required, with increased data analysis needed to better evaluate results (Schenato, 2017). The need for this is particularly evident where there have been discrepancies between measured and modelled data (Yosef et al., 2018), so that models can incorporate more parameters, and possible symptoms of seepage which may alter temperature distributions through an embankment. Alongside this, hysteresis, time dependency and spatial variability caused by contact resistance from air gaps affect relationships between observed temperature change and soil moisture, which lessens the reliability of DTS when calculating moisture content for the purposes of leakage detection (Sourbeer & Loheide, 2016). Concerns over sensitivity of measurement within optical fibre cables is especially true for pressure or strain sensing, which require further demonstrations of an increase in measurement sensitivity for them to be considered sufficiently reliable for hydrogeological applications (Schenato, 2017). Active DTS methods may have the potential to detect seepage and estimate flow rate through timing of a cooling effect on the cable



induced by seepage from a fixed high temperature to a set low temperature. Research into these areas could progress its use as a technique for modelling seepage through water retaining structures.

The dispersion of surface waves in a seismic survey across a levee is poorly understood, depth estimations may be distorted by geometry and the limits of detection and localisation of the signal is not fully understood (Bièvre et al., 2017). Numerical modelling techniques in seismic surveying may be utilised to model wave propagation through embankments and aid understanding of how the seismic signal travels through the leakage zone, allowing thorough evaluation of how a seepage zone evolves (Bièvre et al., 2017).

Induced polarisation (IP) has shown promise for surveying and monitoring water retaining structures, due to the chargeability of clay minerals typically found in earthen embankments, and ability to monitor seepage, since increased water content can enhance polarisation (Martínez-Moreno et al., 2018). Further research into IP would benefit from laboratory experimentation into its use in embankment settings, where hypotheses for features observed in the field could be tested for in a laboratory scale embankment. For example, if IP is suggesting a seepage pathway through an embankment, an experimental dam could be set up to test for this, using parameterisation akin to the real embankment. Alongside this, IP could be used more commonly, in tandem with ERT, to generate more reliable interpretation and assessment of embankment behaviour.

Other research into electromagnetic induction (EMI) could focus on the use of this in more depth for surveying water retaining structures. This thesis and other research have commonly used EMI to produce a conductivity map; however, further use in inverting EMI data of a frequency domain can provide more stringent EMI results (McLachlan et al., 2017), which can be used for greater assessment alongside ERT. Use of calibration techniques, as used elsewhere (Lavoué et al., 2010), could provide more reliable estimation of conductivity from EMI for water retaining structures.

## 8.0 CONCLUSIONS

### 8.1 Thesis Summary

Water retaining structures are societally and economically important barriers used for the storage of water for human use, energy production, storage of contaminants and flood prevention in areas of human and economic importance. The maintenance of water retaining structures is important to prevent loss of water or ingress. However, progressive erosion of the embankment structures by piping, biological processes, scouring and other means can lead to development of seepage pathways and failure. This causes depletion of volume in a reservoir, reducing its efficiency, development of pathways for flooding and contaminants to enter protected aquifers, and slope instability. Therefore, it is vital that such assets are surveyed and monitored. Walkover surveying and geotechnical testing are commonly used to monitor embankments, but the former is limited by lack of visibility for internal structure and obscuration by vegetation, while the latter is limited by spatial constraints. Geophysical techniques have therefore been used to provide comprehensive assessment across embankments, detailing their internal structure. However, there are challenges in obtaining reliable data, with meaningful petrophysical relationships between geotechnical data, and misinterpretation of results because of artificial effects (*e.g.* the 3D effect in electrical resistivity tomography (ERT)).

This thesis has focussed on how our understanding into the 3D effect on ERT on water retaining structures can be improved, enabling a more thorough understanding as to what resistivity profiles might represent in an inversion. This was achieved using synthetic numerical modelling of a fluctuating water level retained by a hypothetical embankment, which was compared to real data, as well as synthetic modelling of the impact of the structural geometry and headpond at Mactaquac Dam, Canada. Alongside this, the use of 3D inversions was compared with 2D inversions at Bartley Dam, UK, for understanding whether 3D effects could be minimised in a 3D inversion. The addition of crosslines to a 3D inversion for the assessment of an improved model was tested for a flood embankment at Paull Holme Strays. Examination of temporal variability in resistivity at Mactaquac and Bartley Dam allowed the

assessment of how dynamic change through time could be impacted by 3D effects and whether use of 3D inversions could improve time-lapse inversions.

The results of the set of case studies show that the water body and structural geometry of the embankment have the potential to induce 3D effects, which will need to be accounted for in an inversion. Inclusion of heterogeneity in the synthetic numerical model for chapter 3 and at Mactaquac Dam induced artefacts in the inversion, which may lead to misinterpretation. Fluctuating water levels and changes in water resistivity can also induce 3D effects, especially when the water is proximal and saline. Time-lapse inversions can be severely hindered by a 3D effect, and it is evident that 3D effects can induce compensatory effects in a time-lapse inversion, which might also cause misinterpretation of ERT. For example, time-lapse inversions at Mactaquac Dam showed a decrease in resistivity with increased water resistivity, which was interpreted as a compensatory effect in the inversion and could lead to misinterpretations.

3D inversions are able to better visualise standalone and time-lapse inversions, where areas of seepage present could be observed more reliably at Bartley Dam. Similarly, inversions at Paull Holme Strays produced more realistic visualisations of the subsurface, especially where crosslines intersected with other ERT lines. 3D inversions generated more appropriate depths of the underlying layer and more realistic structural geometries when compared with 2D inversions. Time-lapse analysis revealed that 2D inversions were often contaminated by artefacts and unrealistic resistivity variations, while 3D inversions generated a more consistent change in resistivity, and changes in resistivity that could be attributed to known ground conditions (*e.g.* increased groundwater levels from rainfall). Interpretation of 3D inversions were able to produce clearer interpretations, where an area of potential seepage was identified at Bartley Dam.

## 8.2 Limitations

The synthetic numerical modelling in chapters 3 and 4 generated results which indicated a need for consideration of the 3D effect when undertaking ERT surveys in water retaining structures, due to the water body and internal structure. However, the ability for these models to be applicable to global embankments is minimal. Each river embankment or dam have unique characteristics (*e.g.* slope angle, internal composition, water body resistivity)

that make a global interpretation over the presence and magnitude of a 3D effect impossible. Moreover, development of a synthetic numerical model which can account for every factor linked to a 3D effect in ERT is difficult. The factors involved are complicated, and generation of a suitable model which accounts for every possible factor is limited by computation and scientific validity. The results have demonstrated the impacts of likely sources for 3D effects, and assumptions made have been stated. It is believed that the results indicated show the need to consider a 3D effect, despite the assumptions in synthetic models, especially since real ERT inversions show potential 3D effects.

3D inversions have, overall, produced more realistic representations than 2D inversions. However, 3D inversions might induce artefacts between different lines in cases where data filtering has been heavily used in one line compared to another, as observed at Paull Holme Strays. This could be mitigated with use of crosslines in a 3D survey. Moreover, 3D inversions at Bartley Dam and Paull Holme Strays were not true 3D surveys and will likely be less reliable than such. Therefore, the inversion assumes a continuous resistivity between ERT lines and variation will not be detected given the lack of cross-line measurements. However, true 3D surveys are time consuming, so use of 3D inversions for surveys that don't include 3D measurements may be beneficial to produce more reliable inversions and include more surveys with the lack of time constraints.

### 8.3 Future Research

For future research it has been suggested that further modelling of 3D effects is undertaken for other water retaining structures besides reservoir dams and flood embankments, alongside other contexts (*e.g.* landslides). The way structural geometry can impact as a 3D effect could be better understood if a more dynamic assessment is undertaken to model how temporal variation of resistivity in regions changes with variations in temperature and groundwater input through the year. This would allow a greater comparison as to how 3D effects impact a real inversion for a given case study. Further assessment of 2D and 3D inversions are suggested to be undertaken for these different scenarios. Development of inversion algorithms for reducing 3D effects would be beneficial for mitigation of artefacts, especially as the risk of 3D effects is unlikely to be nil.

The need to monitor water retaining structures will continue to grow and the use of geophysical investigations of such structures will also inevitably increase. Given its demonstrable sensitivity to moisture content, and the importance of water in embankment failure and degradation, ERT is likely to be one geophysical tool used for this purpose. Incorrect interpretation of geophysical data, such as the 3D effect on ERT, in such a context could have significant consequences and thus the need to assess the reliability of geophysical models and their susceptibility to false positive or negative anomalies remains an important challenge.

## References

- Adams, R. ., Miller, B. ., Kress, W. ., Ikard, S. ., Payne, J. ., & Killion, W. . (2021). Evaluation of Electrical and Electromagnetic Geophysical Techniques to Inspect Earthen Dam and Levee Structures in Arkansas. *Journal of Environmental and Engineering Geophysics*, 26(4), 287–303.
- Advanced Geosciences. (2023). *SuperSting WiFi*. <https://www.agiusa.com/supersting-wifi>
- Agostinetti, N., & Bodin, T. (2018). Flexible Coupling in Joint Inversions: A Bayesian Structure Decoupling Algorithm. *Journal of Geophysical Research: Solid Earth*, 123(10), 8798–8826. <https://doi.org/10.1029/2018JB016079>
- Ahmed, A. S., Revil, A., Abdulsamad, F., Steck, B., Vergniault, C., & Guihard, V. (2020). Induced polarization as a tool to non-intrusively characterize embankment hydraulic properties. *Engineering Geology*, 271(March), 105604. <https://doi.org/10.1016/j.enggeo.2020.105604>
- Akhmetov, Y. M., Shaytorov, V. N., & Assemov, K. M. (2020). *Geophysical survey of earthen dam using*. 50, 249–259. <https://doi.org/10.31577/congeo.2020.50.2.4>
- Almadani, S., Ibrahim, E., Hafez, M., Alfaifi, H., Alharbi, T., Abdelrahman, K., & Abdel-Motaal, E. (2018). Geotechnical investigation of the El-Elb dam site, northwest Riyadh, Saudi Arabia, using 2D resistivity and ground-penetrating radar techniques. *Arabian Journal of Geosciences*, 11(2), 1–14. <https://doi.org/10.1007/s12517-017-3353-x>
- Almog, E., Kelham, P., & King, R. (2011). *Modes of dam failure and monitoring and measuring techniques*. Bristol, United Kingdom: Environment Agency
- Antoine, R., Fauchard, C., Fargier, Y., & Durand, E. (2015). Detection of leakage areas in an earth embankment from GPR measurements and permeability logging. *International Journal of Geophysics*, 2015, 9 pages. <https://doi.org/10.1155/2015/610172>
- Antonovskaya, G., Kapustian, N., Basakina, I., Afonin, N., & Moshkunov, K. (2019). Hydropower dam state and its foundation soil survey using industrial seismic oscillations. *Geosciences (Switzerland)*, 9(4), 1–16.

<https://doi.org/10.3390/geosciences9040187>

Arboleda-Zapata, M., Guillemoteau, J., & Tronicke, J. (2022). A comprehensive workflow to analyze ensembles of globally inverted 2D electrical resistivity models. *Journal of Applied Geophysics*, 196(March 2021), 104512. <https://doi.org/10.1016/j.jappgeo.2021.104512>

Arcila, E. J. A., Moreira, C. A., Camarero, P. L., & Casagrande, M. F. S. (2021). Identification of Flow Zones Inside and at the Base of a Uranium Mine Tailings Dam Using Geophysics. *Mine Water and the Environment*, 40(1), 308–319. <https://doi.org/10.1007/s10230-020-00746-y>

Baglari, D., Dey, A., & Taipodia, J. (2018). A state-of-the-art review of passive MASW survey for subsurface profiling. *Innovative Infrastructure Solutions*, 3(1), 66. <https://doi.org/10.1007/s41062-018-0171-2>

Ball, J., Chambers, J., Wilkinson, P., & Binley, A. (2022). Resistivity imaging : 3D effects with water levels Affiliations : 2 British Geological Survey , Nicker Hill , Keyworth , Nottingham , United Kingdom , NG12 5GG Acknowledgements : *Near Surface Geophysics*, 44pp. <https://doi.org/10.1002/nsg.12234>.

Barnes, A. . (1927). *Cementation of Strata Below Reservoir Embankments*. London, United Kingdom: Institution of Water Engineers.

Bersan, S., Koelewijn, A., & Simonini, P. (2018). Effectiveness of distributed temperature measurements for early detection of piping in river embankments. *Hydrology and Earth System Sciences*, 22(2), 1491–1508. <https://doi.org/10.5194/hess-22-1491-2018>

BGS. (2021a). *BGS PRIME: an early warning system for slope failure*. <https://www.bgs.ac.uk/news/bgs-prime-an-early-warning-system-for-slope-failure/>

BGS. (2021b). *Proactive Infrastructure Monitoring and Evaluation System: PRIME*. <https://www.bgs.ac.uk/geology-projects/geophysical-tomography/technologies/prime/>

Bi, W., Zhao, Y., An, C., & Hu, S. (2018). Clutter Elimination and Random-Noise Denoising of GPR Signals Using an SVD Method Based on the Hankel Matrix in the Local Frequency Domain. *Sensors*, 18(10), 3422. <https://doi.org/10.3390/s18103422>

Bièvre, G., Jongmans, D., Goutaland, D., Pathier, E., & Zumbo, V. (2015). Geophysical

characterization of the lithological control on the kinematic pattern in a large clayey landslide (Avignonet, French Alps). *Landslides*, 13(3), 423–436.

<https://doi.org/10.1007/s10346-015-0579-0>

Bièvre, G., Lacroix, P., Oxarango, L., Goutaland, D., Monnot, G., & Fargier, Y. (2017).

Integration of geotechnical and geophysical techniques for the characterization of a small earth-filled canal dyke and the localization of water leakage. *Journal of Applied Geophysics*, 139, 1–15. <https://doi.org/10.1016/j.jappgeo.2017.02.002>

Bièvre, G., Oxarango, L., Günther, T., Goutaland, D., & Massardi, M. (2018). Improvement of 2D ERT measurements conducted along a small earth-filled dyke using 3D topographic data and 3D computation of geometric factors. *Journal of Applied Geophysics*, 153, 100–112. <https://doi.org/10.1016/j.jappgeo.2018.04.012>

Binley, A. (2015). Tools and Techniques: Electrical Methods. In *Treatise on Geophysics: Second Edition* (Vol. 11). Elsevier B.V. <https://doi.org/10.1016/B978-0-444-53802-4.00192-5>

Binley, A., Daily, W., & Ramirez, A. (1997). Detecting Leaks from Environmental Barriers Using Electrical Current Imaging. In *Journal of Environmental and Engineering Geophysics* (Vol. 2, Issue 1, pp. 11–19). <https://doi.org/10.4133/jeege2.1.11>

Binley, A., Hubbard, S. S., Huisman, J., Revil, A., Robinson, D., Singha, K., & Slater, L. D. (2015). Understanding of Subsurface Processes Over Multiple Scales. *Water Resources Research*, 51, 1–30. <https://doi.org/10.1002/2015WR017016>.Received

Binley, A., & Slater, L. (2020). *Resistivity and Induced Polarization: Theory and Applications to the Near-Surface Earth*. Cambridge University Press.  
<https://doi.org/10.1017/9781108685955>

Birmingham Water Department (1931). *Report of the Water Committee Presented at the Meeting of the Council on Tuesday, the 10th day of March 1931*. Birmingham, United Kingdom: Birmingham Water Department

Bishop, A. . (1955). The use of the slip circle in the stability analysis of slopes. *Geotechnique*, 171(4), 7–17.



- Blanchy, G., Saneiyani, S., Boyd, J., McLachlan, P., & Binley, A. (2020). ResIPy, an intuitive open source software for complex geoelectrical inversion/modeling. *Computers and Geosciences*, 137(August 2019), 104423. <https://doi.org/10.1016/j.cageo.2020.104423>
- Boaga, J. (2017). The use of FDEM in hydrogeophysics: A review. *Journal of Applied Geophysics*, 139, 36–46. <https://doi.org/10.1016/j.jappgeo.2017.02.011>
- Bolève, A., Janod, F., Revil, A., Lafon, A., & Fry, J. J. (2011). Localization and quantification of leakages in dams using time-lapse self-potential measurements associated with salt tracer injection. *Journal of Hydrology*, 403(3–4), 242–252. <https://doi.org/10.1016/j.jhydrol.2011.04.008>
- Bond, A. J., Schuppener, B., Scarpelli, G., & Orr, T. L. L. (2013). Eurocode 7 geotechnical design. In A. V Dimova, Siliva; Nikolova, Borislava; Pinto (Ed.), *Structural Engineer* (Vol. 87, Issue 18, pp. 18–19). <https://doi.org/10.2788/3398>
- Borgatti, L., Forte, E., Mocnik, A., Zambrini, R., Cervi, F., Martinucci, D., Pellegrini, F., Pillon, S., Prizzon, A., & Zamariolo, A. (2017). Detection and characterization of animal burrows within river embankments by means of coupled remote sensing and geophysical techniques: Lessons from River Panaro (northern Italy). *Engineering Geology*, 226, 277–289. <https://doi.org/10.1016/j.enggeo.2017.06.017>
- Boulay, D. E., & Butler, K. E. (2021). Overcoming Signal-to-Noise Challenges with Pole-Dipole Resistivity Monitoring at a Hydroelectric Dam Site. *NSGG: 2nd Conference on Geophysics for Infrastructure Planning, Monitoring and BIM*, 1–5.
- Boulay, D. E., Butler, K. E., Mclean, D. B., & Campbell, I. (2020). *Commissioning an Electrical Resistivity Imaging System for Long Term Seepage Monitoring at a Dam Abutment*. 1–5.
- Bowles, D., Brown, A., Hughes, A., Morris, M., Sayers, P., Topple, A., Wallis, M., & Gardiner, K. (2013). *Guide to risk assessment for reservoir safety management Piloting summary report* (Vol. 1). Wallingford, United Kingdom: Environment Agency
- Boyd, R. (2008). *Nonlinear Optics* (4th ed.). Academic Press.
- Boyle, A., Uhlemann, S., Adler, A., Wilkinson, P. B., Meldrum, P. I., & Chambers, J. E. (2017). Jointly reconstructing ground motion and resistivity for ERT-based slope stability

- monitoring. *Geophysical Journal International*, 212(2), 1167–1182.  
<https://doi.org/10.1093/gji/ggx453>
- Brand, J. H., & Spencer, K. L. (2019). Potential contamination of the coastal zone by eroding historic landfills. In *Marine Pollution Bulletin* (Vol. 146, pp. 282–291).  
<https://doi.org/10.1016/j.marpolbul.2019.06.017>
- BSI. (2013). Eurocode 7: Geotechnical design. In *British Standards* (Vol. 3, Issue February 2009). <https://doi.org/10.2788/3398>
- Butler, K. E. (2022). *Maқтақуақ Dam Electrode Array and Topography*, Jan 27 2022.
- Butler, K. E., & Boulay, D. E. (2020). 3D Resistivity Monitoring for Seepage Assessment at an Earth Dam Abutment: System Design and Early Results. *Fifth International Workshop on Geoelectrical Monitoring, Gelmon*.
- Butler, K. E., Bruce McLean, D., Cosma, C., & Enescu, N. (2019). A borehole seismic reflection survey in support of seepage surveillance at the abutment of a large embankment dam. In J. Lorenzo & W. Doll (Eds.), *Levees and Dams: Advances in Geophysical Monitoring and Characterization* (1st ed., pp. 41–67). Springer International Publishing.  
[https://doi.org/10.1007/978-3-030-27367-5\\_3](https://doi.org/10.1007/978-3-030-27367-5_3)
- Butler, K. E., Danchenko, D., de Gante Carillo, E., Boulay, D. E., Yun, T., MacQuarrie, K. T. B., Campbell, I., & Mclean, D. B. (2023). Towards quantitative spatially resolved estimates of dam seepage by time-lapse electrical resistivity imaging (ERI). *35th Symposium on Application of Geophysics to Engineering and Environmental Problems (SAGEEP)*, 1.
- Canales, R. M., Kozlovskaya, E., Lunkka, J. P., Guan, H., Banks, E., & Moio, K. (2020). Geoelectric interpretation of petrophysical and hydrogeological parameters in reclaimed mine tailings areas. *Journal of Applied Geophysics*, 181, 104139.  
<https://doi.org/10.1016/j.jappgeo.2020.104139>
- Cantré, S., Olschewski, J., & Saathoff, F. (2017). Full-Scale Flume Experiments to Analyze the Surface Erosion Resistance of Dike Embankments Made of Dredged Materials. *Journal of Waterway, Port, Coastal, and Ocean Engineering*, 143(3), 4017001.  
[https://doi.org/doi:10.1061/\(ASCE\)WW.1943-5460.0000375](https://doi.org/doi:10.1061/(ASCE)WW.1943-5460.0000375)

- Cardarelli, E., Cercato, M., & De Donno, G. (2014). Characterization of an earth-filled dam through the combined use of electrical resistivity tomography, P- and SH-wave seismic tomography and surface wave data. *Journal of Applied Geophysics*, *106*, 87–95. <https://doi.org/10.1016/j.jappgeo.2014.04.007>
- Carey, A. M., Paige, G. B., Carr, B. J., & Dogan, M. (2017). Forward modeling to investigate inversion artifacts resulting from time-lapse electrical resistivity tomography during rainfall simulations. *Journal of Applied Geophysics*, *145*, 39–49. <https://doi.org/10.1016/j.jappgeo.2017.08.002>
- Carr, S., Pringle, J. K., Doyle, P., Wisniewski, K. D., & Stimpson, I. G. (2020). Scallywag bunkers: geophysical investigations of WW2 Auxiliary Unit Operational Bases (OBs) in the UK. *Journal of Conflict Archaeology*, *15*(1), 4–31. <https://doi.org/10.1080/15740773.2020.1822102>
- Čejka, F., & Beneš, V. (2015). *Geophysical investigation of the levee in Paull Holme Strays*.
- Chambers, J. E., Gunn, D. A., Wilkinson, P. B., Meldrum, P. I., Haslam, E., Holyoake, S., Kirkham, M., Kuras, O., Merritt, A., & Wragg, J. (2014). 4D electrical resistivity tomography monitoring of soil moisture dynamics in an operational railway embankment. *Near Surface Geophysics*, *12*(1), 61–72. <https://doi.org/10.3997/1873-0604.2013002>
- Chambers, J. E., Wilkinson, P. B., Kuras, O., Ford, J. R., Gunn, D. A., Meldrum, P. I., Pennington, C. V. L., Weller, A. L., Hobbs, P. R. N., & Ogilvy, R. D. (2011). Three-dimensional geophysical anatomy of an active landslide in Lias Group mudrocks, Cleveland Basin, UK. *Geomorphology*, *125*(4), 472–484. <https://doi.org/10.1016/j.geomorph.2010.09.017>
- Charles, J. A., Tedd, P., & Warren, A. (2011). *Delivering benefits through evidence: Lessons from historical dam incidents*. Environment Agency.
- Chen, C., Chen, S.-C., Chen, K.-H., & Liu, Z.-H. (2018). Thermal monitoring and analysis of the large-scale field earth-dam breach process. *Environment Monitoring and Assessment*, *190*, 236–247.
- Chen, H., Lee, C. F., & Law, K. T. (2004). Causative Mechanisms of Rainfall-Induced Fill Slope Failures. *Journal of Geotechnical and Geoenvironmental Engineering*, *130*(6), 593–602.

[https://doi.org/doi:10.1061/\(ASCE\)1090-0241\(2004\)130:6\(593\)](https://doi.org/doi:10.1061/(ASCE)1090-0241(2004)130:6(593))

Chen, X., Guo, Z., Liu, C., Liu, J., & Wu, Q. (2022). Groundwater Detection Using the Pseudo-3D Resistivity Method: A History of Case Studies. *Applied Sciences (Switzerland)*, 12(13).

<https://doi.org/10.3390/app12136788>

Cho, I. K., Ha, I. S., Kim, K. S., Ahn, H. Y., Lee, S., & Kang, H. J. (2014a). 3D effects on 2D resistivity monitoring in earth-fill dams. *Near Surface Geophysics*, 12(1), 73–81.

<https://doi.org/10.3997/1873-0604.2013065>

Cho, I. K., Ha, I. S., Kim, K. S., Ahn, H. Y., Lee, S., & Kang, H. J. (2014b). 3D effects on 2D resistivity monitoring in earth-fill dams. *Near Surface Geophysics*, 12(1), 73–81.

<https://doi.org/10.3997/1873-0604.2013065>

Cho, I. K., Kim, Y. J., & Song, S. H. (2022). Quantitative Evaluation of Leak Index from Electrical Resistivity and Induced Polarization Surveys in Embankment Dams. 25(3), 120–128.

Chopperla, K. S. T., & Ideker, J. H. (2022). Using electrical resistivity to determine the efficiency of supplementary cementitious materials to prevent alkali-silica reaction in concrete. *Cement and Concrete Composites*, 125(September 2021), 104282.

<https://doi.org/10.1016/j.cemconcomp.2021.104282>

Clarke, D., & Smethurst, J. A. (2010). Effects of climate change on cycles of wetting and drying in engineered clay slopes in England. *Quarterly Journal of Engineering Geology and Hydrogeology*, 43(4), 473–486. <https://doi.org/10.1144/1470-9236/08-106>

Conlon, R., & Ganong, G. (1966). The foundation of the Mactaquac rockfill dam. *Engineering Journal*, April, 33–38.

Daily, W., Ramirez, A., LaBrecque, D., & Nitao, J. (1992). Electrical Resistivity Tomography of Vadose Water Movement. *Water Resources Research*, 28(5), 1429–1442.

Danchenko, D., & Butler, K. E. (2022). Time-lapse electrical resistivity imaging (ERI) for embankment-seepage monitoring. In B. Jochum (Ed.), *GELMON 2022: 6th International Workshop on Geoelectric Monitoring* (p. 24).

Davydov, V. A., Fedorova, O. I., Gorshkov, V. Y., & Baydikov, S. V. (2021). Assessment of state of earth dam of Elchovka settling pond by combination of electromagnetic soundings

- and polarization methods. *Studia Geophysica et Geodaetica*, 65(2), 206–218.  
<https://doi.org/10.1007/s11200-020-0114-1>
- deGroot-Hedlin, C., & Constable, S. (2002). Occam's inversion to generate smooth, two-dimensional models from magnetotelluric data. *Geophysics*, 55(12), 1613–1624.  
<https://doi.org/10.1190/1.1442813>
- Descloitres, M., Ribolzi, O., Troquer, Y. Le, & Thiébaux, J. P. (2008). Study of water tension differences in heterogeneous sandy soils using surface ERT. *Journal of Applied Geophysics*, 64(3–4), 83–98. <https://doi.org/10.1016/j.jappgeo.2007.12.007>
- Diab, A. M., Elyamany, H. E., & Abd Elmoty, A. E. M. (2011). Effect of mix proportions, seawater curing medium and applied voltages on corrosion resistance of concrete incorporating mineral admixtures. *Alexandria Engineering Journal*, 50(1), 65–78.  
<https://doi.org/10.1016/j.aej.2011.01.013>
- Dimech, A., Cheng, L. Z., Chouteau, M., Chambers, J., Uhlemann, S., Wilkinson, P., Meldrum, P., Mary, B., Fabien-Ouellet, G., & Isabelle, A. (2022). A Review on Applications of Time-Lapse Electrical Resistivity Tomography Over the Last 30 Years : Perspectives for Mining Waste Monitoring. In *Surveys in Geophysics* (Vol. 43, Issue 6). Springer Netherlands.  
<https://doi.org/10.1007/s10712-022-09731-2>
- Driscoll, R. (1983). The influence of vegetation on the swelling and shrinking of clay soils in Britain. *Geotechnique*, 33(2), 93–105.
- Dunbar, J. B., Galan-Comas, G., Walshire, L. A., Wahl, R. E., Yule, D. E., Corcoran, M. K., Bufkin, A. L., & Llopis, J. L. (2017). *Remote Sensing and Monitoring of Earthen Flood-Control Structures Geotechnical and Structures Laboratory*. Vicksburg, USA: US Army Corps of Engineers.
- Dyer, M., Uti, S., & Zielinski, M. (2009). Field survey of desiccation fissuring of flood embankments. *Proceedings of the Institution of Civil Engineers: Water Management*, 162(3), 221–232. <https://doi.org/10.1680/wama.2009.162.3.221>
- Edwards, R. ., Lee, H., & Nabighian, M. N. (1978). On the Theory of Magnetometric Resistivity (MMR) Methods. *Geophysics*, 43(6), 1176–1203.

- Ekwok, S. E., Ben, U. C., Eldosouky, A. M., Qaysi, S., Abdelrahman, kamal, Akpan, A. E., & Andr  s, P. (2022). Towards understanding the extent of saltwater incursion into the coastal aquifers of Akwa Ibom State, Southern Nigeria using 2D ERT. *Journal of King Saud University - Science*, 34(8), 102371. <https://doi.org/10.1016/j.jksus.2022.102371>
- Enea, A., Iosub, M., & Stoleriu, C. C. (2023). A Low-Cost, UAV-Based, Methodological Approach for Morphometric Analysis of Belci Lake Dam Breach, Romania. *Water*, 15(9), 1655.
- Environment Agency. (2021). *LiDAR Composite DTM 2019 - 1m*. <https://www.data.gov.uk/dataset/3fc40781-7980-42fc-83d9-0498785c600c/lidar-composite-dtm-2019-1m>
- Essex County Council. (n.d.). *Landfill Site Information Sheet, Site Name: Hadleigh Sea Wall*.
- European Union. (2004). *Eurocode 7: Geotechnical Design* (Vol. 1).
- Everett, M. E., & Chave, A. D. (2019). Energy flow in terrestrial controlled-source electromagnetic geophysics. *European Journal of Physics*, 40(6). <https://doi.org/10.1088/1361-6404/ab3de5>
- Fargier, Y., Lopes, S. P., Fauchard, C., Fran  ois, D., & C  te, P. (2014). DC-Electrical Resistivity Imaging for embankment dike investigation: A 3D extended normalisation approach. *Journal of Applied Geophysics*, 103, 245–256. <https://doi.org/10.1016/j.jappgeo.2014.02.007>
- Fell, R., & Fry, J. (2007). *Internal Erosion of Dams and their Foundations* (1st ed.). Taylor & Francis.
- Flores-Berrones, R., Ram  rez-Reynaga, M., & Macari, E. J. (2011). Internal Erosion and Rehabilitation of an Earth-Rock Dam. *Journal of Geotechnical and Geoenvironmental Engineering*, 137(2), 150–160. [https://doi.org/doi:10.1061/\(ASCE\)GT.1943-5606.0000371](https://doi.org/doi:10.1061/(ASCE)GT.1943-5606.0000371)
- Foster, M., & Fell, R. (1999). *A Framework for Estimating the Probability of Failure of Embankment Dams by Internal Erosion and Piping Using Event Tree Methods*. University of New South Wales.

- Furlan, J. P. R., dos Santos, L. D. R., Moretto, J. A. S., Ramos, M. S., Gallo, I. F. L., Alves, G. de A. D., Paulelli, A. C., Rocha, C. C. de S., Cesila, C. A., Gallimberti, M., Devóz, P. P., Júnior, F. B., & Stehling, E. G. (2020). Occurrence and abundance of clinically relevant antimicrobial resistance genes in environmental samples after the Brumadinho dam disaster, Brazil. *Science of the Total Environment*, 726, 138100. <https://doi.org/10.1016/j.scitotenv.2020.138100>
- Gallas, J. D. F. (2020). Self-potential (SP) generated by electrokinesis – Efficiency and low cost dam safety. *Journal of Applied Geophysics*, 180, 104122. <https://doi.org/10.1016/j.jappgeo.2020.104122>
- Gandhi, S. M., & Sarkar, B. C. (2016). Geophysical Exploration. In *Essentials of Mineral Exploration and Evaluation* (pp. 97–123). Elsevier.
- Gariano, S. L., & Guzzetti, F. (2016). Landslides in a changing climate. *Earth-Science Reviews*, 162, 227–252. <https://doi.org/10.1016/j.earscirev.2016.08.011>
- Geuzaine, C., & Remacle, J. . (2020). *Gmsh: A three-dimensional finite element mesh generator with built-in pre- and post-processing facilities*. <https://gmsh.info/>
- Gilks, P., May, T., & Curtis, D. (2001). A review and management of AAR at Mactaquac Generating Station. *Proceedings of the Canadian Dam Association*, 167–177.
- Golebiowski, T., Piwakowski, B., Cwiklik, M., & Bojarski, A. (2021). Application of Combined Geophysical Methods for the Examination of a Water Dam Subsoil. *Water*, 13(21), pp2981.
- Google Earth. (2023). *Google Earth*. Available at: <https://earth.google.com/web/>, Accessed: 03-Aug-2023
- Gopalakrishnan, K., Ceylan, H., Kim, S., & Yang, S. (2017). Wireless MEMS for transportation infrastructure health monitoring. In Uttamchandini (eds.) *Wireless MEMS Networks and Applications*. Cambridge, United Kingdom: Woodhead Publishing
- Guedes, V. J. C. B., Borges, W. R., da Cunha, L. S., & Maciel, S. T. R. (2023). Characterization of an earth dam in Brazil from seismic refraction tomography and multichannel analysis of surface waves. *Journal of Applied Geophysics*, 208 (November 2022).

<https://doi.org/10.1016/j.jappgeo.2022.104893>

Gunn, D. A., Chambers, J. E., Dashwood, B. E., Lacinska, A., Dijkstra, T., Uhlemann, S., Swift, R., Kirkham, M., Milodowski, A., Wragg, J., & Donohue, S. (2018). Deterioration model and condition monitoring of aged railway embankment using non-invasive geophysics. *Construction and Building Materials*, *170*, 668–678.

<https://doi.org/10.1016/j.conbuildmat.2018.03.066>

Hammouri, N. A., Husein Malkawi, A. I., & Yamin, M. M. A. (2008). Stability analysis of slopes using the finite element method and limiting equilibrium approach. *Bulletin of Engineering Geology and the Environment*, *67*(4), 471–478.

<https://doi.org/10.1007/s10064-008-0156-z>

Hayley, K., Bentley, L. R., Gharibi, M., & Nightingale, M. (2007). Low temperature dependence of electrical resistivity: Implications for near surface geophysical monitoring. *Geophysical Research Letters*, *34*(18), 1–5. <https://doi.org/10.1029/2007GL031124>

Hen-Jones, R. M., Hughes, P. N., Stirling, R. A., Glendinning, S., Chambers, J. E., Gunn, D. A., & Cui, Y. J. (2017). Seasonal effects on geophysical–geotechnical relationships and their implications for electrical resistivity tomography monitoring of slopes. *Acta Geotechnica*, *12*(5), 1159–1173. <https://doi.org/10.1007/s11440-017-0523-7>

Hermans, T., Kemna, A., & Nguyen, F. (2016). *Covariance-constrained difference inversion of time-lapse electrical resistivity tomography data*. *81*(5).

<https://doi.org/10.1190/geo2015-0491.1>

Hilbich, C., Fuss, C., & Hauck, C. (2011). Automated time-lapse electrical resistivity tomography (ERT) for improved process analysis and long-term monitoring of frozen ground. *Permafrost and Periglacial Processes*, *22*(4), 306–319.

Hojat, A., Arosio, D., Ivanov, V. I., Loke, M. H., Longoni, L., Papini, M., Tresoldi, G., & Zanzi, L. (2020). Quantifying seasonal 3D effects for a permanent electrical resistivity tomography monitoring system along the embankment of an irrigation canal. *Near Surface Geophysics*, *18*(4), 427–443. <https://doi.org/10.1002/nsg.12110>

Holmes, J., Chambers, J., Meldrum, P., Wilkinson, P., Boyd, J., Williamson, P., Huntley, D., Sattler, K., Elwood, D., Sivakumar, V., Reeves, H., & Donohue, S. (2020). Four-



- dimensional electrical resistivity tomography for continuous, near-real-time monitoring of a landslide affecting transport infrastructure in British Columbia, Canada. *Near Surface Geophysics*, 18(4), 337–351. <https://doi.org/10.1002/nsg.12102>
- Holmes, J., Chambers, J., Wilkinson, P., Meldrum, P., Cimpoiașu, M., Boyd, J., Huntley, D., Williamson, P., Gunn, D., Dashwood, B., Whiteley, J., Watlet, A., Kirkham, M., Sattler, K., Elwood, D., Sivakumar, V., & Donohue, S. (2022). Application of petrophysical relationships to electrical resistivity models for assessing the stability of a landslide in British Columbia, Canada. *Engineering Geology*, 301(February). <https://doi.org/10.1016/j.enggeo.2022.106613>
- Horikoshi, K., & Takahashi, A. (2015). Suffusion-induced change in spatial distribution of fine fractions in embankment subjected to seepage flow. *Soils and Foundations*, 55(5), 1293–1304. <https://doi.org/10.1016/j.sandf.2015.09.027>
- Huitzil, E. V., Flores, M. A. P., Hernández, F. J. E., & Delgado, S. M. (2022). Two-dimensional joint inversion of electromagnetic soundings at low induction numbers and direct current resistivity. *Near Surface Geophysics*, July 2021, 1–14. <https://doi.org/10.1002/nsg.12238>
- Hung, Y. C., Lin, C. P., Lee, C. T., & Weng, K. W. (2019). 3D and boundary effects on 2D electrical resistivity tomography. *Applied Sciences (Switzerland)*, 9(15). <https://doi.org/10.3390/app9152963>
- Hunter, J. A., Crow, H. L., Stephenson, W. J., Pugin, A. J. M., Williams, R. A., Harris, J. B., Odum, J. K., & Woolery, E. W. (2022). Seismic site characterization with shear wave (SH) reflection and refraction methods. *Journal of Seismology*, 26(4), 631–652. <https://doi.org/10.1007/s10950-021-10042-z>
- Ikard, S. J., Revil, A., Jardani, A., Woodruff, W. F., Parekh, M., & Mooney, M. (2012). Saline pulse test monitoring with the self-potential method to nonintrusively determine the velocity of the pore water in leaking areas of earth dams and embankments. *Water Resources Research*, 48(4), 1–17. <https://doi.org/10.1029/2010WR010247>
- Jessop, M., Jardani, A., Revil, A., & Kofoed, V. (2018). *Magnetometric resistivity : a new approach and its application to the detection of preferential flow paths in mine waste*

rock dumps. 222–239. <https://doi.org/10.1093/gji/ggy275>

Jodry, C., Palma Lopes, S., Fargier, Y., Sanchez, M., & Côte, P. (2019). 2D-ERT monitoring of soil moisture seasonal behaviour in a river levee: A case study. *Journal of Applied Geophysics*, *167*, 140–151. <https://doi.org/10.1016/j.jappgeo.2019.05.008>

Jones, D. H., & Ashby, M. F. (2019). *Engineering Materials 1 - An Introduction to Properties, Application and Design* (5th ed.). Butterworth-Heinemann.

Jones, G., Sentenac, P., & Zielinski, M. (2014). Desiccation cracking detection using 2-D and 3-D electrical resistivity tomography: Validation on a flood embankment. *Journal of Applied Geophysics*, *106*, 196–211. <https://doi.org/10.1016/j.jappgeo.2014.04.018>

Jouen, T., Clément, R., Henine, H., Chaumont, C., Vincent, B., & Tournebize, J. (2016). Evaluation and localization of an artificial drainage network by 3D time-lapse electrical resistivity tomography. *Environmental Science and Pollution Research*, *25*(24), 23502–23514. <https://doi.org/10.1007/s11356-016-7366-x>

Kemna, A., Kulesa, B., & Vereecken, H. (2002). Imaging and characterisation of subsurface solute transport using electrical resistivity tomography (ERT) and equivalent transport models. *Journal of Hydrology*, *267*(3–4), 125–146. [https://doi.org/10.1016/S0022-1694\(02\)00145-2](https://doi.org/10.1016/S0022-1694(02)00145-2)

Kessouri, P., Furman, A., Huisman, J. A., Martin, T., Mellage, A., Ntarlagiannis, D., Bucker, M., Ehosioko, S., Fernandez, P., Flores-Orozco, A., Kemna, A., Nguyen, F., Pilawski, T., Saneiyani, S., Schmutz, M., Schwartz, N., Weigand, M., Wu, Y., Zhang, C., & Placencia-Gomez, E. (2019). Induced polarization applied to biogeophysics: recent advances and future prospects. *Near Surface Geophysics*, *17*(6), 595–621. <https://doi.org/10.1002/nsg.12072>

Kihara, M., Hiramatsu, K., Shima, M., & Ikeda, S. (2002). Distributed Optical Fiber Strain Sensor for Detecting River Embankment Collapse. *IEICE Transactions on Electronics*, *2002*(1), 952–960.

Kim, J. K., Wee, S. H., Yoo, S. H., Kim, K. H., Noh, J. S., & Kwon, Y. J. (2021). S-wave velocity structures at Yedang Reservoir Dam inferred from amplification characteristics determined using H/V spectral ratios with background noise. *Exploration Geophysics*,

52(5), 590–599. <https://doi.org/10.1080/08123985.2020.1858280>

- Kofoed, V., Jessop, M. L., & Wallace, M. J. (2011). Unique applications of MMR to track preferential groundwater flow paths in dams, mines, environmental sites and leach fields. *The Leading Edge*, 30(2), 192–204.
- Kofoed, V., Jessop, M., & Wallace, M. (2014). Investigating seepage at the Bartley dam , UK. *Hydropower & Dams*, 4, 2–4.
- Kušnirák, D., Dostál, I., Putiška, R., & Mojzeš, A. (2016). Complex geophysical investigation of the Kapušany landslide (Eastern Slovakia). *Contributions to Geophysics and Geodesy*, 46(2), 111–124. <https://doi.org/10.1515/congeo-2016-0008>
- LaBrecque, D. J. ., & Yang, X. (2001). Difference Inversion of ER Data: a Fast Inversion Method for 3-D In Situ Monitoring. *Journal of Environmental and Engineering Geophysics*, 6(2), 83–89.
- Lapenna, V., & Perrone, A. (2022). Time-Lapse Electrical Resistivity Tomography (TL-ERT) for Landslide Monitoring: Recent Advances and Future Directions. *Applied Sciences (Switzerland)*, 12(3). <https://doi.org/10.3390/app12031425>
- Lavigne, F., Lespinasse, F., Gomez, C., & Vermoux, C. (2013). GPR investigation of Si Pamutung archaeological remains. In *The Settlement of Si Pamutung in Pendang Lawas, North Sumatra (9th-13th Centuries CE)*. Ecole Française d’Extrême-Orient.
- Lavoué, F., Van Der Kruk, J., Rings, J., André, F., Moghadas, D., Huisman, J. A., Lambot, S., LWeihermüller, Vanderborght, J., & Vereecken, H. (2010). Electromagnetic induction calibration using apparent electrical conductivity modelling based on electrical resistivity tomography. *Near Surface Geophysics*, 8(6), 553–561. <https://doi.org/10.3997/1873-0604.2010037>
- Lee, B., & Oh, S. (2018). Modified electrical survey for effective leakage detection at concrete hydraulic facilities. *Journal of Applied Geophysics*, 149, 114–130. <https://doi.org/10.1016/j.jappgeo.2017.08.006>
- Leroy, P., & Revil, A. (2004). A triple-layer model of the surface electrochemical properties of clay minerals. *Journal of Colloid and Interface Science*, 270(2), 371–380.

<https://doi.org/10.1016/j.jcis.2003.08.007>

Lin, C. H., Lin, C. P., Hung, Y. C., Chung, C. C., Wu, P. L., & Liu, H. C. (2018). Application of geophysical methods in a dam project: Life cycle perspective and Taiwan experience. *Journal of Applied Geophysics*, *158*, 82–92.

<https://doi.org/10.1016/j.jappgeo.2018.07.012>

Linde, N., & Doetsch, J. (2016). Joint Inversion in Hydrogeophysics and Near-Surface Geophysics. In A. Moorkamp, M., Lelievre, P., Linde, N., & Khan (Ed.), *Integrated Imaging of the Earth* (pp. 119–135). John Wiley & Sons.

<https://doi.org/10.1002/9781118929063.ch7.1>

Linde, N., Ginsbourger, D., Irving, J., Nobile, F., & Doucet, A. (2017). On uncertainty quantification in hydrogeology and hydrogeophysics. *Advances in Water Resources*, *110*(October), 166–181. <https://doi.org/10.1016/j.advwatres.2017.10.014>

Lobbestael, A. J., Athanasopoulos-Zekkos, A., & Colley, J. (2013). Factor of safety reduction factors for accounting for progressive failure for earthen levees with underlying thin layers of sensitive soils. *Mathematical Problems in Engineering*, *2013*, 1–13.

<https://doi.org/10.1155/2013/893602>

Loke, M. H. (2022). *Rapid 3-D Resistivity & IP inversion using the least-squares method*.

<https://www.aarhusgeosoftware.dk>. Accessed: 03-Agu-2023

Loke, M. H., Acworth, I., & Dahlin, T. (2003). A comparison of smooth and blocky inversion methods in 2D electrical imaging surveys. *Exploration Geophysics*, *34*(3), 182–187.

<https://doi.org/10.1071/EG03182>

Loke, M. H., Chambers, J. E., Rucker, D. F., Kuras, O., & Wilkinson, P. B. (2013). Recent developments in the direct-current geoelectrical imaging method. *Journal of Applied Geophysics*, *95*, 135–156. <https://doi.org/10.1016/j.jappgeo.2013.02.017>

Loke, M. H., Wilkinson, P. B., Chambers, J. E., & Strutt, M. (2014). Optimized arrays for 2D cross-borehole electrical tomography surveys. *Geophysical Prospecting*, *62*(1), 172–189.

<https://doi.org/10.1111/1365-2478.12072>

Loke, M. H., Wilkinson, P. B., Dahlin, T., Chambers, J. E., Uhlemann, S., & Dijkstra, T. (2018).

The use of positivity constraints in 4-D ERT inversion. *EAGE-HAGI 1st Asia Pacific Meeting on Near Surface Geoscience and Engineering*, 1–5.

Loperte, A., Soldovieri, F., Palombo, A., Santini, F., & Lapenna, V. (2016). An integrated geophysical approach for water infiltration detection and characterization at Monte Cotugno rock-fill dam (southern Italy). *Engineering Geology*, *211*, 162–170. <https://doi.org/10.1016/j.enggeo.2016.07.005>

Loveridge, F. A., Butcher, D., Spink, T. W., Briggs, K. M., & O'Brien, A. S. (2010). The impact of climate and climate change on infrastructure slopes, with particular reference to southern England. *Quarterly Journal of Engineering Geology and Hydrogeology*, *43*(4), 461–472. <https://doi.org/10.1144/1470-9236/09-050>

Ma, Z., Nie, L., Deng, Z., Xu, X., Yin, X., Shen, J., Wang, K., & Li, N. (2022). Relationship between Induced Polarization Relaxation Time and Hydraulic Characteristics of Water-Bearing Sand. *Applied Sciences (Switzerland)*, *12*(11). <https://doi.org/10.3390/app12115735>

Maalouf, Y., Bièvre, G., Voisin, C., & Khoury, N. (2022). Geophysical monitoring of a laboratory-scale internal erosion experiment. *Near Surface Geophysics*, *20*(4), 365–383. <https://doi.org/10.1002/nsg.12215>

Martínez-Moreno, F. J., Delgado-Ramos, F., Galindo-Zaldívar, J., Martín-Rosales, W., López-Chicano, M., & González-Castillo, L. (2018). Identification of leakage and potential areas for internal erosion combining ERT and IP techniques at the Negratín Dam left abutment (Granada, southern Spain). *Engineering Geology*, *240*(2017), 74–80. <https://doi.org/10.1016/j.enggeo.2018.04.012>

McLachlan, P., Blanchy, G., & Binley, A. (2021). EMagPy: Open-source standalone software for processing, forward modeling and inversion of electromagnetic induction data. *Computers and Geosciences*, *146*(July 2020), 104561. <https://doi.org/10.1016/j.cageo.2020.104561>

McLachlan, P. J., Chambers, J. E., Uhlemann, S. S., & Binley, A. (2017). Geophysical characterisation of the groundwater–surface water interface. *Advances in Water Resources*, *109*, 302–319. <https://doi.org/10.1016/j.advwatres.2017.09.016>

- Meng, Y., Fang, Y., Wan, M., Su, Q., Tian, B., & Tong, F. (2019). Research of concrete dam leakage detection based on anomaly current field of reservoir water. *Journal of Applied Geophysics*, *160*, 242–253. <https://doi.org/10.1016/j.jappgeo.2018.11.016>
- Mester, A. (2015). *Quantitative Two-layer Inversion and Customizable Sensor Array Instrument for Electromagnetic Induction based Soil Conductivity Estimation*. PhD Thesis. Berlin, Germany: Zentralinstitut für Elektronik.
- Michalis, P., & Sentenac, P. (2021). Subsurface condition assessment of critical dam infrastructure with non-invasive geophysical sensing. *Environmental Earth Sciences*, *80*(17). <https://doi.org/10.1007/s12665-021-09841-x>
- Michalis, P., Sentenac, P., & Macbrayne, D. (2016). Geophysical Assessment of Dam Infrastructure: the Mugdock Reservoir Dam Case Study. *3rd Joint International Symposium on Deformation Monitoring*, 1–6.
- Moore, J. R., Boleve, A., Sanders, J. W., & Glaser, S. D. (2011). Self-potential investigation of moraine dam seepage. *Journal of Applied Geophysics*, *74*(4), 277–286. <https://doi.org/10.1016/j.jappgeo.2011.06.014>
- Moreira, C. A., Guireli Netto, L., Camarero, P. L., Bertuluci, F. B., Hartwig, M. E., & Domingos, R. (2022). Application of electrical resistivity tomography (ERT) in uranium mining earth dam. *Journal of Geophysics and Engineering*, *19*(6), 1265–1279. <https://doi.org/10.1093/jge/gxac082>
- Nations, U. (2005). *National Response ( Balochistan ) Annex-A National Response ( NWFP and AJK ) Annex-B*.
- Nazifi, H. M., Gülen, L., Gürbüz, E., & Pekşen, E. (2022). Time-lapse electrical resistivity tomography (ERT) monitoring of used engine oil contamination in laboratory setting. *Journal of Applied Geophysics*, *197*(December 2021). <https://doi.org/10.1016/j.jappgeo.2022.104531>
- Ning, I., & Sava, P. (2018). *Multicomponent distributed acoustic sensing : Concept and theory*. *83*(2). <https://doi.org/10.1190/geo2017-0327.1>
- Noorani, A. G. (1984). The Inundation of Morvi. *Economic and Political Weekly*, *19*(10), 405–

- Norooz, R., Olsson, P. I., Dahlin, T., Günther, T., & Bernstone, C. (2021). A geoelectrical pre-study of Älvkarleby test embankment dam: 3D forward modelling and effects of structural constraints on the 3D inversion model of zoned embankment dams. *Journal of Applied Geophysics*, *191*. <https://doi.org/10.1016/j.jappgeo.2021.104355>
- Olewi, H., Wang, Y., Xiang, N., Augusthus-Nelson, L., Chen, X., & Shabalin, I. (2018). An experimental study of concrete resistivity and the effects of electrode configuration and current frequency on measurement. *6th International Conference on Durability of Concrete Structures, ICDCS 2018, July*, 592–599.
- Oliveira, L. A., Braga, M. A., Prosdociami, G., de Souza Cunha, A., Santana, L., & da Gama, F. (2023). Improving tailings dam risk management by 3D characterization from resistivity tomography technique: Case study in São Paulo – Brazil. *Journal of Applied Geophysics*, *210*(October 2022), 104924. <https://doi.org/10.1016/j.jappgeo.2023.104924>
- Orr, T. L. L. (2008). EN 1997-1 Eurocode 7. *Dissemination of Information Workshop, February*, 1–24.
- Palacky, G. (1987). Resistivity Characteristics of Geological Targets. In *Electromagnetic Methods in Applied Geophysics-Theory* (pp. 53–129). Society of Exploration Geophysicists.
- Pan, Y., Kuang, C. P., Li, L., & Amini, F. (2015). Full-scale laboratory study on distribution of individual wave overtopping volumes over a levee under negative freeboard. *Coastal Engineering*, *97*, 11–20. <https://doi.org/10.1016/j.coastaleng.2014.12.007>
- Panthulu, T. V., Krishnaiah, C., & Shirke, J. M. (2001). Detection of seepage paths in earth dams using self-potential and electrical resistivity methods. *Engineering Geology*, *59*(3–4), 281–295. [https://doi.org/10.1016/S0013-7952\(00\)00082-X](https://doi.org/10.1016/S0013-7952(00)00082-X)
- Pappalardo, G., Imposa, S., Barbano, M. S., Grassi, S., & Mineo, S. (2018). Study of landslides at the archaeological site of Abakainon necropolis (NE Sicily) by geomorphological and geophysical investigations. *Landslides*, *15*(7), 1279–1297. <https://doi.org/10.1007/s10346-018-0951-y>

- Parra, J. . (1988). Electrical response of a leak in a geomembrane liner. *Geophysics*, *53*(11), 1445–1452.
- Pellicer, X. M., Zarroca, M., & Gibson, P. (2012). Time-lapse resistivity analysis of Quaternary sediments in the Midlands of Ireland. *Journal of Applied Geophysics*, *82*, 46–58.  
<https://doi.org/10.1016/j.jappgeo.2012.02.009>
- Perrone, A., Lapenna, V., & Piscitelli, S. (2014). Electrical resistivity tomography technique for landslide investigation: A review. *Earth-Science Reviews*, *135*, 65–82.  
<https://doi.org/10.1016/j.earscirev.2014.04.002>
- Planès, T., Mooney, M. A., Rittgers, J. B. R., Parekh, M. L., Behm, M., & Snieder, R. (2016). Time-lapse monitoring of internal erosion in earthen dams and levees using ambient seismic noise. *Géotechnique*, *66*(4), 301–312. <https://doi.org/10.1680/jgeot.14.P.268>
- Plattner, A. (2020). GPRPy: Open-source ground-penetrating radar processing and visualization software. *The Leading Edge*, *39*(5), 332–337.
- Polemio, M., & Lollino, P. (2011). Failure of infrastructure embankments induced by flooding and seepage: A neglected source of hazard. *Natural Hazards and Earth System Science*, *11*(12), 3383–3396. <https://doi.org/10.5194/nhess-11-3383-2011>
- Popescu, M., Șerban, R. D., Urdea, P., & Onaca, A. (2016). Conventional geophysical surveys for landslide investigations: Two case studies from Romania. *Carpathian Journal of Earth and Environmental Sciences*, *11*(1), 281–292.
- Pringle, J. K., Jervis, J. R., Hansen, J. D., Jones, G. M., Cassidy, N. J., & Cassella, J. P. (2012). Geophysical Monitoring of Simulated Clandestine Graves Using Electrical and Ground-Penetrating Radar Methods: 0-3Years After Burial. *Journal of Forensic Sciences*, *57*(6), 1467–1486. <https://doi.org/10.1111/j.1556-4029.2012.02151.x>
- Pringle, J. K., Stimpson, I. G., Zoon, S. M., Caunt, S., Lane, V. S., Husband, C. R., Jones, G. M., Cassidy, N. J., & Styles, P. (2008). Geophysical characterization of derelict coalmine workings and mineshaft detection: A case study from Shrewsbury, United Kingdom. *Near Surface Geophysics*, *6*(3), 185–194. <https://doi.org/10.3997/1873-0604.2008014>
- Pringle, J. K., Westerman, A. R., Clark, J. D., Guest, J. A., Ferguson, R. J., & Gardiner, A. R.



- (2003). The use of vertical radar profiling (VRP) in GPR survey of ancient sedimentary strata. *Geological Society Special Publication*, 211, 225–246.  
<https://doi.org/10.1144/GSL.SP.2001.211.01.19>
- Purvance, D. T., & Andricevic, R. (2000). On the electrical-hydraulic conductivity correlation in aquifers. *Water Resources Research*, 36(10), 2905–2913.  
<https://doi.org/10.1029/2000WR900165>
- Pytharouli, S., Michalis, P., & Raftopoulos, S. (2019). From theory to field evidence: Observations on the evolution of the settlements of an earthfill dam, over long time scales. *Infrastructures*, 4(4). <https://doi.org/10.3390/infrastructures4040065>
- RadExPro. (2023). *RadExPro*. <https://radexpro.com/>
- Rahimi, S., Moody, T., Wood, C. M., Kouchaki, B. M., Barry, M., Tran, K., & King, C. (2019). Mapping Subsurface Conditions and Detecting Seepage Channels for an Embankment Dam Using Geophysical Methods: A Case Study of the Kinion Lake Dam. *Journal of Environmental and Engineering Geophysics*, 24(3), 373–386.
- Rahimi, S., Wood, C. M., Coker, F., Moody, T., Bernhardt-Barry, M., & Mofarraj Kouchaki, B. (2018). The combined use of MASW and resistivity surveys for levee assessment: A case study of the Melvin Price Reach of the Wood River Levee. *Engineering Geology*, 241, 11–24. <https://doi.org/10.1016/j.enggeo.2018.05.009>
- Revil, A. (2012). Spectral induced polarization of shaly sands: Influence of the electrical double layer. *Water Resources Research*, 48(2), 1–23.  
<https://doi.org/10.1029/2011WR011260>
- Revil, A., & Cathles III, L. M. (1999). Permeability of shaly sands and  $r_2$  is the bulk tortuosity. *Water Resources*, 35(3), 651–662.
- Revil, A., & Jardani, A. (2010). Stochastic inversion of permeability and dispersivities from time lapse self-potential measurements: A controlled sandbox study. *Geophysical Research Letters*, 37(11), 1–5. <https://doi.org/10.1029/2010GL043257>
- Revil, A., Karaoulis, M., Johnson, T., & Kemna, A. (2012). Review: Some low-frequency electrical methods for subsurface characterization and monitoring in hydrogeology.

- Hydrogeology Journal*, 20(4), 617–658. <https://doi.org/10.1007/s10040-011-0819-x>
- Revil, A., Soueid Ahmed, A., Coperey, A., Ravanel, L., Sharma, R., & Panwar, N. (2020). Induced polarization as a tool to characterize shallow landslides. *Journal of Hydrology*, 589(August), 125369. <https://doi.org/10.1016/j.jhydrol.2020.125369>
- Rhoades, N., Manteghi, J. ., Shouse, W., & Alves, P. J. (1989). (1989) Soil Electrical Conductivity and Soil Salinity: New Formulations and Calibrations. *Soil Sciences*, 439, 433–439.
- Richards, K. S., & Reddy, K. R. (2007). Critical appraisal of piping phenomena in earth dams. *Bulletin of Engineering Geology and the Environment*, 66(4), 381–402. <https://doi.org/10.1007/s10064-007-0095-0>
- Richards, K. S., & Reddy, K. R. (2014). Kinetic Energy Method for Predicting Initiation of Backward Erosion in Earthen Dams and Levees. *Environmental and Engineering Geoscience*, 20(1), 85–97.
- Rinaldi, V., Guichon, M., Ferrero, V., Serrano, C., & Ponti, N. (2006). Resistivity Survey of the Subsurface Conditions in the Estuary of the Rio de la Plata. *Journal of Geotechnical and Geoenvironmental Engineering*, 132(1), 72–79. [https://doi.org/10.1061/\(asce\)1090-0241\(2006\)132:1\(72\)](https://doi.org/10.1061/(asce)1090-0241(2006)132:1(72))
- Ringeri, A., Butler, K. E., & McLean, D. B. (2016). Long term monitoring and numerical modelling of self-potential for seepage surveillance at Mactaquac dam, New Brunswick, Canada. *Proceedings of 69th Canadian Geotechnical Conference*, 8 pp.
- Rittgers, J. B., Revil, A., Planes, T., Mooney, M. A., & Koelewijn, A. R. (2015). 4-D imaging of seepage in earthen embankments with time-lapse inversion of self-potential data constrained by acoustic emissions localization. *Geophysical Journal International*, 200(2), 756–770. <https://doi.org/10.1093/gji/ggu432>
- Robinson, D., Binley, A. M., Crook, N., Day-Lewis, F. D., Ferre, T. P. ., Grauch, V. J. ., Knight, R., Knoll, M., Lakshimi, V., Miller, R., Nyquist, J., Pellerin, L., Singha, K., & Slater, L. D. (2008). Advancing process-based watershed hydrological research using near-surface geophysics: a vision for, and review of, electrical and magnetic geophysical methods. *Hydrological Processes*, 22, 3604–3605. <https://doi.org/10.1002/hyp>

- Rosas-Carbajal, M., Linde, N., Kalscheuer, T., & Vrugt, J. A. (2014). Two-dimensional probabilistic inversion of plane-wave electromagnetic data: Methodology, model constraints and joint inversion with electrical resistivity data. *Geophysical Journal International*, 196(3), 1508–1524. <https://doi.org/10.1093/gji/ggt482>
- Rucker, C., & Gunther, T. (2011). The simulation of finite ERT electrodes using the complete electrode model. *Geophysics*, 76(4). <https://doi.org/10.1190/1.3581356>
- Russell, E. J. F., & Barker, R. D. (2010). Electrical properties of clay in relation to moisture loss. *Near Surface Geophysics*, 8(2), 173–180. <https://doi.org/10.3997/1873-0604.2010001>
- Sandmeir. (2023). *Reflex-w*. <https://www.geomatrix.co.uk/software/ground-penetrating-radar/reflex-w/>
- Sandrin, T. R., Dowd, S. E., Herman, D. C., & Maier, R. M. (2009). Aquatic Environments. In *Environmental Microbiology* (Second Edi). Elsevier Inc. <https://doi.org/10.1016/B978-0-12-370519-8.00006-7>
- Sazal, Z., Sanuade, O., & Ismail, A. (2022). Geophysical Characterization of the Carl Blackwell Earth-Fill Dam: Stillwater, Oklahoma, USA. *Pure and Applied Geophysics*, 179(8), 2853–2867. <https://doi.org/10.1007/s00024-022-03078-w>
- Schenato, L. (2017). A Review of Distributed Fibre Optic Sensors for Geo-Hydrological Applications. *Applied Sciences*, 7(9), 896. <https://doi.org/10.3390/app7090896>
- Schuster, R. . (1998). *The Loma Prieta, California earthquake of October 17, 1989* (D. K. Keefer (ed.)). Washington D.C, USA: USGS. <https://pubs.usgs.gov/pp/pp1551/pp1551c/>
- Secretary of State. (2002). *The Landfill (England and Wales) Regulations 2002*. <https://www.legislation.gov.uk/uksi/2002/1559/contents/made>
- Segura, F. R., Nunes, E. A., Paniz, F. P., Paulelli, A. C. C., Rodrigues, G. B., Braga, G. Ú. L., dos Reis Pedreira Filho, W., Barbosa, F., Cerchiaro, G., Silva, F. F., & Batista, B. L. (2016). Potential risks of the residue from Samarco’s mine dam burst (Bento Rodrigues, Brazil). *Environmental Pollution*, 218, 813–825. <https://doi.org/10.1016/j.envpol.2016.08.005>
- Sentenac, P., Benes, V., & Keenan, H. (2018). Reservoir assessment using non-invasive geophysical techniques. *Environmental Earth Sciences*, 77(7), 1–14.

<https://doi.org/10.1007/s12665-018-7463-x>

Shao, S., Yang, X., & Jia, C. (2022). Combining multi-source data to evaluate the leakage pollution and remediation effects of landfill. *Journal of Hydrology*, 610(December 2021), 127889. <https://doi.org/10.1016/j.jhydrol.2022.127889>

Sharma, P. V. (1997). *Environmental and Engineering Geophysics* (1st ed.). Cambridge University Press.

Shearwater. (2023). *Reveal Software*. <https://www.shearwatergeo.com/4/reveal-software>

Sherard, J. L., Decker, R. S., & Ryker, N. L. (1972). Piping in earth dams of expansive clay. *ASCE Speciality Conference: Performance of Earth and Earth Supported Structures.*, 589–626.

Singha, K., Day-Lewis, F. D., Johnson, T., & Slater, L. D. (2015). Advances in interpretation of subsurface processes with time-lapse electrical imaging. *Hydrological Processes*, 29(6), 1549–1576. <https://doi.org/10.1002/hyp.10280>

Sjödahl, P., Dahlin, T., Johansson, S., & Loke, M. H. (2008). Resistivity monitoring for leakage and internal erosion detection at Hällby embankment dam. *Journal of Applied Geophysics*, 65(3–4), 155–164. <https://doi.org/10.1016/j.jappgeo.2008.07.003>

Sjödahl, P., Dahlin, T., & Zhou, B. (2006). 2.5D resistivity modeling of embankment dams to assess influence from geometry and material properties. *Geophysics*, 71(3). <https://doi.org/10.1190/1.2198217>

Slater, L. (2007). Near surface electrical characterization of hydraulic conductivity: From petrophysical properties to aquifer geometries - A review. *Surveys in Geophysics*, 28(2–3), 169–197. <https://doi.org/10.1007/s10712-007-9022-y>

Slater, L., Barrash, W., Montrey, J., & Binley, A. (2014). Electrical-hydraulic relationships observed for unconsolidated sediments in the presence of a cobble framework. *Water Resources & Reservoir Engineering*, 50(7), 5721–5742. <https://doi.org/10.1002/2013WR014631>.Received

SLB. (2023). *VISTA Desktop Seismic Data Processing Software*. <https://www.software.slb.com/products/vista>

Smith, P. et al., (2016). *Paull Holme Strays Ground Investigation Factual Report*. Leeds, United

Kingdom: Environment Agency.

Soil Mechanics. (1989). *Bartley Reservoir*. Available at:

<https://mapapps2.bgs.ac.uk/geoindex/home.html?layer=BGSBoreholes>. Accessed: 03-Aug-2023

Sourbeer, J. J., & Loheide, S. P. (2016). Obstacles to long-term soil moisture monitoring with heated distributed temperature sensing. *Hydrological Processes*, 30(7), 1017–1035.

<https://doi.org/10.1002/hyp.10615>

Sungkono, Husein, A., Prasetyo, H., Bahri, A. S., Monteiro Santos, F. A., & Santosa, B. J. (2014).

The VLF-EM imaging of potential collapse on the LUSI embankment. *Journal of Applied Geophysics*, 109, 218–232. <https://doi.org/10.1016/j.jappgeo.2014.08.004>

Tabrizi, A. A., Elalfy, E., Elkholy, M., Chaudhry, M. H., & Imran, J. (2017). Effects of compaction on embankment breach due to overtopping. *Journal of Hydraulic Research*, 55(2), 236–

247. <https://doi.org/10.1080/00221686.2016.1238014>

Taner, M. ., Cook, E. ., & Neidell, N. S. (1970). *Limitations of the Reflection Seismic Method; Lssons from Computer Simulations*. 35(August), pp551-573.

Tawil, H., & Harriman, B. (2001). Aquifer Performance Under the Mactaquac Dam.

*Proceedings of the Canadian Dam Association*, 99–109.

Telford, W. M., Geldart, L. P., & Sheriff, R. E. (1990). *Applied Geophysics*. Cambridge University Press.

Tresoldi, G., Arosio, D., Hojat, A., Longoni, L., Papini, M., & Zanzi, L. (2019). Long-term

hydrogeophysical monitoring of the internal conditions of river levees. *Engineering Geology*, 259(August 2018), 105139. <https://doi.org/10.1016/j.enggeo.2019.05.016>

Trottet, M., Juda, P., Schiller, A., & Renard, P. (2023). Identification of near-surface karst cavities using the posterior population expansion inverse method applied to electrical resistivity data. *Advances in Karst Sciences*, 160, 179–184.

Tso, C. H. M., Kuras, O., Wilkinson, P. B., Uhlemann, S., Chambers, J. E., Meldrum, P. I., Graham, J., Sherlock, E. F., & Binley, A. (2017). Improved characterisation and modelling of measurement errors in electrical resistivity tomography (ERT) surveys. *Journal of*

- Applied Geophysics*, 146, 103–119. <https://doi.org/10.1016/j.jappgeo.2017.09.009>
- Turki, N., Elaoud, A., Gabtni, H., Trabelsi, I., & Khalfallah, K. K. (2019). *Agricultural soil characterization using 2D electrical resistivity tomography (ERT) after direct and intermittent digestate application*.
- Uhlemann, S., Chambers, J., Wilkinson, P., Maurer, H., Merritt, A., Meldrum, P., Kuras, O., Gunn, D., Smith, A., & Dijkstra, T. (2016). Four-dimensional imaging of moisture dynamics during landslide reactivation. *Journal of Geophysical Research: Earth Surface*, 122(1), 398–418. <https://doi.org/10.1002/2016JF003983>
- Vagnon, F., Comina, C., & Arato, A. (2022). Evaluation of different methods for deriving geotechnical parameters from electric and seismic streamer data. *Engineering Geology*, 303(December 2021), 106670. <https://doi.org/10.1016/j.enggeo.2022.106670>
- van Beek, V. M., de Bruijn, H. T. J., Knoeff, J. G., Bezuijen, A., & Förster, U. (2010). Levee Failure Due to Piping: A Full-Scale Experiment. *International Conference on Scour and Erosion*. [https://doi.org/doi:10.1061/41147\(392\)27](https://doi.org/doi:10.1061/41147(392)27)
- Vargas, C. O. (2019). Analysis and Seismic Design of Tailings Dams and Liquefaction Assessment. *Advances in Soil Mechanics and Geotechnical Engineering*, 392–416.
- VBA. (2014). *Paull Holme Strays ground investigation report*.
- Verdet, C., Anguy, Y., Sirieix, C., Clément, R., & Gaborieau, C. (2018). On the effect of electrode finiteness in small-scale electrical resistivity imaging. *Geophysics*, 83(6), EN39–EN52. <https://doi.org/10.1190/geo2018-0074.1>
- Vilbig, R. A. (2013). *Air-Coupled and Ground-Coupled Ground Penetrating Radar Techniques*. PhD Thesis. Boston, USA: Northeastern University Massachusetts. <https://repository.library.northeastern.edu/files/neu:848>
- Wang, F., Okeke, A. C. U., Kogure, T., Sakai, T., & Hayashi, H. (2018). Assessing the internal structure of landslide dams subject to possible piping erosion by means of microtremor chain array and self-potential surveys. *Engineering Geology*, 234(December 2016), 11–26. <https://doi.org/10.1016/j.enggeo.2017.12.023>
- Wang, Y., Guo, N., Wang, S., & Gu, Y. (2016). Detection of internal erosion in embankment

dams. *International Forum on Energy, Environment and Sustainable Development, Ijeesd*, 87–101.

Whiteley, J. S., Chambers, J. E., Uhlemann, S., Wilkinson, P. B., & Kendall, J. M. (2019).

Geophysical Monitoring of Moisture-Induced Landslides: A Review. *Reviews of Geophysics*, 57(1), 106–145. <https://doi.org/10.1029/2018RG000603>

Whiteley, J. S., Watlet, A., Kendall, J. M., & Chambers, J. E. (2021). Brief communication: The role of geophysical imaging in local landslide early warning systems. *Natural Hazards and Earth System Sciences*, 21(12), 3863–3871. <https://doi.org/10.5194/nhess-21-3863-2021>

Wilkinson, P. B., Chambers, J. E., Meldrum, P. I., Gunn, D. A., Ogilvy, R. D., & Kuras, O. (2010).

Predicting the movements of permanently installed electrodes on an active landslide using time-lapse geoelectrical resistivity data only. *Geophysical Journal International*, 183(2), 543–556. <https://doi.org/10.1111/j.1365-246X.2010.04760.x>

Wilkinson, P. B., Chambers, J. E., Uhlemann, S., Meldrum, P., Smith, A., Dixon, N., & Loke, M.

H. (2016). Electrical Resistivity Tomography Monitoring Data. *Geophysical Research Letters*, 43(3), 1166–1174. <https://doi.org/10.1002/2015GL067494>. Received

Xiangang, J., Jiahua, H., Yunwei, W., Zhipan, N., Fenghui, C., Zuyin, Z., & Zhanyuan, Z. (2018).

The influence of materials on the breaching process of natural dams. *Landslides*, 15(2), 243–255. <https://doi.org/10.1007/s10346-017-0877-9>

Xiangang, J., Wei, Y., Wu, L., & Lei, Y. (2018). Experimental investigation of failure modes and

breaching characteristics of natural dams. *Geomatics, Natural Hazards and Risk*, 9(1), 33–48. <https://doi.org/10.1080/19475705.2017.1407367>

Yang, K. H., & Wang, J. Y. (2018). Closure to discussion of “experiment and statistical

assessment on piping failures in soils with different gradations.” *Marine Georesources and Geotechnology*, 36(3), 376–378. <https://doi.org/10.1080/1064119X.2017.1321072>

Yosef, T. Y., Song, C. R., & Chang, K. T. (2018). Hydro-thermal coupled analysis for health monitoring of embankment dams. *Acta Geotechnica*, 13(2), 447–455.

<https://doi.org/10.1007/s11440-017-0571-z>

- Yun, T., Butler, K. E., & MacQuarrie, K. T. B. (2022). Investigation of seepage near the interface between an embankment dam and a concrete structure: monitoring and modelling of seasonal temperature trends. *Canadian Geotechnical Journal*, 59, 1–44.
- Zhang, J., & Revil, A. (2015). 2D joint inversion of geophysical data using petrophysical clustering and facies deformation. *Geophysics*, 80(5), M69–M88.  
<https://doi.org/10.1190/geo2015-0147.1>
- Zhu, Y., Visser, P. J., Vrijling, J. K., & Wang, G. (2011). Experimental investigation on breaching of embankments. *Science China Technological Sciences*, 54(1), 148–155.  
<https://doi.org/10.1007/s11431-010-4208-9>
- Zumr, D., David, V., Jeřábek, J., Noreika, N., & Krása, J. (2020). Monitoring of the soil moisture regime of an earth-filled dam by means of electrical resistance tomography, close range photogrammetry, and thermal imaging. *Environmental Earth Sciences*, 79(12), 1–11.  
<https://doi.org/10.1007/s12665-020-09052-w>




# Appendix A – Resistivity Imaging of river embankments: 3D effects due to varying water levels in tidal rivers (accepted manuscript)

Received: 5 October 2021 | Accepted: 17 August 2022

DOI: 10.1002/nsg.12234

ORIGINAL ARTICLE

Near Surface Geophysics 

## Resistivity imaging of river embankments: 3D effects due to varying water levels in tidal rivers

John Ball<sup>1,2</sup>  | Jonathan Chambers<sup>2</sup>  | Paul Wilkinson<sup>2</sup>  | Andrew Binley<sup>1</sup> 

<sup>1</sup>Lancaster Environment Centre, Lancaster University, Bailrigg, Lancaster, UK

<sup>2</sup>British Geological Survey, Keyworth, UK

### Correspondence

John Ball, Lancaster Environment Centre, Lancaster University, Bailrigg, Lancaster, LA1 4YQ, UK.  
Email: j.ball@lancaster.ac.uk

### Funding information

British Geological Survey; Engineering and Physical Sciences Research Council

### Abstract

Electrical resistivity tomography (ERT) has seen increased use in the monitoring the condition of river embankments, due to its spatial subsurface coverage, sensitivity to changes in internal states, such as moisture content, and ability to identify seepage and other erosional process with time-lapse ERT. Two-dimensional ERT surveys are commonly used due to time and site constraints, but they are often sensitive to features of anomalous resistivity proximal to the survey line, which can distort the resultant inversion as a three-dimensional (3D) effect. In a tidal embankment, these 3D effects may result from changing water levels and river water salinities. ERT monitoring data at Hadleigh Marsh, UK, showed potential evidence of 3D effects from local water bodies. Synthetic modelling was used to quantify potential 3D effects on tidal embankments. The modelling shows that a 3D effect in a tidal environment occurs (for the geometries studied) when surveys are undertaken at high water levels and at distances less than 4.5 m from the electrode array with 1 m spacing. The 3D effect in the modelling is enhanced in brackish waters, which are common in tidal environments, and with larger electrode spacing. Different geologies, river water compositions, and proximities to the model parameters are expected to induce a varied 3D effect on the ERT data in terms of magnitude, and these should be considered when surveying to minimize artefacts in the data. This research highlights the importance of appropriate geoelectrical measurement design for tidal embankment characterization, particularly with proximal and saline water bodies.

### KEYWORDS

electrical resistivity tomography, embankment, modelling, site effect

## INTRODUCTION

Flood embankments are essential defence infrastructure for protecting sites of societal and economic importance. Such structures can suffer deterioration through time because of internal erosion processes (e.g., piping and suffusion) (Almog et al., 2011; Bersan et al., 2018; Planès et al., 2016; Wang et al., 2018; Yang & Wang, 2018), external erosion (e.g., animal burrowing and scouring by rivers) (Borgatti et al., 2017; Dunbar et al., 2017; Jones et al., 2014) and slope failure

(Dunbar et al., 2017). Therefore, regular monitoring of flood embankments is vital to identify degradation, which may lead to failure of its serviceability limit state through, for example, seepage or slumping.

Traditionally, monitoring of flood embankments involves walkover surveying and geotechnical investigations. Walkover surveys are limited by an inability to detect internal problems where there is no expression of embankment degradation (e.g., soil swelling) at the surface and obscuration by vegetation (Jones et al., 2014; Sentenac et al., 2018). Geotechnical investigations can

This is an open access article under the terms of the [Creative Commons Attribution License](https://creativecommons.org/licenses/by/4.0/), which permits use, distribution and reproduction in any medium, provided the original work is properly cited.

© 2022 The Authors. *Near Surface Geophysics* published by John Wiley & Sons Ltd on behalf of European Association of Geoscientists and Engineers.

*Near Surface Geophysics* 2023;21:93–110.

[wileyonlinelibrary.com/journal/nsg](https://onlinelibrary.wiley.com/journal/nsg) | 93

11790644, 2022, 1, Downloaded from https://onlinelibrary.wiley.com/doi/10.1002/nsg.12234 by British Geological Survey, Wiley Online Library on [23/08/2022]. See the Terms and Conditions (<https://onlinelibrary.wiley.com/terms-and-conditions>) on Wiley Online Library for rules of use; OA articles are governed by the applicable Creative Commons License

provide reliable and relevant data for assessment of the internal conditions of the embankment, but are limited by low spatial and volumetric coverage (Michalis et al., 2016), where extensive investigation is difficult due to their invasive and destructive nature, and the parameters obtained from such investigations are only reliable for the location of the sampling point (Cardarelli et al., 2014).

Geophysical techniques have been increasingly utilized because they are non-invasive (Michalis et al., 2016), are sensitive to changes in the sub-surface which may indicate structural degradation (Jones et al., 2014; Moore et al., 2011) and have the potential to infer geotechnical properties through appropriate petrophysical relationships, as obtained from intrusive investigations and subsequent geotechnical monitoring (Chambers et al., 2014; Gunn et al., 2018; Zhang & Revil, 2015). One commonly used geophysical technique for monitoring flood embankments is electrical resistivity tomography (ERT) (e.g., Amabile et al., 2020; Bièvre et al., 2018; Camarero et al., 2019; Fargier et al., 2014; Jodry et al., 2019; Jones et al., 2014; Michalis & Sentenac, 2021; Rittgers et al., 2015; Tresoldi et al., 2018) due to its sensitivity to porosity, clay content, pore water conductivity (Binley & Slater, 2020), moisture content (Fargier et al., 2014) and internal structure (Chambers et al., 2014), making it useful for detecting subsurface changes which may indicate embankment degradation.

Despite the greater spatial coverage possible with ERT compared to standard geotechnical sampling, and ability to image sub-surface conditions, uncertainties in interpretation of data still exist. One such problem is the 3D effect, in which proximal, but off-survey, resistivity distributions can influence the resistivity values directly beneath the ERT line; Fargier et al., 2014; Hung et al., 2019; Nimmer et al., 2008) under a 2.5D assumption. These can arise from factors such as topographic effects, heterogeneous geology and features of anomalous resistivity nearby, such as a buried pipeline. In a river embankment setting, a key source of a three-dimensional (3D) effect is likely to be the river. Furthermore, a river of a variable stage (water level) and/or fluid electrical conductivity (e.g., from tidal influence) may lead to temporally variability of such 3D effects. Further references to a 3D effect on the data will be related to river-induced effects unless otherwise stated.

On embankments, ERT data are commonly acquired using linear (two-dimensional "2D") electrode arrays, because of the relatively fast inversions and fieldwork convenience, where ERT surveys on an embankment are typically set up on the crest, parallel to the river bank. The 2.5D inversion method (following references to 2D inversion imply the 2.5D assumption) assumes that the resistivity does not vary in the direction perpendicular to the vertical plane below the line. The perpendicular topographic variations of the embankment and chang-

ing water levels to the side violate this assumption (Cho et al., 2014). As such, the data acquired from a 2D survey may be influenced by features adjacent to the survey, for example, lower resistivities from an adjacent river may be mapped onto a 2D survey along a dam crest creating artefacts that are not present in reality.

Normalization methods and combined models have been used to remove influence of some 3D effects which apply to all ERT surveys, such as topography (e.g., Bièvre et al., 2018; Fargier et al., 2014). Other authors have looked at specific 3D effects which might impact ERT data. For example, Hung et al. (2019) investigated the impact on ERT data of a pipe buried proximal to a 2D electrode array. They examined the effects of resistivity ratios between pipeline resistivity and the modelled geology resistivity, pipeline size, embedded depth, electrode spacing, and distance from the source of the 3D effect to the electrode array. Through this, they identified that resistivity ratios of less than 0.1 and large pipeline sizes induce greater 3D effects; pipeline emplacement at greater depths will induce weaker 3D effects, and electrode spacing variations had minimal change in the magnitude of 3D effect observed. This suggests that an adjacent river will induce a significant 3D effect on an ERT survey, given its larger size than a pipeline.

Laboratory (scaled physical model) experimentation has also been used by Hojat et al. (2020) to explore the 3D effect induced by rivers. Their experiment involved filling a plexiglass tank, containing a scaled model of a river levee, with water. Surveys were undertaken at various water levels to represent seasonal variations in water level, and a significant 3D effect was induced by the water body. Through this, they observed changes in apparent resistivity to true resistivity ratios with different electrode spacings. Through laboratory experimentation, it was shown that the 3D effect is larger with increased electrode spacings, because of greater depths of investigation inducing larger sensitivities at depth and hence greater coverage that is potentially affected by adjacent resistivities (Hojat et al., 2020). Further synthetic modelling showed that 3D effects have the potential to decrease with a further increase of electrode spacing, as a decrease in shallow resolution will result in the source of the 3D effect having smaller impact on neighbouring data (Hojat et al., 2020) when the source has a fixed position. The 3D effect varies with seasonality, where peak distortions in resistivity in the ERT array are present within winter, predominantly at greater depths below the surface (Tresoldi et al., 2019).

This study aims to build upon these previous approaches to investigate the effect of a tidal influence of a river on ERT data obtained from surveys on the embankment crest. Synthetic models simulating varying water levels and salinities, for a homogeneous and heterogeneous embankment, are used to investigate the relationship between measurement and survey design and 3D artefacts, for the purpose of identifying improved

ERT deployment approaches for tidal embankment monitoring. Previous research has produced contrasting conclusions regarding the relationship between electrode spacing and the magnitude of the 3D effect (e.g., Hojat et al., 2020; Hung et al., 2019). Therefore, further synthetic modelling will be used to help confirm the effect of electrode spacing on the magnitude of 3D effect present from a river proximal to an ERT array.

Alongside synthetic modelling, time-lapse ERT monitoring from the Hadleigh Marsh field site on the Thames estuary, United Kingdom, is used to illustrate potential 3D effects in ERT applied to flood defence monitoring. The series of modelling experiments applied to a synthetic river embankment is performed to examine resistivity features representing a watercourse adjacent to a survey line impact on ERT data. We then offer recommendations on approaches to mitigate a 3D effect, including survey design recommendations and application of methodologies during inversion.

## SYNTHETIC MODELLING

### Methodology

To quantitatively assess the impact of the 3D effects resulting from tidal variations on 2D ERT data parallel to a watercourse, in terms of river water level and resistivity, two synthetic modelling scenarios were designed to simulate a river retreating with a waning tide. In both models, an electrode array, consisting of 48 electrodes at 1 m spacing, was located along the embankment, parallel to the watercourse (see, Figure 1). The embankment crest is 3 m wide, and the array is situated at the midpoint of the crest width. The riverside slope angle is  $14^\circ$ , and the river has a maximum width of 27.8 m. In the associated finite element mesh, the modelled river extended for 101 m beyond the first and last electrode in the orientation parallel to the array. This ensured that the river was sufficiently long to reduce boundary effects or influences on the data from resistivity contrasts between the end of the river in the mesh and the background region. Topography was included in the inversion in order to account for its influence on the ERT data. Scenario one involved a homogeneous embankment, while scenario two included a clay core of differing resistivity to explore the impact of such heterogeneity. The embankment geometry is shown in Figure 1.

Utilizing the mesh generation software Gmsh (Geuzaine & Remacle, 2020), a 3D unstructured finite element mesh was generated, allowing creation of regions representing the river, embankment and clay core for scenario two, each of which can be assigned specific resistivity values. Once the mesh was generated and resistivities were assigned to the river, embankment and clay core, the ERT code R3t (Binley & Slater, 2020) was used to compute a forward model

for a specific scenario. R3t was used, instead of 2D modelling software, due to the ability of a 3D modelling set-up to incorporate external features into the model. Once the forward model was complete, 2% random (Gaussian) noise was added to the resultant apparent resistivities. Following this, the data were inverted in 3D, in order to simulate an inversion of ERT data with an adjacent river which could potentially induce anomalous artefacts in the inversion. The inversions for all models incorporated the 3D geometry of the embankment, enabling topography to be accounted for, reducing the 3D effect associated with this. Each inversion utilized smoothness-constrained (i.e.,  $L_2$  norm) regularization.

Wenner, Schlumberger, and dipole–dipole array configurations were modelled in order to determine the likely impact of a 3D effect based on array configuration. For this, using a river level of 2.95 m at a 1.7-m distance from the electrodes, models were run with electrode sequences corresponding to each configuration and synthetic measurements could then be compared. From this, the electrode configuration with the most severe 3D effect was selected for subsequent modelling. For all electrode configurations, an a spacing of 1–4 m was selected. The Schlumberger array had an  $n$  of 1–9, and the dipole–dipole configuration had an  $n$  of 1–9.

In order to study the effect of changes in river level, the finite element mesh was adjusted for a given river level; the modelled river was decreased by 5 cm vertically, and the riverfront was retreated 20 cm laterally per model scenario (see Figure 1b), which represented a waning tide. The initial conditions were a river that was 1.7 m from the electrode array, at a river height 5 cm lower than the crest elevation (see Figure 1). For each river level, four separate forward models and inversions were undertaken, where river resistivities were assigned as 1, 5, 10 and 20  $\Omega\text{m}$  for each scenario, in order to account for varied river salinities. Once the inversions for each modelled river salinity were completed for the given river level, the synthetic river level was decreased and models were run as before. From this, resistivity values underlying the electrode array could be obtained, allowing comparison between models as to the magnitude of the 3D effect with changing water levels and river salinities. The process described was repeated for every reduction in river level until there was no observed change in resistivity underlying the ERT array from a 3D effect after inversion for all modelled river resistivities.

The homogeneous river embankment was assumed to consist of a clay fill, representing a common construction material for embankments. The assumed resistivity of the embankment was taken to be 40  $\Omega\text{m}$ , based on typical resistivity values for clay (Palacky, 1987). The second modelling scenario consisted of a more conductive clay core, set at 10  $\Omega\text{m}$ , with a more resistive 40  $\Omega\text{m}$  infill, to test for effects of heterogeneity in a set-up representative for such embankments. The water in estuarine environments is typically brackish (Sandrin et al., 2009),

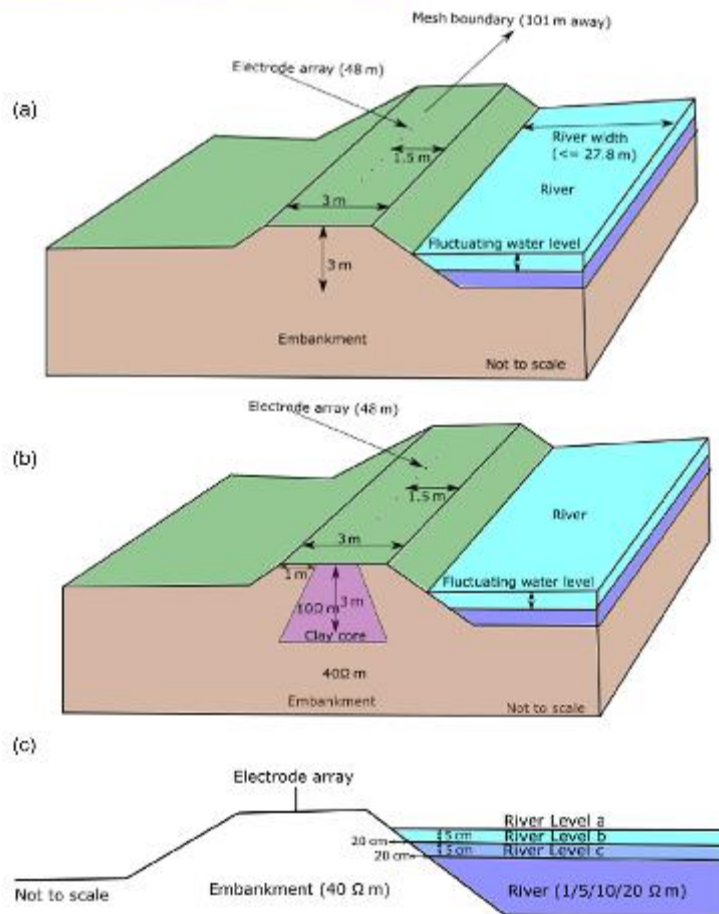


**FIGURE 1** Geometrical representations of the synthetic model problem. (a) The layout of the embankment, river and electrode array orientation for the homogeneous model. The electrode array is located parallel to the river and is situated at the centre of the embankment crest. (b) The heterogeneous model, including the clay core. (c) A 2D cross-sectional image of the synthetic embankment, showing the adjustments to river geometries with each iterant model and modelled river resistivities, representing salinity changes.

so models included ranges of resistivities typical of more brackish water and freshwater, 1, 5, 10, and 20  $\Omega\text{m}$ , the latter representing freshwater rivers with some tidal influence (Palacky, 1987). In addition, modelling procedures were repeated for different electrode spacings to observe the effect of spacing on the associated 3D effect from a tidal setting.

### Synthetic modelling results

The synthetic models were developed and analysed to explore three variables: the effect of a change in dis-

tance between the river and the electrode array; the change in river electrical conductivity (representing a change in salinity); and the electrode spacing used for the survey. Through this, the nature and severity of the 3D effect resulting from changes in salinity and water level can be understood and therefore methods to mitigate the impact can be made. In embankments with greater crest heights, a larger electrode spacing may be chosen to achieve greater depth penetration. Therefore, greater electrode spacings have been modelled to determine potential impacts of a 3D effect where a different electrode setup may be selected for this survey scenario.

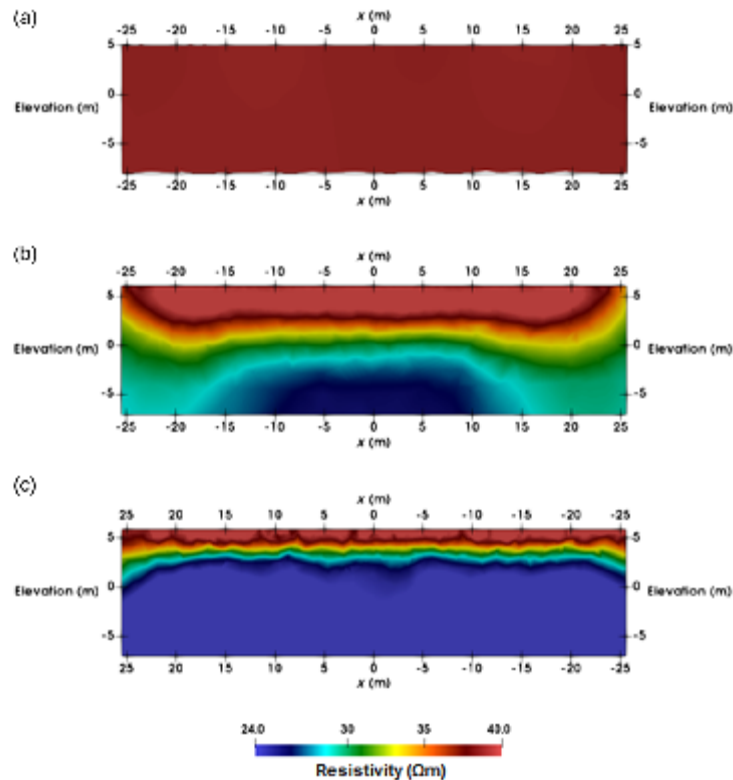


**FIGURE 2** Inversions, showing the 3D effect resulting from differing array types, where the Inverse Image represents the synthetic subsurface resistivity distribution directly beneath the electrode array. (a) Wenner configuration. (b) Schlumberger configuration. (c) Dipole-dipole configuration. For each configuration the river is 1.7 m from the embankment, the river is 0.5 m below crest height, and the river resistivity is  $1 \Omega\text{m}$ . The resistivity of the embankment is  $40 \Omega\text{m}$ . In each image, the embankment height is 5 m.

### Array configurations

The results for the synthetic modelling of Wenner, Schlumberger, and dipole-dipole arrays, using the homogeneous embankment model, are shown in Figure 2. For comparison, the maximal river level was selected, using  $1 \Omega\text{m}$  as a river resistivity, in order to demonstrate the maximum possible impact of a 3D effect from each array type.

As shown in Figure 2, the resistivities for the dipole-dipole array (Figure 2c) are more affected by a 3D effect than the other array configurations, suggesting a greater lateral (off-plane) sensitivity for this array. For the Wenner array (Figure 2a), with a spacing of 1 m, there is unlikely to be any significant 3D effect, but it may be more of an issue if greater electrode spacings are selected for a survey. The Schlumberger array (Figure 2b) shows influence from a 3D effect induced by the river, but with

poorer model resolution compared with dipole-dipole. Therefore, for the purpose of the further synthetic modelling a dipole-dipole array has been selected because of the greater apparent sensitivity to off-plane effects.

### Distance of river from the electrode array

Selected inversions taken from the different modelled river levels were chosen for assessing the resistivities directly underlying the ERT survey for both modelling scenarios. For each model in the homogeneous embankment scenario, the embankment resistivity is  $40 \Omega\text{m}$ , so a significant deviation from this, which gives greater distortion than what can be expected from noise alone, is inferred to be a 3D effect, induced by the modelled river. Likewise, for the heterogeneous model, the clay core resistivity is  $10 \Omega\text{m}$ , with a  $40\text{-}\Omega\text{m}$  background

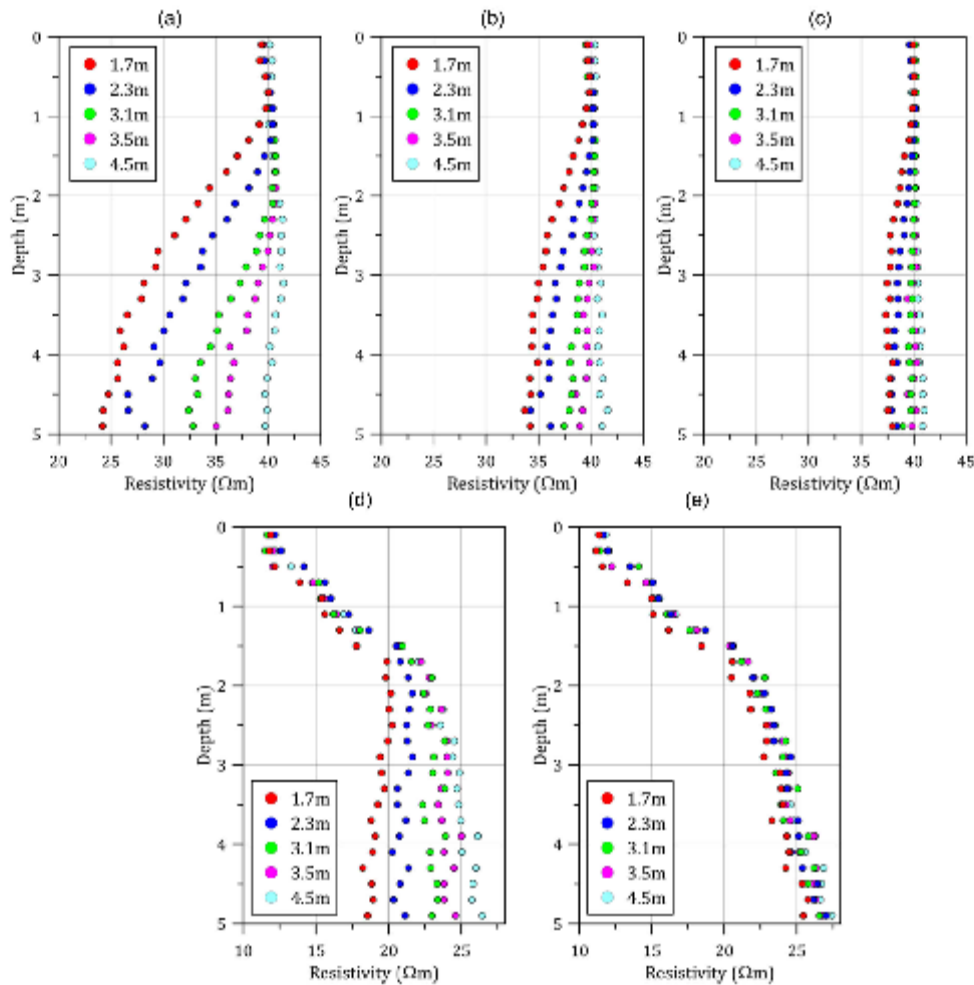


**FIGURE 3** Profiles of resistivity variation below the synthetic ERT array for different river levels in different modelled river resistivities (a) where the river is  $1 \Omega\text{m}$  and the model is homogeneous. (b)  $5 \Omega\text{m}$  and the model is homogeneous. (c)  $10 \Omega\text{m}$  and the model is homogeneous. (d)  $1 \Omega\text{m}$  and the model is heterogeneous. (e)  $10 \Omega\text{m}$  and the model is heterogeneous. The models associated with a river of  $20 \Omega\text{m}$  are not shown, due to the lack of distorted resistivities underlying the electrode array for all distances from the river to the electrode.

resistivity for the remainder of the subsurface, meaning deviations from this represent influence from a 3D effect. Figure 3 is a representation of the resistivities at various depths beneath the ERT array for the synthetic models, showing the resistivities for each modelled water level.

From the models, as is evident in Figure 3, there is a distinct effect on resistivities located at greater depths below the ERT line, while at depths less than 1 m the effect is negligible. As expected, the effect is more severe

where the river is closer to the electrode array, with less pronounced distortions to resistivity with decreasing river level. For the most proximal river level in the homogeneous model, resistivities can reduce by approximately  $15 \Omega\text{m}$  at depths of 3.5 m below the array when the river is least resistive. The magnitude of the effect reduces until the river reaches 4.5 m from the electrode array, where the resistivities approximate to  $40 \Omega\text{m}$  for every modelled river resistivity (i.e., there is no 3D

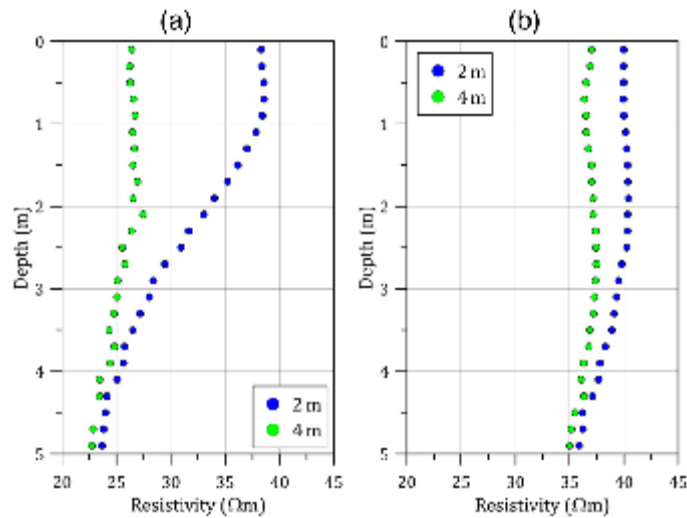


FIGURE 4 Resistivities directly underneath the modelled ERT array across the embankment crest, showing resistivity across depth below the surface, for different electrode spacings. (a) When the river is 1.7 m from the electrode array. (b) When the river is 3.5 m from the electrode array.

effect). Slight discrepancies in the trend with depth are likely impacts of adding 2% noise to the apparent resistivities prior to inversion. The noise does not obscure the trend in the models, indicating that anomalous resistivities from the inversion can be ascribed to the 3D effect induced by changing river levels or salinities, as opposed to random background effects, in a real-life scenario where noise will be present.

In the heterogeneous models (Figures 3d and 4e), with decreasing river level there is no obvious associated trend in resistivity at shallow depths, indicating that resistivity variation is driven by influences from the embankment and 2% added Gaussian noise, not effects from the river at approximately 0.0–1.5 m depth. This is in contrast to depths below 1.5 m, where the resistivities are noticeably less resistive with higher river levels, more proximal to the electrode array. As with the homogeneous model, this indicates that the 3D effect from the river is more pronounced with depth, using a 1-m electrode spacing, and embankment heterogeneity does not obscure such a trend in 3D effect.

### River salinity

The plots in Figure 3 also show a distinct reduction in resistivity with increased modelled river salinities for both a homogeneous and heterogeneous embankment. It is evident from Figure 3 that the trend of the resistivities for modelled river levels is less steep with increased

river resistivity. The effect is most pronounced for the modelled river salinity of 1 Ωm, with a clear decrease in resistivity at depth when the river is proximal to the electrode array. When the modelled river is 20 Ωm, negligible 3D effects are seen. This indicates that a significant 3D effect in river embankments will be most prominent in estuarine environments where water is likely to be brackish. With higher modelled resistivities for the river, which represent freshwater environments, the associated 3D effect is negligible across all river levels. In conditions like this, freshwater is unlikely to induce an impact (provided the array is far enough away from the water body) and a 3D effect would be limited to estuarine or coastal environments.

As a decrease in salinity also reduces the magnitude of the 3D effect in the heterogeneous scenario at depths shallower than the base of the modelled core, it indicates that the bulk of the induced 3D effect, at shallow depth, arises from changes in river level and associated resistivity. However, for all models the resistivity does not trend towards the modelled value of 40 Ωm. This is likely a result of the embankment heterogeneity and modelled clay core values above influencing resistivity values at greater depth.

### Electrode spacing

Plots of resistivities underneath the ERT array for different electrode spacings are shown in Figure 4. The river resistivity is set at 1 Ωm, and selected distances

of electrode array from the river (1.7 m and 3.5 m) are shown for comparison. The plots show the effect of electrode spacing of the electrode array, utilizing the same mesh characteristics. It is evident that with increased electrode spacing there is an associated decrease in resistivity at the ERT array. For an electrode spacing of 4 m, marked decreases of resistivity to 25  $\Omega\text{m}$  are present at shallow depths when the river is most proximal, whereas this is not the case for electrode spacings of 2 m. The results from electrode spacings of 1 m are not shown in the figure, because resistivities are marginally higher, and similar in trend to 2 m spacing. This indicates that for large surveys with very large electrode spacings there will be a significant 3D effect at the ERT array at all depths, which would obscure any underlying features which may be present underneath the embankment when the river level is most proximal to the electrode array. This suggests that for smaller electrode spacings the higher resolution and the shorter influence distances from the river help reduce the 3D effect, especially at shallow depths.

### Embankment heterogeneity

Resistivities for the modelling of the more heterogeneous embankment, consisting of clay core, are represented in Figure 3d,e. Resistivity values proximal to the surface, in the region of the 10- $\Omega\text{m}$  clay core, varied between 11  $\Omega\text{m}$  and 13  $\Omega\text{m}$ . This indicates that the 40- $\Omega\text{m}$  infill modelled for the rest of the embankment has a weak influence on resistivities at shallow depth. Therefore, embankment heterogeneity and complexity are potential sources of a 3D effect, which may influence interpretation of data.

Resistivities at depth, below the clay core, do not trend towards the set value of 40  $\Omega\text{m}$ , levelling out at 25–30  $\Omega\text{m}$ . This is likely due to embankment heterogeneity and weak measurement sensitivity at depth: resistivities in the region below the clay core are influenced by the resistivity assigned to the core.

Overall, trends in resistivity between the homogeneous and heterogeneous models are similar, with decreasing resistivities at depth with declining river levels and salinities.

### Sensitivity distribution

As outlined in Binley and Slater (2020), there are a number of image appraisal methods available for assessing an inverse model. The computational demands of calculating a model resolution matrix are often prohibitive for 3D problems, and so a cumulative sensitivity approach (see, Binley & Slater, 2020) is adopted here. Figure 5 shows a cumulative sensitivity distribution (produced by R3t) for the synthetic modelling, using 1 m electrode

spacing, for when the river level is at its lowest. It can be seen from this that there is measurement sensitivity within the region of the river, indicating that a 3D effect can be detected by the array for this and all other scenarios, where the river will be more proximal to the array.

### HADLEIGH MARSH

The Hadleigh Marsh embankment is approximately 4 km long and 65 m wide (Essex County Council, n.d.). The embankment serves as a flood defence on the northern margin of the Thames estuary and is situated on an eroding coastline (Brand & Spencer, 2019). The present embankment consists of a historic clay embankment, which was subsequently raised in the 1980s using household and commercial landfill waste, capped with puddled clay (Brand & Spencer, 2019). Historical maps suggest that an embankment has existed since the 19th century. Current embankment construction predates required legislation for records of such embankments to be kept, so comprehensive details of waste composition are unknown (Secretary of State, 2002). Hadleigh Marsh is situated in an SSSI (site of special scientific interest), it is a marine-protected area (Brand & Spencer, 2019) and is within the bathing water zone of influence catchments for eight public beaches along the Thames (Environment Agency, 2017). Therefore, it is imperative that the integrity of the embankment is maintained to a suitable standard, so that waste material and leachates do not contaminate the local environment.

Geophysical characterization was undertaken at Hadleigh Marsh to reveal embankment structure and moisture-driven processes within the asset that could be related to tidal forcing, contaminant transport and slope stability. To facilitate long-term monitoring, an automated ERT measurement system, referred to here as PRIME (Holmes et al., 2020), was installed at the site. The system enables near-real-time ERT data collection and has been powered by batteries charged by a solar panel, with remote operation and data retrieval achieved through a 4G telemetric link. The system was attached to five linear electrode arrays, with two orientated approximately parallel to the estuary front and three perpendicular (Figure 6). ERT surveys on all electrode arrays were generally acquired once every 3 days for each line from the April 2017 to present. The electrodes spacings were 2 m, utilizing dipole–dipole measurement configurations with a spacings of 2–46 m and  $n$  in the range of 1–7, where an  $a$  spacing is the current and potential dipole sizes and  $n$  is the current and potential dipole separation.

Time-lapse ERT data from the site were inverted to visualize changes in resistivity with differences in tides, using ResIPy (Blanchy et al., 2020). Initial inversions focused on 2D inversions of line L2 (Figure 6), which was



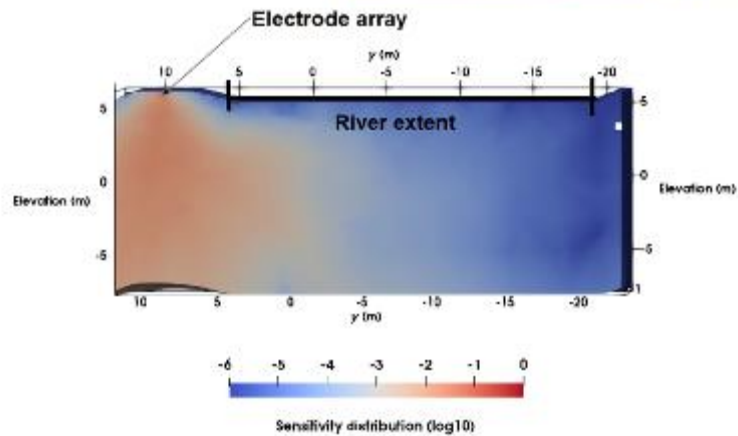


**FIGURE 5** Cumulative sensitivity distribution for the synthetic model outputted from R3t, including an outline of the river region and electrode array for where the river is at its furthest. This sensitivity map is cropped half-way across the mesh, in the direction perpendicular to the embankment, to show how sensitivity is distributed. The electrode array is located at 9.5 m in the  $y$  orientation.



**FIGURE 6** Layout of the PRIME array at Hadleigh Marsh, where L1 and L2 are ERT lines parallel to the riverfront and P1–P3 are ERT lines perpendicular.

the closest line to the estuary and for which the greatest 3D effect due to tidal influence was expected. As with the synthetic model, it is approximately parallel to the river course but is not located on the embankment crest. The 2D time-lapse inversions were undertaken using the difference inversion method (LaBrecque & Yang, 2001). A 3D inversion was also undertaken, incorporating all ERT lines as a means of addressing whether anomalies present in line L2 from a 2D inversion were a result of 3D effects on 2D data. Tidal information taken from the

nearby Sheerness tidal gauge (obtained from the British Oceanographic Data Centre) provided the tidal ranges across the year and was used for selection of data for time-lapse analysis based on the tidal cycle. For each time-lapse inversion, a period of low tide, corresponding with survey timings, was selected for the reference model and the time-lapse inversion continued until the next high tide occurred during the survey period. Several tidal cycles were selected for separate time-lapse inversions, taken at different points in the year, in order

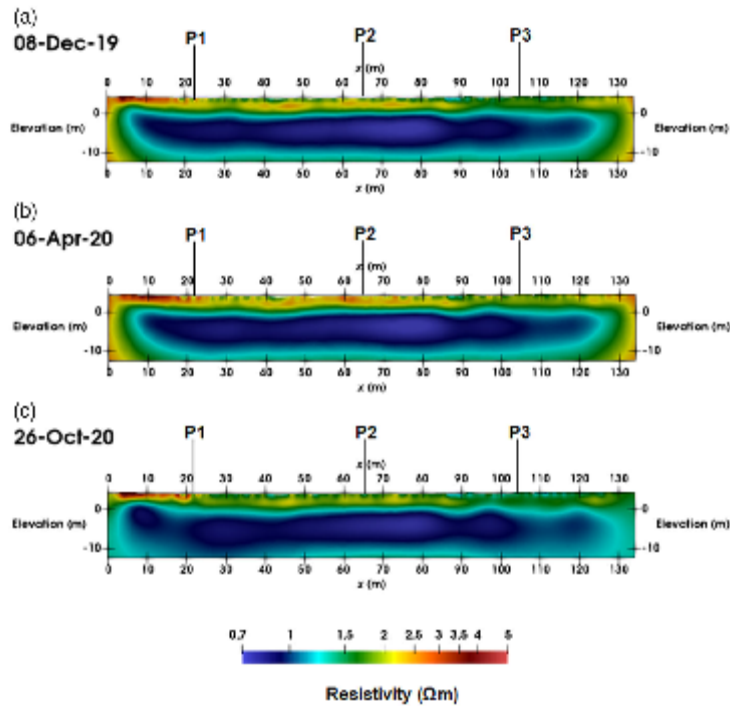


**FIGURE 7** 2D inversions of the ERT data taken from L2 at Hadleigh Marsh (see Figure 2) where each inversion represents the start of a tidal cycle, where it is at a tidal minimum. (a) A reference inversion from 08-Dec-19 (water level 1.08 m). (b) 03-Apr-20 (water level: 1.65 m). (c) 26-Oct-20 (water level: 1.95 m). Water levels were taken from Sheerness tidal gauge, so water levels are an analogous correspondence to Hadleigh Marsh.

to help assess the seasonal impact. For each time-lapse inversion, the reference model was selected as that corresponding to a tidal minimum; data from subsequent dates in that tidal cycle were included for the inversion (the last dataset corresponding to the point prior to the next tidal minimum).

### Hadleigh Marsh results

To explore the potential 3D effect of the River Thames on 2D ERT data at Hadleigh Marsh, 2D inversions were undertaken on the most proximal line to the river, L2, and the intersecting orthogonal lines, P1-P3 (Figure 6). Representative inversions of L2 are shown in Figure 7, taken from the start of a waxing tidal cycle for their respective time cycle and as such represent the initial tidal minimum. In order to demonstrate the tidal nature of any associated 3D effects, a subsequent time-lapse inversion was undertaken when tides were increasing, where the data from Figure 7 were used as a reference dataset, and any changes have been related to

these tidal variations. Figure 8 shows the results of the time-lapse inversion.

The reference inversions for all data sets shown in Figure 7 indicate a conductive subsurface adjacent to the river, where resistivity values are typically less than 10  $\Omega\text{m}$ . However, the upper 2 m is slightly more resistive than at greater depths. It is possible that this is a feature of this section of the embankment, or an effect of prior weather conditions, where greater depths are likely to be more saturated and therefore less resistive. However, a 3D effect resulting from a river is likely to induce a conductive feature at depth, as evident in the synthetic modelling, where decreased resistivities are present at depths below 2 m from the surface. This may explain the trends observed, creating difficulties in the reliability of interpretation. In order to observe changes due to a 3D effect induced by tide, time-lapse inversions have been shown at different points in the tidal cycle, where water level was higher than in the reference inversion.

The difference inversions for L2 show generally small changes in resistivity from the start of the tidal cycle to a time of high-water level. In most inversions, a decrease

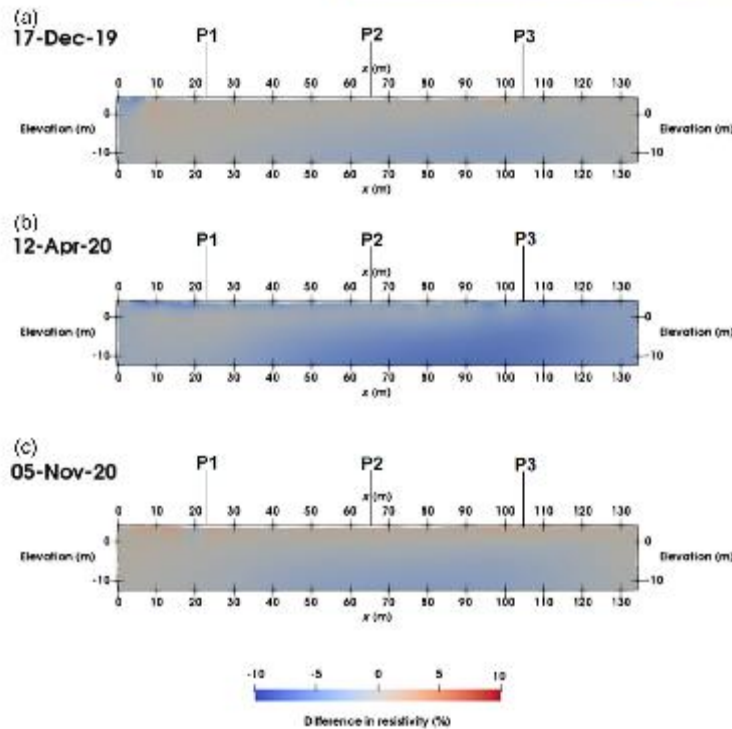


**FIGURE 9** 2D difference Inversions for L2 at Hadleigh Marsh. Each difference Inversion shown corresponds to the reference Inversion of the same letter shown in Figure 7. (a) 17-Dec-19 (water level: 5.64 m, reference inversion: 03-Dec-19). (b) 12-Apr-20 (water level: 5.75 m, reference Inversion: 03-Apr-20). (c) 05-Nov-20 (water level: 5.47 m, reference Inversion: 26-Oct-20). Water levels were taken from Sheerness tidal gauge, so water levels are an analogous correspondence to Hadleigh Marsh.

in resistivity of greater than 5% is noted from depths lower than 5 m for approximately 80 m across the embankment to the left of the section. This is potentially an effect induced by the proximal river, where higher tides are inducing a stronger 3D effect at depths where potential 3D effects are noted in the reference inversions. This part of the section is most proximal to the river (Figure 6), which gives weight to this interpretation. However, due to the low magnitudes, other lateral effects or over/underfitting of data cannot be ruled out. At shallow depths, resistivity variation is not significantly affected by tidal action. Overall, the data show some potential impact at depths, which may correspond to a 3D effect from the river. The April 2020 dataset shows the greatest decrease in resistivity through time, likely due to the ground being less saturated, meaning resistivity contrasts between river and ground beneath the electrode array will be larger.

The 2D inversions of P1-P3 (Figure 9) are generally more resistive than L2, which is assumed to be a result

of the landfill infill, with less resistive anomalies close to the river Thames. Subsequent time-lapse inversions of P1-P3 (Figure 10) show an overall increase in conductivity, assumed to be a result of infiltration from rainfall due to the presence of rainfall in the days following the December reference inversion.

Data from all five electrode lines (see, Figure 6) were utilized in a 3D time-lapse inversion for each tidal cycle at Hadleigh Marsh. Several inversions were run for various tidal cycles across the PRIME monitoring period at Hadleigh Marsh (08-Dec-19 to 17-Dec-19); Figure 11 shows a fence diagram of a selected reference inversion for the ERT, at low tide.

The 3D inversion shows a general consistency in resistivity across each ERT line for the December 2019 dataset. The perpendicular lines, P1-P3, are generally resistive, with similar magnitudes to their 2D inversion counterparts (see Figure 9). Whereas, L1 and L2 are less resistive than P1-P3, which is believed to be influence from the Thames adjacent to L2 and the

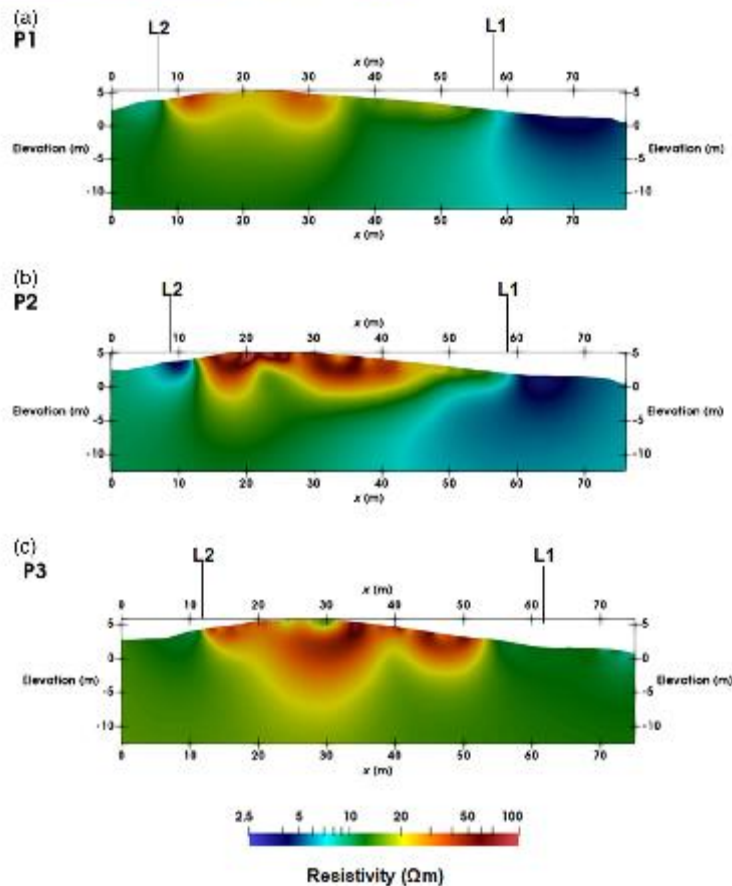


FIGURE 9 2D Inversions of lines P1–P3 on 08-Dec-19. (a) Line P1. (b) Line P2. (c) Line P3.

watercourse located adjacent to L1. The region of lower resistivity at depth in L2, observed in the 2D inversions in Figure 7, is not present in the 3D inversion. This implies that it might be a 3D effect that is resolved in a 3D inversion. Through incorporation of the more resistive P1–P3 and L1, the result is a more representative inversion. The general consistency between resistivities through lines indicates that the 3D inversion is able to provide a more reliable representation of the subsurface without influence of a 3D effect. However, the regions in the 3D model between lines P1–P3 are associated with low levels of resolution due to the large line spacings and are therefore not displayed in Figures 11 (and Figure 12, discussed below). Correlation of resistivities within the inversion, mitigating against such 3D effects, is believed

to occur where the orthogonal lines cross (i.e. at the intersection between L2 and P1).

To further identify potential changes with a tidal cycle, the results of a 3D difference inversion are shown in Figure 12. The results reveal a distinct change in resistivity at shallow depths. In the 2D inversions and synthetic modelling, it was noted that artefacts induced by the 3D effect were present at depth. The 3D inversions do not show a significant change in resistivity at equivalent depths. Therefore, with a similar resistivity distribution to 2D time-lapse inversions and reduced artefacts in lines proximal to the river, it has been suggested that the 3D inversions are able to successfully visualize subsurface conditions with some mitigation of the 3D effect.

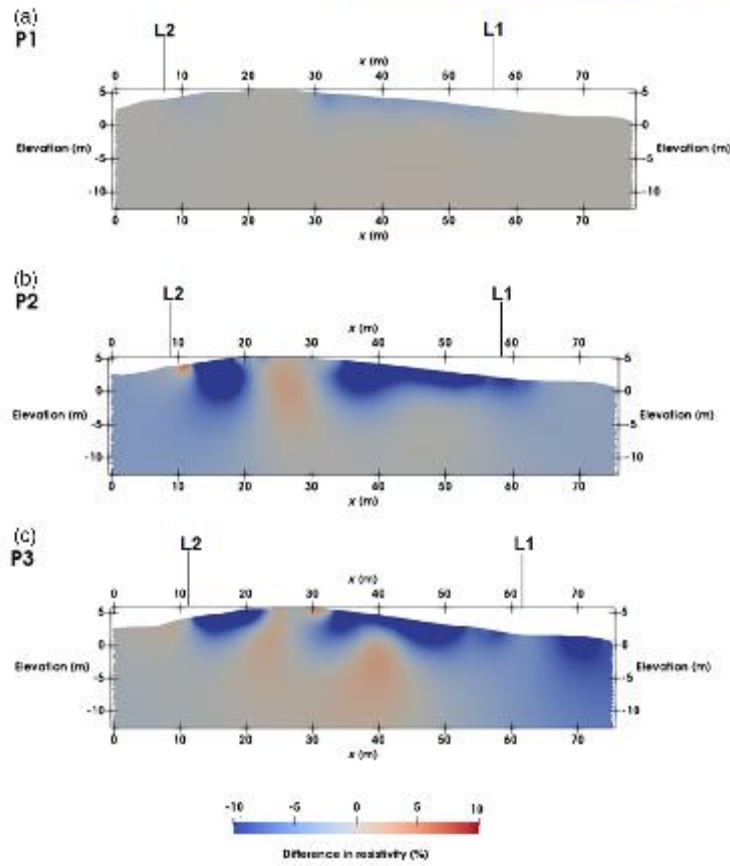


FIGURE 10 2D difference inversions of lines P1–P3 on 08-Dec-19. (a) Line P1. (b) Line P2. (c) Line P3.

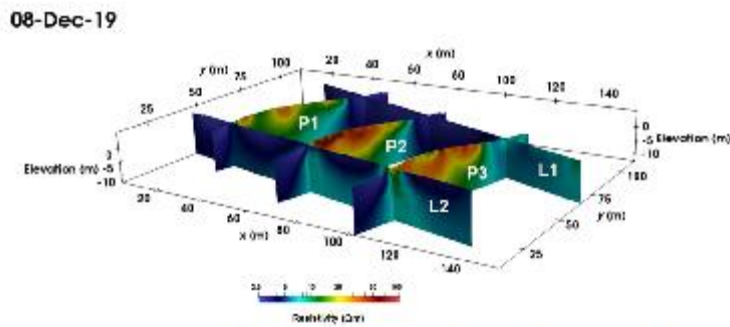


FIGURE 11 3D reference inversion for Hadleigh Marsh, taken from the beginning of the tidal cycle (08-Dec-19), where the maximum tidal ingress is lowest. L2 is adjacent to the River Thames.

17-Dec-19

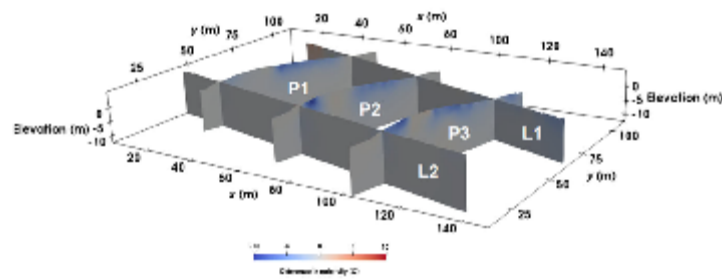


FIGURE 12 A 3D time-lapse inversion for Hadleigh Marsh (17-Dec-19), using Figure 11 as a reference, taken from a time period where the maximum tidal height was at its peak. L2 is adjacent to the River Thames.

## DISCUSSION

The synthetic modelling explored the effects of changing river salinity and river level upon resistivities beneath the array. For a scenario of a clay embankment with a homogeneous resistivity of  $40 \Omega\text{m}$ , it has been determined (for the given geometry) that there are unlikely to be any noticeable effects when the river is 4.5 m away from the electrode array and 0.75 m below crest height (for the geometry of this particular model). Within this limit, resistivity will be decreased at greater depths than 2 m underneath the electrode array where electrode spacings are 2 m or less. The nature of the homogeneous embankment is highly idealized, as it is unlikely that a real embankment will be homogeneous, and the trend and magnitude of affected resistivities are highly impacted by the given parameters. For instance, if the embankment resistivity is higher, higher resistivities from the modelled river would likely induce an effect and the resistivities modelled in this case study could create a greater resistivity contrast. Consequently, the trend of resistivity at depth could be more severe and noticeable at river levels deeper and further away from the electrode array than in this synthetic model. In a more coastal environment embankment, resistivities will likely be smaller than that of the synthetic model ( $40 \Omega\text{m}$ ). However, modelling a larger embankment resistivity enables more universal applicability, such as for tidally influenced rivers, where river salinity will be low, and to enable comparison between freshwater and saltwater settings.

Different slope angles would enable the possibility of the river to decline further vertically for the lateral movement of the river away from the electrode array. Therefore, with steeper slope angles there could be a more pronounced 3D effect possible, given the river is still proximal, laterally, to the electrode array with increased declines vertically and may be within an influence zone. For embankments with larger heights

and wider bases, larger electrode spacings may be chosen for greater depths of investigation. Therefore, embankment geometry is needed to be understood to assess the characteristics of a 3D effect, where different crest heights, base widths and slope angles may impact survey design, the extent of a 3D effect and its magnitude.

The second modelling scenario, with a clay core incorporated into the embankment, provided an opportunity to assess the effect of heterogeneity within the embankment on the 3D effect in the ERT inversions. As with the homogeneous embankment, there was a distinct increase of resistivity at depth with higher river levels, closer to the electrode array. Therefore, the increased heterogeneity modelled within the embankment does not obscure the 3D effect associated with the river at shallow depths. However, embankment heterogeneity influences the inverted model at greater depths, resulting in modelled resistivities from deviating from the true values.

Resistivities of the river have a large influence on the magnitude of the 3D effect. For less resistive river waters, such as brackish conditions typically associated with estuaries, there is likely to be a pronounced 3D effect. Whereas, the higher freshwater resistivities induced negligible 3D effects on the synthetic ERT survey. This highlights the greater need to be aware of potential 3D effects, particularly in estuarine environments, and a need to account for such when working with data obtained from these environments. Freshwater river fluctuations are less likely to induce a 3D effect in environments similar to the synthetic model. However, natural embankments will be more complex, comprising a greater range of resistivities, where elevated water saturation will likely decrease resistivities in the embankment close to the river. This is more difficult to model for generation of 3D effects in a generalized manner or to differentiate the influence of the two contributing

factors (river water level change and changes in soil water content). A heterogeneous model was developed, but no single synthetic modelling scenario is likely to represent a real embankment.

Real resistivities of an embankment will vary over a scale of centimetres and the composition may be highly varied and form irregular layers. The range of resistivities for typical embankment infill, including clay infill, can be higher or lower than what was modelled (Palacky, 1987), so with more resistive infill freshwater may induce a 3D effect with larger ranges in values.

River geometries for the synthetic model have been assumed to be close to the crest height at its peak. Many rivers will be at lower depths and further lateral distances to the electrode array in many survey settings, which could mean they are beyond any influence zone to the ERT data. As such, this shows that for many cases it will be unlikely that large artefacts will be induced in the ERT data, arising from river level fluctuations, and that this study represents a more extreme scenario (e.g., rising water level after a storm event). However, the highly variable nature of a real-life setting to the synthetic model means that there may be some contexts where a 3D effect is likely, due to a strong resistivity contrast between embankment infill and river or highly saline water. Therefore, it is suggested that river levels with the tide and anticipated resistivities of the river and local geology are known for the survey, in order to enable an estimation of whether a 3D effect is likely.

Electrode spacings of 1, 2 and 4 m were modelled in our synthetic study. It was noted that there is a steep decrease in shallow resistivity with increased electrode spacing, due to the lower resolution at shallower depths, resulting in a greater influence zone for the river to impact data. A larger depth of penetration with increased electrode spacing will enable a 3D effect to be reliably detected at greater depths below the electrode array. Resistivities resulting from 1 m or 2 m spacing give similar values, but electrode spacings 4 m give marked distortions in resistivity, including at shallow depth. This suggests that when shallow resolution is poorer, there is greater influence from the river as a 3D effect when there are fewer resistivity values at shallow depths beneath the ERT array. All electrode spacings show some distortion at resistivity at greater depth.

The analysis of inversions at Hadleigh Marsh indicates the potential for a 3D effect to influence data and potentially mislead interpretation through artefacts being introduced to the data. The most notable is a feature of abnormally low resistivity located at 2 m depth in survey line L2 when inverted in 2D. This corresponds to observed regions of lower resistivity in the synthetic modelling study, caused by the river. With increased maximum tide height during the month, as observed in the time-lapse inversions, there is a decreased resistivity at depth in the area of L2 closest to the river. This

suggests that the anomalous region of lower resistivity in L2 is probably a 3D effect resulting from the river, which could incorrectly be interpreted to be a region of saline water beneath the array instead. At high tide, resistivities are over 5% less resistive at depth than at low tide. Therefore, sites with pronounced tidal ranges will experience greater potential 3D effects, and sites which are more resistive will see greater resistivity contrasts between artefacts induced by a 3D effect and the embankment resistivity, potentially leading to a greater degree of misinterpretation. When data are inverted in 3D, there is no noticeable conductive region at depth in L2, indicating that 3D inversions could rectify the observed 3D effect in L2 and that incorporating a 3D inversion scheme could aid interpretation of ERT data in tidal settings.

Previous research on an off-centre pipeline had inferred that electrode spacing is unlikely to alter 3D effect magnitudes (Hung et al., 2019), whereas laboratory experimentation and synthetic modelling of different electrode spacings with a change in water infiltration had suggested that increased electrode spacings would increase the 3D effect until shallow resolution had decreased substantially (Hojat et al., 2020). The synthetic modelling here indicates with increased electrode spacing there is more severe decrease in resistivity from a 3D effect, supporting that electrode spacing does alter 3D effect magnitudes. It is therefore suggested that where the suspected source of a 3D effect is larger than the survey, electrode spacings are kept to a minimum feasible level for survey requirements to reduce a 3D effect on surveying at shallow depths if the survey is to be inverted in 2D.

To account for such issues when they are expected, it is suggested that 3D ERT inversions are undertaken where the survey locations are proximal to a river. 3D inversions can incorporate the full embankment geometry and also the resistivity of the adjacent water course. A 3D inversion would reduce the potential artefacts resulting from a 3D effect linked to the river, as observed at Hadleigh Marsh. Ideally, this would involve a 3D ERT survey geometry, which would allow greater restriction of resistivities across the embankment area. However, time and geometrical constraints may prevent a true 3D ERT survey. Utilization of a 3D inversion scheme across all lines at Hadleigh Marsh reduced the 3D effect, suggesting that this suppressed 3D effects from 2D inversion, and previous research indicates that incorporating 3D coverage of potential measurements suppresses the 3D effect (Sjödahl et al., 2006). Whereas, with a singular ERT line in the synthetic model the 3D effect is noticeable. Therefore, to constrain 3D effects, the survey should ideally incorporate more than one line in a series of arrays which cross-cut each other across the survey region and can then be inverted using a 3D approach.

If designing a time-lapse ERT set-up, it is recommended that a reconnaissance survey is undertaken for design of the time-lapse system, where several surveys are run during the day at different times, and with more than one survey line, to account for the effect of distance from the river. This will enable interpretation of how any 3D effect present varies with tide across the day and survey distance from the river, for optimal survey design for later time-lapse monitoring. From the interpretation of the reconnaissance survey, electrode arrays can be located outside of areas with suspected 3D effects present and survey times set for when the tide is forecast to be low, although this will clearly limit to potential to monitor the integrity of the barrier under such events. For surveys close to a river that could create 3D effects, survey design should ideally include several arrays, which are proximal to each other and provide orthogonal coverage of the area. Such surveys, coupled with recognition of the river feature in any forward modelling, will allow fully 3D inversions to be carried out, eliminating 3D effects due to the watercourse.

Future research involving mathematically determining the extent of likely influence for a range of given parameters (e.g., embankment infill resistivity, number of layers, river resistivity) could enable specification for survey design, giving boundaries for survey design as to where 3D surveying may be necessary to mitigate potential 3D effects. Investigation of more complex embankment geometries could be developed to account for 3D effects in other embankment settings. Also, normalization techniques could be developed to reduce the influence of a proximal river, as Fargier et al. (2014) and Bièvre et al. (2018) have utilized for reducing topographic-induced artefacts.

## CONCLUSIONS

A synthetic modelling exercise was developed to assess the change in 3D effect associated with changing river levels, salinities and electrode spacings for a homogeneous and heterogeneous embankment. From this, it was seen that there is a clear 3D effect induced with river resistivities associated with more brackish water, indicating that estuaries are likely to induce a 3D effect on proximal surveys. The 3D effect is noticeable at river distances less than 4.5 m in lateral distance and 0.75 m in vertical height from the electrode array and embankment crest height, respectively. Therefore, a significant 3D effect is most likely where ERT surveys are taken on the riverside flank of an embankment and are unlikely to be impacted where surveys are taken on the landward side. Though specific boundaries for where a 3D effect from a tidal river may be influential are controlled by embankment geometry, the local geology and water content and it is suggested that local conditions are

considered for each survey, since the 3D effect may have a greater or smaller influence distance for different scenarios.

Using time-lapse inversion data taken from tidal cycles at Hadleigh Marsh and modelling of a synthetic embankment, the impacts of the 3D effect have been identified and evaluated, where the nature of the synthetic model has guided interpretation of the presence of the 3D effect at the site and given assessment to whether a 3D effect from tidal action is likely to be experienced in ERT surveys. At Hadleigh Marsh, there was an associated resistive low in data adjacent to the Thames, at depths equivalent to observed 3D effects in the synthetic modelling and areas most proximal to the river, indicating that there is a likelihood that a 3D effect is impacting the data. With greater resistivities, such effects will be more distinguishable and the anomalous resistivities may lead to misinterpretation. This shows a need to address 3D effects resulting from estuaries, which has been explored further in synthetic modelling to assess likely extents of a 3D effect in this environment.

Electrode spacings of 2 m or less in survey sequences have been suggested (for the geometry studied here) to minimize the potential influence from the river on the ERT survey at shallow depths. Alongside this, we recommend that 3D ERT surveying is set up on the riverside of an embankment to reduce artefacts from the water body with a greater degree of resolution in the inversion. If this is not possible, it is suggested that several linear ERT arrays are used (e.g. parallel and/or orthogonal survey lines), which can be inverted using a 3D scheme to reduce potential 3D effects. This study highlights the potential for a 3D effect to be induced in estuarine environments, due to the likely saline water and potential high resistivity contrasts. Future work in this field will involve modelling of more complex embankment geologies and means of reducing any effect

## ACKNOWLEDGEMENTS

The time-lapse ERT survey was obtained using the British Geological Survey Proactive Infrastructure Monitoring Evaluation System (PRIME). The tidal data obtained for designing the time-lapse inversion setup were from the British Oceanographic Data Centre, taken from a tidal gauge located in Sheerness, Essex. This research has been aided through studentship funding from the EPSRC (SEF6818) and BGS BUFI studentship. BGS authors publish with permission of the Executive Director of the BGS (UKRI). The authors are grateful to the associate editor and two anonymous reviewers for their comments.

## DATA AVAILABILITY STATEMENT

The data which supports the research can be made available upon request of the author.



## Appendix B – Input File Codes for Modelling

Input file codes for ERT models used in this thesis have been made available at <https://github.com/jsball93/appendixb>. This contains examples of input scripts required for processing using R2/R3t, where there are associated folders for each case study (synthetic modelling (chapter 3), Hadleigh Marsh, Mactaquac Dam, Bartley Dam and Paull Holme Strays). Each folder contains an example from the ERT modelling and does not include every inverse model run for each case study.

Details of the script input files (r2 or r3t.in, protocol.dat and mesh or mesh3d.dat) can be found in the user guides for R2 and R3t, available here: <http://www.es.lancs.ac.uk/people/amb/Freeware/R3t/R3t.htm>

A readme is present in each folder, describing what is included in each folder.